MODELLING ANISOTHERMAL RECRYSTALLIZATION IN AUSTENITIC STAINLESS STEELS

by
Gareth John Hopkin
Fitzwilliam College
Cambridge

A dissertation submitted for the degree of
Doctor of Philosophy,
at the University of Cambridge,
November 2001

To my parents

When you are experiencing stress in the workplace, there is nothing more soothing than herbal tea. Make the tea in a large mug, add a generous spoonful of organic honey, then pour the contents over the desktop PC of the person who's been getting up your nose.

– Alistair Beaton 1999

Preface

This dissertation is submitted for the degree of Doctor of Philosophy at the University of Cambridge. The research reported herein was carried out under the supervision of Professor H.K.D.H. Bhadeshia FRS at the department of materials science and metallurgy between October 1997 and December 2000. Except where suitable acknowledgements and references are made to the contrary, this work is to the best of my knowledge, original. Neither this, nor any substantially similar dissertation has been or is being submitted for any degree, diploma or other qualification at this, or any other, university. The length of this dissertation does not exceed 60,000 words.

Elements from chapter 6 of this work appeared in the following publication:

G.J. Hopkin and H.K.D.H. Bhadeshia, Proceedings of the 21^{st} Risø International symposium on Materials Science: *Recrystallization – Fundamental Aspects and Relations to Deformed Microstructure*, Editors: N. Hansen, X. Huang, D. Juul Jensen, E.M. Lauridsen, T. Leffers, W. Pantleon, T.J. Sabin and J.A. Wert. Risø National Laboratory, Roskilde, Denmark. 2000.

Gareth John Hopkin

January 2001

Acknowledgements

I would like to thank Professor A.H. Windle for the provision of laboratory facilities in the Department of Materials Science and Metallurgy at the University of Cambridge.

I am very grateful to my supervisor, Professor Harry Bhadeshia, who, has been a boundless source of inspiration to me. I would like to thank the members, past and present, of the phase transformations research group. Special thanks should go to Dr Dave Cole, Dr Lalam Sree Harsha, Dr Carlos Capdevilla Montes, Dr Mike Lord, Dot Downs, Dr Francisca Garcia Caballiero, Dr Philippe Opdenacker and of course Eur. Ing. John Street.

I am indebted to the Avesta Polarit United Kingdom Foundation for Research and Development and Dr. David Dulieu for financial support and the opportunity to undertake this work. I am further indebted to David for his informative and enlightened help with this project. Thanks are also due to Andy Backhouse, Keith Wilford and John Hobson for the provision of samples and data and also to Hans Nordberg for numerous discussions.

I would like to thank my family for their support over my long stay in Cambridge. Finally, I would also like to thank my friends, who have kept me as sane as I ever was – Helen, Jo, Alastair, Neal, Nicky, Roly, Colleen, Cliff, Andrew and Christopher: *"Thank you"*

Abstract

In industry, stainless steel strip is produced by a system of casting, followed by hot and cold rolling. The steel, at this stage may be unacceptably hard for its final use. To alleviate this problem the steel is annealed in order to soften it and improve its ductility. Softening occurs mainly via a process of *recrystallization*, involving the process of nucleation and growth of new, more perfect crystallites which consume the deformed structure.

The kinetics of this process have been represented by overall transformation kinetics theory (also known as KJMA or Avrami theory). This theory was first developed in the late 1930s and since then has been proven to be applicable in a number of different scenarios, from recrystallization to simultaneous multiphase transformations. Overall transformation kinetics was taken as the starting point for this study, but, as demonstrated in chapter 6, the simple version of the theory failed to properly describe the process of recrystallization. The problem could be resolved by taking into account the fact that recrystallization initiates at the grain boundaries. The bulk of the kinetics modelling in this work is therefore based on Cahn's theories for grain boundary nucleated phase transformations. It will be demonstrated that these give a physical and analytically sound description of the recrystallization process.

With recent dramatic increases in available computing power, it has become possible to apply regression techniques which previously would have been too complicated and time consuming. Neural networks are an example of such a regression technique. Historically, numerical analysis has been carried out using methods such as linear regression. The methods produce a line of 'best fit' for the data and are describe in chapter 3, however they are often not sufficiently flexible to capture the complexity in the data. In this study, non-linear neural networks have been used to model the annealing behaviour of different types of stainless steel.

The initial neural network model (as described in chapter 5) was trained using a laboratory dataset as an illustration of the flexibility and power of this method. The neural network models described in chapter 7 are an application of this technique to a dataset gathered from the furnaces of an industrial supplier of stainless steels. Here, the models were trained so as to predict the variation of certain commercially important considerations, such as strip hardness, ultimate tensile strength and recrystallized grain size. The results and success of the models are also described.

All models produced are viewed in the light of their applicability to the industrial process of annealing, and how this may improve the efficiency of stainless steel production.

The final chapter of this dissertation indicates the conclusions that may be drawn from this work. Furthermore, it illustrates where this work may be extended and highlights any points still requiring development.

Included in the appendix is a full copy of the original FORTRAN77 computer code for the overall transformation kinetics model.

List of symbols used

a	factor in Newtonian heating
a^B	kinetic parameter in Cahn theory
A	total grain boundary area
A'	area transformed
A_A	area fraction transformed
A'_e	extended area transformed
A_{Ae}	extended area fraction transformed
$\mathbf{b}$	the Burgers vector
b^B	kinetic parameter in Cahn theory
b, d, c	elements in deformation matrix
c_1	ΔG calculation constant characterised by Dingley and McClean (1967)
$\mathbf{C}$	convarience matrix in Gaussian process
$C_{1\rightarrow 2}$	column labels
d_W	working distance in SEM
D	dataset in neural network
D_S	grain size
E_B	interfacial energy for capped region
E_D	test error in neural network
E_{DL}	the energy of a dislocation
E_{SQ}	regulariser in energy minimisation of neural network
E_w	regularisation parameter in neural network
E_ν	energy change due to spherical cap
f	shape factor
f^B	principal function in Cahn theory of site saturated transformation
$\mathbf{F}$	the force on a boundary in CLS solute drag model
$\mathbf{F}_{retard}$	retarding force on a boundary in a CLS solute drag model
$\mathbf{F}_{zen}$	the Zener pinning pressure
G	Gibbs free energy
G^*	activation energy for nucleation
G_a	number of grains per unit area
G_C	ΔG independent grain boundary activation energy term
G_{Ca}	variable derived for nucleation by Cahn (1956)

G_v	change in energy per unit volume upon bulging
h	the Planck constant
h_i	hidden unit output in neural network
H	hardness
$\mathcal{H}$	neural network model
J	rate of flux of atoms across α/β boundary
k	the Boltzmann constant
k_{Av}	constant in generalised Avrami equation
K_c, K_{sf}, K_v	constants in microstructural path models
K_1^j, K_2^j	constants derived for nucleation by Cahn (1956)
K_{CLS}^1, K_{CLS}^2	constants in the CLS solute drag model
l	length of grain
L	length of bulge
$\bar{L}$	mean linear intercept
LPE	log predictive error
M	grain boundary mobility
$M(\mathbf{w})$	energy minimisation parameter in neural network
n	Avrami exponent
n_G	exponent of ΔG during nucleation
N	number of hidden units in neural network
N_{VS}	number of grains per unit volume
$\dot{N}$	nucleation frequency per unit volume
$\dot{N}_{AA}$	nucleation rate per unit area accounting for zones of transformed boundary
$\dot{N}_B$	nucleation frequency per unit area
N_0	number of nucleation sites per unit volume
O^b	plane surface area of plane P_l
O^B	total plane surface area in a volume V
O_e^β	extended area of recrystallized grains intersected by a plane
O^β	true area of recrystallized grains intersected by a plane
${}^\nu O^B$	grain boundary area per unit volume
P_l, P_o	a plane
$P(\mathcal{H}_i)$	plausibility of $\mathcal{H}_i$
$P(D)$	plausibility of D
$P(D\|\mathcal{H}_i)$	plausibility of D given $\mathcal{H}_i$ (the evidence)

$P(D\|\mathbf{w},\mathcal{H}_i)$	plausibility of D given $\mathbf{w}$ and $\mathcal{H}_i$
$P(\mathcal{H}_i\|D)$	plausibility of $\mathcal{H}_i$ given D
$P(\mathbf{w}\|D,\mathcal{H}_i)$	plausibility of $\mathbf{w}$ given D and $\mathcal{H}_i$ (posterior probability)
$P(\mathbf{w}\|\mathcal{H}_i)$	plausibility of $\mathbf{w}$ given $\mathcal{H}_i$
q	function in microstructural path model
Q	activation energy for atom to jump across α/β boundary
Q_C	variable derived for nucleation by Cahn (1956)
r	radius
r_{zen}	radius of incoherent particle
R	ideal gas constant
R_B	radius of spherical cap
R_R	rolling reduction
S_u	the entropy of the universe
$\mathbf{S}$	deformation matrix
S_1, S_2	strip labels
S_ν	interfacial area per unit volume between recrystallized and deformed grains
t	time
$\mathbf{t}$	target matrix
t_1, t_2	times during Scheil calculation
$t_{1'}$	equivalent time during Scheil calculation
t_m	target in experimental database of a neural network
T	temperature
T_f	true furnace temperature
T_{ff}	indicated furnace temperature
T_R	room or ambient temperature
U_{sd}	solute drag interaction energy
V	volume of sample
V'	true volume transformed
V'_e	extended volume transformed
w, w_i, w_{ij}	weights in neural network model
$\mathbf{w}$	vectorial set of neural network parameters (w_i and θ_j)
$\mathbf{w}_{MP}$	most probable values of $\mathbf{w}$
x_i, x_{ij}	neural network or linear regression input variables
x_N	normalised value of x_i

x_{min}	minimum value of x_i
x_{max}	maximum value of x_i
$\mathbf{x}_n$	input matrix in Gaussian process
$\bar{y}$	predicted value from committee of neural networks
y_i	predicted value from neural network or linear regression
y_m	predicted value of t_m from neural network or linear regression
α_c	control parameter in neural network
β	control parameter in neural network
β_{dinc}	width of diffraction peak
γ	surface energy per unit area
γ_{SFE}	stacking fault energy
γ_{LA}	surface energy per unit area of tilt grain boundary
Γ_1, Γ_2	grains
δ	thickness of foil or wire
δ_ς	jump distance across boundary
$\delta t_{1\rightarrow 4}$	time increments in anisothermal calculation
ΔG	driving force for recrystallization
ΔG_v	driving force for nucleation per unit volume
ΔG_{Class}	the classical energy needed to form a nucleus
ΔG_{CMX}	the maximum value of ΔG_{Class}
ΔG_{mc}	Monte Carlo driving force for recrystallization
ΔG_{SIGBM}	driving force for strain induced grain boundary migration
$\Delta G_{v\Gamma 1}, \Delta G_{v\Gamma 2}$	energy per unit volume
ΔH_act	difference in enthalpy between activated and deformed states
ΔH_o	change in enthalpy of the object
ΔH_s	change in enthalpy of the surroundings
ΔS_{act}	difference in entropy between activated and deformed states
ΔS_o	change in entropy of the object
ΔS_s	change in entropy of the surroundings
ΔS_u	change in entropy of the universe
ϵ_{dinc}	inhomogeneous lattice strain
ζ	fraction recrystallized
ζ_e	extended fraction recrystallized
θ	misorientation angle

θ_m	misorientation angle where high angle properties commence
θ_i	bias in neural network
θ_{LR}	bias in linear regression
κ	angle between two dislocations
λ	distance from grain boundary
μ	shear modulus
μ_{GP}	mean vector in a Gaussian process
ν	characteristic frequency of an atom
ν_m	Gaussian noise in neural network
ν_T	temperature independent nucleation frequency term
ν_V	attempt frequency of nucleation per unit volume
$\nu_{\tau 3}, \nu_{\tau 2}, \nu_{\tau 1}, \nu_{\tau}$	grain volumes
ξ_v	the volume fraction of incoherent second phase particles
Ξ	variable in Cahn kinetics model
ϱ	distance from plane
ρ_D	the dislocation density in the deformed structure
ρ_{RX}	the dislocation density in the recrystallized structure
$\bar{\sigma}$	error associated with committee of neural networks
σ_f	flow stress
σ_ν	perceived Gaussian noise in neural network
σ_w	perceived significance of input in neural network
τ	incubation period for recrystallization nucleus
Υ	velocity
χ_x	concentration of element x
ψ	angle at which backscattered electron is emitted in SEM
Ω	number of permutations

CHAPTER 1

BRIEF INTRODUCTION TO STAINLESS STEEL AND REASONS FOR STUDY

1.1 Stainless steel

Stainless steels are iron base alloys which contain a minimum of 10.5 wt.% chromium. The beneficial effects of chromium additions for corrosion and oxidation resistance were known in a limited way in the mid 19^{th} century, but significant commercial exploitation started only in the second decade of the 20^{th} century.

A wide range of further alloying elements can be used to control the mechanical, physical and corrosion resisting properties of stainless steels. As a result, there is a large family of compositions which can be classified in broad terms by the crystal structures of their matrices.

Stainless steels are used in many high and low technology applications, from the manufacture of cutlery to components for advanced satellites. It has become part of the fabric of modern living and is used daily by almost every member of the developed world.

1.2 Physical properties of stainless steels

The phases (crystal structures) that may be observed in a simple iron, nickel, chromium ternary alloy at ambient pressure are α/δ, γ, σ and α'. α and δ are both referred to as ferrite and are structurally identical *i.e.* body-centred cubic. γ is commonly referred to as austenite and is face-centred cubic (cubic close-packed). σ is an intermetallic compound of iron and chromium and is body-centred tetragonal. α' is either body-centred cubic or tetragonal (depending on the exact composition). However, unlike α or δ, α' (known as martensite) is formed by a displacive decomposition of γ, leading to a metastable and highly strained microstructure consisting of laths or plates. The Fe–Cr phase diagram is illustrated in Fig. 1.1.

A commercially produced stainless steel will usually fall into one of the following classes:

i) Austenitic stainless steels with a face-centred cubic crystal structure.

ii) Ferritic stainless steels with a body-centred cubic crystal structure.

iii) Martensitic stainless steels with a body-centred cubic or body-centred tetragonal crystal structure and being formed by displacive decomposition of austenite.

iv) Duplex stainless steels containing both austenite and ferrite.

Commercial stainless steels are usually designed not to contain σ phase. This is because it has a bad influence on mechanical properties at room temperature *e.g.* poor ductility (Honeycombe and Bhadeshia, 1995).

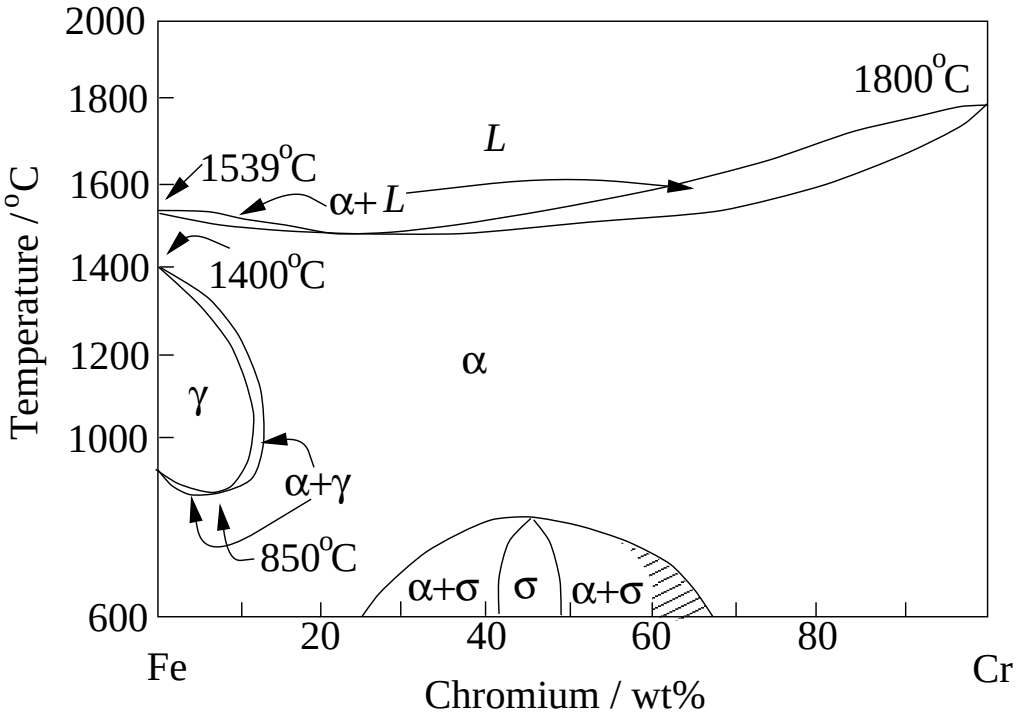

Fig. 1.1 The Cr-Fe phase-diagram (adapted from Honeycombe and Bhadeshia 1995)

Whilst chromium is a key element in stainless steels, other elements also influence their characteristics. Therefore, stainless steels are often classified by reference to a Schaeffler-Schneider diagram (Fig. 1.2). This gives the expected final microstructure for a given chemistry after cooling from a high temperature, such as in the welding process, by inspecting nickel and chromium equivalents which may be calculated thus:

$$\text{Cr equivalent} = \chi_{\text{Cr}} + 2\chi_{\text{Si}} + 1.5\chi_{\text{Mo}} + 5\chi_{\text{V}} + 5.5\chi_{\text{Al}} + 1.75\chi_{\text{Nb}} + 1.5\chi_{\text{Ti}} + 0.75\chi_{\text{W}} \quad (1.1)$$

$$\text{Ni equivalent} = \chi_{\text{Ni}} + \chi_{\text{Co}} + 0.5\chi_{\text{Mn}} + 0.3\chi_{\text{Cu}} + 25\chi_{\text{N}} + 30\chi_{\text{C}} \quad (1.2)$$

wherein χ_x is the weight percentage of element x present (Honeycombe and Bhadeshia, 1995).

Of the four microstructural classes, the most widely used family is the austenitic steels. Additions of principally nickel, but also manganese with nitrogen, are used to stabilise the austenitic structure to room temperature or below. There are many compositions based around additions of 18 wt% chromium and 9 wt% nickel to iron within an early patent from Krupp (1912), whose investigations may be credited with the introduction of austenitic stainless steels. A significant later development was the recognition of the beneficial effect of molybdenum in improving corrosion resistance. Stainless steels are corrosion resistant because the chromium spontaneously forms a thin, protective passive film on the surface of the steel.

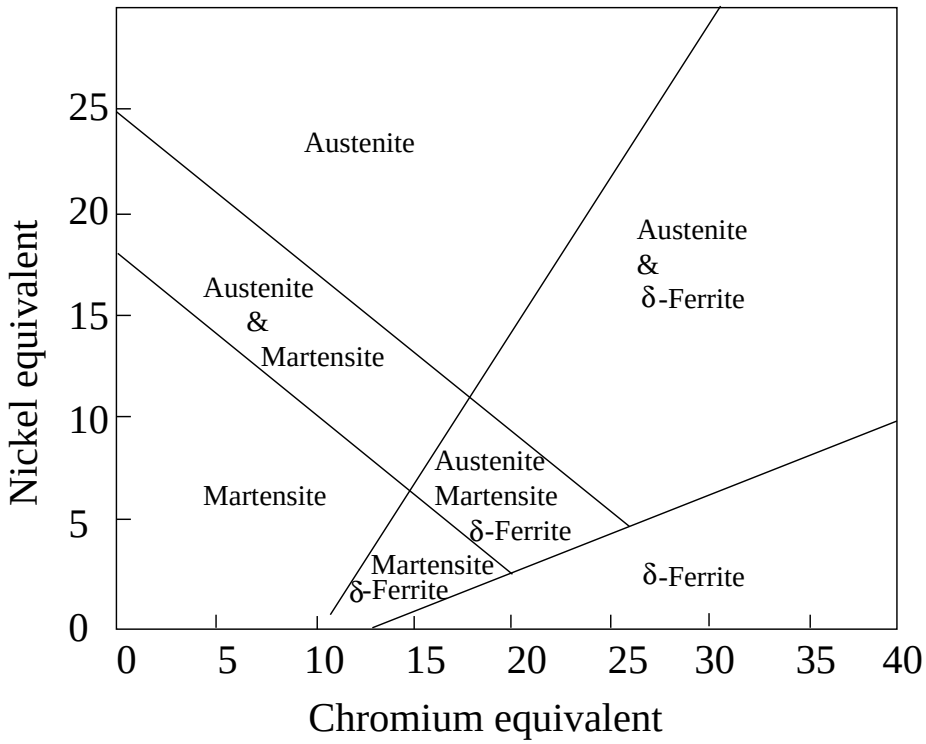

Fig. 1.2 Schaeffler-Schneider diagram giving the basic effect of alloying additions on the structure of Cr-Ni stainless steels (Schneider and Climax Molybdenum Co., 1960)

Molybdenum enhances this passive film by making it stronger and helping it to re-form quickly if it is disrupted by chlorides. Increasing the molybdenum content increases the pitting and crevice corrosion resistance of stainless steels. From Krupp's early work a wide range of compositions have been developed with increasing chromium and molybdenum contents, resulting in high alloy austenitic stainless steels which, with iron contents of around 50 wt%, lie on the borderline between the austenitic stainless steels and nickel-base corrosion resistant alloys.

The family of austenitic stainless steels, studied in this thesis, ranges from an 18 wt% chromium – 8 wt% Nickel low carbon steel to those containing higher levels of chromium and nickel (20 wt% and 25 wt% respectively in this work), with other principle additions of molybdenum, manganese, nitrogen, copper, tungsten, silicon, niobium and titanium.

1.3 Dislocation theory

1.3.1 Dislocations in close-packed metals

This study is concerned with austenitic stainless steels which have a cubic close-packed structure. Slip deformation generally occurs on the {111} close-packed planes and in the $\langle 1\bar{1}0\rangle$ close-packed directions, which are parallel to the shortest lattice vectors. Slip occurs via a dislocation mechanism with a Burgers vector $\mathbf{b} = \frac{a_L}{2}\langle 1\bar{1}0\rangle$, wherein a_L is the lattice

parameter. A dislocation is an imperfection in the lattice and will have associated strain fields. The strain distribution around an edge dislocation is illustrated in Fig. 1.3.

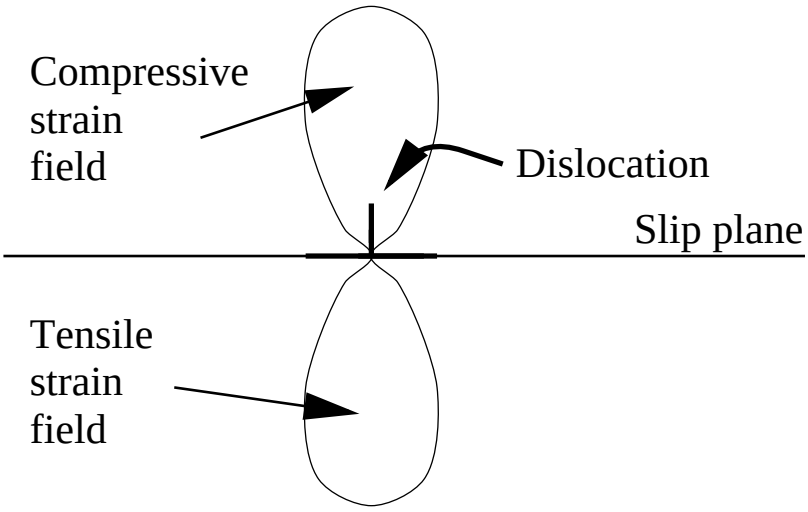

Fig. 1.3 Schematic illustration of strain fields around an edge dislocation

If two different dislocations of a similar sign lie on adjacent planes they may align if they are free to do so. The motion of the dislocations is caused by the strain fields indicated in Fig. 1.3. Compressive strain fields are attracted to tensile strain fields and vice versa. This is illustrated in Fig. 1.4.

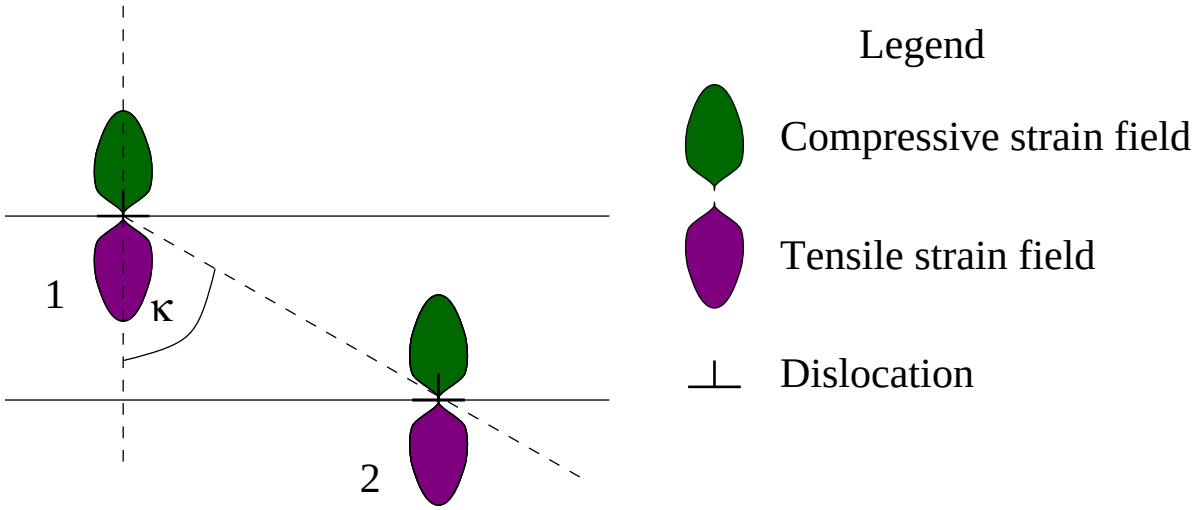

Fig. 1.4 Two dislocation of the same sign but on different planes

Assuming that dislocation 1 is pinned in some way (*e.g.* by an impurity atom) and that dislocation 2 is free to move along the lower plane, if angle κ is less than 45°, then dislocation 2 is attracted to dislocation 1 and will move towards it until it reaches a stable position at $\kappa = 0°$. If angle κ is greater than 45°, then dislocation 2 is repelled and moves away towards

infinity ($\kappa = 90°$). If the two dislocations have opposite signs, they would repel if $\kappa < 45°$ and attract if $\kappa > 45°$, with a stable position $\kappa = 45°$. Dislocations of the same sign on the same plane will repel each other, however, dislocations of opposite signs on the same plane attract and will annihilate one another. These interactions will eventually cause the formation of walls and clusters of dislocations. This process is called polygonisation and is illustrated in Fig. 1.5.

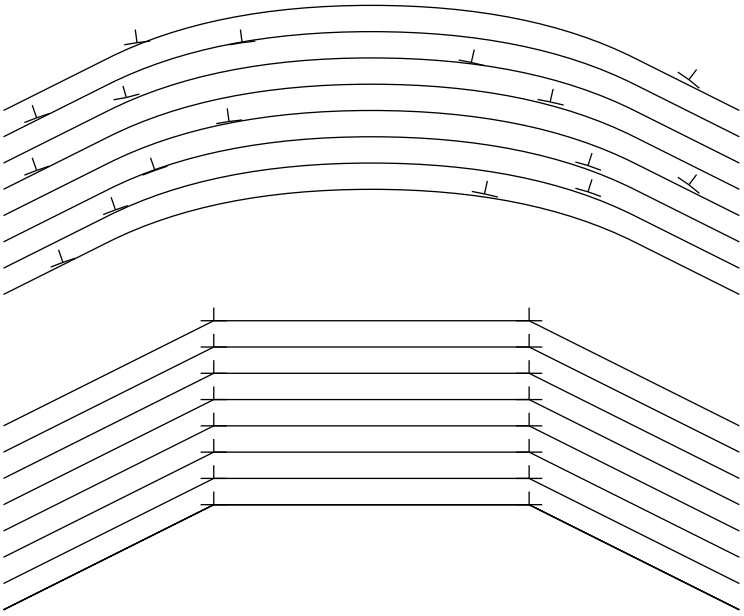

Fig. 1.5 Edge dislocations on adjacent slip planes lining up, forming tilt boundaries and hence a dislocation substructure. A form of polygonisation.

Close-packed metals are made up of close-packed planes (Fig. 1.6) stacked up on top of each other in a periodic fashion.

A cubic close-packed (ccp) metal has its close-packed {111} planes in a stacking sequence ...ABCABC ..., which is in contrast to the corresponding sequence in a hexagonal close-packed (hcp) metal which has its close-packed {001} planes in the sequence ...ABAB .... The Burgers vector, **b**, in a ccp metal is generally $(a_L/2)\langle 110\rangle$, which, on Fig. 1.6 corresponds to $\overrightarrow{B_1B_2}$. The energy per unit length of a dislocation E_{DL} may be approximated as:

$$E_{DL} = \frac{1}{2}\mu|\mathbf{b}|^2 \tag{1.3}$$

where μ is the shear modulus of the matrix. This means that the energy may be lowered by splitting the Burgers vector from $\overrightarrow{B_1B_2}$ into components $\overrightarrow{B_1C}$ and $\overrightarrow{CB_2}$. The latter two have smaller Burgers vectors which are not lattice vectors and hence are referred to as "partial dislocations". Between the two partial dislocations there will be an area where the atoms do not have the correct stacking sequence; this is called a stacking fault with an energy per unit area

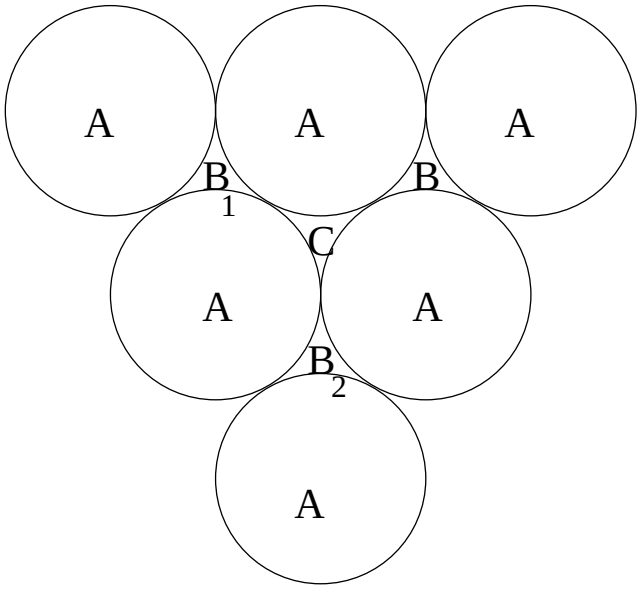

Fig. 1.6 A close-packed plane A, above which B and C represent the possible positions of atoms in the layer above.

of γ_{SFE}. Materials with a low value of γ_{SFE} will, at equilibrium, have widely spaced partial dislocations and those with a high value of γ_{SFE}, will have closely spaced partial dislocations or the dislocation may even remain undissociated.

Dislocation annihilation is minimal for materials with low γ_{SFE} since dissociation hinders climb and cross slip which are the basic mechanisms of recovery† (Humphreys and Hatherly 1996). Moreover, materials with a low value of γ_{SFE} will not tend to polygonise because the dislocations cannot easily climb or cross slip and the strain fields associated with partial dislocations are much more diffuse than for discrete dislocations.

1.3.2 Work hardening

When a single crystal sample of a cubic close-packed metal such as aluminium or stainless steel is stressed, at first it will deform elastically with the stretching of bonds, after which dislocations within the sample will start to move. As discussed in the previous section, cubic close-packed systems slip on the $\{111\}\langle 1\bar{1}0\rangle$ system. Of the twenty four equivelent slip systems, the one that is activated depends on the orientation of the tensile axis, in general it will be the system with the highest Schmidt factor $\cos\phi\cos\lambda$ where ϕ is the angle between the plane normal and the tensile axis and λ is the angle between the slip direction and tensile

† There is no formal definition of recovery, however, a generally applicable definition would be; "*... any modification of properties, during annealing, which occurs before the appearance of new strain-free recrystallized grains, regardless of how refined the experimental technique used to detect the new grains...*" (Byrne 1965)

axis. As deformation progresses, the tensile axis rotates towards the slip direction thereby activating other slip systems.This leads to work hardening. Strain compatibility requirements in a polycrystalline sample can require the simultaneous operation of five separate slip systems in each grain.

Cold work therefore induces a high density of dislocations and defects in general, leading to an increase in hardness and a decrease in ductility. These changes may be undesirable but can be "reversed" by annealing to induce recrystallization.

1.4 Recrystallization

Because each dislocation is a defect with an associated energy, a material with a high dislocation density contains stored energy which drives recovery and recrystallization. Recrystallization is the process by which new grains of low dislocation density form in a deformed material and consume those with high dislocation density. This process may be split into the two processes of nucleation and growth, as illustrated in Fig. 1.7.

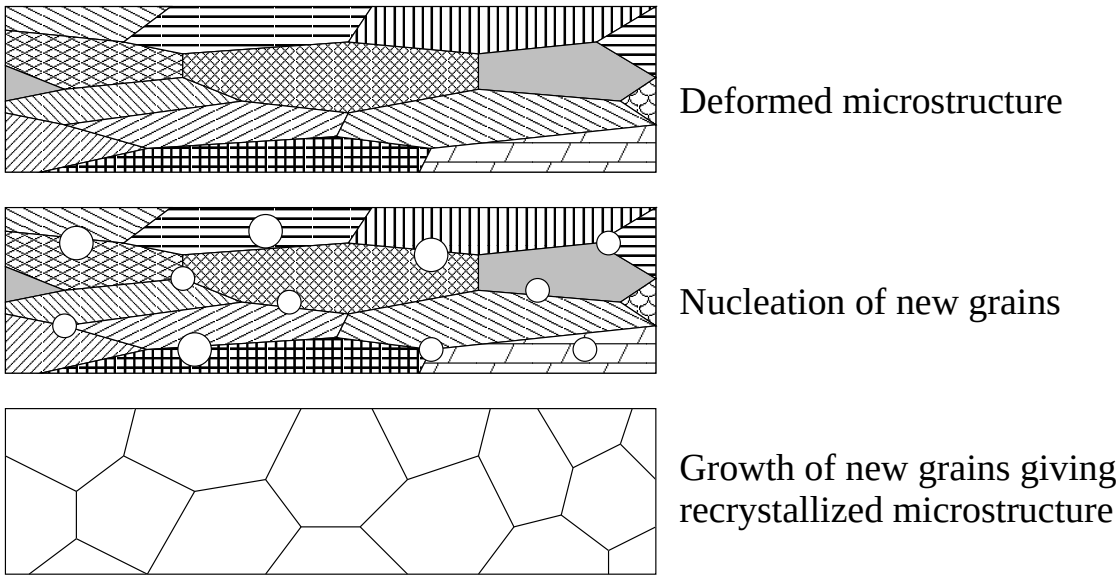

Fig. 1.7 Schematic of recrystallization process

In materials such as aluminium and austenitic stainless steel there are no phase transformations which can be utilised to control important physical and mechanical properties after casting. Therefore recrystallization is the principal way by which these properties may be manipulated.

The main aim of this work is to model the recrystallization process with particular attention to anisothermal annealing as used in industry. This is expanded upon in chapter 2.

1.5 Industrial annealing of stainless steel

The majority of stainless steel produced is in the form of wide (> 1000 mm), thin (< 5 mm) strip. A typical process route for strip is as follows:

Liquid stainless steel is cast continuously and cut into slabs which are subsequently re-heated and hot-rolled from a thickness of approximately 200 mm to within the range 3-10 mm to provide coils of "hot band". These coils are then annealed at approximately 1050 °C to produce a softened, equiaxed grain structure before descaling and cold-rolling. Typical cold-rolling reductions are between 10% and 90%. In addition to the reduction in gauge, cold-rolling also improves surface finish and the geometrical tolerances of the strip as compared with the hot-rolled product.

As discussed in §1.2, austenitic stainless steels work harden during deformation. The degree of work hardening will be a function of the chemical composition and deformation history. Unless the material is required in the work hardened state (*e.g.* spring steels), one or more annealing stages will be needed.

In a modern steel plant, strip is generally annealed on a continuous basis as a part of the process cycle. It is therefore imperative that the correct furnace calibration is achieved so as to move the steel through the furnace at a rate which keeps pace with the rest of the production cycle, whilst still producing the desired microstructure for the fixed strip geometry.

Modern continuous annealing furnaces are usually of a multi-zone configuration and must necessarily be able to satisfactorily anneal a wide range of steels. This includes a whole spectrum of compositions as well as a number of different thicknesses, rolling histories and, possibly, surface conditions. A schematic diagram of a multi zone furnace for continuous annealing is shown in Fig. 1.8.

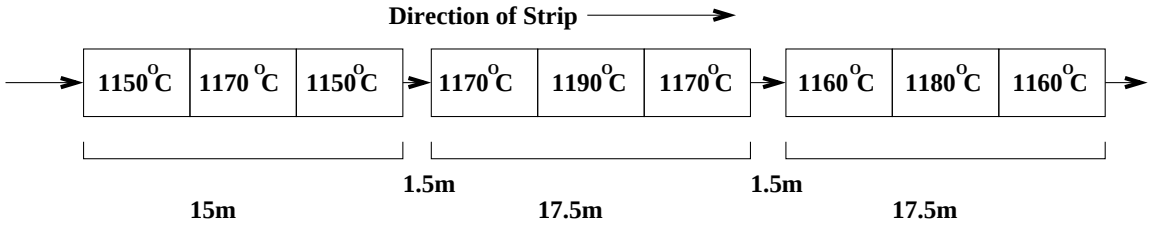

Fig. 1.8 Schematic layout of zones in a production furnace. The nominal temperatures indicated for each section may be varied to suit the strip gauge.

This furnace configuration is quite typical of those used around the world in the production of stainless steel. The full annealing line consists of three banks, each consisting of three gas fired furnaces separated by small air gaps. A coil of steel is unwound and passed through the

furnace and then wound up again on the other side. Once one coil is exhausted, a second is welded onto the tail of the first and the process is thereby made truly continuous. The temperatures of the individual furnaces are chosen to provide a rapid heating rate followed by a period of roughly isothermal annealing.

Secondly, because of pressure considerations, the inner of each bank of three furnaces is set to a higher temperature than the outer furnaces. This limits the number of settings that the annealing line as a whole may take up, the final settings are an optimisation between the target strip heating curve and furnace operating constraints.

Direct measurement of the strip temperature inside the furnace is difficult. A common method of monitoring the temperature of any particular furnace is with thermocouples embedded in the furnace walls. However, it cannot be guaranteed that the part of the furnace which is monitored is at the same temperature as the region containing the strip.

A schematic temperature profile for strip passing through a furnace of this type is given in Fig. 1.9.

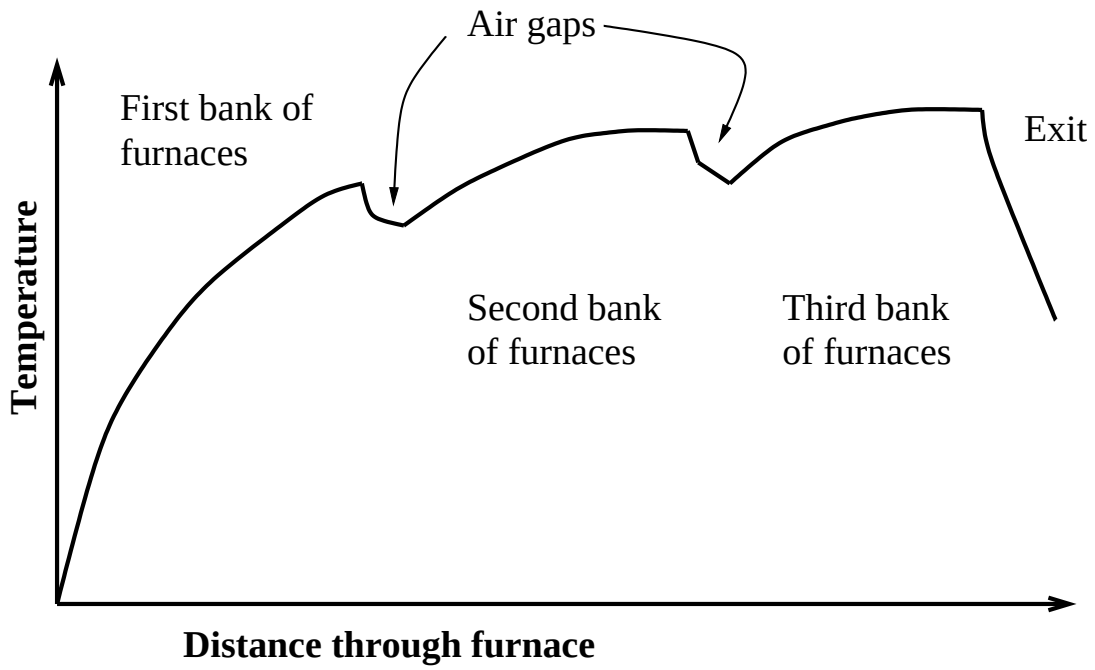

Fig. 1.9 Schematic of the variation of strip temperature as it passes through an annealing line. (Backhouse 2000, private communication)

The principal control parameters in the annealing process are the "line speed" *i.e.* the speed at which the strip travels through the furnace, and the temperature/fuel/air and oxygen input settings for each of the individual zones. The factors which are expected to effect the annealing behaviour of a strip are:

i) Gauge (thickness of material).

ii) Chemical composition of the coil.

iii) Initial microstructure.

iv) Deformation history.

v) Surface characteristics (which control heating rate).

vi) Thermal properties

In current practice accumulated knowledge of response to the annealing process is used to specify conditions. It is clear therefore that modelling the industrial annealing process is far from trivial and certain of the key parameters are difficult to quantify and/or measure on-line. Thus the main objective of this programme of work was to develop models which might be used to help in the prediction of the response of a given strip feedstock to an available annealing cycle and, conversely, to select annealing conditions to optimise strip output characteristics.

1.6 Forward to main body of work

In the industrial process described in this chapter, there is a need for a model which fully describes the annealing behaviour of stainless steels. Properties such as hardness, which are important to the end user, may then be modelled and controlled. This thesis contains work on two different models; a kinetic model, based on the physics of recrystallization and an empirical model based on data fitting techniques.

The following two chapters describe the current status of each method followed by chapters dealing with experiments and models.

CHAPTER 2

KINETIC MODELLING

Kinetic modelling has been at the forefront of the analysis of recrystallization since Kolmogorov published the first of overall transformation theory paper in 1937. This chapter focuses on the development of this theory from 1937 onwards and how recrystallization is driven by the stored energy of the dislocations.

2.1 Thermodynamics

When a fuel is burnt it releases energy, this energy may be harnessed to drive a motor, a reaction or left to dissipate into the surroundings. Everyday, we see reactions which liberate energy which provide heat, work or is squandered by letting it dissipate into the surroundings. This energy may come from any source, from fuel in an internal combustion engine, to a chemical battery cell, to the heat liberated when a dislocation is annihilated (*c.f.* §1.3). Thermodynamics, the study of energy transformations, is the mathematical tool used to quantify and compare these observations.

2.1.1 The laws of thermodynamics

The mathematics of thermodynamics can be expressed in the following series of laws (summarised by Atkins 1994):

Law N°	Description
0	If A is in thermal equilibrium with B and B is in thermal equilibrium with C, then A is in thermal equilibrium with C
1	The internal energy of an isolated system is constant
2	The entropy (disorder) of an isolated system increases in the course of a spontaneous reaction
3	At absolute zero temperature the entropy (disorder) of a perfect solid is zero

2.1.2 Application of theory

Looking at the second law of thermodynamics, and defining entropy (S_u) as a measure of disorder of the universe, we see that a reaction will occur if, and only if, the entropy of the universe increases as a consequence, *i.e.* $\Delta S_u > 0$. In this case the isolated system is the universe, which comprises the reaction components and the surroundings. If we consider the

entropy of the universe to be made up of the entropy of the reaction components S_o and the entropy of the surroundings S_s, we see:

$$\Delta S_u = \Delta S_o + \Delta S_s \tag{2.1}$$

According to the first law of thermodynamics, the internal energy (in this case enthalpy) of a closed system is constant, *i.e.* $\Delta H_o = -\Delta H_s$, wherein ΔH_o is the change in enthalpy of the reaction and ΔH_s is the change in enthalpy of the surroundings. Assuming the surrounds are large as compared with the reaction components, the temperature T may be considered constant, and therefore the effect of the reaction on the surroundings will be reversible *i.e.* $\Delta S_s = \Delta H_s/T$. Therefore we see that:

$$\Delta S_u = \Delta S_o - \frac{\Delta H_o}{T} \tag{2.2}$$

$$-T\Delta S_u = -T\Delta S_o + \Delta H_o \tag{2.3}$$

The advantage of equation (2.3) is that all calculations regarding the surroundings have been eliminated and only the reaction need be considered. If we define:

$$\Delta G = \Delta H_u - T\Delta S_u \tag{2.4}$$

knowing that the first law of thermodynamic states that $\Delta H_u = 0$ and combining equations (2.3) and (2.4) we see that ΔG is simply calculated as:

$$\Delta G = \Delta H_o - T\Delta S_o \tag{2.5}$$

ΔG (the change in Gibbs free energy) represents the driving force for the reaction. This derivation is rigourous for any isothermal closed system and has the advantage that, so long as the temperature of the surroundings is constant, the thermodynamic universe may be analysed by simple inspection of the reaction components.

2.2 The driving force for recrystallization

As described in chapter 1, when a material is deformed, the density of dislocations and other defects increases, often by two or more orders of magnitude. The energy associated with these defects means that a recrystallized structure is thermodynamically more stable than one that is deformed. This energy difference provides the driving force for recrystallization ΔG.

$$\Delta G = (\rho_D - \rho_{RX}) \times E_{DL} + E_{PGB} \tag{2.6}$$

wherein ρ_D is the dislocation density before recrystallization, ρ_{RX} is the dislocation density after recrystallization, E_{DL} is the energy per unit length of a dislocation (equation 1.3) and E_{PGB} is the energy of other defects and inhomogeneities such as vacancies and grain boundaries extended during deformation. Generally $\rho_{RX} \ll \rho_D$ and therefore, ρ_{RX} may by neglected, giving:

$$\Delta G = \rho_D E_{DL} + E_{PGB} \tag{2.7}$$

It is difficult to measure ΔG. It may however be estimated using direct methods or determined indirectly by monitoring some physical or mechanical property.

2.2.1 Direct methods

2.2.1.1 Calorimetry

The stored energy may be measured directly using a differential scanning calorimeter (DSC). In this method, a sample is heated continuously and the energy flux required to maintain the sample at the same temperature as the reference material is measured. Upon recrystallization the energy stored in the dislocations will be expressed as heat. This heat will affect the energy flux into the sample and thereby may be evaluated. A number of authors have utilised this method (*e.g.* Schmidt 1989, Haessner 1990, Ryde *et al.* 1990). Schmidt (1989) has thereby confirmed quantitatively the relationship between recovery and γ_{SFE} as described in chapter 1. His results for metals with differing values of γ_{SFE} as a function of shear strain are given in Table 2.1.

Material studied	Al	Pb	Cu	Ag
Purity	99.999 at%	99.999 at%	99.997 at%	99.999 at%
γ_{SFE} / J m^{-2}	26	15	4.7	2.6
Shear strain	6.75	5.97	6.75	5.2
Stored energy / kJ mol^{-1}	69.6	21.5	216	220
Energy expended during deformation / J mol^{-1}	3151	1400	5592	4914
Stored energy / Energy expended	0.022	0.015	0.039	0.045
ρ_D (calculated) / m$^{-2} \times 10^{15}$	3.1	1.7	10	8.7

Table 2.1: Calorimetric data for recrystallization of materials after deformation at 77 K (Schmidt 1989)

As expected, a high value of γ_{SFE} disfavours dissociation of dislocations and therefore promotes cross-slip and climb. This leads to a reduced value of stored energy in aluminium

and lead. Moreover, in copper and silver (lower γ_{SFE}), the ratio of stored energy to energy expended during deformation is higher than in aluminium and lead (higher γ_{SFE}). This too can be explained by the fact that dissociated dislocations have less freedom of motion than undissociated dislocations. This is reflected in the higher values of dislocation density for lower γ_{SFE} materials.

2.2.1.2 X-Ray line broadening

X-ray diffraction works by "reflecting" radiation off crystallographic planes within the sample. Different planes in the lattice reflect by different angles. When a material is deformed the crystallographic lattice is strained and therefore this will have an effect on the reflection obtained in X-ray analysis. Homogeneous lattice strains will simply change the size of the unit cell and hence the position of the diffraction peak. However, inhomogeneous strains will alter the lattice size differently in different crystallites, it will also alter the size of the lattice differently as a function of direction within one crystallite. This means that, upon forming a diffraction pattern from many such crystallites, the observed peak becomes broader. The reason for this is because each unit cell is a slightly different size and therefore will diffract at a subtly different angle, leading to a spreading of the peak. The increase in the breadth (β_{dinc}) of this peak and the diffraction angle θ_{Bragg} may be directly related to the internal strain in the system ϵ_{dinc} such that:

$$\beta_{dinc} = 2\epsilon_{dinc} \tan \theta_{Bragg} \tag{2.8}$$

A full appraisal of this technique has been given by Jeffrey (1971).

The differences in stored energy measured this way and via calorimetry can be striking. For example a heavily cold worked metal will have a value of stored energy in the range 8–80 J mol^{-1} when measured using X-Ray line broadening. A similar metal when examined using calorimetry may have a value of 250–800 J mol^{-1} (Humphreys and Hatherly 1996)!

2.2.1.3 TEM observations

Dislocations may be counted directly in a transmission electron microscope, hence the stored energy may be calculated. This method can be inaccurate, since many dislocations can be introduced during sample preparation and handling (Fig. 2.1). Moreover, dislocations may escape from the surface of the sample because of its small size. Furthermore, after relatively small amounts of cold work (upwards of 5% strain), the dislocation density can be so high so as to make identification and counting of dislocations difficult using transmission electron microscopy.

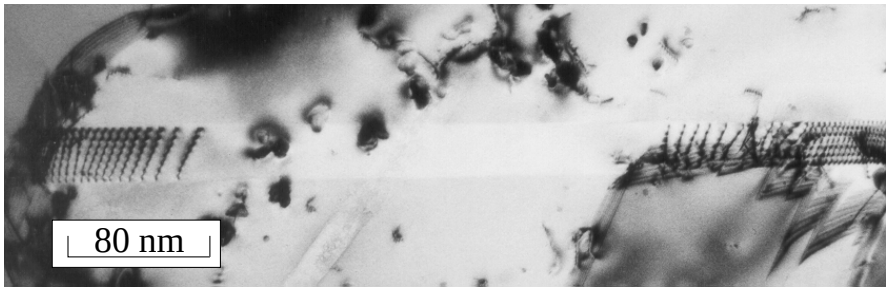

Fig. 2.1 TEM micrograph of a sample of a type 302 stainless steel annealed for 30 minutes at 720 °C showing dislocations in a recrystallized grain. No deliberate deformation was applied to the sample after annealing. These dislocations all lie on a single plane within the observed crystallite, therefore they are almost certainly deformation induced. Hence it may be concluded that these dislocations were induced during grinding or handling of the sample after the annealing procedure was terminated. (Hopkin, unpublished work)

2.2.1.4 Comparison of different direct methods

Transmission electron microscope dislocation counting methods are inapplicable to heavily deformed materials because observing single dislocations is all but impossible.

The difference between calorimetric and X-ray diffraction methods is a cause for concern and caution must be exercised when interpreting the data. A possible explanation for the discrepancy lies in what each method actually measures. Calorimetry measures heat flux directly, whereas X-ray diffraction measures internal lattice strains. As described in §1.3, dislocations align themselves so as to minimise strain energy. This will have no effect of factors such as the core energy of the dislocation. The core energy of an edge dislocation is associated with the core distortions, these are so large that they cannot be accounted for using elastic theory. The X-ray method takes no account of this core energy, whereas, it is included in the calorimetric measurements. Generally, in calculations of the energy of a dislocation, the core energy is neglected (*e.g.* Cottrell 1975). Whilst this may be applicable for an isolated dislocation, it is likely not to be so for a tangle of dislocations. Therefore, the calorimetric measurements are likely to be the more accurate of these two methods.

2.2.2 Indirect methods

2.2.2.1 Calculation of stored energy from sub-grain structure

If the deformed microstructure consists of sub-grains, the stored energy may be calculated by considering the density and misorientation of the sub-grain boundaries. This work was pioneered by Dillamore *et al.* (1972). However, the method is not applicable in this work since the low value of γ_{SFE} in austenitic stainless steels prevents the formation of a clear sub-grain

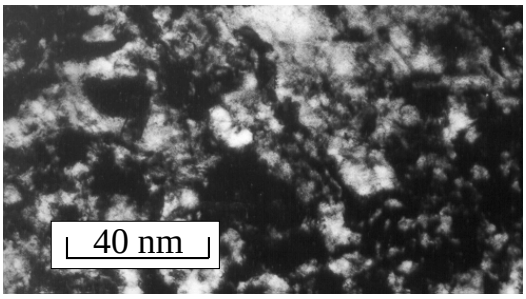

Fig. 2.2 TEM micrograph showing a sample of 302 stainless steel annealed for 30 minutes at 720 °C showing an indistinct sub-grain structure. (Hopkin, unpublished work)

structure (Fig. 2.2).

2.2.2.2 Calculation of stored energy from mechanical properties

As discussed in §2.2.2.1, the dislocation density in materials with even a small amount of cold work can be impossible to measure (Fig. 2.2). However an estimate of the dislocation density (and hence the stored energy) may be made from the flow stress σ:

$$\sigma = c_1 \mu |\mathbf{b}| \rho_D^{1/2} \tag{2.9}$$

where c_1 is a constant of the order of 0.5. This equation has been shown to hold for a wide range of materials (McElroy and Szkopiak 1972, Dingley and McClean 1967). Combining equation (2.9) and equation (2.7) and assuming E_{PBG} may be neglected† giving:

$$\Delta G = E_{DL} \left(\frac{2\sigma}{\mu |\mathbf{b}|} \right)^2 \tag{2.10}$$

Combining equation (2.10) with equation (1.3):

$$\Delta G = \frac{1}{2} \mu |\mathbf{b}|^2 \times \left(\frac{4\sigma^2}{\mu^2 |\mathbf{b}|^2} \right)$$

$$\Delta G = \frac{2\sigma^2}{\mu} \tag{2.11}$$

The answers obtained from this model are generally quite low, comparable with the data obtained through X-ray diffraction. However, the trends in the data are accurately reproduced.

2.2.3 Application of these data to modelling

Kinetic modelling using overall transformation kinetics has been studied since the theory was first developed in the 1930s. A large number of general review papers exist on the subject (*e.g.* Speich and Fisher 1966, Humphreys 1992, Humphreys 1997, Doherty *et al.* 1997,

† This approximation should hold true for the recrystallization process as illustrated by Schmidt (quoted by Haessner 1990). Point defects tend to anneal out prior to recrystallization. Therefore they do not contribute to ΔG during the process of recrystallization.

Bhatia 1997, Rollett 1997, Bhadeshia 1997, Carr 1997, Vandermeer 2000) these give data from recrystallization experiments, however little progress on practical modelling has been made over and above overall transformation kinetics. This will be discussed further in the following sections (overall transformation kinetics are reviewed comprehensively in §2.5). All of the papers detailed above rely on thermodynamic data to calibrate and power their models. It is clear therefore, that only through the study of thermodynamics can a model of kinetic microstructural evolution may be produced.

2.3 The kinetics of grain growth

The kinetics of grain boundary motion are well understood. (*e.g.* Christian 1975, Putnis 1992).

2.3.1 Mathematical description

The velocity Υ of a grain boundary is controlled by the thermally activated migration of atoms across the grain boundary and its associated energy barrier Q:

$$\Upsilon = \delta_\varsigma \nu \exp\left(-\frac{Q}{RT}\right)\left[1 - \exp\left(-\frac{\Delta G}{RT}\right)\right] \tag{2.12}$$

where δ_ς is the jump distance across the boundary (see Fig. 2.3). ν is the characteristic frequency (kT/h in Eyring's theory), ΔG is the driving force grain boundary motion, in the present work this is the difference in stored energy between the grains α and β on either side of the boundary (Fig. 2.3). T is the absolute temperature, R is the ideal gas constant, k is the Boltzmann constant and h is the Planck constant.

This equation is a simple product of a number of factors. Firstly ν is the frequency with which the jump across the boundary is attempted, but this will not always be successful because the atom must have sufficient energy to overcome the energy Q; the probability of success is expected to be $\exp\left(-\frac{Q}{RT}\right)$ giving the overall rate of transfer of atoms from α to β as proportional to $\nu \exp\left(-\frac{Q}{RT}\right)$. However, atoms may also undertake jumps across the higher activation barrier $Q+\Delta G$ from β to α, this will occur at a rate proportional to $\nu \exp\left(-\frac{Q+\Delta G}{RT}\right)$. Therefore the net flux of atoms (J) from α to β is given by:

$$J = J(\alpha \rightarrow \beta) - J(\beta \rightarrow \alpha) \tag{2.13}$$

$$J = \left[\nu \exp\left(-\frac{Q}{RT}\right)\right] - \left[\nu \exp\left(-\frac{Q+\Delta G}{RT}\right)\right] \tag{2.14}$$

$$J = \nu \exp\left(-\frac{Q}{RT}\right)\left[1 - \exp\left(-\frac{\Delta G}{RT}\right)\right] \tag{2.15}$$

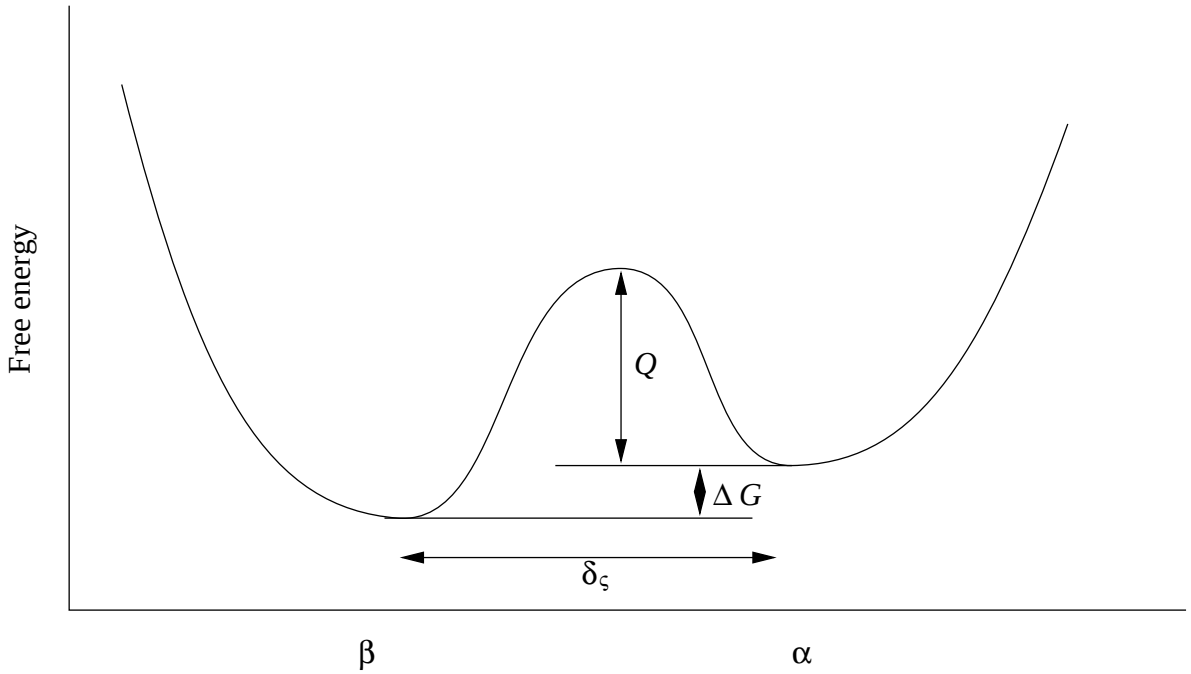

Fig. 2.3 Schematic of the free energy for atom transfer across the α/β interface

To convert this from a rate of atom transfer into a velocity simply requires multiplication by the distance jumped by each atom as it crosses the boundary δ_ς, thus:

$$\Upsilon = \delta_\varsigma \nu \exp\left(-\frac{Q}{RT}\right)\left[1 - \exp\left(-\frac{\Delta G}{RT}\right)\right] \tag{2.16}$$

if ΔG is small then this may be approximated to:

$$\Upsilon = \left\{\frac{\delta_\varsigma \nu}{RT} \times \exp\left(-\frac{Q}{RT}\right)\right\} \times \Delta G \tag{2.17}$$

The term multiplying ΔG is also known as the mobility M such that:

$$\Upsilon = M\Delta G \tag{2.18}$$

2.3.2 Solute drag

Stainless steels contain large quantities of solutes, far in excess of those known to influence grain boundary mobilities via a solute drag mechanism. The effect of small changes in solute concentration are expected to be small when compared with the profound effect of solute atoms on pure materials. Even a small amount of solute which segregates (or desegregates) to the grain boundaries is enough to decorate that boundary and therefore dramatically slow grain boundary migration. In fact, many authors simply ignore this effect completely (*e.g.*

Sha and Bhadeshia 1997). However, there exists a mathematical framework to describe solute drag developed initially by Lücke and Detert in 1957 for dilute solutions. This model has subsequently been extended upon by Cahn (1962) and Lücke and Stüwe (1963) and then further extended by Bauer (1974), Hillert and Sundman (1976) and Hillert (1979) to account for high alloy materials.

The Cahn-Lücke-Stüwe (CLS) model is, to this day, the most widely accepted of all of the models of the effects of solute on grain boundary mobility. It is the starting point for most semi-quantitative modelling in this area.

The basis of CLS theory is that the energy of an atom at or near the boundary is different in energy by a factor U_{sd} to similar atoms in the bulk. It follows that there will be a force of value $\mathrm{d}U_{sd}/\mathrm{d}\lambda_{sd}$between the boundary and the solute atom, where λ_{sd} is the distance between the solute atom and the boundary. This force may be positive or negative depending on the value of U_{sd}. The total force on the grain boundary ($\mathbf{F}$) will be the equal and opposite to the sum of the forces on all the individual solute atoms interacting with that boundary, such that:

$$\mathbf{F} = \sum \frac{\mathrm{d}U_{sd}}{\mathrm{d}\lambda_{sd}} \tag{2.19}$$

The result of this interaction is that an excess (or possibly a deficit) of solute builds up in the region of the grain boundary, this is commonly referred to as an atmosphere. The concentration of solute element x near a grain boundary (χ_x) within a material having an average concentration χ_{x_0} of solute x may be calculated as:

$$\chi_x = \chi_{x_0} \exp\left(-\frac{U_{sd}}{kT}\right) \tag{2.20}$$

The variation of U_{sd}, $\mathbf{F}$, and χ_x as a function of λ_{sd} are shown schematically in Fig. 2.4.

When a boundary begins to move the atmosphere of solute will, initially, be left behind and hence will exert a retarding force on the boundary. As the boundary velocity increases, this atmosphere will lag still further behind the boundary.

At low velocities, the relationship between the retarding force on the boundary ($\mathbf{F}_{retard}$) and the velocity is found to be:

$$\mathbf{F}_{retard} = \frac{\Upsilon}{M} + K^1_{CLS}\chi_{x_0}\Upsilon \tag{2.21}$$

where M is the mobility as defined in the previous section, χ_{x_0} is the average concentration of solute x and K^1_{CLS} is a constant. It should be noted that the activation energy for boundary migration Q is dependent on the exactly how the diffusivity of the solute varies with λ_{sd} and

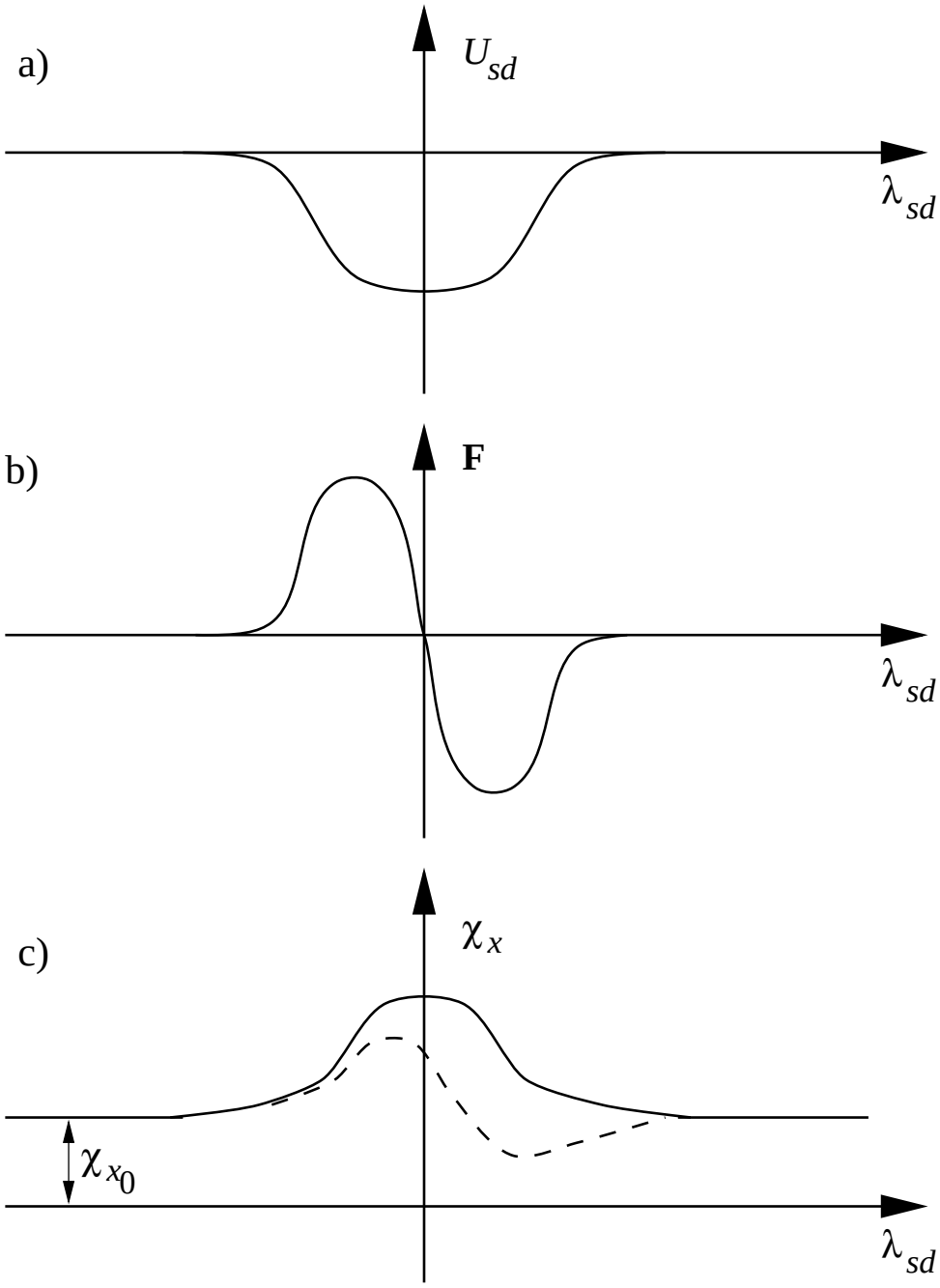

Fig. 2.4 Schematic variations of U_{sd} (a), **F** (b), and χ_x (c) with λ_{sd} for a stationary boundary. The dotted line on Fig. 2.4 c) illustrates the expected shape of the curve if the boundary was moving from left to right. (after Lücke and Detert (1957), Cahn (1962) and Lücke and Stüwe (1963))

also how U_{sd} varies with λ_{sd}. Both of these profiles must be assumed, Hillert (1979) has demonstrated that choice of these parameters has a profound effect on the final results the model gives. In the same paper, Hillert assumed that diffusivity was not constant across the sample, but was in fact higher at the boundary than in the bulk. Using this approach the

author found that the amount of drag expected was much lower than for diffusivity is assumed to be constant.

At intermediate velocities, the retarding force is very difficult to calculate and most models of this behaviour differ greatly in their predicted values. However, at high velocities *i.e.* when the solute atoms can no longer keep pace with the boundary another limiting case is found.

$$\mathbf{F}_{retard} = \frac{\Upsilon}{M} + \frac{\chi_{x_0}}{K_{CLS}^2 \Upsilon} \tag{2.22}$$

where K_{CLS}^2 is a constant

As might be expected for a situation where solute has no time to partition to the grain boundary and the solute concentration profile remains flat, M and Q remain at values which approximate to those in a pure metal.

Cahn (1962) and Lücke and Stüwe (1963) combined the models for low and high velocity thus:

$$\mathbf{F}_{retard} = \frac{\Upsilon}{M} + \frac{K_{CLS}^1 \chi_{x_0} \Upsilon}{1 + K_{CLS}^1 K_{CLS}^2 \Upsilon^2} \tag{2.23}$$

As expected, the retarding force is a function of boundary velocity, being zero at $\Upsilon = 0$ and increasing rapidly with increasing Υ, reaching a maximum and then dropping off as Υ continues to increase.

2.3.3 Zener drag

The previous section dealt with the interaction of solute in a coherent solid solution with the motion of a grain boundary. A distribution of incoherent particles hinder can also the motion of a grain boundary. If a spherical particle of radius r_{zen} is diametrically intersecting a grain boundary then the total area of grain boundary will be reduced by πr_{zen}^2. Hence the total energy of that grain boundary will be reduced by $\gamma \pi r_{zen}^2$. This means that it is energetically favourable for particles to sit at the grain boundary and hence exert a retarding force.

Zener (originally reported by Smith, 1948) calculated the pinning pressure ($\mathbf{F}_{zen}$) due to a random distribution of incoherent second phase particles as:

$$\mathbf{F}_{zen} = \frac{3\xi_v \gamma}{2r_{zen}} \tag{2.24}$$

where ξ_v is the volume fraction of incoherent second phase particles. As reviewed by Nes *et al.* other authors have tried to extend upon this original analysis, however, the essence of Zener's model remains the same.

2.4 Nucleation

A generally accepted definition of a recrystallization nucleus (Humphreys and Hatherly, 1996) is: *'a crystallite of low internal energy growing into deformed material from which it is separated by a high angle grain boundary'.* † Conventional nucleation theory supposes that the nucleus is formed by random thermal atomic fluctuations. This is unlikely for the following reasons:-

- the driving force for recrystallization is generally very small so that the critical size which has to be generated by thermal fluctuation is so large that it can be optically visible. Such large fluctuations are incredibly improbable;
- the interfacial energy of the required grain boundary is very high.

The actual measured nucleation rate is greater by a factor of approximately 10^{50} (Rollett, 1997) than that calculated by homogeneous nucleation theory. It is now generally accepted that recrystallization nuclei consist of small pre-existing volumes within the deformed structure, which are relatively free from defects. There are three predominant theories consistent with this idea.

2.4.1 Strain induced grain boundary migration (SIGBM)

Strain induced grain boundary migration is a process by which a defect-free area at a high angle grain boundary in the deformed microstructure, may bulge over into an adjacent higher energy grain (Fig. 2.5).

If two adjacent grains Γ_1 and Γ_2 have different stored energies per unit volume $\Delta G_{v\Gamma 1}$ and $\Delta G_{v\Gamma 2}$ respectively, then there will be a driving force per unit volume $\Delta G_{SIGBM} = \Delta G_{v\Gamma 1} - \Delta G_{v\Gamma 2}$ for the lower energy grain (Γ_2) to grow at the expense of the higher energy grain (Γ_1). This can occur by a bulge forming as shown in Fig. 2.6.

For a nucleus to grow freely it must, at the point where it becomes hemispherical (Bunn *et al.*1997), release more energy through creating new volume of recrystallized material than it needs to consume to create the new interface between it and the unrecrystallized material. For the geometry illustrated in Fig. 2.6, the interfacial energy associated with this capped region (E_B) at the hemispherical condition is given by:

$$E_B = 2\pi R_B^2 \gamma \tag{2.25}$$

† The term "high angle" may be misleading, since it is well known that for certain high misorientation boundaries such as $\Sigma = 3$ coincidence site lattice, the boundary energy is low and hence mobility is low. "High mobility" grain boundary would be a better term to use in this context.

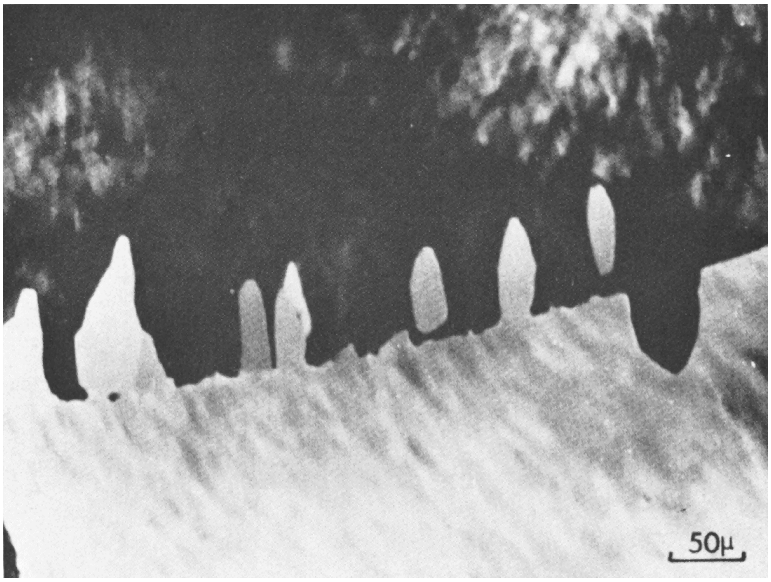

Fig. 2.5 Optical micrograph showing strain-induced grain boundary migration in aluminium (Bellier and Doherty, 1977)

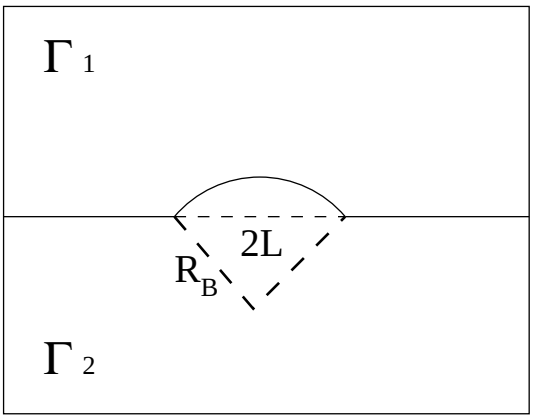

Fig. 2.6 Schematic mechanism of strain-induced grain boundary migration

where R_B and L are as given in Fig. 2.6 and γ is the surface energy per unit area. Therefore:

$$\frac{\mathrm{d}E_B}{\mathrm{d}R_B} = 8\pi R_B \gamma \tag{2.26}$$

Also there has been a lowering of energy for the system because a section of low energy grain (Γ_2 of energy $\Delta G_{v\Gamma 2}$) has replaced a section of high energy grain (Γ_1 of energy $\Delta G_{v\Gamma 1}$). This will lead to an free energy change associated with the capped region G_v:

$$G_v = \frac{2}{3}\pi R_B^3 \Delta G_{SIGBM} \tag{2.27}$$

Therefore:

$$\frac{\mathrm{d}G_v}{\mathrm{d}R_B} = 4\pi R_B^2 \Delta G_{SIGBM} \tag{2.28}$$

where ΔG_{SIGBM} is the difference in energy per unit volume between the two grains (*i.e.* $\Delta G_{v\Gamma 1} - \Delta G_{v\Gamma 2}$).

For the bulge to grow it is necessary for $\frac{\mathrm{d}G_v}{\mathrm{d}R_B} > \frac{\mathrm{d}E_B}{\mathrm{d}R_B}$ and hence

$$R_B > \frac{2\gamma}{\Delta G_{SIGBM}} \tag{2.29}$$

i.e. for the hemispherical condition:

$$L > \frac{2\gamma}{\Delta G_{SIGBM}} \tag{2.30}$$

This model has been extended by Bate and Hutchinson (1997) who postulated that during boundary bulging from a low energy into a high energy region the sub-grain structure will be "dragged" behind the advancing bulge as illustrated in Fig. 2.7.

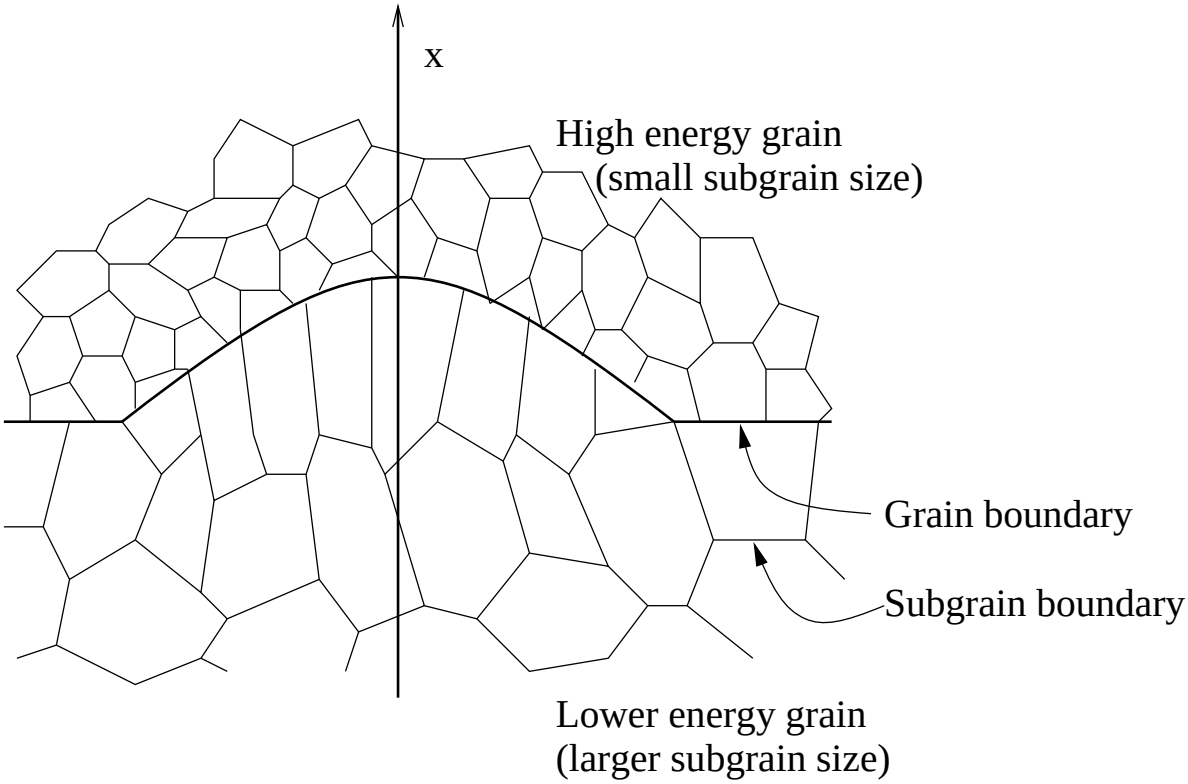

Fig. 2.7 Lower energy grain (larger sub-grains) bulging into an adjacent higher energy grain (small sub-grains) dragging the sub-grain structure with it as it bulges (adapted from Bate and Hutchinson, 1997)

This will tend to retard the bulging process. However this model can only be applied to materials where a sub-grain structure exists (*e.g.* high stacking fault energy materials such as aluminium).

The reason that the substructure must be dragged along as the grain boundary bulges is that behind the bulging grain boundary are a number of subgrains, each with a slightly different misorientation. As the grain boundary bulges, the subgrains behind the advancing boundary will also advance as illustrated in Fig. 2.7. These subgrains are, however, still misoriented with respect to one another. It follows that it is geometrically necessary to have a boundary between such subgrains. Hence, with each incremental grain boundary advance, a subgrain boundary will form between the advancing subgrains. The authors of the paper drew no conclusions as to the exact mechanism of the formation of this boundary.

2.4.2 Sub-grain coalescence model

In the SIGBM model the required "high angle" grain boundary is assumed to be present, but in practice nuclei have also been observed to form in regions of the material located away from grain boundaries. This observation can be explained by sub-grain rotation and sub-grain boundary migration. In this model, several sub-grains coalesce to form a nucleus above a critical size for abnormal sub-grain growth, the coalescence also leads to a large misorientation so that the nucleus is bordered by a mobile grain boundary.

Subgrain rotation, which is a component of the coalescence process, is dependent on the stability of sub-grain structures which determine the time taken for the creation of a nucleus for a number of reasons:

Firstly, an array of sub-grains, separated boundaries having misorientations of less than 10°, is an intrinsically unstable microstructure‡, but significant sub-grain growth will occur only in the absence of fast growing, high energy, high angle grain boundaries.

Secondly, an array of grains/sub-grains separated by high angle grain boundaries will undergo stable continuous growth if all grains/sub-grains are of approximately equal size.

This can be explained using the Read-Shockley equation (Read and Shockley 1950) for energy of a low angle tilt grain boundary (γ_{LA}):-

$$\gamma_{LA} = \gamma \frac{\theta}{\theta_m} \left(1 - \ln \frac{\theta}{\theta_m} \right) \tag{2.31}$$

where γ and θ_m are the values of boundary energy and misorientation when the boundary takes on high angle characteristics (θ_m is usually taken to be about 15°). This equation is based on the assumption that the boundary consists of a wall of dislocations wherein the greater the number of dislocations in the wall, the greater angle of tilt of the boundary.

‡ Each subgrain boundary has an associated energy, the energy of the array will be minimised by growth and/or eradication of these boundaries

This calculation omits one aspect of high angle grain boundaries. It assumes that at any angle above about 15° the boundary can be considered as 'high angle' and hence mobile. But for certain well defined orientations there will be a good fit between adjacent grains. This occurs at low values of coincidence site lattice parameters (Reed-Hill and Abbaschian, 1994). This means that strictly the terms "high angle grain boundary" and "high mobility grain boundary" are not necessarily interchangeable.

By inspection of Fig. 2.8, which is a graphical illustration of equation (2.31) , we see that a boundary of angle 5° has an energy (as a fraction of the high angle grain boundary energy) of 0.700. If we consider two grain boundaries, both initially having a misorientation of 5° the average normalised energy of these boundaries will also be 0.700. If a number of dislocations migrate from one boundary to the other, then sub-grain rotation will occur. Consequently, the misorientation angles of both boundaries will change. A rotation of 1°, changes the misorientations of the above two boundaries to 4° and 6°having boundary energies of 0.619 and 0.767 respectively, giving an average energy of 0.693. The rotation is thus favoured by a reduction in energy of 0.007. However, the activation energy for a dislocation to migrate across the grain boundary may be quite high (*c.f.* in heavily worked materials, the yield stress may go up beyond much as 400 MPa making dislocation motion difficult) and therefore this process will be slow. Moreover, if the initial boundaries to have a misorientation of 10°, the energetic advantage of dislocation migration to form two boundaries at 9° and 11° would only be 0.003. This means that sub-grain rotation time increases as the average misorientation angle increases.

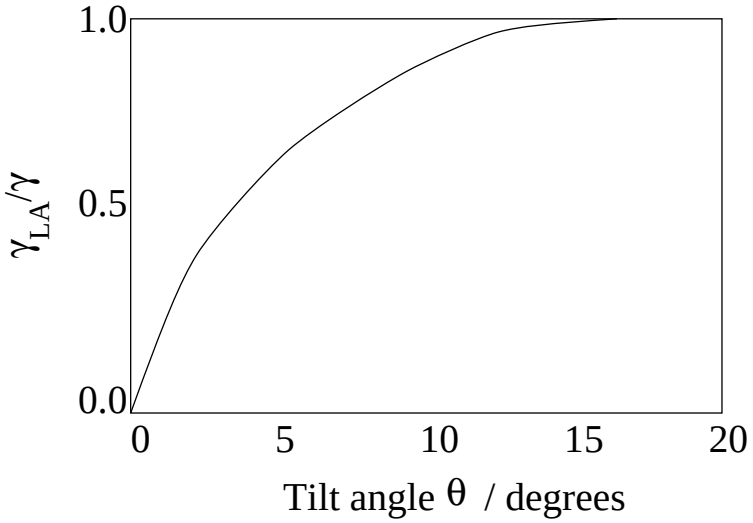

Fig. 2.9 Graph showing the variation of the normalised value of grain boundary energy as a function of misorientation across a low angle grain boundary (adapted from Read, 1953)

In a Monte Carlo model by Hayakawa and Spuznar (1997), the nucleation process was based upon sub-grain rotation as described by Li (1962). Nucleation was permitted only near the grain boundaries and a total of five sub-grains were deemed to coalesce during the formation of the nuclei. It was possible to estimate the recrystallization texture, assuming that the grains have different values of stored energy proportional to their Taylor factor (experimental data suggests that an adjustment should be used for large Taylor factors where this relationship breaks down). Hence, certain grains with a higher Taylor factor will have higher dislocation densities than others and thus smaller sub-grain sizes. These smaller sub-grains will coalesce more quickly, since the diffusion distance is relatively small. It follows that nuclei derived from heavily deformed material will dominate the recrystallized structure. It should, therefore, be possible to predict not only the fraction recrystallized but also the texture following recrystallization.

2.4.3 Preformed nucleus model

There is no generally accepted definition of what the "*preformed nucleus model*" physically means. Many authors take this to encompass any model where classical nucleation is not occurring *e.g.* Humphreys and Hatherly 1996, who suggest that recrystallization nuclei must originate from the deformed microstructure since the recrystallized texture is related to the original texture (*e.g.* Hutchinson 1998). This approach would therefore consider SIGBM and sub-grain coalescence as subdivisions of the preformed nucleus model. In this dissertation, the preformed nucleus model will be used to describe the theory that there are certain "non-deformed" (or lightly deformed) volumes within the deformed microstructure which upon annealing are free to grow.

Cahn (1949), was the first to postulate the nucleus to be a single sub-grain having at least one high mobility grain boundary and also being sufficiently large as to have an energetic advantage over its neighbours and hence to grow at their expense. Doherty (1974) illustrated that the major problem was finding out why exactly one subgrain should suddenly grow abnormally at the expense of the surrounding material. He also showed that for a moderately deformed aluminium showing a subgrain size of 1 μm, the final observed grain size after recrystallization was 100 μm. This means that only 1 subgrain in a million makes the transition from a subgrain to a recrystallization nucleus.

There is little evidence to suggest that there are viable nuclei already present in a deformed structure and no modern literature that supports this view. Furthermore, the preformed nucleus model is directly contradicted by the observations of several others (*e.g.* Anderson and Mehl 1945) who observed an incubation period before which nucleation was not apparent,

hence a pre-existing viable nucleus could not be present.

Moreover, others (Hayakawa and Spuznar, 1997 and Li, 1962) assume that the smaller sub-grains will form the new nuclei *via* coalescence; the smaller the sub-grain, the smaller the diffusion distance for dislocations and hence smaller sub-grains can coalesce more easily. This means that for a sub-grain to form a recrystallization nucleus, it must be in a region where no larger sub-grains exist, otherwise its growth might be stifled. This would imply an area of high dislocation density build-up, *e.g.* grain boundaries and transition bands, having a smaller sub-grain size is more predisposed to sub-grain coalescence and hence nucleus formation (see Fig. 2.10). This is borne out by experimental observations and therefore also suggests that a single large subgrain will not make a viable recrystallization nucleus.

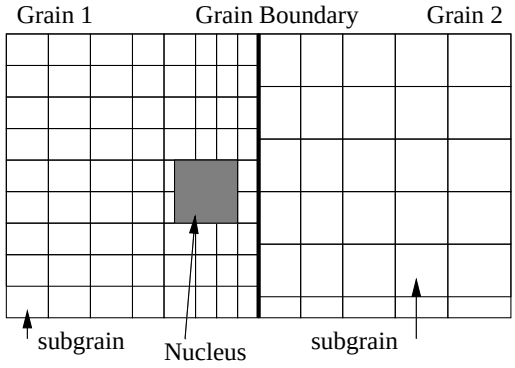

Fig. 2.10 Schematic drawing of nucleus forming from small sub-grains (Hayakawa and Spuznar, 1997)

2.4.4 Accuracy of models

It is widely accepted that modelling the nucleation process is the most difficult and contentious part of the modelling of recrystallization. Unlike growth calculations, there is no single model, or even family of models, which is generally accepted to be physical and to be a good fit to experimental data. There is a lot of literature debating which of the models illustrated in this section (if any) is the most generally applicable. This has been summarised and further elucidated by Hutchinson (1992).

2.5 Overall transformation kinetics

Many models use the KJMA or Avrami equation. This starts with the calculation for the volume of a grain ($\nu_{\tau 3}$) nucleated at time τ and growing in three dimensions is given as:

$$\nu_{\tau 3} = f\Upsilon_x\Upsilon_y\Upsilon_z\left(t-\tau\right)^3 \tag{2.32}$$

where f is a shape factor, which in conjunction with anisotropic growth rates, describes the geometric shape of the growing grain. For ellipsoidal grains the value of f will be $\frac{4}{3}\pi$, and $f = 16$ for cuboidal. These are derived from the fact that the 'radius' of the growing grain in the x direction will be $(\Upsilon_x \times (t - \tau))$, where Υ_x is the growth rate in the x direction, τ is the incubation period prior to which the grain has zero volume, t is the time into the annealing process.

For a recrystallizing thin foil of thickness much less than the typical diameter of a growing grain, the value of $\nu_{\tau 3}$ which represents the volume in three dimensions is not valid. For a thin foil the majority of the growth occurs in two dimensions, therefore the calculation for volume can be approximated to a disc of thickness δ and radii $\Upsilon_x(t - \tau)$ and $\Upsilon_y(t - \tau)$ in the x and y directions respectively, i.e. 2-dimensional recrystallization, where δ is the thickness of the foil. Thus the volume of a grain is given by:

$$\nu_{\tau 2} = f\Upsilon_x\Upsilon_y\delta\,(t - \tau)^2 \tag{2.33}$$

where f for an elliptical plate is π, this is by analogy with the simple equation for the volume of a circular disc: $\nu = \delta\pi r^2$ if r is taken to be $\Upsilon(t - \tau)$. Similarly for a thin wire of diameter δ (1-dimensional recrystallization) the volume of a grain becomes :

$$\nu_{\tau 1} = f\delta^2\Upsilon_x\,(t - \tau)^1 \tag{2.34}$$

where f for cylindrical grains is $\pi/2$, similarly by analogy with the volume of a cylinder $\nu_\tau 1 = \pi(\delta^2/4)l$ where l is the length of the grain in the direction of the wire.

Particles growing from different regions must at some point impinge. This means that the actual volume transformed will be less than the sum of the volumes of particles growing as if there were no impingement. The latter sum is known as an 'extended volume' (V_e') which arises by letting transformation occur throughout the specimen, ignoring the presence of any previously transformed regions. Assuming a constant nucleation rate, V_e' is given by:

$$V_e' = \int_{\tau=0}^{t} \dot{N}Vf\Upsilon_x\Upsilon_y\Upsilon_z(t - \tau)^3 \mathrm{d}\tau \tag{2.35}$$

where $\dot{N}$ is the nucleation rate per unit volume.

Extended volume must now be converted into the true volume. The probability of a volume element falling in untransformed material is simply $(1 - V'/V)$ where V is the total volume of the sample and V' is the true volume transformed. Therefore:

$$\mathrm{d}V' = (1 - V'/V)\mathrm{d}V_e' \tag{2.36}$$

By invoking the definitions

$$\frac{V'}{V} = \zeta \qquad \text{and} \qquad \frac{V'_e}{V} = \zeta_e$$

ζ_e is the extended fraction transformed it follows that:

$$\mathrm{d}\zeta = (1-\zeta)\mathrm{d}\zeta_e \tag{2.37}$$

hence:

$$\int \mathrm{d}\zeta_e = \int \frac{\mathrm{d}\zeta}{(1-\zeta)} \tag{2.38}$$

$$\zeta_e = -\ln(1-\zeta) \tag{2.39}$$

using the boundary conditions that at $\zeta_e = 0$, $\zeta = 0$, it follows that:

$$-\ln(1-\zeta) = f\Upsilon_x\Upsilon_y\Upsilon_z \int_{\tau=0}^{\tau=t} (t-\tau)^3 \dot{N}\mathrm{d}\tau \tag{2.40}$$

$$\zeta = 1 - \exp\left\{ -\int_{\tau=0}^{\tau=t} \dot{N}\left(f\Upsilon_x\Upsilon_y\Upsilon_z(t-\tau)^3\right)\mathrm{d}\tau \right\} \tag{2.41}$$

$$\zeta = 1 - \exp\left\{ -f\Upsilon_x\Upsilon_y\Upsilon_z\dot{N}t^4/4 \right\} \tag{2.42}$$

For two-dimensional growth *e.g.* thin sheet this gives:

$$\zeta = 1 - \exp\left\{ -f\Upsilon_x\Upsilon_y\delta\dot{N}t^3/3 \right\} \tag{2.43}$$

and for one-dimensional recrystallization:

$$\zeta = 1 - \exp\left\{ -f\Upsilon_x\delta^2\dot{N}t^2/2 \right\} \tag{2.44}$$

On the other hand, when a constant number of pre-existing nuclei is considered then the time exponent in each case is reduced by one. This is because all the particles start growing at time zero:

$$\zeta = 1 - \exp\left(-fN_0\Upsilon_x\Upsilon_y\Upsilon_z t^3\right) \tag{2.45}$$

where N_0 is the total number of nuclei per unit volume.

Equations (2.35) through to (2.38) are members of the family of equations known as "KJMA" or "Avrami" theory. The whole family is often referred to in its general form:

$$1 - \zeta = \exp\left(-k_{Av}t^n\right) \tag{2.46}$$

or

$$\ln\left[\ln\left(\frac{1}{1-\zeta}\right)\right] = n\ln t + \ln k_{Av} \qquad (2.47)$$

where n and k_{Av} are governed by the details of nucleation and growth. With the above assumptions, values of the 'Avrami exponent' n between 3 and 4 are expected for bulk samples.

2.6 Applicability of overall transformation kinetics

The "KJMA" family of equations have provided the theoretical framework for the majority of kinetic models for recrystallization produced to date. At least one of these equations has been quoted in the majority of papers in the literature about kinetic modelling of phase transformations since 1939. The KJMA approach provides an easily adaptable mathematically simple solution which has been proven to have a great deal of predicative power.

The applicability of this approach is not limited to the study of recrystallization. It is obviously applicable to any reaction $\alpha \rightarrow \beta$ where there is no chemical difference between α and β. The approach has been extended successfully to account for components of different compositions and even multiple components growing simultaneously (Jones and Bhadeshia, 1992).

However, the published data indicate that some of the assumptions inherent in the approach are invalid. By studying experimental data graphically using equation (2.47)‡ it is seen that the value of the 'Avrami exponent' n is rarely 4, more usually lying between 1 and 2. For the alloys specified in Table 2.1a, the spread of data is summarised in Table 2.2b† .

Reference	C	Si	Mn	P	S	Cr	Mo	Ni	Cu	N	Al	Nb	Ti	Ag	O_2	Balance
Hutchinson *et al.* (1989)	-	-	-	-	.0011	-	-	-	-	-	-	-	-	.0018	-	Cu
Hayakawa & Spuznar (1997)	.0036	-	.2	-	.008	-	-	-	-	.003	0.51	.005	.067		-	Fe
Sandberg & Sandström (1986a,1986b)	.017	.4	1.44	.012	.013	17.6	4.4	12.8	.025	.19	-	-	-	-	-	Fe
Speich & Fisher (1966)	.019	3.27	.083	.12	-	-	-	-	-	.006	-	-	-	-	.016	Fe
Tsuji *et al.* (1994)	.002	.15	.18	.012	.003	18.6	-	-	-	-	-	-	-	-	-	Fe
Andersin & Mehl (1945)	-	.008	-	-	-	-	-	-	.022	-	-	-	.002	-	-	Al

Table 2.2: a) Compositions of steels from the literature (wt%).

The only data to give a value for n between 3 & 4 are those by Anderson and Mehl (1945). The specimens were produced by elongating 5.1% in tension. However for all other quoted papers the mode of deformation is known to be rolling, where the applied true strain

‡ Plots of $\ln(\ln(1/(1-\zeta)))$ against $\ln(t)$ are commonly referred to as 'Avrami plots'

† For all papers data were obtained using a point counting method, except in the paper by Hayakawa and Spuznar (1997) where the exact method is not specified.

Reference	Material	Avrami exponent (n)	Rolling Reduction(%)
Hutchinson *et al.* (1989)	Copper	2.67* to 1.76**	80
Hayakawa & Spuznar (1997)	Steel	1.56	93
Sandberg & Sandström (1986a,1986b)	Austenitic stainless steel	1.10	'wrought'
Speich & Fisher	Si steel	≈2	unknown
Tsuji *et al.* (1994)	Ferritic stainless steel	1.28	70
Anderson & R Mehl (1945)	Aluminium	3.5	unknown
Hutchinson *et al.* (1973)	Copper-Gold	1.3 to 2.1	90

Table 2.2: b) Table of different experimental 'Avrami exponents' n measured for different materials after differing amounts of deformation.
**for a small grained* $(15\ \mu m)$ *parent metal*
***for a large grained* $(50\mu m)$ *parent metal*

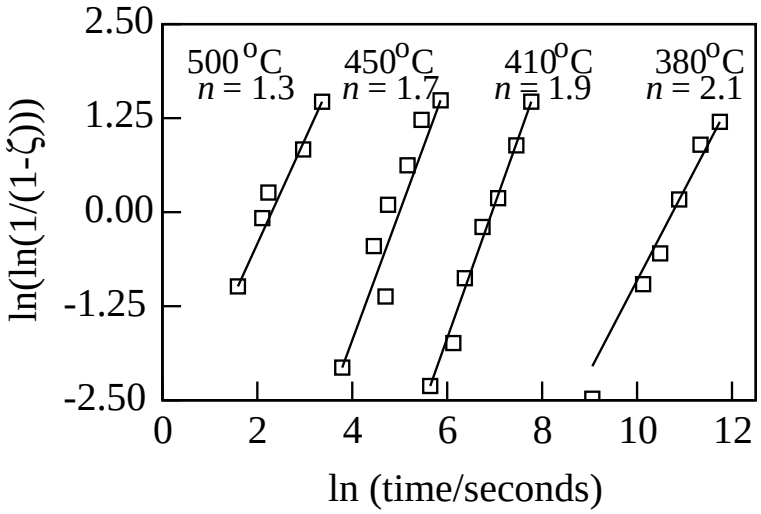

Fig. 2.11 'Avrami Plot' of data from Hutchinson *et al.* (1973)

is much greater, in the range -1.2 to -2.7 compared with the tensile strain of 0.05 used by Anderson and Mehl. It may be the case that the more severely deformed rolled samples show greater inhomogeneity of nucleation behaviour during recrystallization*.

2.6.1 Application of overall transformation kinetics

There have been a large number of models based on overall transformation kinetics produced since the publication of Kolmogorov's original work. There are also a number of review papers (*e.g.* Humphreys 1997, Speich and Fisher 1966, Doherty *et al.* 1997, Bhatia 1997,

* Features such as 'transition bands' which are regions of localised very high strain have been linked with nucleation *c.f.* §2.4. Such features are only present in materials which have undergone severe deformation.

Rollett 1997, Bhadeshia 1997, Carr 1997) concentrated on this area.

There are very few models present in the modern literature literature which apply overall transformation kinetics physically and directly. One such model is by Sha and Bhadeshia (1997) where the authors model the recrystallization behaviour of mechanically alloyed iron and nickel-base materials. Some success was achieved in predicting the final grain size as a function of the recrystallization start temperature. However they presented no data relating to fraction recrystallized as a function of time, therefore the model they produced, which was semi-physical with an Avrami exponent n of 4, was never fully tested.

Another example of a directly applied overall transformation kinetics model was given by Nes *et al.* (2000). In this work the authors studied an aluminium-magnesium-manganese alloy and used the assumption that nucleation was random and that site saturation was occurring (experimental evidence for the validity of these assumptions was given by Daaland and Nes, 1996). The authors used an advanced method for calculating the nucleation rate from the deformed microstructure and also thereby predicting the texture of the final recrystallized product. The equation to describe the variation of fraction recrystallized with time was given as:

$$\zeta = 1 - \exp\left(-\frac{4\pi}{3} N_{TotNes} \Upsilon^3 t^3\right) \tag{2.48}$$

wherein N_{TotNes} was the total number of nuclei per unit volume (taken to be constant) and was a complex function of the availability of different nucleation sites.

There was some success in modelling recrystallization texture, however, only in a small fraction of the illustrated ζ against t curves is a satisfactory fit observed. The experimental curves were usually displaced significantly from the theoretical curves on the time axis and when theoretical curves and experimental evidence did happen to coincide, often the slope of the experimental curve did not have the expected gradient. This would imply that the value of n enforced on the system was incorrect.

In the great majority of the literature published since the 1970s, overall transformation kinetics has been treated as an empirical function based loosely around equation (2.46):

$$1 - \zeta = \exp(-k_{Av} t^n) \tag{2.46}$$

where k_{Av} and n are treated as empirical fitting constants. Examples of this type of modelling are present in a large number of papers. One good example of such behaviour is given in a paper by Barraclough and Sellars (1979). Here the authors do not attempt to relate the values of k_{Av} and n to physical parameters such as growth rate of nucleation rate, they do however

comment on the empirical values of n calculated being between 1 and 2 and therefore having physical meaning.

Sandberg and Sandström (1986a,1986b) studied three different stainless steels (AISI 316L, AISI 316LN and DIN 1.4439). Similarly to the previous authors, they did not seek to physically justify k_{Av} and n, however their empirical overall transformation kinetics type model predicted the annealing data well. They also relate strain and differences in deformation history to variations in physical properties such as hardness as a function of annealing time and temperature. The model produced gives satisfactory results, however scatter in the data is very large. All equations given within this work were empirically derived.

In the paper on recrystallization of copper by Hutchinson *et al.*(1989), an empirically derived overall transformation kinetics type equation is given in a similar way to the papers by Sandberg and Sandström (1986a,1986b). Hutchinson *et al.* also study the variation of the driving force as the reaction progresses. It is clear from the discussions in the literature (*e.g.* Hutchinson 1992) and in §2.4 that it is energetically favourable for nuclei to form in highly strained portions of the deformed microstructure. The existence of inhomogeneity on the microstructural level after heavy deformation as is backed up by experimental observation.

Included in Fig. 2.12 is on optical micrograph of a 70% cold rolled type 302 stainless steel etched with Calling's reagent. The etch has preferentially attacked the more heavily deformed grains. This illustrates the fact that dislocation density and therefore driving force for recrystallization (*c.f.* §2.2.2.2) is not evenly distributed across the microstructure.

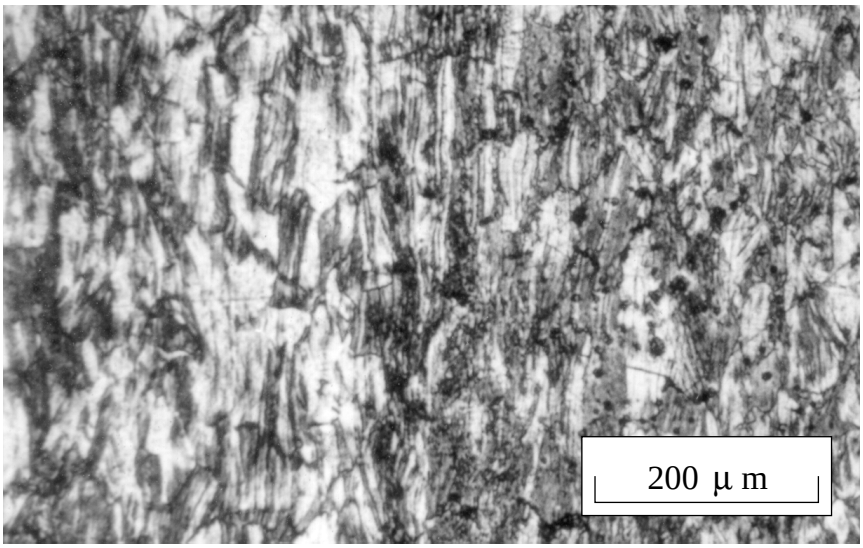

Fig. 2.12 Sample of a 70% cold rolled type 302 stainless steel etched with Kalling's reagent. This sample shows clear regions of heavy and light deformation. (Hopkin, unpublished work)

This work is further reinforced by microhardness hardness measurements of the light and dark grains. It was found that the average hardness (measured as a Vickers hardness with a load of 200g) for the light grains was 372 HV (±24 HV) compared with a hardness of 461 HV (±35 HV) for the darker grains (Hopkin, unpublished work). When these numbers are applied to equation (2.11) we see that the driving force for recrystallization in the light grains is only 65% of that for the darker grains.

Similar differences have led Hutchinson *et al.* (1989) to conclude that it is highly dubious that kinetic parameters derived from conventional analysis have physical meaning. To counteract this they have assumed that driving force for recrystallization (ΔG) is a function of time (t) and fraction recrystallized (ζ) such that:

$$\frac{\mathrm{d}\zeta}{\mathrm{d}t} \propto -\frac{\mathrm{d}\Delta G}{\mathrm{d}t} \tag{2.49}$$

This analysis is therefore capable of dealing with variation in ΔG from preferential recrystallization of most highly deformed areas and also from recovery.

2.7 Cahn-modified overall transformation kinetics

All of the models described above have been applied to recrystallization neglecting the fundamental observation that nucleation does not generally occur at random. The grain boundaries of the original microstructure play a vital role as recystallization sites. As we will see later such sites may become saturated with nuclei and hence expect variations in the Avrami parameters as recrystallization progresses. One of the first papers to discuss the variation of n with time was by Cahn (1956), reviewed by Christian (1975), treating heterogeneous nucleation at grain boundaries, edges or corners.

2.7.1 Mathematical description of Cahn-modified overall transformation kinetics

Consider a plane P_l, of area O^b. An extended area transformed O_e^β can be defined as; the area of intersection on plane P_l of extended recrystallizing grains located at a distance ϱ from the plane. Taking the real area of recrystallized material in the plane to be O^β, and assuming the intersections are randomly positioned, a fraction $(1 - O^\beta/O^b)$ of the elements that make up $\mathrm{d}O_e^\beta$ will also contribute to $\mathrm{d}O^\beta$, where $\mathrm{d}O_e^\beta$ and $\mathrm{d}O^\beta$ are increments in area over a time increment $\mathrm{d}\tau$. Hence:

$$\mathrm{d}O^\beta = (1 - O^\beta/O^b)\mathrm{d}O_e^\beta \tag{2.50}$$

That is:

$$O_e^\beta/O = -\ln(1 - O^\beta/O^b) \tag{2.51}$$

For the physical boundary condition that when $O_e^\beta = 0$ then $O^\beta = 0$.

For a grain growing isotropically with a boundary velocity Υ and which has nucleated at a time τ and at a distance ϱ from the plane of interest, the area of intersection is given by $\pi\{\Upsilon^2(t-\tau)^2 - \varrho^2\}$ for $\Upsilon(t-\tau) > \varrho$. For a time increment $\delta\tau$, for any given plane on which nuclei are forming at a rate $\dot{N}_B$ the rate of change of O_e^β will be:

$$\mathrm{d}O_e^\beta = \pi O^b \dot{N}_B \{\Upsilon^2(t-\tau)^2 - \varrho^2\}\mathrm{d}\tau \tag{2.52}$$

Integrating this in τ from $\tau = 0$ to t or equivalently from 0 to $(t - \varrho/\Upsilon)$ and introducing the variable $\Xi = \varrho/\Upsilon t$ such that:

$$O_e^\beta = \frac{\pi O^b \dot{N}_B \Upsilon^2 t^3 (1 - 3\Xi^2 + 2\Xi^3)}{3} \tag{2.53}$$

for $\Xi > 1$ and zero for $\Xi < 1$.

Hence if we treat ϱ as a variable taking any value between $\pm\infty$ and initially assuming that nuclei from neighbouring grain boundaries do not interact with each other, we see:

$$V_e' = \int_{\varrho=-\infty}^{\infty} O^\beta . \mathrm{d}\varrho = 2\Upsilon t \int_0^1 \{1 - \exp(-O_e^\beta)\}\mathrm{d}\Xi \tag{2.54}$$

$$= 2O^b \left(\frac{\Upsilon}{\dot{N}_B}\right)^{\frac{1}{3}} f^B(a^B) \tag{2.55}$$

where:

$$a^B = (\dot{N}_B \Upsilon^2)^{\frac{1}{3}} t \tag{2.56}$$

and:

$$f^B(a^B) = a^B \int_0^1 \left[1 - \exp\left\{\left(-\frac{\pi}{3}\right)(a^B)^3(1 - 3\Xi^2 + 2\Xi^3)\right\}\right] \mathrm{d}\Xi \tag{2.57}$$

If a large number of boundaries is considered such that the total area of boundaries is $O^B = \Sigma O^b$, and substituting O^B in the above in place of O^b an expression for the extended (not true) volume can be produced. This is because impingement between grains on the same boundary is accounted for and no account has been taken of impingement between grains growing from different boundaries. Thus as before invoking the relationship between true and extended volume:

$$V_e' = -V' \ln(1 - \zeta) \tag{2.29}$$

Thus:

$$\zeta = 1 - \exp\left\{-(b^B)^{-\frac{1}{3}} f^B(a^B)\right\} \tag{2.58}$$

Where:

$$b^B = \frac{\dot{N}_B}{\{8(^{\nu}O^B)^3\Upsilon\}} \tag{2.59}$$

in which $^{\nu}O^B$ is the grain boundary area per unit volume. This has two limiting solutions, firstly when a^B is very small:

$$\zeta = 1 - \exp\left(\frac{-f^B\dot{N}_B\Upsilon^3 t^4}{3}\right) \tag{2.60}$$

which is exactly the same as the "KJMA" ("Avrami") equation. And secondly at large a^B the solution is:

$$\zeta = 1 - \exp(-2^{\nu}O^B\Upsilon t) \tag{2.61}$$

Bearing in mind that $a^B = (\dot{N}_B\Upsilon^2)^{1/3}t$, that is a^B is time dependent, it becomes possible for the value of n, the Avrami exponent, to change during the course of the transformation. In practice however, due to competition between $\dot{N}_B$ and Υ it is rare to see slopes corresponding to both $n = 1$ and $n = 4$ on the same Avrami plot. Measurements are generally only possible for $\zeta = 0.01 \rightarrow 0.99$.

2.7.2 Application of Cahn-modified overall transformation kinetics

There have been surprisingly few papers describing models of Cahn modified overall transformation kinetics . This may be due to the lack of a non-numerical solution to the problem, meaning that to use this approach a great deal of computing power needs to be available. This has not been the case until quite recently and current computer capability explains a resurgence in the use of this approach. Two of the latest papers on the subject were given by Hopkin and Bhadeshia (2000, described in chapter 6) and Vandermeer and Rath (2000).

The former of these illustrates an entirely physical model of recrystallization in a type 302 stainless steel annealed under laboratory conditions. The models were made anisothermal by using the Scheil rule (this will be expanded upon in §6.4.1). The degree of fit obtained was satisfactory although the error bars present in the dataset were large and only one particular grade and one rolling reduction of stainless steel was studied. However, although simplistic, this paper demonstrates the power of the Cahn-modified overall transformation kinetics approach in producing physically meaningful accurate models of recrystallization. The model also indicated that site saturation was occurring and that the final number of nuclei present in the sample was a function of the annealing temperature.

The latter of these two papers also produced a model directly from Cahn-modified overall transformation kinetics. The data for this model were taken from a microstructural path model

calculation (see §2.8), from a 0.06 wt% nitrogen doped single crystal of iron and an undoped single crystal of iron. This model also illustrated that site saturation was occurring and that the final number of nuclei present in the sample was a function of annealing temperature. It too managed to explain all the available data with a good degree of fit using an unaltered Cahn-modified overall transformation kinetics model. However, the mathematics of the equations used to model nucleation and growth are not given and therefore this cannot be referred to as a totally non-empirical model. This work further illustrates the power of Cahn-modified overall transformation kinetics in describing the kinetics of recrystallization.

2.8 Microstructural path model

There has been interest in the calculation of the interfacial area between recrystallizing grains and unrecrystallized grains. This forms the basis of the microstructural path model, first proposed by Speich and Fisher (1966), leading to the equation:

$$S_v = K_{sf}\zeta(1-\zeta) \tag{2.62}$$

where ζ is fraction recrystallized, S_v is the interfacial area per unit volume between recrystallized and unrecrystallized grains and K_{sf} is a constant. This function was derived empirically by comparison with experimental data. However, Cahn (1967) pointed out that it is implausible in terms of the nucleation and growth structure because at $\zeta = 0$ the first grains recrystallizing would have to come into existence at a relatively large size, and subsequently not grown very much. Hence Cahn-modified the equation to give:

$$S_v = K_c\zeta^{2/3}(1-\zeta)^{2/3} \tag{2.63}$$

The above equations are both symmetrical about $\zeta = 0.5$ (see Fig. 2.13). However, this symmetry is not reflected in the experimental data. Vandermeer *et al.* (1991,1995) have attempted to provide a better model, with:-

$$S_v = K_v\zeta^q \tag{2.64}$$

where q and K_v are highly complicated functions of nucleation and growth. This development however provides only a minor improvement in the fit with experimental data, well within the scatter of results.

This work has been further expanded upon to relate observations to number of grains present per unit volume. (Vandermeer *et al.* 1991,1995)

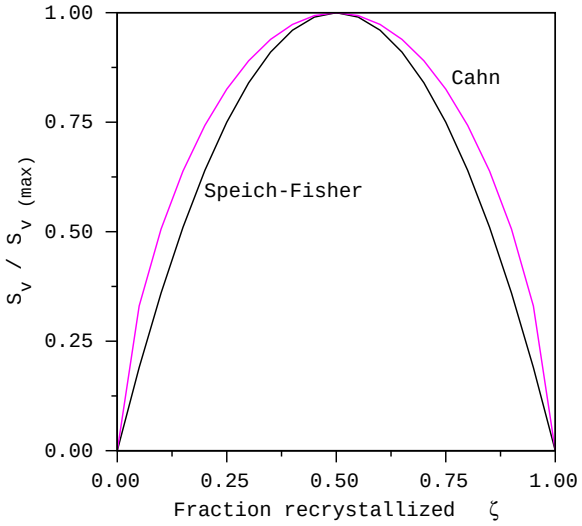

Fig. 2.13 Graph showing variation of S_v with ζ from both Speich-Fisher and Cahn equations

2.9 Monte Carlo modelling

Currently, a popular method of modelling recrystallization is by the use of Monte Carlo models. These involve a simulated grain structure consisting of an array of discrete points, each of which is assigned an integer corresponding to an "orientation". Adjacent points having identical values are part of the same grain whereas adjacent points with different values are separated by a grain boundary.

The name Monte Carlo comes from the use of a random number generator within the program. This is used to reassign the identifying integer for each cell. The resulting change in 'energy' associated with changing this number ΔG_{mc} is then calculated by considering the total area of grain boundary. If the energy of the system is reduced then this change is accepted. Otherwise the change is accepted with a probability of $\exp(-\Delta G_{mc}/RT)$. Hence in general the system will move towards its lowest energy state, but small perturbations from this energy minimisation process are still possible.

Extending this to recrystallization requires a nucleation frequency and an activation energy for nucleation, together with a difference in energy between the recrystallized and unrecrystallized grains.

There has been extensive work done in this area, notably by Srolovitz *et al.* (1986,1988), Rollett *et al.* (1992) and Hayakawa and Spuznar (1997). Srolovitz *et al.* and Rollett *et al.* consider only recrystallization in two dimensions and start with an isotropic microstructure. This gives a value of the Avrami exponent n for specific assumptions about nucleation and

growth, for example. For the two-dimensional 'samples', a constant number of nuclei gives $n = 2$ as expected. One interesting point is that the exponent does not stay constant throughout the simulation; it can be smaller for initial stages of growth, where the surface to volume ratio is very much higher than for the average grain. This value of n also deviated towards the end of the simulation.

The model by Hayakawa and Spuznar (1997) used a three-dimensional array of 'rolled' Voronoi grains elongated in a way so as to mimic the structure produced by rolling of sheet steel. The calculated value of n was 1.77 as compared with the experimental value of 1.56.

However, there remain some difficulties with Monte Carlo methods. Firstly the grain structure has to be assigned using some artificial construction as in Fig. 2.14 (e.g. Voronoi tessellations).

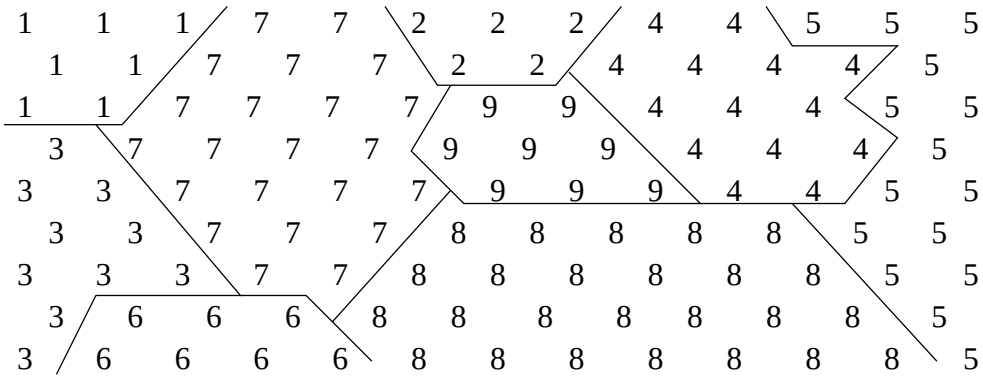

Fig. 2.14 Illustration of a typical Monte Carlo 'grain structure'

This will require either a large number of measurements with the results then entered into the computer or, alternatively, an idealised structure has to be assumed. Real time measurements of the evolution of the structure are not possible since the progress of the transformation is measured in Monte Carlo steps (MCS), one MCS being one iteration through changing the value of a lattice point and calculating its stability. Quantitative values of interfacial energy and activation energies cannot be calculated, because the lattice of points used does not correspond to a lattice of atoms, this means that Monte Carlo modelling is not kinetic or physical modelling in the true sense. The method is also particularly computationally intensive. This said, the results produced appear to be a very good representation of the actual observed microstructures.

2.10 Conclusion

Most investigations into recrystallization kinetics rely on KJMA type calculations treated either physically or empirically. Physical, unmodified overall transformation kinetics models do not give a good fit with experimental evidence, the values of the Avrami exponent n being between 3 and 4 by calculation as compared with 1 and 2 by experiment. Cahn (1956) modified the Avrami theory for heterogeneous nucleation at grain surfaces. This equation has no non-numerical solution and has rarely been applied.

It will be demonstrated in this dissertation that Cahn-modified overall transformation kinetics can be applied to recrystallization so as to solve these discrepancies.

CHAPTER 3

EMPIRICAL MODELLING

The definition of the word "*empirical*" as given in the Oxford English dictionary is:

> **Empirical** *adj* **1** based or acting on observation or experiment, not on theory. **2** *Philos.* regarding sense data as valid information. **3** deriving knowledge from experience alone.

The distinction between an purely empirical model and a purely physical model is therefore that the latter is based upon a fundamental understanding of the underlying process which is being modelled, whereas, the former simply examines the available data and infers knowledge of the behaviour of the system from there.

3.1 The need for empirical models

The development of a new material requires an extensive understanding of how processing and other factors will affect the properties of the final product. Although in some cases good theoretical models exist, there remain numerous problems for which a quantitative understanding does not exist. In fact many essential engineering properties, because of their complex dependencies on a large number of variables, cannot yet been predicted in any useful way (Table 3.1).

The current lack of quantitative models arises because such properties are dependent on large numbers of inter-related variables. Although the trained metallurgist possesses a qualitative understanding of many of these problems (*e.g.* a chaotic microstructure will lead to improved toughness due to crack deflection), these are experimental observations and not easily expressed quantitatively.

Whenever the complexity of a system becomes overwhelming from a fundamental perspective and simplification of the problem is not useful, pattern recognition techniques can be extremely rewarding. A good model must satisfy a minimum of two criteria:

1) It must describe experimental observations with as few arbitrary parameters as possible (*i.e.* it must follow Occam's razor, the principle that unnessicarily complex models should not be preferred to simpler ones).

2) It must make predictions that may be experimentally verified.

Conventional empirical models satisfy the second criterion, but only partially satisfy the

Property	Relevance
Yield strength	All Structural application
Ultimate tensile strength	All structural applications
YS/UTS ratio	Tolerance to plastic overload
Elongation	Resistance to brittle fracture
Uniform elongation	Related to YS and UTS
Non uniform elongation	Related to inclusions
Toughness	Tolerance to defects
Fatigue	Cyclic loading life assessments
Stress corrosion	Slow corrosion and cracking
Creep strength	High temperature service
Creep ductility	safe design
Creep-fatigue	Fatigue at creep temperatures
Elastic modulus	deflection, stored energy
Thermal expansivity	Thermal fatigue/stress/shock
Hardness	Tribological properties

Table 3.1: Mechanical properties still to be expressed by quantitative models (Bhadeshia 1999a)

first. There is no reasonable way of judging, in a conventional empirical model, as to how many of the parameters are arbitrary since the underlying science is not known.

3.2 Linear regression models

Historically, linear regression has been a popular and useful method where data are best-fitted to a linear relationship. That is, an equation is produced to describe a required output y, as the sum of inputs x_i each multiplied by a weight w_i plus a bias θ_{LR} such that $y = \sum_i w_i x_i + \theta_{LR}$. An example of this is the bainite reaction-start temperature B_S in steels which may be given as (Steven and Haynes 1956):

$$B_S(^\circ\mathrm{C}) = \underbrace{830}_{\theta_{LR}} \underbrace{-270}_{w_C} \times c_C \underbrace{-90}_{w_{Mn}} \times c_{Mn} \underbrace{-37}_{w_{Ni}} \times c_{Ni} \underbrace{-70}_{w_{Cr}} \times c_{Cr} \underbrace{-83}_{w_{Mo}} \times c_{Mo} \qquad (3.1)$$

where c_i is the weight percent of element i.

This equation assumes a linear relationship between B_S and c_i, and that there is no interaction between different elements. This is unlikely to be the case because, for instance,

molybdenum is a strong carbide former and therefore there must be interaction between c_C and c_{Mn}. Therefore any method of regression will suffer because the structure of the equation must be chosen before the analysis and any one structure, although it fits experimental data well in one region of input space, may not in others.

3.3 Non-linear regression

To improve on linear regression, it is necessary to increase the flexibility of the regression models but, at the same time, avoid fitting the model to the noise in the data as well as the trends.

Given a suitably flexible function and framework of model, non-linear regression models have the potential to contain a number of internal fitting parameters that tends to infinity. This is because the more internal fitting parameters we have the more potential for flexibility there is in the model and an infinitely flexible model will always fit a given dataset perfectly. A highly flexible function, when modelling a noisy dataset, may model the noise in the data. This phenomenon is called 'over-fitting'.

Assuming that all input parameters are precise, the fit of the model may be evaluated by comparing the predicted values (y_j) with the measured values (t_j) *e.g.* :

$$E_D \propto \sum_j \left(t_j - y_j\right)^2 \tag{3.2}$$

In general, as the complexity of the model increases the fit of the model gets better and therefore E_D will reduce. To check for over-fitting, the dataset is split into two parts, the training and test datasets. The former is used to create a model and the latter to test how any particular model generalises to unseen data. The model calculates E_D for the test dataset, which it has not previously seen, as the complexity of the model increases E_D will initially decrease in value, when over-fitting starts to occur E_D will start to increase. This is illustrated in Fig. 3.1.

3.4 Bayesian probability theory

The derivation described in the previous section provides a useful qualitative comparison, but over-parameterised models which randomly happen to fit the test data well will also be favoured by this method. This contravenes Occam's razor, therefore a more rigourous method of model comparison is needed. Bayesian probability theory is the mathematical framework which makes this possible.

Bayesian probability was first conceived by Bayes (1763) and Laplace (Stigler, 1986) and developed by Jeffreys (1939). Bayes' law assigns probabilities to different models describing

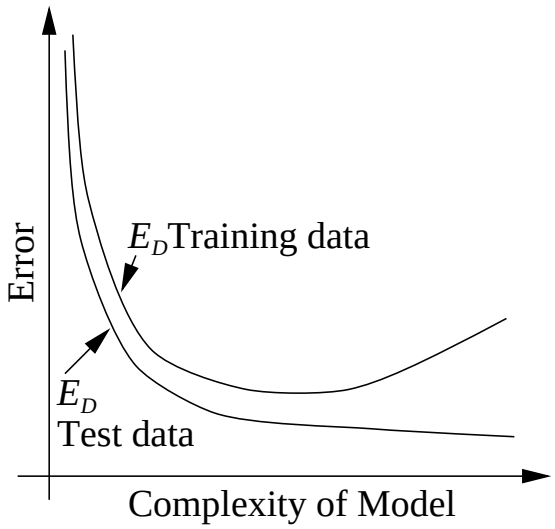

Fig. 3.1 Schematic of variation of E_D with model complexity

the plausibility of each model $\mathcal{H}_i$. Each model makes predictions about how likely a dataset D is, given the model $\mathcal{H}_i$ is true. These predictions describe a probability distribution $P(D|\mathcal{H}_i)$ (the probability of D given $\mathcal{H}_i$). If the dataset D is the actual experimental dataset, the plausibility of $\mathcal{H}_i$ given D ($P(\mathcal{H}_i|D)$) is the product of $P(\mathcal{H}_i)$ the plausibility of the model before observing the dataset and $P(D,|\mathcal{H}_i)$. Mathematically this is given as:

$$P(\mathcal{H}_i|D) = \frac{P(\mathcal{H}_i) \times P(D|\mathcal{H}_i)}{P(D)}. \tag{3.3}$$

$P(D)$ is included as a normalising constant to ensure $P(\mathcal{H}_i|D)$ sums to unity over the input space.

For a given model $\mathcal{H}_i$ predicting a data-point R the accuracy of the prediction is modelled as a probability distribution $P(R|\mathcal{H}_i)$ (the probability that the point R is correct given $\mathcal{H}_i$) known as the evidence for R.

A data-point R will exist somewhere within the range of possible outputs of the model $\mathcal{H}_i$†. Therefore if the model $\mathcal{H}_i$ has a vectorial set of internal weights and biases $\mathbf{w}$ which exist over a range of values $\mathbf{w}_{-\infty}$ to $\mathbf{w}_{+\infty}$, the integral of $P(R|\mathcal{H}_i)$ from $\mathbf{w}_{-\infty}$ to $\mathbf{w}_{+\infty}$ is unity. That is, finding R somewhere within the range of possible outputs of $\mathcal{H}_i$ is certain.

If the model fits the data well, the value of the evidence will peak sharply at R. If the model does not fit well, this peak will be broader with a lower maximum value. A well-fitting model can therefore be distinguished as having a high peak in the evidence.

Implausibly complex models will always fit data. However, such models will contain a large number of arbitrary fitting parameters. $P(R|\mathcal{H}_i)$ must be unity when integrated across

† If a model is incapable of predicting a data-point R it will have a zero value of $P(\mathcal{H}_i)$ and therefore will be disregarded by Bayes' law

all of these parameters, the greater the number of parameters to integrate over, the more spread out the unit of probability will become thus decreasing the height of the peak in the evidence.

Therefore the height of the evidence peak not only penalises badly fitting models but also over complicated models. This Bayesian treatment is a quantitative embodiment of Occam's Razor.

To train a model $\mathcal{H}_i$, the program must infer what the model's parameters $\mathbf{w}$ might be given the data set D. Using Bayes' rule the plausibility of a model $\mathcal{H}_i$ given a dataset D is:

$$P(\mathbf{w}|D,\mathcal{H}_i) = \frac{P(D|\mathbf{w},\mathcal{H}_i)P(\mathbf{w}|\mathcal{H}_i)}{P(D|\mathcal{H}_i)}. \tag{3.4}$$

The normalising constant $P(D|\mathcal{H}_i)$ (the probability of D given all values of $\mathcal{H}_i$ also known as the evidence for $\mathcal{H}_i$) in this case is commonly ignored since it is irrelevant to the choice of $\mathbf{w}$. Gradient based methods are used to locate maxima in the value of $P(\mathbf{w}|D,\mathcal{H}_i)$, which define most probable values for the parameters ($\mathbf{w}_{MP}$). $P(\mathbf{w}|D,\mathcal{H}_i)$, known as the posterior probability, can therefore be summarised by $\mathbf{w}_{MP}$ and error bars on these parameters. These error bars are obtained by analysis of the curvature of the posterior. Flat posterior probability curves give large error bars as the values of $\mathbf{w}_{MP}$ could lie anywhere at the bottom of the probability well. Conversely, sharp posterior curves mean the value of $\mathbf{w}_{MP}$ are well defined, and therefore errors in $\mathbf{w}_{MP}$ will be small. Error bars in the predictions are a combination of the error in $\mathbf{w}$ and the perceived noise in the data σ_ν.

If a model is trained on a dataset D of experimentally obtained results t_m for a given set of input parameters x_m, for each value of t_m a model can produce an predicted output $y_m(x_m)$. Assuming there is noise in the dataset D and that the model is correct, the values of t_m will lie scattered about the model values $y_m(x_m)$. Such that:

$$t_m = y_m(x_m) + \nu_m \tag{3.5}$$

ν_m is conventionally a zero mean Gaussian noise of standard deviation σ_ν. σ_ν is calculated by consideration of Bayes' law, however, due to the complexity of the problem, it will not be expanded on in this work; a comprehensive derivation has been reviewed by MacKay (1992).

3.5 Neural network computational structures

A 'neural network' is a method of non-linear regression as introduced in §3.3. Neural networks have been used successfully in modelling numerous materials science problems (*e.g.* Narayan *et al.* 1999, Garvard *et al.* 1996, Brun *et al.* 1999, Lalam *et al.* 2000, Cole *et al.*

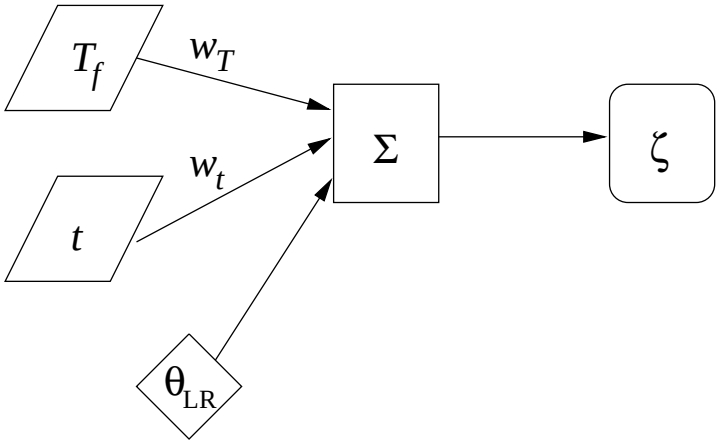

Fig. 3.2 Schematic of linear regression analysis of fraction recrystallized of the general form $y = \sum_i w_i x_i + \theta_{LR}$

1999, Bhadeshia 1999b, Svensson and Bhadeshia 1998). Fig. 3.2 represents a linear regression analysis of the recrystallization process, wherein furnace temperature T_f and annealing time t are the inputs to predict the output of fraction recrystallized ζ.

This treatment of recrystallization would be grossly inaccurate since the linear form of the regression is incapable of producing the true shape of the recrystallization curve.

The neural network approach follows the same basic structure, but is made non-linear by using the above sum as the argument of a non-linear function such as the hyperbolic tangent, such that:

$$h = \tanh\left(\sum_j w_j^{(1)} x_j + \theta^{(1)}\right) \tag{3.6}$$

and:

$$y = w^{(2)} h + \theta^{(2)} \tag{3.7}$$

wherein x_j is an input value (*e.g.* furnace temperature T_f), $w_j^{(1)}$ and $w^{(2)}$ are weights and $\theta^{(1)}$ and $\theta^{(2)}$ are biases.

The output y is a weighted and biased form of the output from the hyperbolic tangent, the output from the hyperbolic tangent is not observed by the operator and is therefore referred to as the hidden unit. The hyperbolic tangent function is generally used because of its flexibility. This flexibility may not be enough to describe the full complexity of the system. Therefore, a combination of hyperbolic tangents are used, such that:

$$h_i = \tanh\left(\sum_{ij} w_{ij}^{(1)} x_j + \theta^{(1)}\right) \tag{3.8}$$

$$y = \sum_i w_i^{(2)} h_i + \theta^{(1)} \tag{3.9}$$

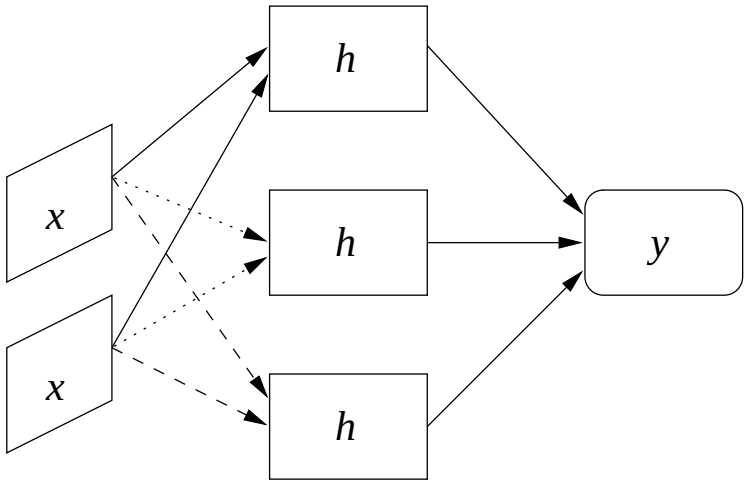

Fig. 3.3 Schematic of neural network regression analysis

The structure of this arrangement is illustrated in Fig. 3.3.

The neural network structure of a combination of hyperbolic tangents illustrated in Fig. 3.3 allows a very large amount of flexibility in the output this is illustrated in Fig. 3.4.

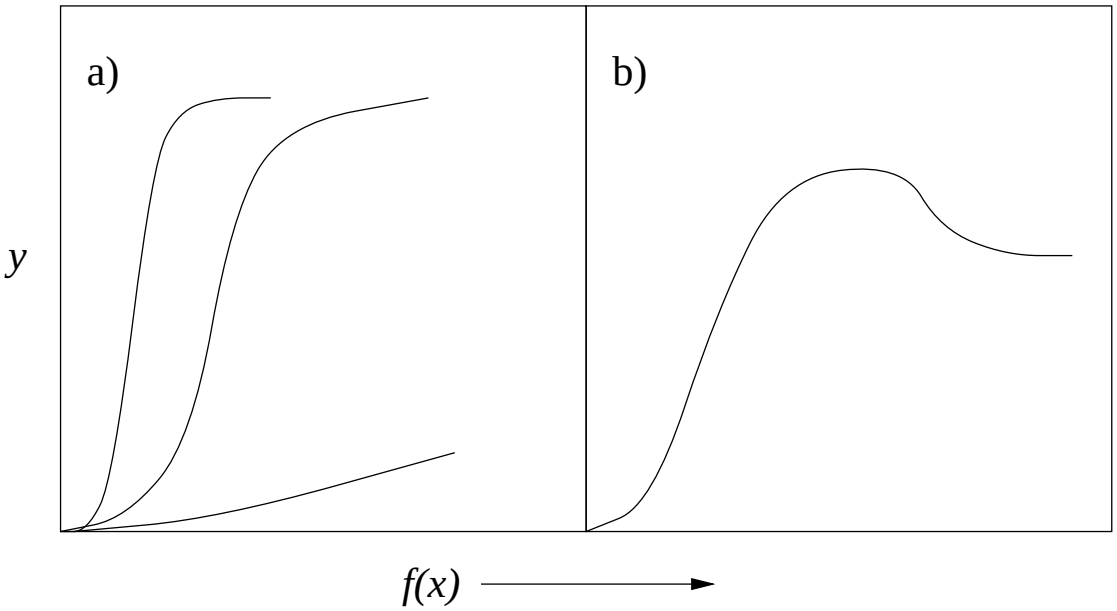

Fig. 3.4 a) Three different hyperbolic tangents with differing values of w_i **b)** Two hyperbolic tangents combined to produce a more complex model

3.6 Applications of neural networks

Neural networks are a well recognised and respected method of regression. They have been used to predict behaviours as diverse as information management and retrieval (Chen and Dhar 1991) to mapping land cover (Tatem *et al.* 2000); however this study will concentrate on their applications in materials science.

Owing to the flexibility of the system, in theory, any arbitrarily complex system showing a systematic, non-periodic dependence on a given set of input variables (x_i) may be modelled. Using Bayesian statistics the possible problem of over-parameterisation may be avoided. In essence, neural networks should be able to predict systematic behaviour in any system.

3.6.1 Industrial relevance of non-linear regression

Most industrial processes already involve some degree of empiricism and an approximate relationship between industrial parameters and final properties is known. There are very few cases of industrial processes being run using laboratory models because industrial working parameters are generally not easily transformed into analytical inputs. Although typically industrial processes are controlled and reproducible, many are not easily quantifiable. *e.g.* Cole *et al.* (1999) where creep rupture strength is predicted from 32 separate variables, including mode of cooling. The different modes include: i) furnace cooling, ii) air cooling iii) water or oil quenching. Each of these methods will produce different microstructures identifiable to the metallurgist. However, defining an overall parameter which embodies the range of different cooling rates through the bulk of the sample for use in a theoretical model to predict creep properties will be prohibitively complex. Neural networks have sufficient flexibility to convert non-calibrated and non-calibratible input parameters into a meaning full output, given that the input parameter has a meaningful effect on the output.

The industrial annealing process has a number of difficult-to-calibrate parameters *e.g.* furnace temperature T_f, initial strip condition *etc.* Therefore it is an ideal candidate for empirical modelling. Currently stainless steels are annealed by comparison with previous annealing results within a given grade. However there is still a good deal of noise in the results (Backhouse, 2000).

3.7 Gaussian processes

Gaussian process models, similarly to neural networks, are a nominally infinitely flexible fitting technique. They also rely on Bayesian probability theory to ensure Occam's razor is not contravened (*i.e.* over-parameterisation does not occur). A Gaussian process works by calculating a joint probability distribution function for the complete set of experimental data

$(\mathbf{t} = (t(\mathbf{x_1}), t(\mathbf{x_2}), \cdots)$:

$$P(\mathbf{t}|\mathbf{C}, \{\mathbf{x}_n\}) = \frac{1}{Z} \exp\left(-\frac{1}{2}(\mathbf{t} - \mu_{GP})^T \mathbf{C^{-1}} (\mathbf{t} - \mu_{GP})\right) \tag{3.10}$$

Wherein $\mathbf{C}$ is the covariance matrix (matrix describing effect of the inputs $(\mathbf{x}_n)$ plus how interactions between pairs, triplets, quads *etc.* of inputs effect the output), the number of dimensions needed to describe $\mathbf{C}$ is equal to the number of inputs in the database and μ_{GP} is the mean vector. $P(\mathbf{t}|\mathbf{C}, \{\mathbf{x}_n\})$ gives the probability of the entire dataset $\mathbf{t}$ given an input matrix $\mathbf{x}_n$ and a matrix of interaction factors $\mathbf{C}$. This is in direct contrast to a neural network which works out the probability of a given model for a given data-point.

Full explanations of Gaussian processes are available in the literature(*e.g.* Gibbs 1997). A full comparison between Gaussian processes and neural networks is also available (Tancret *et al.* 1999).

The major disadvantages of Gaussian processes are that the size of the covariance matrix $\mathbf{C}$ grows exponentially with the number of inputs and although some (if not most) of these interactions will be disregarded by Bayes theory, they must all be trained and tested. This means computational intensity increases exponentially with number of inputs. Also, since this is a probability distribution across the whole dataset, when the model is far from a data-point it will become unsure. In the case of neural networks this will be illustrated by large error bars, but trend prediction will still continue. In the case of Gaussian processes if the model is unsure the probability $P(\mathbf{t}|\mathbf{C}, \{\mathbf{x}_n\})$ will tend to zero, *i.e.* trends will no longer be predicted.

3.8 Conclusions

There is an indisputable need for empirical modelling to predict behaviour for which there is currently no physical numerical model. Traditionally this has been done with linear regression, however utilising the advances in computer power we may now use more complex modelling methods to confidently give accurate answers.

Modern regression analysis techniques such as neural networks and Gaussian processes are nominally infinitely flexible. This flexibility could lead to erroneous results if fitted blindly to a dataset, but using Bayesian probability theory this problem may be avoided. Regression techniques have the ability to produce quantitative answers from industrial data which is physically non-quantifiable (*e.g.* mode of cooling). Therefore they are ideally suited to situations where direct analytical measurements are difficult (*e.g.* the temperature of strip inside a furnace).

From the point of view of the industrialist, neural networks are the most useful of the above techniques. This is because they provide quantitative answers from industrial parameters (*e.g.*

roll pressures, nominal furnace settings) and once trained are not excessively computationally intensive. Moreover they may highlight the factors which are most significant in the regression within a non-linear framework.

CHAPTER 4

EXPERIMENTAL METHODOLOGY

4.1 Production of samples

The material for all experimental work was provided in the form of strip or sheet by Avesta Polarit Ltd., from the Stocksbridge or Shepcote Lane works. The rolled sheet was cut into squares of 1 cm×1 cm using a guillotine, tin-snips or scissors depending on the gauge of the material in question.

4.1.1 Initial sample production method

The first experiments used a type 302 stainless steel (chemical details of this steel are given later in the thesis in Table 6.2) which was placed into a porcelain boat, which was then put into a furnace at a specified, stable temperature. These samples were water quenched, then mounted and polished after which 6 hardness measurements were made per sample using a standard Vickers hardness machine with a load of 5 kg. A database of annealing time (t), furnace temperature (T_{ff}) and final hardness (H) was compiled. As will be explained in chapter 5, this method proved to be inadequate, therefore the procedure below was adopted instead.

4.1.2 Revised sample production method

A second dataset was obtained using the same sample geometry, but with each sample resistance welded to a K-type thermocouple. For the methodology described in §4.1.1, the samples were introduced into the furnace via the furnace door. This operation allows the hot air in the furnace to escape, causing a sudden drop in furnace temperature of approximately 50 °C. The temperature begins to recover on closing the furnace door, but may overshoot its original value by some 25 °C. This instability in temperature (totalling 75 °C) can be avoided by introducing the samples into the furnace through a chimney vent at the top of the furnace using the thermocouple wire as a support as illustrated in Fig. 4.1.

The temperature of each sample was monitored as a function of time such that a comprehensive heating curve could be recorded for every sample. A database was compiled of the true furnace temperature T_f, representing the final stable temperature achieved by the sample in the furnace, annealing time t, taken as the total time the sample spends in the furnace and the final hardness H. In measuring the hardness, areas in the vicinity of the thermocouple weld were avoided.

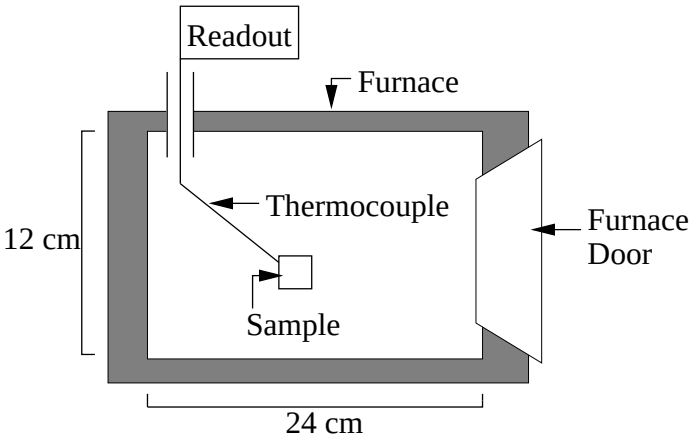

Fig. 4.1 Schematic illustration of the experimental equipment

The parameters needed for kinetic analysis *i.e.* fraction recrystallized, recrystallized grain size *etc.*, are not as easily obtained, therefore several different methods were investigated as described below.

4.2 Conventional Metallurgical Techniques

It is normal in measuring the grain size and other microstructural details for the sample to be mounted, polished and etched, followed by observation using either reflected light or scanning electron microscopes. Two standard methods of etching were chosen and investigated (Vander-Voort, 1984):

i) A saturated solution of $FeCl_3$ in concentrated HCl with a HNO_3 activator. This etch proved to attack the steel too quickly for effective control, leaving a dark brown residue over the surface of the steel. It's use was therefore discontinued.

ii) Electrolytic etching at 17V using a 20% solution of oxalic acid ($H_2C_2O_4$) in distilled water. There was limited success with this method. Although it did tend to pick out grain boundaries within the recrystallized grain structure. The samples became intensely pitted with grain boundaries delimited by a series of pits. The deformed microstructures were difficult to interpret and small recrystallized grains (of a size comparable with the pit width of circa 0.1 μm) could not be resolved. Scanning electron microscopy images of samples etched in this way are included in Fig. 4.2.

Conventional metallurgical techniques were discontinued, due to the poor quality of the images obtained.

4.3 Tint Etching

To avoid oxidation and carborisation during annealing at 1100 °C or more, pre-polished samples were sealed in silica tubes containing pure argon gas at a pressure of one twentieth of

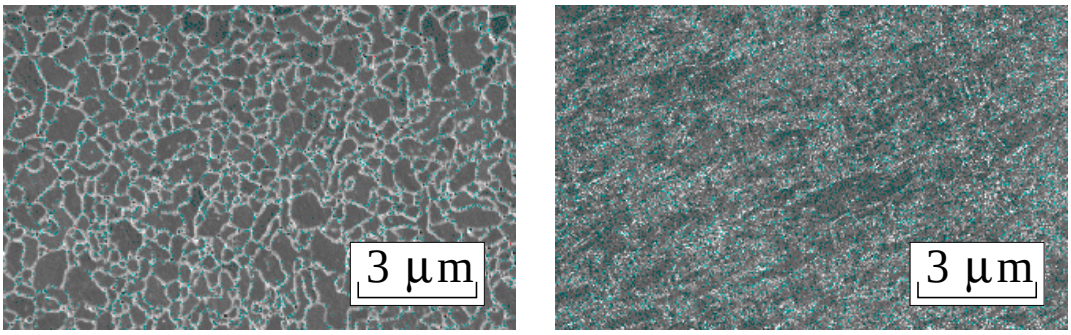

Fig. 4.2 Recrystallized microstructure in type 302 stainless steel viewed in a CamScan S2 scanning electron microscope using secondary electron imaging at 20 kV. **a)** Recrystallized microstructure formed by resistance heating of sample using a resistance welder. **b)** Grains and other details of microstructure difficult to observe.

an atmosphere. On completion of the heat treatment the tubes were removed from the furnace, held above a reservoir of water and fractured, thus allowing the sample to be quenched by the water therein. It was noticed that the microstructure of the samples could be observed clearly without further etching. This is due to a thin layer of surface oxide with preferential oxidation at the grain boundaries (Fig. 4.3).

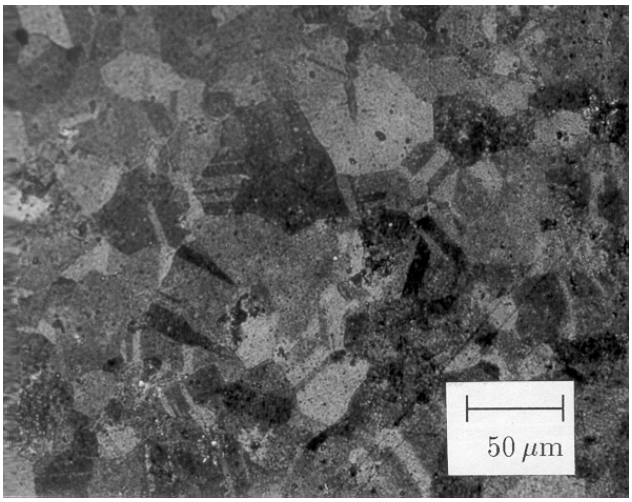

Fig. 4.3 A tint etched sample annealed at 900 °C for 490 min.

However, this method proved to be applicable only to fully recrystallized microstructures for two reasons. Firstly, the partially recrystallized regions could not be observed because the sample needed to be above approximately 900 °C for oxide formation (*i.e.* high enough to

cause complete recrystallization. Secondly, since the samples were encapsulated in silica tubes, a thermocouple could not be attached. Consequently the temperature could not be measured accurately. This method was therefore discontinued.

4.4 Transmission Electron Microscopy

Transmission electron microscopy (TEM) methodology has been reviewed extensively in the literature (*e.g.* Seigel 1964) and will not be discussed here.

For electrons to be transmitted and not absorbed, the observed sample must be exceedingly thin (of the order of 100 nm). As a consequence, sample preparation is not trivial. Discs of annealed stainless steel, each with a diameter of 3 mm, were punched out and then manually ground down to a thickness of approximately 50 μm. These specimens were then electropolished at approximately 17 V in a solution of 5% perchloric acid in an 80/20 ethanol/glycerol mixture until a small perforation developed in the sample. The area around the perforation was then inspected using a JEOL 200CX transmission electron microscope with an accelerating voltage of 200 kV.

The sample was inspected using a combination of bright field and dark field imaging. In both cases recrystallized and unrecrystallized grains could be seen with great clarity. Moreover features such as annealing twins, grain boundaries in the deformed structure, dislocations and recrystallization nuclei could be easily recognised.

4.4.1 Results from transmission electron microscopy

Fig. 4.4a is a micrograph of a typical recrystallized grain in which annealing twins can be observed. Annealing twins are distinguished from deformation twins by their strain-free straight edges and well-defined corners. Fig. 4.4b shows the superimposed diffraction beams from the pair of twins on the central grain illustrated in Fig. 4.4a, this confirms that the twins share a common {111} face.

Because of the large amount of prior cold work, it was impossible to quantify the dislocation density of the unrecrystallized regions using transmission electron microscopy. Fig. 4.5 is an illustration of this problem, showing a dark unrecrystallized region towards the left of picture adjacent to a recrystallized grain. In the recrystallized grain there is a set of dislocations which were probably induced during the polishing/grinding process since, in the image, these may be identified as separate features. There is no guarantee that it will always be possible to distinguish these artifacts of preparation from features induced by the rolling process.

Recrystallization nuclei were frequently observed at the prior austenite grain boundaries. This is illustrated in Fig. 4.6

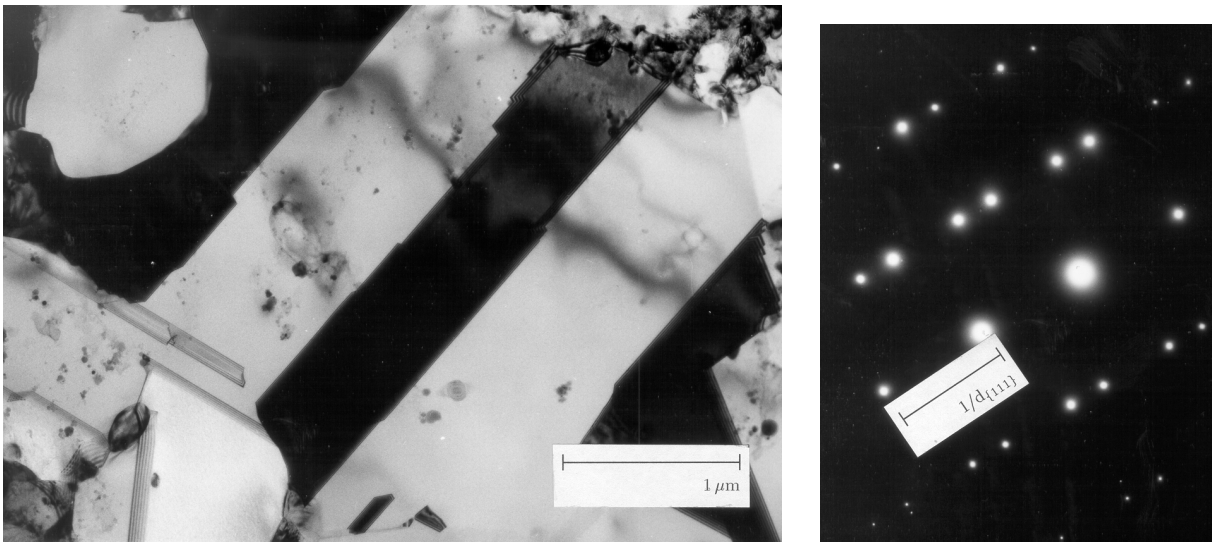

Fig. 4.4 a) A TEM micrograph from a type 302 austenitic stainless steel annealed for 1 hour at 685 °C and then etched as described above. It shows clear annealing twins and a small region of unrecrystallized material in the top right-hand corner of the micrograph. **b)** Diffraction pattern obtained from selected area diffraction of twins only. This diffraction pattern is fully indexed for each twin in **c)**.

4.4.2 Problems with transmission electron microscopy

TEM is the most accurate method of characterising partially recrystallization microstructures available, but there are a number of problems associated with this methodology.

Firstly, sample production is both tedious and time-consuming. Secondly, samples often have only a very small observable, electron-transparent area, as illustrated in Fig. 4.7.

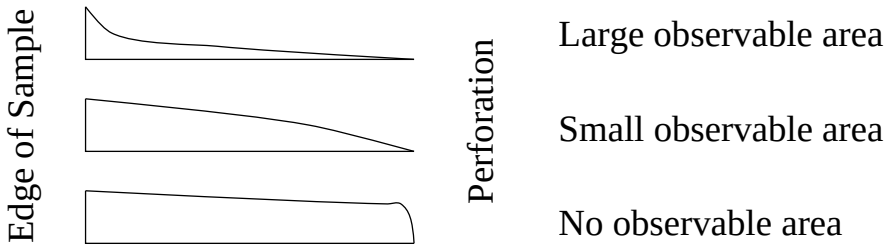

Fig. 4.7 Differences in electropolishing of TEM samples leading to different thickness gradients and hence different areas of electron-transparent material.

Moreover, the time taken to get an acceptable image from a TEM is of the order of one hour requiring skilled calibration and a full understanding of the peculiarities of both TEM methodology and also the particular machine in question.

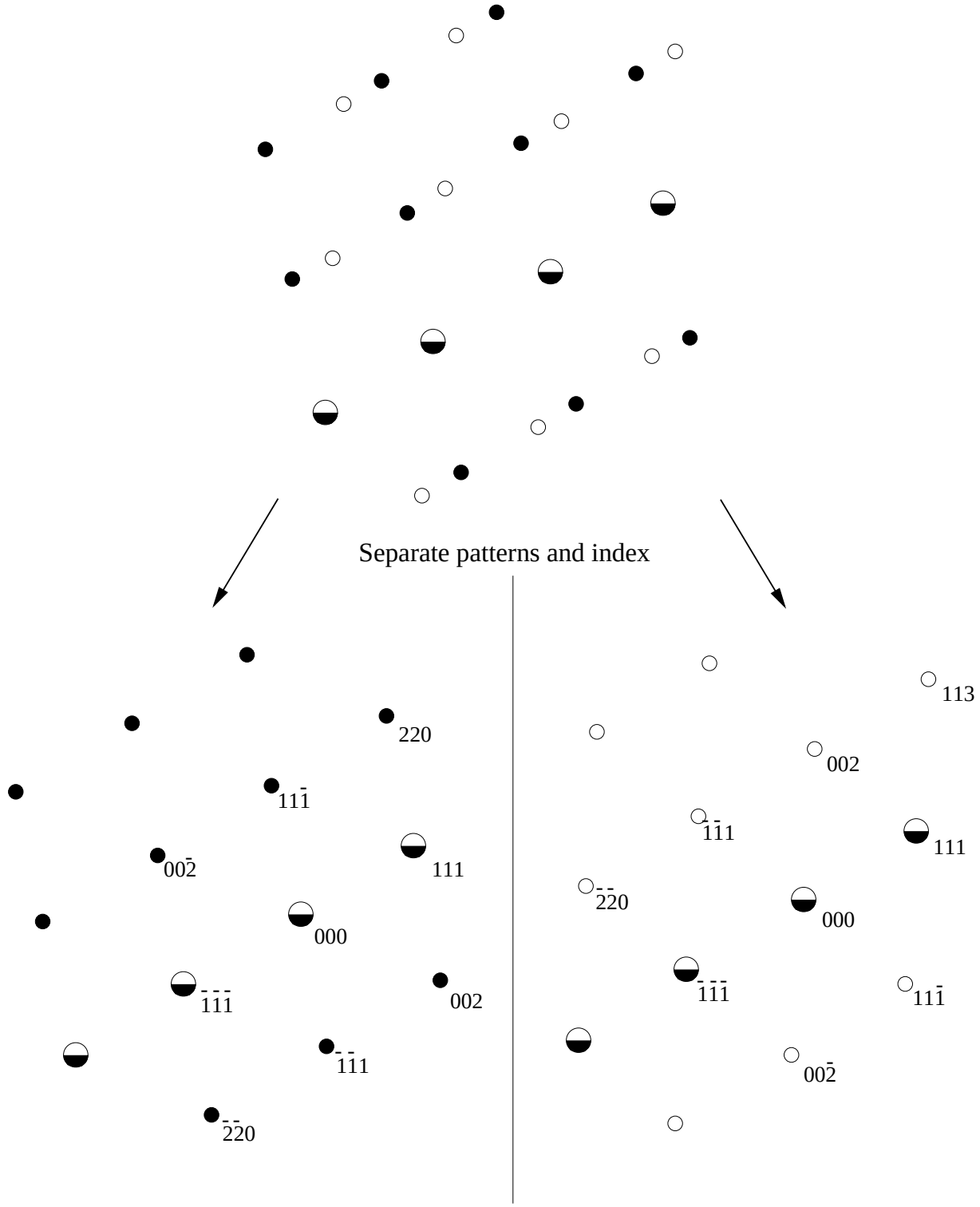

Fig. 4.4c) Indexing of the pattern Fig. 4.4b) which has been split into two different patterns, one for either twin, represented by the filled and open circles, each indexed separately above. These patterns coincide on a specific set of hhh spots indicating that these planes are parallel in both twins *i.e.* the twin plane is a $\{111\}$ plane.

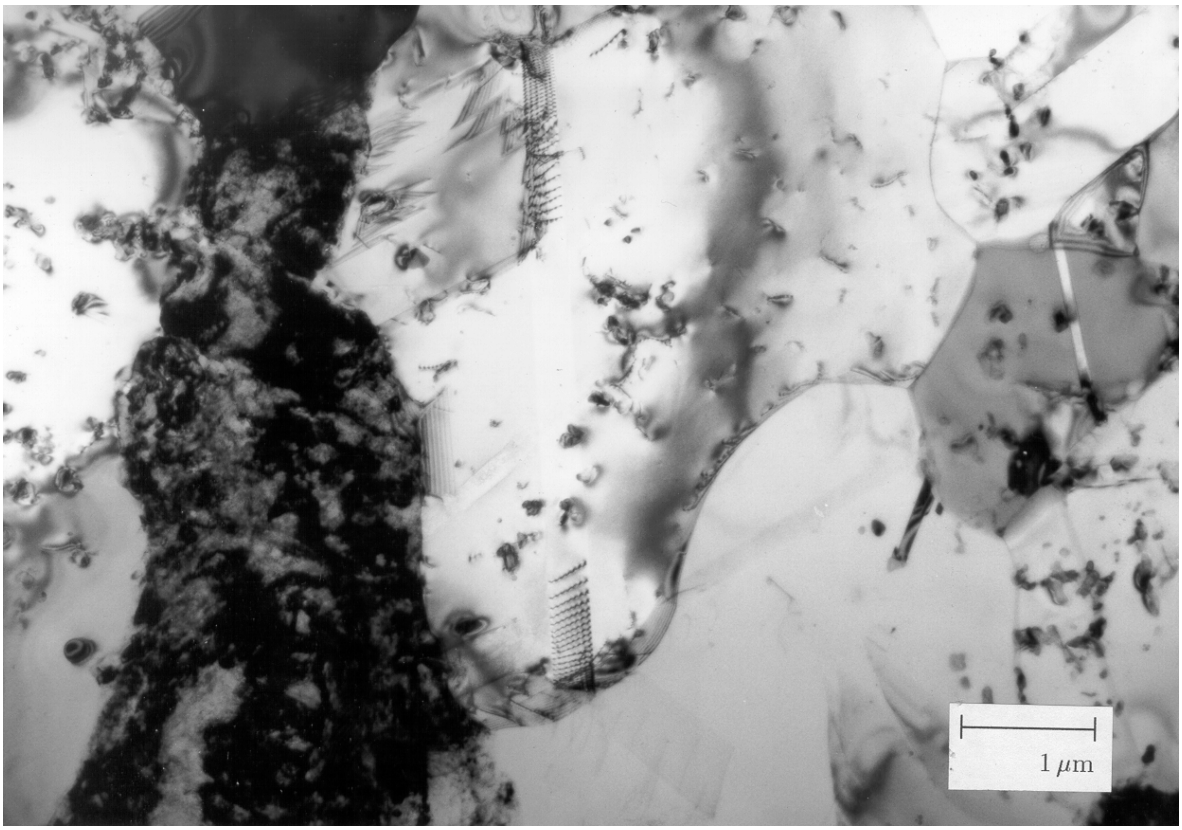

Fig. 4.5 TEM micrograph of recrystallized and unrecrystallized regions in a type 302 stainless steel annealed for 1 hour at 704 °C , exhibiting grinding induced dislocations in recrystallized grains

Finally and most importantly, the volume of material observed during a three hour session on a TEM with a very well prepared sample would be of the order of $1 \times 10^{-18}\text{m}^3$ meaning that it is impossible to get information which can be confidently deemed to be representative of the bulk sample. In fact, a well recognised estimate of the total volume of material ever studied under a TEM is 0.1 mm^3. TEM is nevertheless useful in observing features such as those indicated in figures 4.5 and 4.6, however, it cannot be used to calculate parameters such as fraction recrystallized.

4.5 Scanning Electron Microscopy

During scanning electron microscopy (SEM) a beam of electrons is scanned along the surface of a sample causing electrons to be emitted from the sample. These latter electrons are collected and converted into an electrical signal which is in turn amplified to form an image on a phosphorescent screen. Therefore anything causing a variation in the excitation of electrons from the sample *e.g.* topology, will give a corresponding contrast on the screen and hence form an image. A schematic diagram of the SEM is given in Fig. 4.8.

Fig. 4.6 A TEM micrograph from a type 302 stainless steel annealed for 1 hour at 685 °C illustrating nucleation occurring on the grain boundaries of the deformed structure

There are two "types" of electrons which exit from the specimen. Firstly the primary or backscattered electrons, these are formed by "reflection" of the electrons from the sample. The energy of a backscattered electron is of the order of the accelerating voltage used (usually about 20 keV). The primary electron detector has a shield over it at approximately -50 V, this allows high energy electrons past, but low energy electrons are excluded. Secondly, secondary electrons, are low energy ($\approx$ 150 eV), therefore they are attracted to the detector by a positive potential (200 V) on the mesh covering the detector. Since only those secondary electrons generated near the surface of the sample can escape, they are particularly useful for the observation of sample topology.

4.5.1 The Position of the Backscatter Detector

Backscattered electrons do not just sample the surface of the specimen, in fact they derive from an interaction volume† within the sample. The exact shape of the interaction volume varies with accelerating voltage, being a hemisphere at low voltages (1–5 kV) to a pear shape

† The interaction volume of a sample is the volume from which backscattered electrons

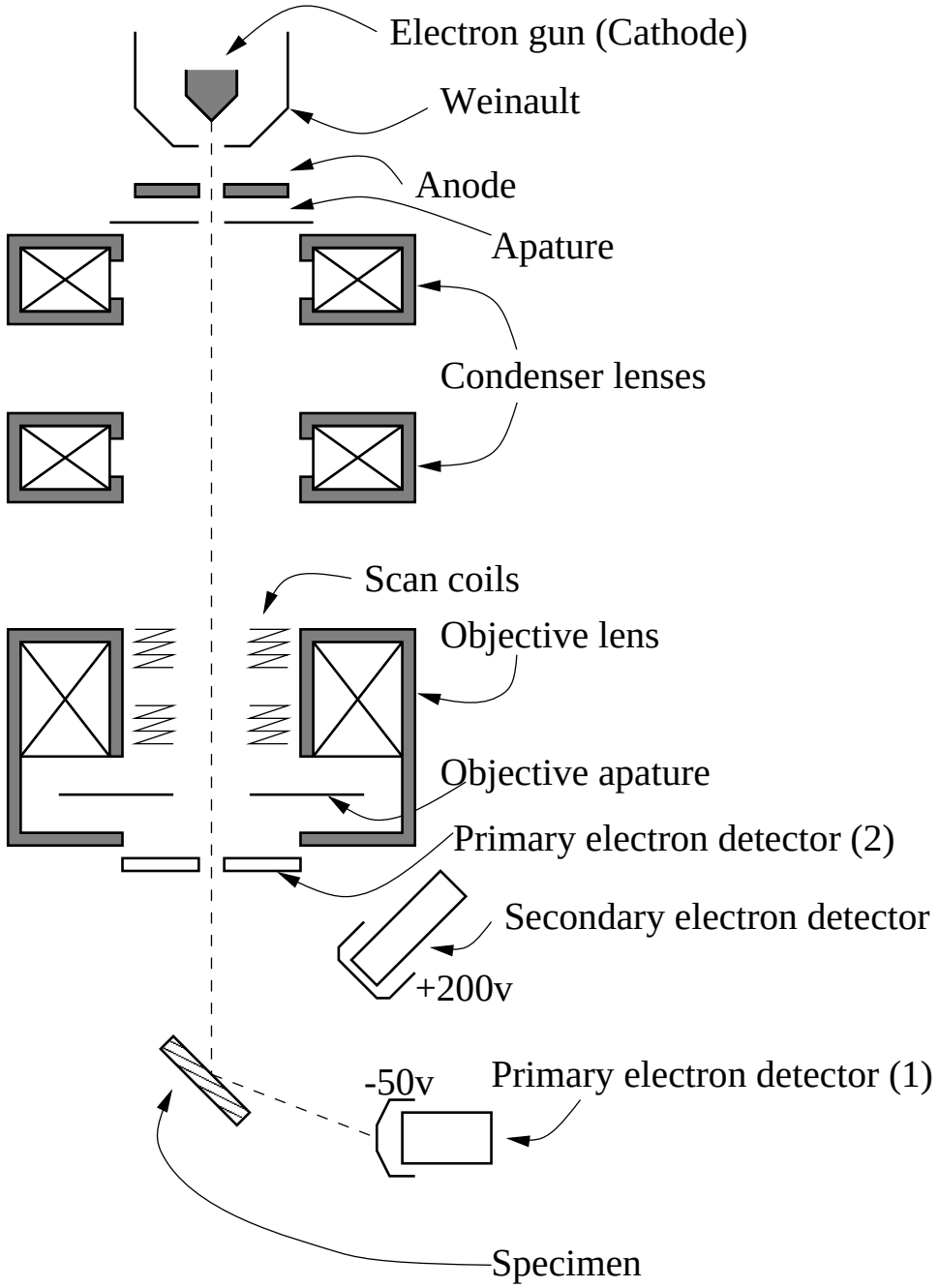

Fig. 4.8 Schematic illustration of a Scanning electron microscope (adapted from Reed-Hill and Abbaschian, 1994)

at higher voltages (<15 kV). To maximise the number of backscattered electrons produced, the sample is conventionally tilted so that a greater area of the interaction volume intersects the surface of the sample (Fig. 4.9). With a tilted sample the primary electron detector must be moved to a position where the most backscattered electrons are being reflected, this is

may be produced when an electron beam impinges on the surface of a sample

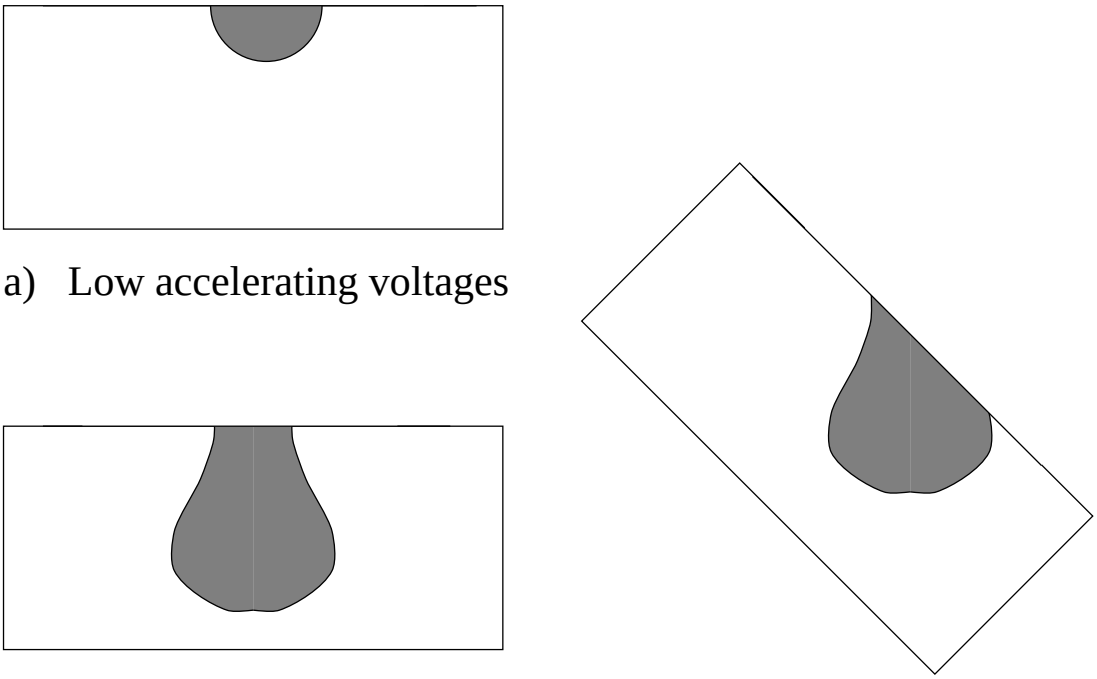

Fig. 4.9 The interaction volume as a function of accelerating voltage and sample position. **a)** Low accelerating voltage giving a small hemispherical interaction volume. **b)** High accelerating volume giving a large pear shaped interaction volume. **c)** High accelerating volume giving large pear shaped interaction volume; sample is tilted thereby giving a larger area of interaction volume intersecting the sample surface and hence increased yield of backscattered electrons.

illustrated in Fig 4.8 as primary electron detector (1).

The other standard position of a backscatter detector is directly above the sample (position 2 in Figure 4.8). This necessitates that the detector has a hole at its centre so that the electron beam is not blocked.

4.5.2 Channelling Contrast

Backscattered electrons are generated when electrons incident on the sample come into close proximity to the nucleus of an atom therein. Since these electrons cannot pass through the nucleus, they are simply reflected back with an energy of the order of 15 keV. The mechanics of this reflection are beyond the scope of this work, however they have been reviewed many times in the literature (*e.g.* Otley 1972). It is however safe to assume that the quantity of electrons reflecting will be dependent on the crystal structure and orientation of crystallites in

the sample.

Each crystallite in a polycrystalline sample will, in general, have a different orientation. These differences in orientation lead to differences in yield of backscattered electrons. Under normal operating circumstances this effect is small enough to be of little consequence. However, when the microscope is optimised to collect backscattered electrons, this effect may be observed as differences in contrast between grains. This is referred to as channelling contrast.

The effects of channelling contrast are observed less strongly as the sample is inclined, therefore the sample is kept flat and the backscatter detector is held in position 2 (figure 4.8). It is usual to keep the working distance (d_W) between objective aperture and the sample at a maximum to give the large depth of field (Otley 1972). However, this arrangement not only means that the electrons have to travel a greater distance between the sample and the detector, but also more electrons scatter away from the detector (*c.f.* Fig. 4.10).

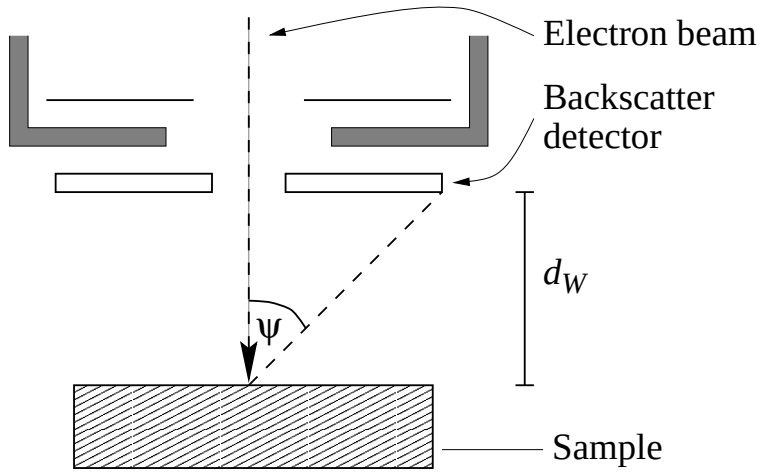

Fig. 4.10 Schematic illustration of electrons impinging on sample and being backscattered

By inspection of Fig. 4.10, for a fixed diameter of backscatter detector, as the working distance d_W increases the maximum angle at which an electron may be backscattered and still be detected ψ is reduced. Since electrons can be scattered at any angle, as d_W is reduced the number of electrons reaching the detector will increase.

Therefore, for maximum channelling contrast, the sample is placed normal to the electron beam and as close to the detector as possible

4.5.3 Sample preparation for channelling contrast images

Sample preparation was keyed to increase the channelling contrast and avoid any other forms of contrast. Samples were mounted and polished before masking off part of the surface using a non-conductive tape to leave a naked area of approximately 10 mm^2. They were

then immersed in an electropolishing solution of 1 part perchloric acid to 8 parts ethanol to 2 parts glycerol and electropolished at approximately 17 V. A brown gelatinous film of oxidised material was allowed to form on the surface of the sample during electropolishing. It was observed that without this film the sample failed to polish. The experimental arrangement is illustrated in Fig. 4.11.

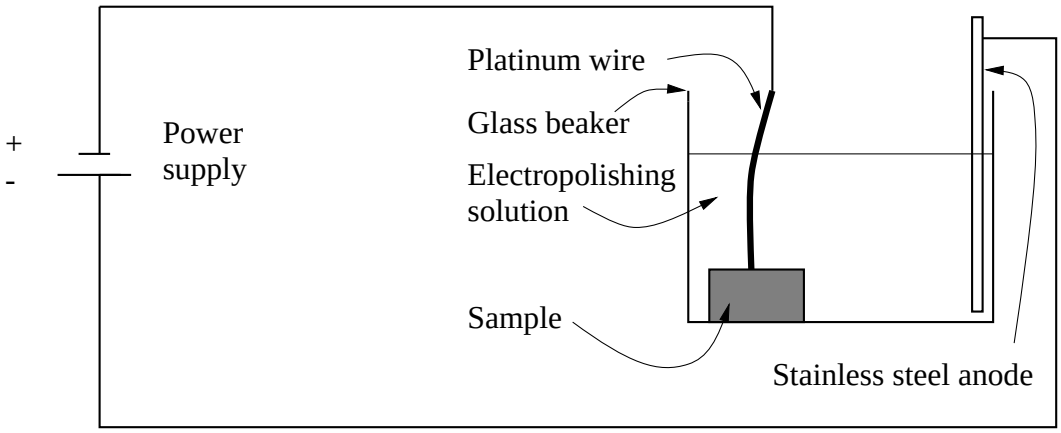

Fig. 4.11 Electropolishing technique for production of samples for channelling contrast imaging.

This electropolishing treatment was necessary to remove any deformation that may have been introduced into the surface of the sample during the polishing and grinding process to minimise any distortion of the lattice which would in turn blur the channelling contrast. The polishing also promotes surface flatness and hence avoids any topological contrast.

4.5.4 Other factors effecting channelling contrast

To measure fraction recrystallized and other microstructural properties, it is convenient to have a two dimensional image of a section through the material. However, images produced using backscattered electrons derive from a finite volume of material associated with the interaction volume (§4.5.1). If this interaction volume crosses a grain boundary within the sample, the channelling contrast from the two adjacent regions will be combined. One way to avoid this is to lower the accelerating voltage but this leads to a decrease in the yield of backscattered electrons. To avoid this further problem the size of the probe can be increased, thereby increasing the current of the electron beam, however this too leads to a drop in image resolution.

A CamScan S2 microscope was calibrated so as to produce the clearest image by finding the optimum balance between the above three factors, the final setup was an accelerating

voltage of 20 kV with a working distance of 9 mm. The objective aperture size and spot size were unspecified but both were approaching the maximum achievable on the equipment used (*i.e.* large spot and wide aperture).

An example image using channelling contrast of a type 904 stainless steel (details in Table 6.4) annealed for 2 minutes at a nominal furnace temperature of 950 °C is included in Fig. 4.11. The grain boundaries and other microstructural features are not as clearly delimited as they would be in a TEM image. However, sample preparation time was reduced by a fact or four, time spent on microscope was approximately halved and much larger areas may be inspected with photographic film costs cut by a factor of ten.

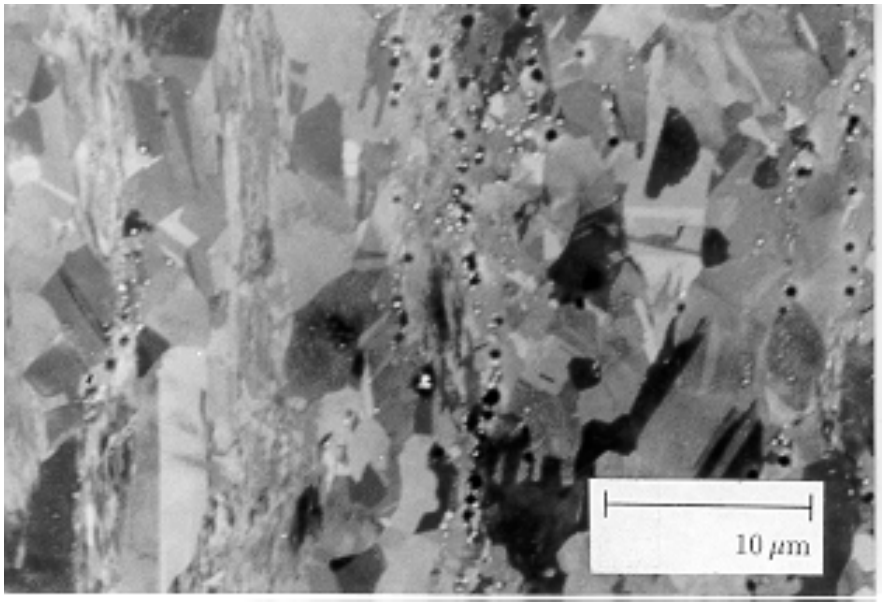

Fig. 4.12 A channelling contrast image of a type 904 stainless steel annealed for 2 minutes at a nominal furnace temperature of 950 °C

4.6 Image analysis

A standard image analysis machine cannot distinguish recrystallized grains from those which are unrecrystallized. This is due to a lack of contrast. The only way to derive useful information from these images is to first interpret them manually. This was done by manually counting numbers of grains per unit area of sample and by placing a sheet of acetate over the photograph and transferring the structure of the sample onto the acetate using marker pens. This reproduction of the sample was then analysed using a SeeScan image analyser and all further results were derived from that analysis.

CHAPTER 5

RESULTS AND NEURAL NETWORK MODELLING

The aim of the analysis presented here is to verify the applicability of the neural network approach for modelling recrystallization in stainless steels, based on new data from carefully controlled experiments. The great advantage that this approach has for industrial applications is that the final customers' requirements may be controlled directly by considering the industrial variables such as rolling reduction, nominal furnace temperature *etc.* The neural network approach will be extended thus in chapter 7.

5.1 The neural network model.

Neural network modelling was performed according to a method devised by MacKay (1992). This model is a neural network of the structure shown in Fig 3.4 made non-linear by utilising the hyperbolic tangent function as described in equations 3.8 and 3.9, the model fitting and comparison methods were based on the Bayesian techniques outlined in §3.4. The model has been developed to have variable error bars, these are a combination of two main considerations:

1) If there is a large amount of scatter in the dataset (*i.e.* noisy data) there is a corresponding increase in the size of the error-bar.
2) Regions of input space which have no corresponding experimental data have large error bars on the predicted value.

These factors are illustrated schematically in Fig. 5.1 although the mathematics of these functions are highly complicated and are well beyond the scope of this work. A full derivation is available in MacKay's original work (MacKay 1992).

5.1.1 Training the model

To allow direct comparison between the effects of different variables such as t and T_f, they must have the same range of values. Thus all variables were normalised into the range ± 0.5 as follows:

$$x_N = \frac{x - x_{min}}{x_{max} - x_{min}} - 0.5 \tag{5.1}$$

where, x is a variable whose minimum and maximum values are x_{min} and x_{max} are the minimum and maximum values respectively of the variable in the original dataset and x_N is the normalised value of x. These normalised data then go forward to train the Bayesian framework

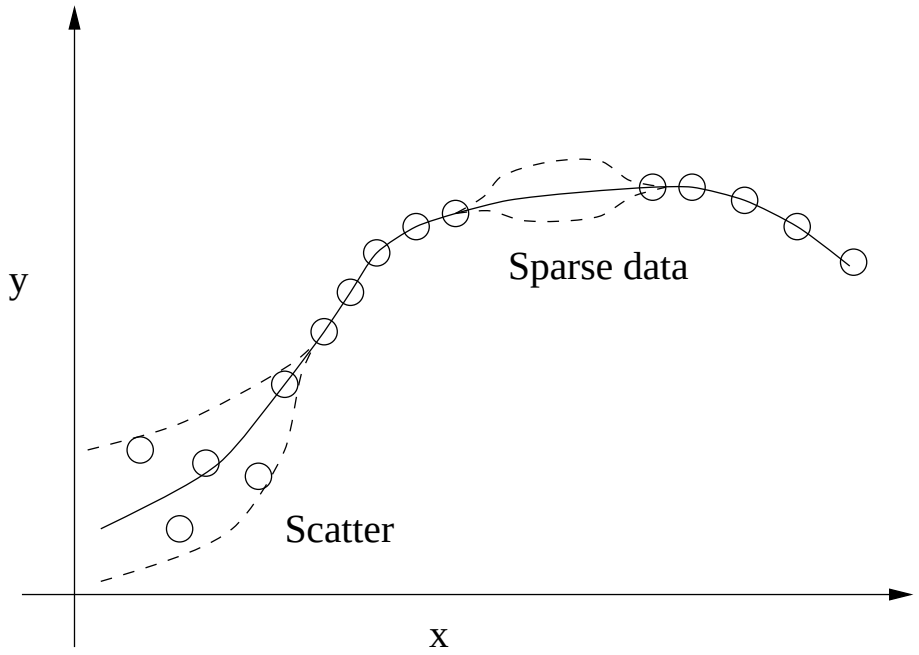

Fig. 5.1 Illustration of the uncertainty of fitting a function in a region of space where the data is either sparse or noisy (adapted from MacKay 1992). The dashed lines represent calculated error bounds and circles represent training data.

of the model as described in chapter 3. They will be used to determine the weights and biases given in equations 3.8 and 3.9 by minimisation of the following function.

$$M(\mathbf{w}) = \beta E_{SQ} + \sum_{c} \alpha_c E_{w(c)} \tag{5.2}$$

For a model with parameters $\mathbf{w}$ (including both weights w and biases θ) and a set of inputs x^m it is possible to estimate the output $y(x^m;\mathbf{w})$, which corresponds to a measured value of output t^m. This is used to define the squared error E_{SQ} thus:

$$E_{SQ}(\mathbf{w}) = \frac{1}{2}\sum_{m}[y(x_m;\mathbf{w}) - t^m]^2 \tag{5.3}$$

The parameter β is defined as $1/\sigma_\nu^2$ wherein σ_ν is the perceived noise in the data as given by equation 3.5.

To avoid the problem of over-fitting (Fig 3.1) *regularisers* E_w are also included in the calculation of $M(\mathbf{w})$. These favour smooth solutions to $y(x^m;\mathbf{w})$ such that fitting to noise is avoided. For the model in question (MacKay 1992) the "*automatic relevance determination model*" for regularisation has been used; Regression analysis is often used because the relationship between input and output is not known. It is safer, therefore, to include all variables that might affect the output and allow the relevance of each input to be determined by the

analysis. This model "eliminates" irrelevant inputs by using a regularisation parameter σ_w where $\sigma_w^2 = 1/\alpha$ and α is given in equation 5.2. A large value of σ_w implies that the input is capable of explaining a significant amount of variation in y.

During training, the weights ($\mathbf{w}$) are at first set to random values, the training process is concerned with the optimisation of these values. In the Bayesian framework outlined in chapter 3, the model is not defined by a unique set of weights but a probability distribution of weights. This accounts for uncertainty of fitting needed to describe noisy data.

5.1.2 Selecting the optimum models

As was illustrated in §3.3 the degree of fit may be assessed by considering the test error E_D (see equation 3.2). Apart from noise, experimental data may contain errors due to mistakes in the database (*e.g.* numbers entered into database in the wrong order), such data may show large deviation from the fitted model. The test error tends to exaggerate the effect of these outliers and hence may give a misleading impression as to the fit of a model. The log predictive error (LPE), as defined below minimises the effect of these outliers.

$$LPE = \sum_m \frac{1}{2}(t_m - y_m)^2/\sigma_y^{m^2} + \log\left(\sqrt{2\pi}\sigma_y^{m^2}\right) \tag{5.4}$$

The random starting values of the weights ($\mathbf{w}$) can, to some extent, influence the final solution. This is because on training, the program uses gradient based methods of fitting, this may find minima in the test energy which may not be global. Consequently, a variety of starting values for $\mathbf{w}$ are used in addition to different numbers of hidden units, this generates a large number of models. In regions of uncertainty, individual models will differ in their predictions. In such circumstances an averaged set of solutions from several models may predict more accurately than a single model. This averaging procedure is known as forming a committee of models.

The first step, in forming a committee is to rank the models in increasing order of log predictive error (LPE). A committee is formed by combining the best N models giving a mean prediction $\bar{y}$:

$$\bar{y} = \frac{1}{N}\sum_{i=1}^{N} y_i \tag{5.5}$$

wherein y_i is the estimate from the i^{th} ranked model. The error associated with this committee prediction ($\bar{\sigma}$) is given as:

$$\bar{\sigma}^2 = \frac{1}{N}\left(\sum_{i=1}^{N}\sigma_i^2 + \sum_{i=1}^{N}(y_i - \bar{y})^2\right) \tag{5.6}$$

wherein σ_i is the error associated with the i^{th} model. Values of $\bar{\sigma}$ are compared for different combinations of models such that the optimum size of a committee is determined by a minimum in $\bar{\sigma}$.

5.2 Initial neural network database

The creation of the experimental database has been discussed in §4.1.1 and §4.1.2. The database discussed in §4.1.1 used the nominal temperature of the furnace instead of a direct measurement of sample temperature. This was proved to be unreliable; Samples annealed at 800 °C for 10 minutes had hardness varying between 240 HV and 400 HV irrespective of the number of times the experiment was repeated. The furnace used consists of a refractory box with four wall mounted heating elements. The temperature is controlled by a porcelain shielded thermocouple mounted towards the top of the furnace.

It is important to note that the control thermocouple is shielded from the radiative heat of the elements whereas samples are not. If the furnace dips below its ideal temperature (as will happen when the furnace door is opened) the elements will provide extra heat to bring the furnace back up to temperature. In this case radiative heat from the elements impinges directly upon the the sample, however, the control thermocouple is protected from this radiation. This means that the sample will heat up more quickly than the control thermocouple and will often reach a temperature in excess of the temperature indicated by the control thermocouple. Furthermore, by inserting another thermocouple into the furnace, variations in temperature of up to 40 °C were found depending on the location of this second thermocouple.

Therefore, a sample placed in a furnace may experience a heating regime vastly different from the nominal settings on the furnace. Temperature variations due to furnace operation and inaccuracy in temperature measurements will be so great that using the indicated temperature of the furnace will produce unacceptably inaccurate results. Other methods of sample production were therefore investigated.

5.3 Revised neural network database

To overcome these difficulties a new database was created which included temperatures directly measured on the sample, as described in §4.1.2. A neural network model was then created to predict hardness H as a function of true furnace temperature T_f and time t.

The range of values for the database is given in Table 5.1 along with the mean and standard deviation in those values.

Fig. 5.2 shows the perceived noise σ_ν in the measured hardness as a function of the number of hidden units in the model. The value of σ_ν at first drops with increasing number of hidden

Variable	Minimum	Maximum	Mean	Standard Deviation
T_f / K	805	1182	983	82
t / s	600	1260000	61140	195600
H / HV5	176	477	282	74

Table 5.1: Table showing minimum, maximum, mean and standard deviation of values input into the first neural network model

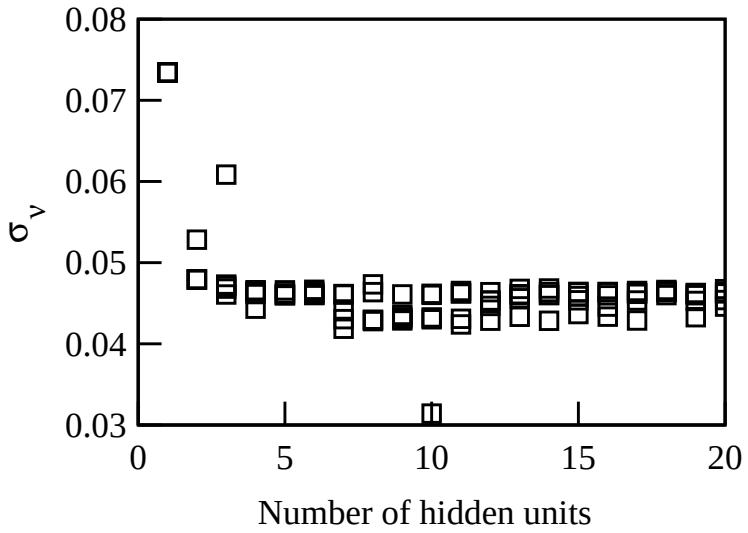

Fig. 5.2 Variation in σ_ν as a function of the number of hidden units. Several values are presented for each value of hidden units because each network was trained with a different set of initial values for w.

units but quickly levels out at about 7 hidden units.

There is a model at 10 hidden units which has an exceptionally low value of σ_ν. Similar behaviour is observed in the value of test error (Fig. 5.3)

Comparisons of different committees of models were performed, the optimum committee was a single model of 10 hidden units. This "committee" was then retrained using the entire experimental dataset. Predictions from this model were then compared with the original dataset as shown in Fig. 5.4. It can be seen that there is excellent agreement between values for most of the data. However there is a large discrepancy at a predicted value of approximately 270 HV.

5.3.1 Reasons for poor fit

A similar region of poor fit was observed in all of the trained models and committees. In fact the problem of poor fit does not lie with the neural network approach, but rather with the

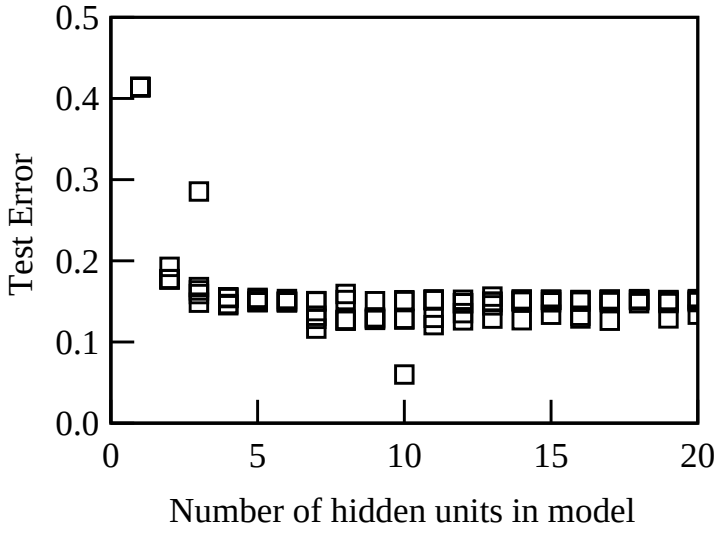

Fig. 5.3 Variation in test error E_D as a function of the number of hidden units. Several values are presented for each set of hidden units because the training for each network started with a variety of random seeds.

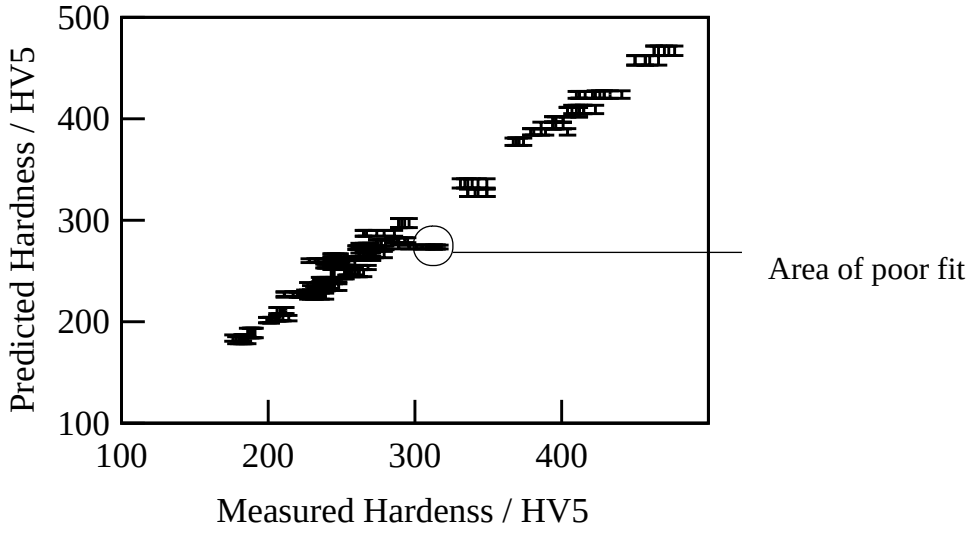

Fig. 5.4 Measured hardness against predicted hardness for the optimum committee of one model of ten hidden units. Error bars include fitting error and the perceived noise in the data.

method of implementation. As with any data fitting method, if the program does not have all the relevant input information, it cannot give meaningful output. On further examination of the dataset, it was seen that for any given furnace temperature, different samples are likely to experience different heating rates. Experimental heating profiles had been taken for each of the samples. All experimental heating curves followed an equation of the general form:

$$T = T_f - (T_f - T_R) \exp(-at) \tag{5.7}$$

wherein T_R is the ambient temperature outside the furnace and a is a material and interface specific constant. This behaviour is indicative of interface controlled (Newtonian) heating. An example heating curve is given in Fig. 5.5.

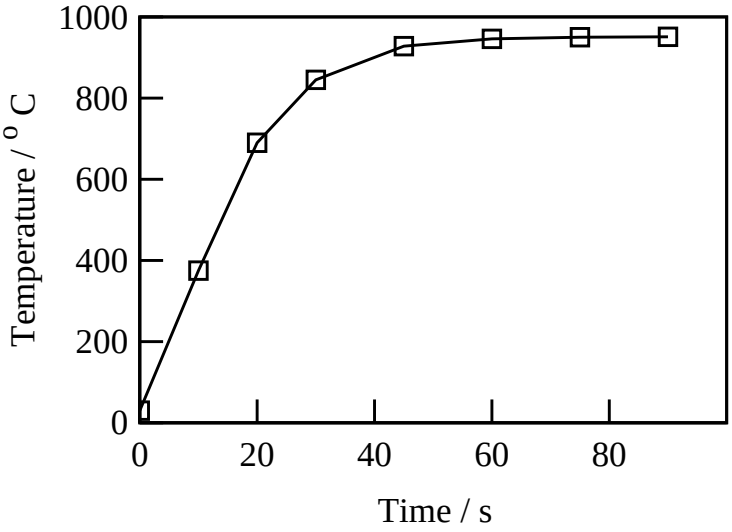

Fig. 5.5 Example of an experimental heating curve obtained from a sample annealed in accordance with the standard annealing regime outlined in chapter 4.

Room temperature varied very little between different heat treatments, therefore, by simply adding an extra input of the temperature of the sample at $t = 30$ s (T_{30}), it becomes possible to completely describe the heating profile of the sample. This is illustrated in Fig. 5.6.

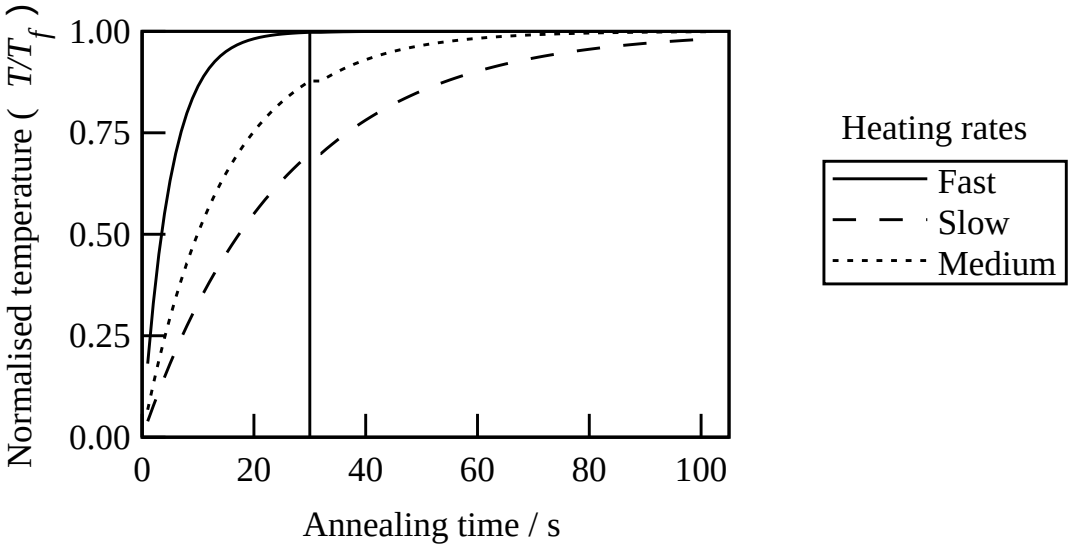

Fig. 5.6 Three different samples all with the same final temperature (normalised as T/T_f) and all of the form $\left(\frac{T}{T_f} = 1 - \left(\frac{T_R - T_f}{T_f}\right) e^{(-at)}\right)$, but all with different heating rates and hence different values of T_{30}

5.4 Second revision of neural network database

A new model was trained as described previously but including the values for T_{30}. This model was then tested to see how predictions of the short term annealing cycles was affected. The fit was greatly improved as shown in Fig. 5.7.

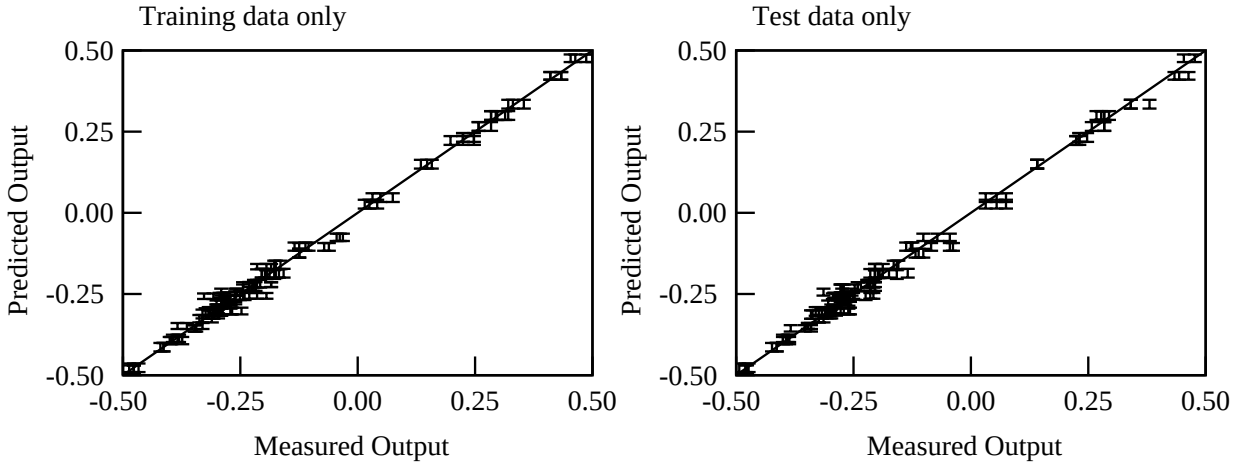

Fig. 5.7 Example outputs from the best neural network model with heating rates included in input data, neural network seed 3 and 12 hidden units. Output is the hardness (H) normalised into the range ± 0.5

Notice that almost all points are within $\pm\sigma$ of the $x = y$ line, points deviating far from this line are most unlikely in the absence of mitigating factors such as input errors, and such outliers indicate a bad model. The model was improved further by adding points for $t = 0$ s and $T < 300$ °C where samples retain full hardness.

The value of the perceived noise in the hardness (σ_ν) as calculated for each model is shown in Fig. 5.8.

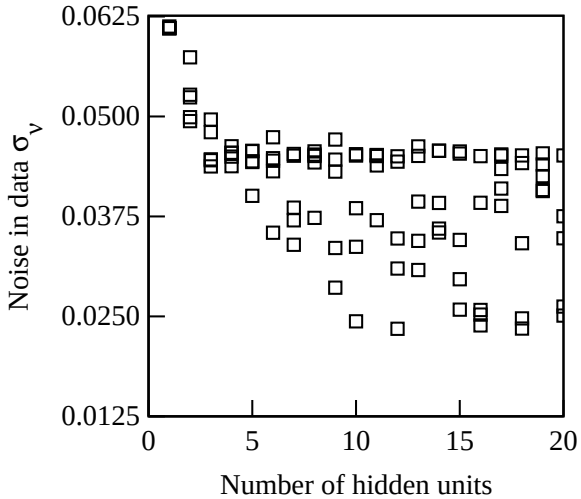

Fig. 5.8 Variation of perceived noise σ_ν in the hardness with number of hidden units.

One hundred models configured differently in terms of number of hidden units and random seed (the initial values of **w** before optimisation) were trained. The relative importances of the different input parameters can be investigated by comparing σ_w for each input. σ_w values are analogous to partial correlation coefficients and express the ability of a variable to explain the corresponding variations in the output. Values of σ_w are included in Fig. 5.9; they may be compared directly since the all data have been normalised.

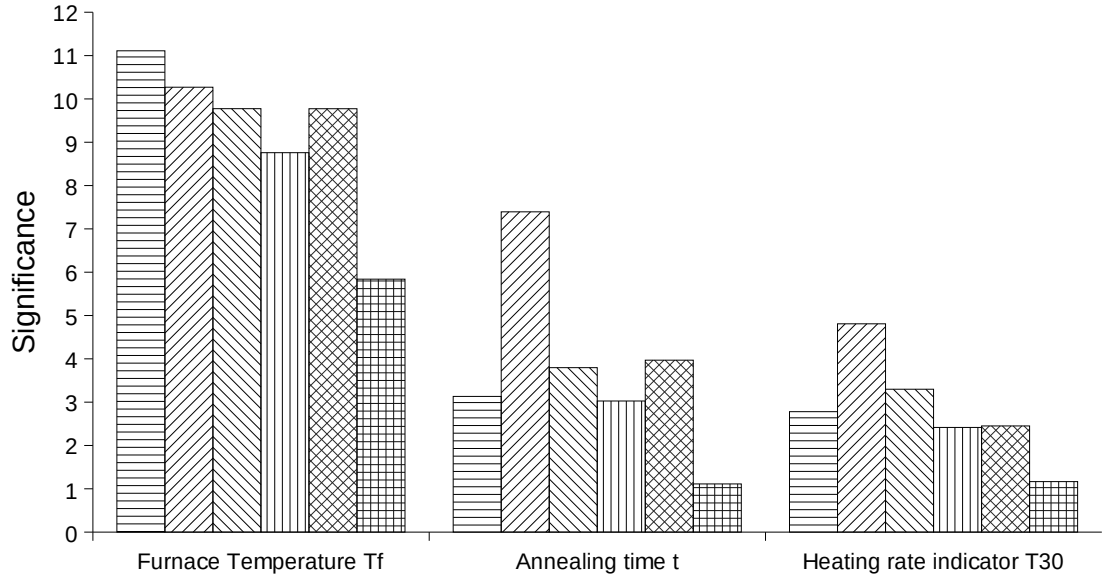

Fig. 5.9 Bar chart showing the perceived significance (σ_w) for each input variable. The six bars plotted per input correspond to each of the six members of the optimum committee.

From Fig. 5.9 it can be seen that different models assign different values of σ_w for the same inputs. It is possible therefore that a committee of models may make a better prediction than any single model. The optimum committee can be evaluated by comparing the test error with the number of models in the committee (Fig. 5.10).

A committee of the six best models was found to be the optimum combination, these were retrained on the entire dataset without changing the complexity of any one model. The committee was then tested on the entire dataset, by comparing predicted hardness with the measured values from the dataset. The results are shown in Fig. 5.11.

The only change in configuration or training routine of the model was the inclusion of the heating rates. Therefore the improvement in the fit of the model may entirely be attributed to this fact. Moreover it emphasises the importance of heating rate as well as the more normally considered annealing parameters of furnace temperature and time.

This committee was then used to make predictions across a range of temperatures and

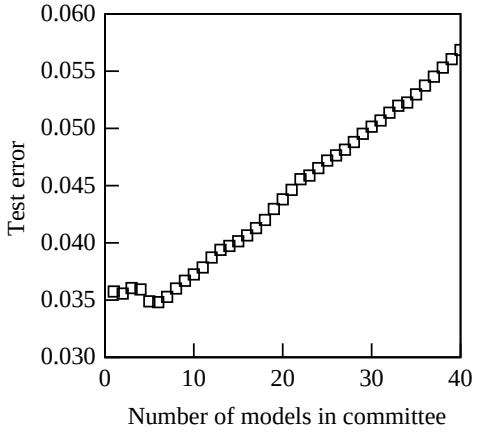

Fig. 5.10 Variation of test error with number of models in committee

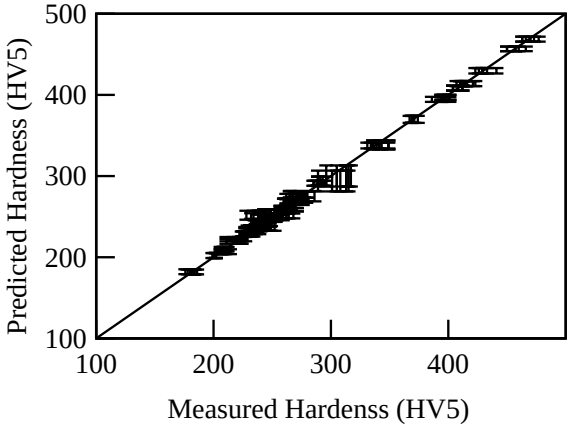

Fig. 5.11 Comparison between the predicted and measured values for all data, the predictions being calculated using the committee of 6 models between 10 and 20 hidden units

times to examine and understand the predicted trends. A selection of predictions is illustrated in Fig. 5.12.

Although the uncertainty in these predictions is large, generally accepted metallurgical trends may be observed. For the evolution of hardness with time at constant temperature (Fig. 5.12 **a**), the expected drop off in hardness with time is observed. It should be noted that as time increases so too does the uncertainty in the prediction, this reflects the sparseness of the dataset for long annealing cycles. By contrast in Fig. 5.12 **b** there are certain points along the temperature axis where the error bounds are small, these small error bounds indicate that there are well fitting data corresponding to those conditions. Between these points the error bars become larger, reflecting sparse data in these regions. The expected shape of this curve would be an initial drop off in hardness followed by a levelling out at higher temperatures when full recrystallization occurs. Within the bounds of the error, this behaviour is observed.

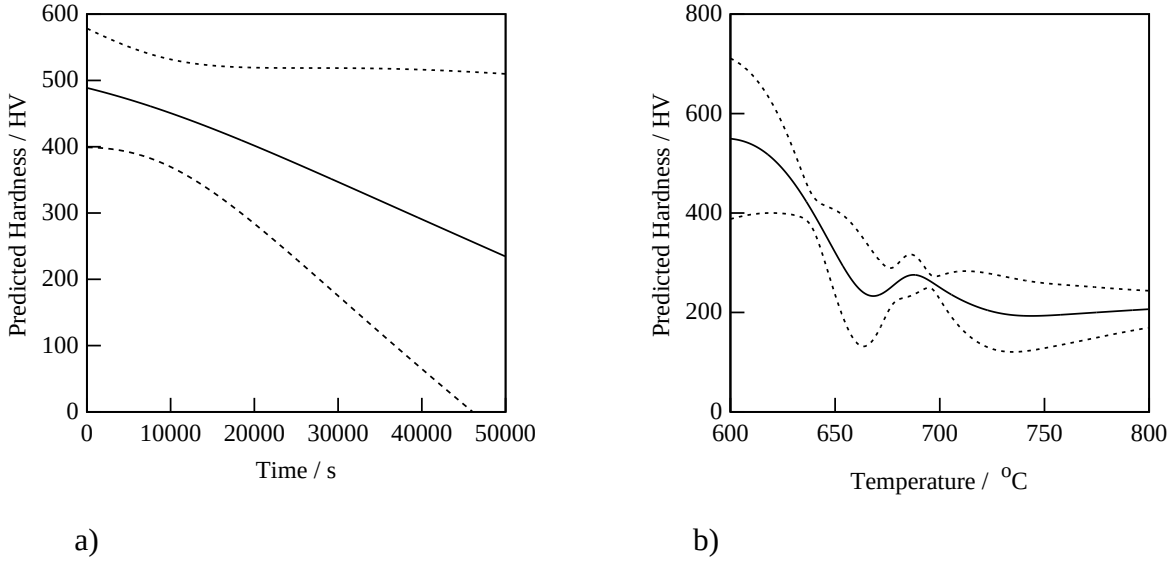

Fig. 5.12 Example predictions from committee neural network model with heating rates included in input data, **a)** $T_f = 625\,^{\circ}\mathrm{C}$. **b)** $t = 60$ s. Both predictions were for a single heating rate calculation, *i.e.* a single value of a in the Newtonian heating rate calculation. Solid lines represent predictions and dotted lines represent error bounds.

5.5 Neural network applicability

Neural network techniques are suitable for modelling recrystallization. The fit of the model is greatly improved (Fig. 8) on inclusion of heating rate data, therefore by examination of neural network models not only has an accurate description of the annealing process been produced, but moreover the model has identified that furnace temperature and annealing time alone provide an insufficient description of the annealing process. This indicates that the heating of the sample to the annealing temperature is a significant part of the heat treatment.

CHAPTER 6

RESULTS AND KINETIC MODELLING

There have been numerous kinetic models produced for recrystallization in a number of different materials. However, these models either show poor fit to the data or use overall transformation kinetics theory in a somewhat empirical manner which limits the interpretation of the results (chapter 2). The purpose of this investigation was to produce a model using overall transformation kinetics theory in a manner which correctly reflects the physical metallurgy of the process.

6.1 Growth kinetics

A well accepted equation describing the velocity of a grain boundary (Christian, 1975) is:

$$\Upsilon = \delta_\varsigma \nu \exp\left(-\frac{Q}{RT}\right)\left[1 - \exp\left(-\frac{\Delta G}{RT}\right)\right] \tag{2.15}$$

which may be simplified to:

$$\Upsilon = M\Delta G \tag{2.17}$$

As discussed in §2.3, many of the parameters in this equation are difficult to measure or derive from first principles. The jump distance (δ_ς) of an atom across the boundary is taken to be approximately the size of an iron atom (3 Å) and the attempt frequency (ν) is assumed to be given by the Eyring equation $\nu = kT/h$. The activation energy (Q) for the atomic jumps across the boundary, will be similar to that for self diffusion in the bulk when the boundary concerned is coherent, but may be smaller that this when there is a lot of free volume as there is at an incoherent interface (Christian 1975, Vandermeer 2000).

6.1.1 Estimation of ΔG

There are a number of ways in which the driving force for recrystallization, ΔG, can be deduced, as described in §2.2. Direct measurements of either ΔG or ρ_D can be used without interpretation in a recrystallization model. This advantage is offset by the fact that measurements made using different methods (*e.g.* TEM and calorimetry) can give values of stored energy which sometimes differ by orders of magnitude (Humphreys and Hatherly 1996). It is therefore doubtful that these methods give answers which are sufficiently accurate enough to use in models of recrystallization. This is similarly true of X-ray line broadening methods and TEM observations.

Indirect methods derive ΔG from measurements of parameters such as sub-grain size although the relationships involved can often be imprecise. Sub-grain size can be converted

into dislocation density and hence ΔG. The relationship between ΔG and flow stress (equation 2.10) is used widely and has been verified experimentally (McElroy and Szkopiak 1972). The flow stress may be easily inferred with good reliability from hardness measurements and is often used in industrial applications (Jackson, 1997; Backhouse and Wilford, 1999). This method is simple, the results are reproducible and above all, rapidly produced. Moreover, it has been demonstrated in the literature (McElroy and Szkopiak 1972) that measurements of flow stress provide as accurate a description of the trends in the variation of ΔG as analytical methods.

6.1.2 Final choice of model for ΔG

Having assessed the literature, it was decided that flow stress provided the most reliable repeatable measurement and therefore was the best indicator of the stored energy prior to recrystallization. Moreover, this method provides results rapidly and may easily be related to data from the industrial process of stainless steel production.

6.2 Nucleation Kinetics

The three most widely accepted theories to explain nucleation in recrystallization have been reviewed in §2.4. Li's (1962) sub-grain coalescence model (*c.f.* 2.4.2) requires sub-grain boundaries to coalesce and hence generate a sufficiently misoriented crystal which constitutes a nucleus. This method is not applicable to austenitic stainless steels which have a low value of γ_{SFE} in comparison to other materials (*e.g.* aluminium), this prevents sub-grain formation (*c.f.* §1.2.1 and Fig.2.2). No distinct sub-grains were observed in any of the materials studied in the present work using transmission electron microscopy (*c.f.* Fig. 2.2).

The bulk of the experimental evidence available implies that the mechanism of nucleation of recrystallization is strain-induced grain boundary migration (SIGBM) (*c.f.* §2.4.1) (Humphreys and Hatherly, 1986). However, this should not be taken as proof of this method being applicable in all situations. Often the nucleation process is impossible to experimentally observe, this may suggest either a different nucleation process is occurring in these cases, or that the bulges are too small to observe.

The third possibility, a preformed nucleus (§2.4.3), can be discounted because it predicts that the recrystallization nuclei occur predominantly in the least deformed areas, in contradiction to experimental observations of nucleation at transition bands. It also predicts a zero incubation time, which is not always observed (*e.g.* Anderson and Mehl 1945).

The most applicable model for the present study is the strain induced grain boundary migration model (SIGBM). This fits with experimental observations of nucleation occurring on prior grain boundaries (*c.f.* Fig. 4.6) and is more likely that sub-grain rotation because no

distinct subgrain structure was observed (*c.f.* Fig. 2.2).

The nucleation rate is often measured by counting the number of nuclei observed per unit area on a cross-section of the partially recrystallized microstructure. There are a number of problems with this approach:

i) Since the sample is recrystallizing and the grains will be impinging, the nucleation rate cannot be taken as a simple function of time and number of nuclei per unit area. The nucleation rate will be also be a function of growth rate and fraction recrystallized. Furthermore, growth rate cannot be inferred directly from the grain size as this too will be a function of the impingement rate and hence the fraction recrystallized.

ii) If nucleation is not uniformly distributed throughout the material, the section for inspection must be chosen carefully so as to display a representative area for the whole sample.

iii) Ideally samples should heat up to their final annealing temperature from room temperature instantaneously. However real samples cannot behave this way and require a finite amount of time to come up to temperature. An isothermal nucleation rate is therefore only an approximation to what actually happens.

6.2.1 Measurement of the number of grains per unit area (G_a)

Consider the case of a number of randomly distributed nuclei in a homogeneous matrix observed on a plane P_O (Fig. 6.1a). A comparison of the observations at times t_1 and t_2, shows that there are stereological problems in estimating the nucleation rate from number density of particles observed on a plane section.

However, for certain nucleation geometries and kinetics this problem can be neglected. In the case of a type 302 stainless steel, experimental observation suggests that nucleation occurs primarily on planar boundaries parallel to the sheet surface (these may be considered as being similar to elongated grain boundaries, see Fig. 4.6). Since all samples were cut and mounted normal to the rolling direction these planar features intersect the surface of the sample as shown in Fig. 6.1b).

In general, if nucleation occurs continuously on plane P_O the nucleation rate will be a complex function of the number of grains per unit area (G_a), the growth rate and time. The measurement of G_a must be taken over an area sufficient to be representative of the three dimensional microstructure of the material. Measurements of G_a were taken across the full breadth of the sample and at different depths into the sample by grinding a single sample to

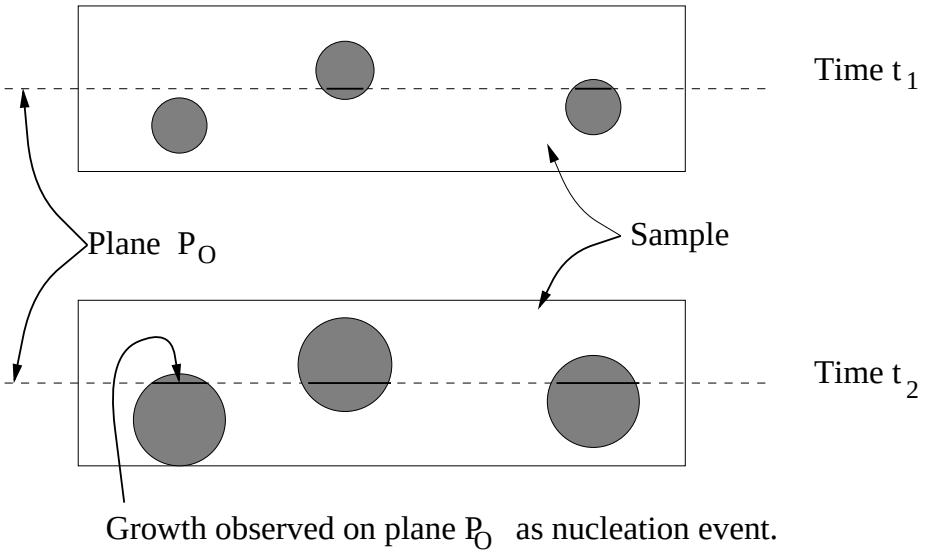

Fig. 6.1a) Illustration of the potential pitfalls of counting number of grains per unit area.

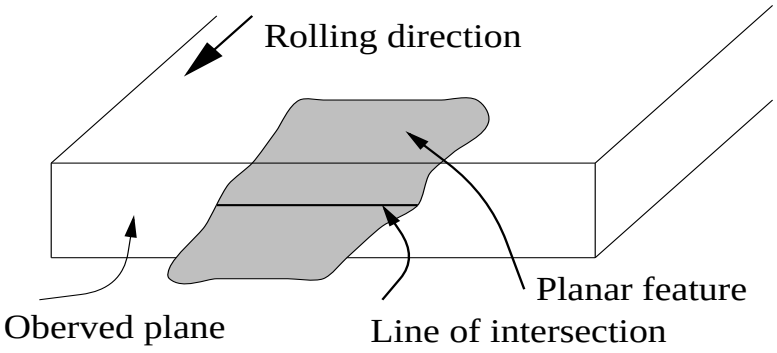

Fig. 6.1b) Planar feature intersecting the observed plane.

different extents to ensure accurate results.

Drawing conclusions from the simple observation of G_a is misleading and nucleation rates cannot be directly inferred. However, limited simple analysis of G_a for this geometry of nucleation is possible. If the value of G_a, is observed not to vary with time, it can be concluded that there is no nucleation occurring. However, if there is any variation in the value of G_a with time, no conclusions may be drawn without further analysis.

6.2.2 Observations of G_a

Samples of a type 302 stainless steel were annealed and then observed using channelling

contrast imaging as described in chapter 4. Micrographs of size 12.7×17.8 cm (at circa 5000× magnification) were used to count the number of grains per unit area. These data along with grain size measurements (mean linear intercept), fraction recrystallized (ζ) and Newtonian heating rate indicator (a) are given in Table 6.1. Error bounds given are the standard deviation of all measurements taken.

ζ	Grain size/μm	Grains per μm^2	a / s^{-1}	Temp. / °C	Time / s
0.70 ± 0.12	3.16 ± 0.28	0.12 ± 0.01	0.035	709	1200
0.54 ± 0.13	2.86 ± 0.34	0.13 ± 0.01	0.035	709	600
0.62 ± 0.09	2.95 ± 0.65	0.13 ± 0.04	0.035	707	660
0.85 ± 0.07	2.94 ± 0.22	0.16 ± 0.02	0.035	723	615
0.85 ± 0.07	2.82 ± 0.15	0.17 ± 0.01	0.035	728	660
0.12 ± 0.06	2.13 ± 0.67	0.08 ± 0.03	0.07	880	30
0.84 ± 0.07	3.12 ± 0.25	0.14 ± 0.02	0.07	830	45

Table 6.1: Dataset showing similarity of number of grains per unit area

From the data for annealing experiments at 709 °C and 707 °C, the number of nuclei per unit area (G_a) is, within the limits of experimental error, constant and thereby independent of fraction recrystallized. This suggests that site saturation has occurred.

6.2.3 Model for nucleation

As discussed earlier, it is reasonable to assume a strain induced grain boundary migration (SIGBM) model for nucleation. The nucleation rate per unit volume was calculated as:

$$\dot{N} = \nu_V \exp\left(-\frac{G^*}{kT}\right) \tag{6.1}$$

Where G^* is the activation energy for the grain boundary bulging ($2\gamma/L$, equation 2.23) and ν_V is the attempt frequency for grain boundary bulging per unit volume taken as a fitting constant.

6.3 Overall transformation kinetics model

The first model produced assumed random nucleation occurring at a rate $\dot{N}$ and an isotropic growth rate Υ, such that:

$$\zeta = 1 - \exp\left(-\pi \Upsilon^3 \dot{N} t^4/3\right) \tag{6.2}$$

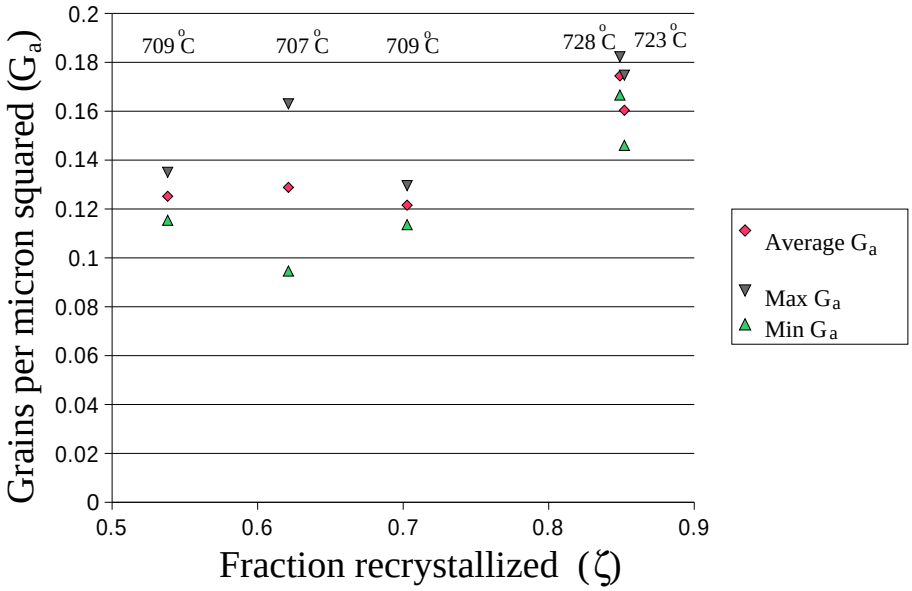

Fig. 6.1 Chart of fraction recrystallized against number of grains per square micron (G_a) for samples annealed at stated temperatures.

Utilising equations (2.10) to describe ΔG, (2.15) to describe Υ, (6.1) to describe $\dot{N}$ and choosing appropriate values for the fitting factors, an estimation of the fraction recrystallized was produced (Fig. 6.2).

This model has a number of shortcomings, the most obvious of which is that it can only be used for an isothermal anneal. Under normal circumstances this will never be the case. The equation was adapted for anisothermal annealing as follows.

6.4 Anisothermal overall transformation kinetics model

The anisothermal anneal is treated as a series of concurrent isothermal annealing steps using the Scheil rule (Fig. 6.3).

Considering an initial temperature T_1, an increment in time t_1 is allowed to elapse to allow ζ_1 to transform. The temperature is then appropriately incremented. The time taken to achieve a fraction recrystallized ζ_1 is calculated and then incremented again thus producing a net fraction recrystallized ζ_2 This process is repeated as needed until the sum of all the time increments equals the total time of the anneal.

An example output of fraction recrystallized against time is given in Fig. 6.4. The Avrami exponent n in this calculation will have a value of 4 because this is assumed in the calculation of ζ. This cannot be illustrated graphically because the gradient of $\ln(\ln(1/(1\text{-}\zeta)))$ against

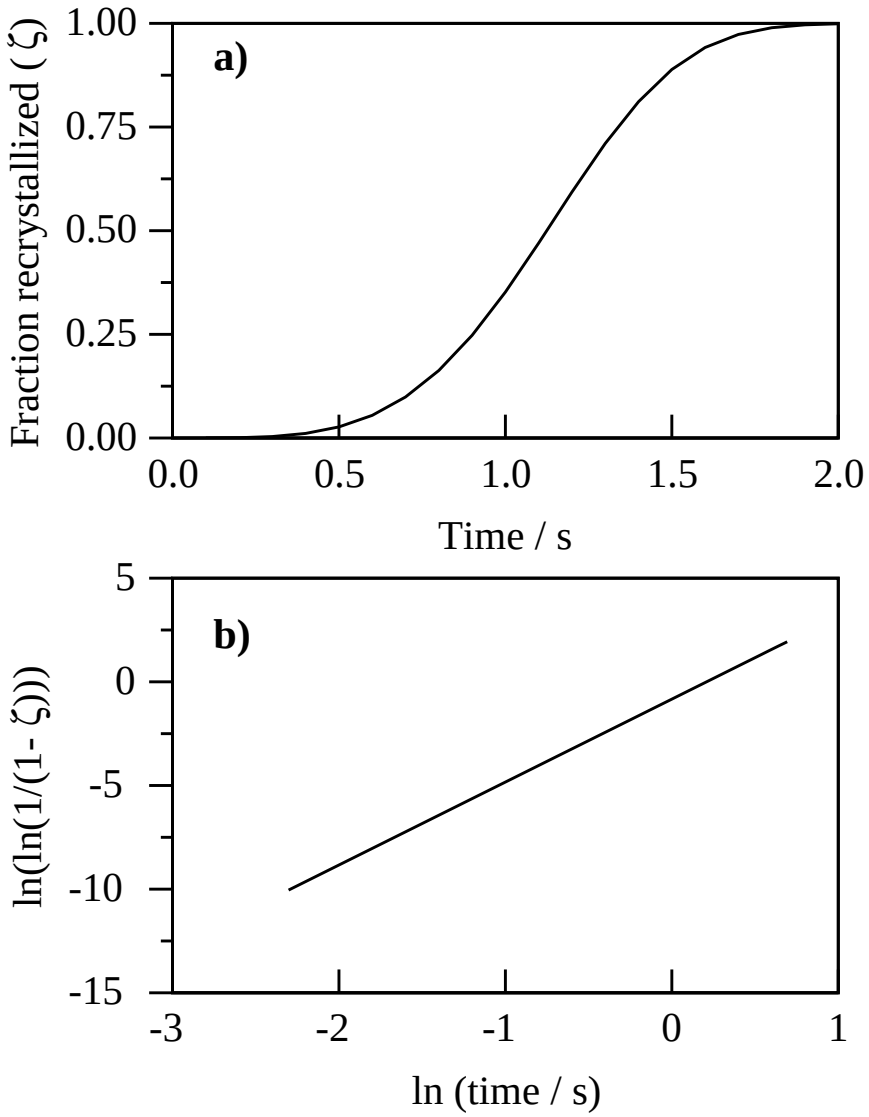

Fig. 6.2 a) Chart of fraction recrystallized vs time at 970 °C from simple overall transformation kinetics model showing classic sigmoidal shape. **b)** "Avrami plot" of $\ln(\ln(1/(1\text{-}\zeta)))$ vs ln(time) showing a gradient of 4, indicating that the Avrami exponent n is 4

$\ln(t)$ is affected by the variations in temperature.

The recrystallization curve in Fig. 6.4 is shifted to the right with respect to Fig. 6.2a) because the sample takes a finite time to come up to the annealing temperature. This illustrates how misleading the neglect of the sample heating time can be.

The Scheil rule can only be applied when the reaction is isokinetic *i.e.* when nucleation and growth vary in exactly the same way with temperature and also if either nucleation or growth is temperature independent.

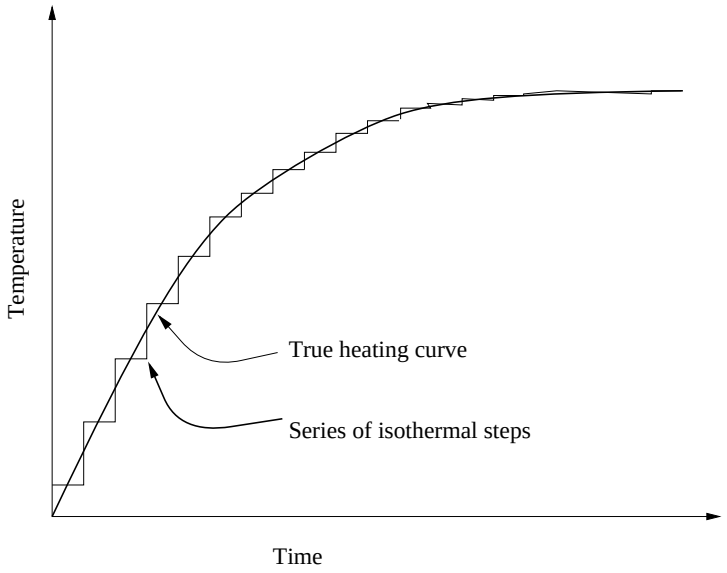

Fig. 6.3 Anisothermal heating regime split up into a series of isothermal step for use in the Scheil rule method of calculating anisothermal recrystallization parameters

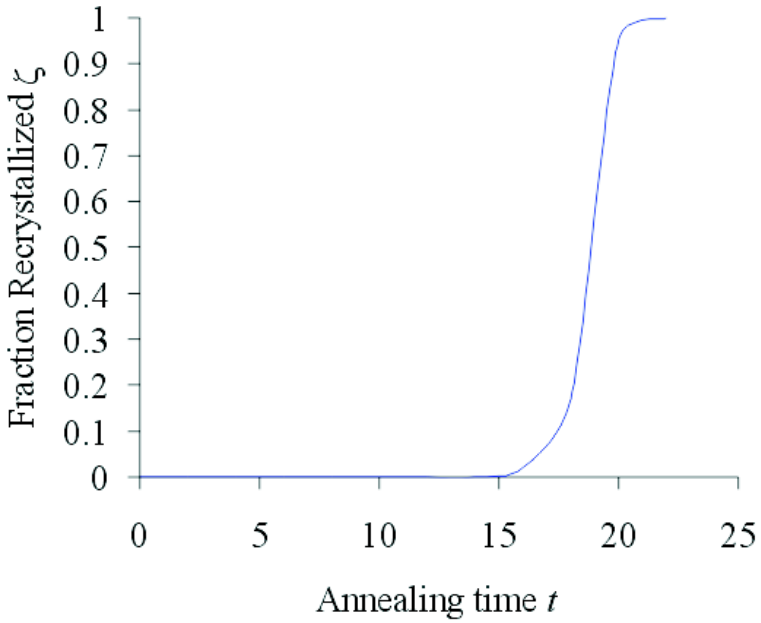

Fig. 6.4 Output from anisothermal recrystallization calculation (furnace temperature 970 °C). Because of finite heating rate the curve is shifted significantly to the right with respect to that in Fig. 6.3a).

6.4.1 Experimental evidence for applicability of Scheil rule

Experimental evidence of the validity of the Scheil approach, as least as far as type 302

stainless steel is concerned, comes from three sources.

Firstly, in figure 6.2 the observed number of grains per unit area does not vary with fraction recrystallized. This implies that site saturation has occurred and therefore the Scheil approach should be valid.

Secondly, experimental data show that the measured Avrami exponent n comes out at approximately 1 as shown in Fig. 6.5

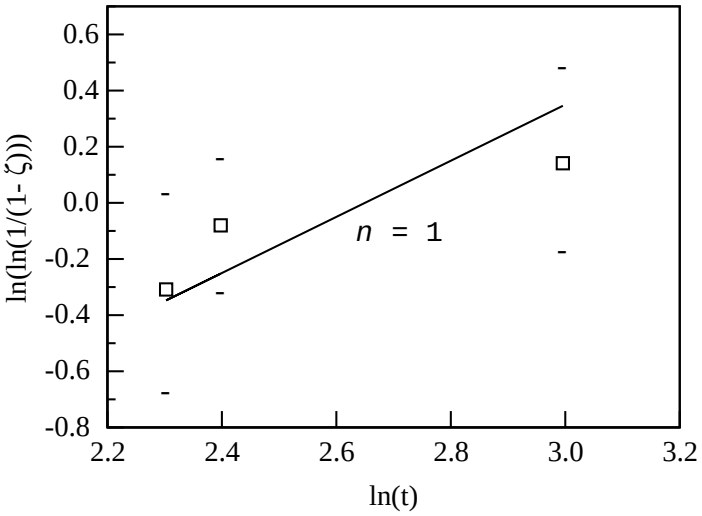

Fig. 6.5 "*Avrami Plot*" of $\ln(\ln(1/(1\text{-}\zeta)))$ against $\ln(t)$ for a type 302 stainless steel annealed at 708 °C (point at $\ln(t) = 2.30$ annealed at 710 °C) showing an Avrami exponent $n \approx 1$. Values of n less than 1 have no physical meaning.

Thirdly, an experiment may be performed to check if the isokinetic approximation is justified. A single sample was given two isothermal anneals both of which would be expected to give rise to a finite fraction recrystallized. If the resultant microstructure consisted of a bimodal distribution of grains, then the isokinetic approximation cannot be used because the growth rate and nucleation rates will be varying differently.

A sample of a type 302 stainless steel was annealed for 10 minutes at 699 °C and then a further 5 minutes at 723 °C . The resultant distribution of grains areas was measured and is shown in Fig. 6.6. This single mode grain size distribution suggests that the Scheil rule is applicable.

The weight of the evidence therefore points towards the validity of the Scheil approximation.

6.5 Simple Cahn kinetics model

If site saturation occurs the observed value of n will deviate from an initial high value

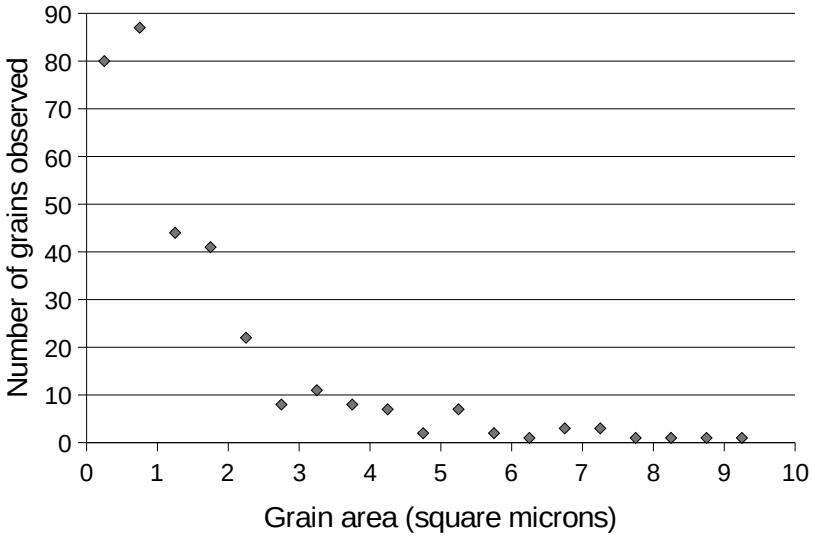

Fig. 6.6 Distribution of grain areas in two-step annealed sample of 302 stainless steel.

of 4. Although site saturation, at first sight, should only lead to a reduction in n from 4 to 3 since nucleation rate is eliminated from the analysis, the growth morphology can become one-dimensional which can further reduce n to a value of 1.

The expected value of $n = 4$ comes from the dependency of the volume recrystallized on number of nuclei and the size of each nucleus. Hence for a constant nucleation rate and spherical growth, number of nuclei is proportional to t^1 and the volume of each nucleus is proportional to t^3; overall this gives $n = 4$.

In the case of grain boundary nucleation as explained by Cahn (1956) and reviewed in detail in this work (§2.7) the grain boundaries may saturate early in the annealing cycle. This has been shown mathematically to lead to a value of $n = 1$, however it was not explained in chapter 2 what this means physically.

Knowing that site saturation has occurred, nucleation has finished and therefore the total number of nuclei is no longer dependent on time. This means the factor $n = 1$ is due to grain growth alone. The Avrami exponent n being equal to 1 indicates that growth is occurring in one spatial dimension only. This is because growth is not possible in the plane of the saturated grain boundary since it has already been consumed by recrystallized grains, therefore only growth perpendicular to the plane is possible, giving $n = 1$. This is illustrated in Fig. 6.7.

6.5.1 Mathematical description of site saturation model

The mathematical description of site saturation due to Cahn (1956) was described in §2.7. It can be summarised by the following equations using the same nomenclature as in chapter 2:

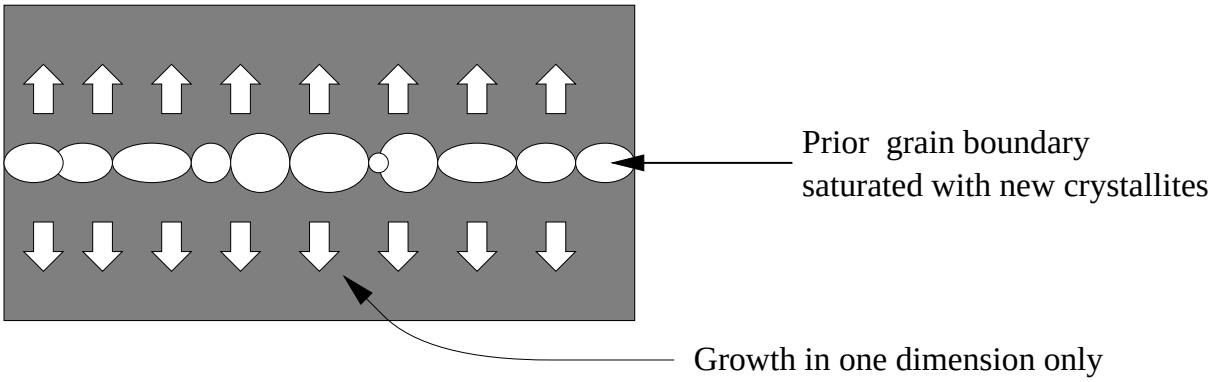

Fig. 6.7 Nucleation on grain boundaries leading to growth of recrystallization nuclei in one dimension only and hence $n = 1$

$$\zeta = 1 - \left\{ -(b^B)^{-\frac{1}{3}} f^B(a^B) \right\} \tag{2.58}$$

$$f^B(a^B) = a^B \int_0^1 \left[1 - \exp\left\{ \left(-\frac{\pi}{3} \right) (a^B)^3 (1 - 3\Xi^2 + 2\Xi^3) \right\} \right] .\mathrm{d}\Xi \tag{2.57}$$

$$a^B = (\dot{N}_B \Upsilon^2)^{\frac{1}{3}} t \tag{2.56}$$

$$b^B = \frac{\dot{N}_B}{\{8(^{\nu}O^B)^3 \Upsilon\}} \tag{2.50}$$

Equation (2.57) has no analytical solution and therefore must be evaluated numerically. The integration was solved iteratively using 100 steps of Ξ, each of value 0.01.

6.5.1.1 The grain boundary area per unit volume

The parameter $^{\nu}O^B$ is the total area of grain boundary per unit volume; for a material with an equiaxed grain structure:

$$^{\nu}O^B = 2/\bar{L} \tag{6.3}$$

where $\bar{L}$ is the mean linear intercept between grain boundaries.

Plastic deformation causes the surface to volume ratio of an equiaxed grain to increase greatly. The value of $^{\nu}O^B$ increases with rolling reduction. A mathematical treatment of this problem was given by Czinege and Reti (1977) and Singh and Bhadeshia (1998). Assuming that the equiaxed grain structure consists of a series of space-filling tetrakaidecahedra, the ratio of initial surface area (A_0) of the tetrakaidecahedron to the final surface area after rolling (A) is given by:

$$\frac{A}{A_0} = \frac{b + 3\left(b\sqrt{1 + 2b^2c^4} + \sqrt{b^2 + 2c^2}\right) + c\sqrt{2(1 + b^4c^2)}}{3bc(2\sqrt{3} + 1)} \tag{6.4}$$

where b and c are two of the principal distortions (ratios of the final to the initial lengths of unit vectors along the principle axes). The third principal distortion d may be eliminated since to maintain constant volume, $bcd = 1$. Moreover, in this study, only the specific case of rolling (*i.e.* approximately the plane-strain condition) is considered. During plane-strain conditions we know that $d = 1$ and therefore $bc = 1$ giving $b = 1/c$. This means that equation (6.4) may be reduced to:

$$\frac{A}{A_0} = \frac{b + 3\left(b\sqrt{1 + 2b^{-2}} + \sqrt{b^2 + 2b^{-2}}\right) + b^{-1}\sqrt{2(1 + b^2)}}{3\left(2\sqrt{3} + 1\right)} \tag{6.5}$$

The dimension b is along the rolling direction, d the transverse direction and c the normal direction as illustrated in Fig. 6.8.

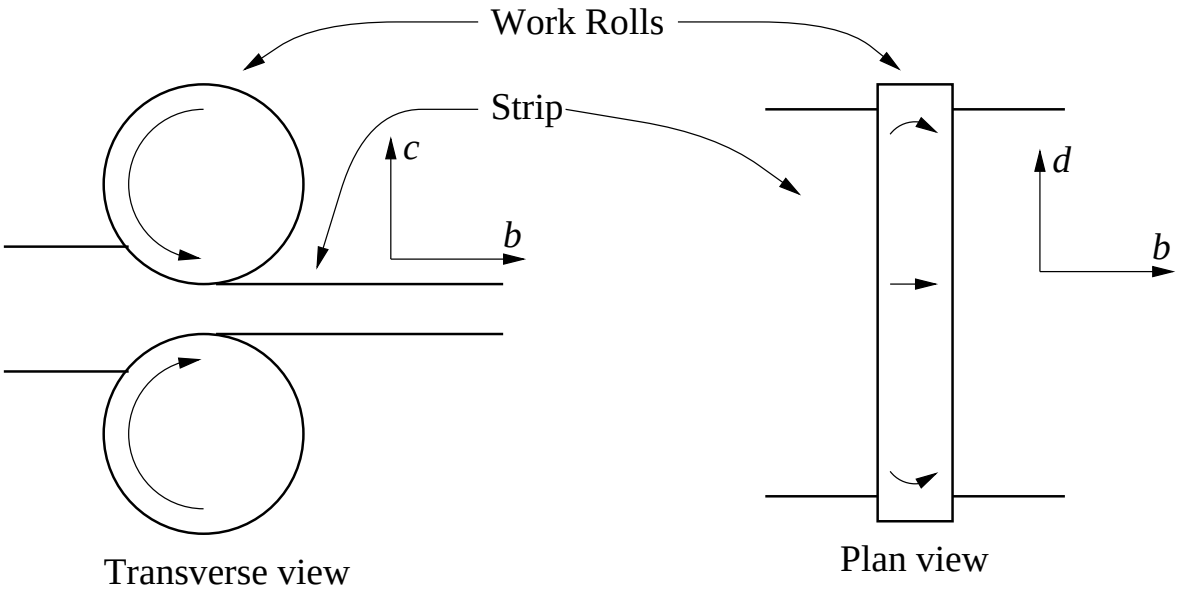

Fig. 6.8 Schematic illustration of rolling process

In industrial processing the amount of deformation put in during rolling is measured as a rolling reduction (R_R):

$$R_R = 1 - \left(\frac{\text{Final thickness}}{\text{Initial thickness}}\right) \times 100\% \tag{6.6}$$

which gives:

$$c = 1 - R_R \tag{6.7}$$

and hence

$$b = \frac{1}{(1 - R_R)} \tag{6.8}$$

Considering equations (6.5) and equation (6.8) we see that if a grain size is known for the material before deformation, the amount of grain boundary per unit volume may be calculated

using the rolling reduction. Industrially, the grain size prior to rolling may be measured "on-line" using ultrasonic measuring equipment. Ultrasonic grain size measurements for unrolled feed-stock are not currently taken during production, but this method is being used successfully to determine the final grain size after the annealing process.

It is worth noting that this derivation assumes that deformation is homogeneous which may not always be true.

Using values of initial grain size and rolling reduction, this calculation may be incorporated into the model for grain boundary nucleated recrystallization giving an accurate value of the amount of grain boundary area per unit volume (${}^{\nu}O^{B}$).

6.5.1.2 Grain boundary nucleation kinetics

During grain boundary nucleation it is necessary to consider impingement along the boundary using an extended area concept. By assuming that nucleation occurs at random across the grain boundary and that these grains then grow out from the point of nucleation with a velocity Υ, an extended area transformed A'_e for a sample containing an area A of grain boundary, can be calculated as:

$$A'_e = \int_{\tau=0}^{t} A\dot{N}\pi\Upsilon^2 t^2 \mathrm{d}t \tag{6.9}$$

$$A'_e = \pi A\dot{N}\Upsilon^2 t^3/3 \tag{6.10}$$

Invoking equation (2.29) in two dimensions we obtain the relationship between extended area fraction transformed and true area fraction transformed A':

$$\mathrm{d}A' = (1 - A'/A)\mathrm{d}A'_e \tag{6.11}$$

Defining $A'_e/A = A_{Ae}$ and $A'/A = A_A$, equation (6.11) may be simplified thus:

$$\mathrm{d}A_A = (1 - A_A)\mathrm{d}A_{Ae} \tag{6.12}$$

$$A_{Ae} = -\ln(1 - A_A) \tag{6.13}$$

upon combining equation (6.6) and equation (6.13) we observe:

$$A_A = 1 - \exp\left(-\frac{\pi\dot{N}\Upsilon^2 t^3}{3}\right) \tag{6.14}$$

If the number of nuclei on a particular boundary O at a time t is N then:

$$N = \int_0^t \dot{N}_{AA}\mathrm{d}t \tag{6.15}$$

where $\dot{N}_{AA}$ is the nucleation rate per unit area of boundary accounting for the fact that transformed boundary will not be able to support nucleation. However, since nucleation can only occur on untransformed boundary:

$$\dot{N}_{AA} = (1 - A_A)\,\dot{N} \tag{6.16}$$

Where $\dot{N}$ is the nucleation rate per unit area of untransformed grain boundary. Therefore, combining equations (6.14), (6.15) and (6.16) we see:

$$N = \int_0^t \dot{N} \exp\left(-\frac{\pi \dot{N} \Upsilon^2 t^3}{3}\right) .\mathrm{d}t \tag{6.17}$$

This integration may only be solved numerically.

6.5.1.3 Output from simple Cahn kinetics model

A grain boundary nucleation model for recrystallization was produced based on equations (2.50), (2.56), (2.57) and (2.58), along with growth rate and nucleation rate calculations as given in §6.1 and §6.2 respectively. The standard plots of fraction recrystallized (ζ) against time (t) and the 'Avrami plot' are included in Fig. 6.9.

The plot of ζ against t does not show the classical sigmoidal shape predicted by standard overall transformation kinetics but instead a steep initial rise, followed by a levelling off.

The "Avrami plot" of $\ln(\ln(1/(1\text{-}\zeta)))$ against $\ln(t)$ shows two different slopes. The first part of the annealing cycle shows a slope of $n = 4$ as would be expected from a standard overall transformation kinetics model with random nucleation and three dimensional growth. However at $\ln(t) \approx -2.5$ (*i.e.* $t \approx 0.08$ s) this slope changes to $n = 1$. This change indicates the onset of site saturation, followed by one dimensional growth. The change in the value of n is rarely observed in experimental data because it would require a very specific relationship betweenΥ, $\dot{N}$ and ${}^{\nu}O^{\beta}$ and because experiments have inadequate resolution. Usually, therefore, only $n = 1$ or $n = 4$ is observed, not both. This model provides a good fit to the observed isothermal annealing curves in the data (*e.g.* Hutchinson *et al.* 1973).

However, annealing in an industrial context is concerned with the maximisation of throughput. The heat-treatments are therefore done on a continuous annealing production line (fig 1.7). The strip is heated gradually as it passes through the furnace. The steel strip is not heated isothermally so it is necessary to adapt any kinetic model for anisothermal heat treatment.

6.6 First anisothermal Cahn kinetics model

The model was coded using FORTRAN77. The driving force for recrystallization (ΔG) was calculated as in §6.1.1 (equation 2.10) and the growth velocity Υ as in §2.3. The nucleation

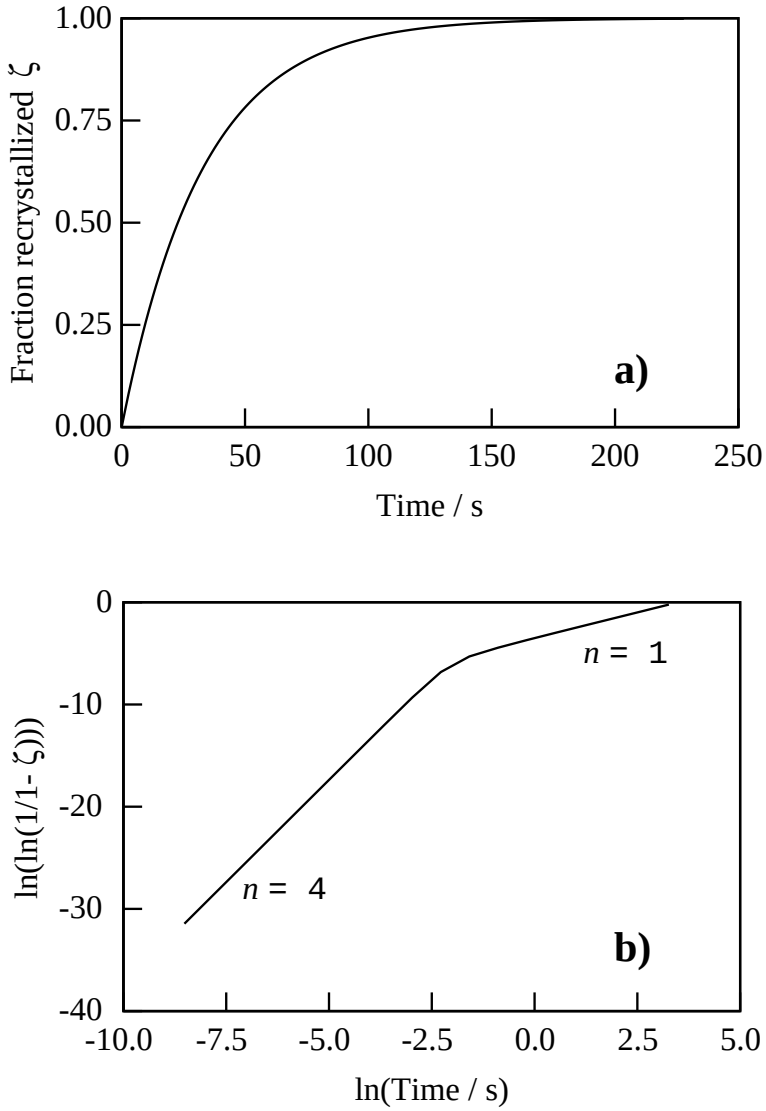

Fig. 6.9 All figures are predicted data for a theoretical isothermal anneal at 900 °C for times specified. **a)** Chart of fraction recrystallized against time from isothermal Cahn kinetics model. **b)** "Avrami plot" of $\ln(\ln(1/(1\text{-}\zeta)))$ vs ln(time) showing an initial gradient of 4, indicating that the Avrami exponent n is 4 during the initial moments of the annealing cycle. However at $\ln(t) > 2.5$ (*i.e.* $t \approx 0.08$ s) the gradient of the slope changes to 1 indicating that site saturation has occurred. Moreover, this occurs when $\zeta \approx 0.05$ which means all of the observable part of the annealing process will be in the $n = 1$ regime.

rate was calculated in a similar fashion to §6.2. Equation (6.1) gives the nucleation rate per unit volume ν_v, however this is not valid in the case of Cahn kinetics because nucleation is limited to the grain boundaries. Therefore the pre-exponential factor ν_V was altered to ν_N, the nucleation attempt frequency per unit area, such that:

$$\dot{N} = \nu_N \exp\left(-\frac{G^*}{RT}\right) \tag{6.18}$$

This process was then made anisothermal using the Scheil approach detailed in §6.4.1.

It is useful when applying the Scheil approximation to express time as the dependent variable so that the equivalent times may be calculation easily. For example, equation 6.2:

$$\zeta = 1 - \exp\left(-\pi \Upsilon^3 \dot{N} t^4/3\right) \tag{6.2}$$

may be rearranged thus: may be rearranged $\zeta = 1 - \exp\left(-\pi \Upsilon^3 \dot{N} t^4/3\right)$. This is trivial because the time t may be made the subject of the equation, thus:

$$t = \left(\sqrt[4]{\frac{\pi \Upsilon^3 \dot{N}}{3} \ln\left(\frac{1}{1-\zeta}\right)}\right)^{-1} \tag{6.19}$$

However, this is not possible for grain boundary nucleated kinetics where the kinetic functions are a lot more complex (*e.g.* equation 2.57). Nevertheless, the time may be extracted numerically beginning with a guessed value. Unfortunately this procedure is exceedingly computer intensive, to ensure accurate answers upwards or 100,000 iterations were needed for each time increment.

A model was therefore produced and trained using data obtained at or near 709 °C . Example graphs from this temperature are given in Fig. 6.10(a–d).

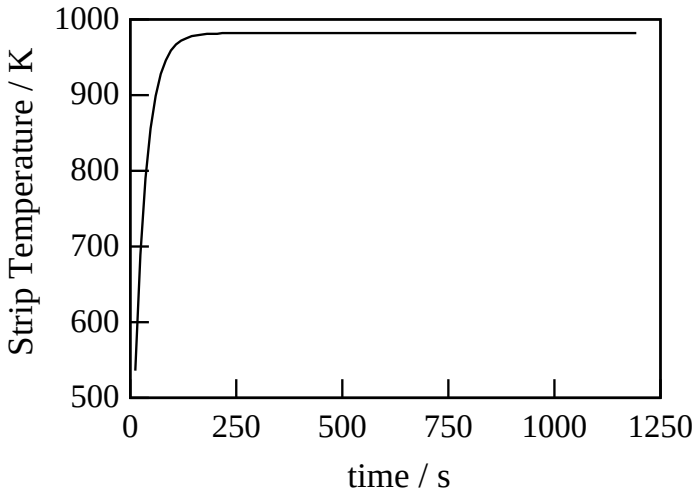

Fig. 6.10 a) Graph showing the variation of the strip temperature with time. The strip is subject to a Newtonian heating regime *i.e.* $t = t_f - (T_f - T_R)\exp(-at)$. In this case the furnace temperature (T_f) is set to 709 °C (982 K)

However, it was observed that although an good fit could be produced for data at a single temperature, the fit across a range of temperatures could not be reproduced. This is illustrated

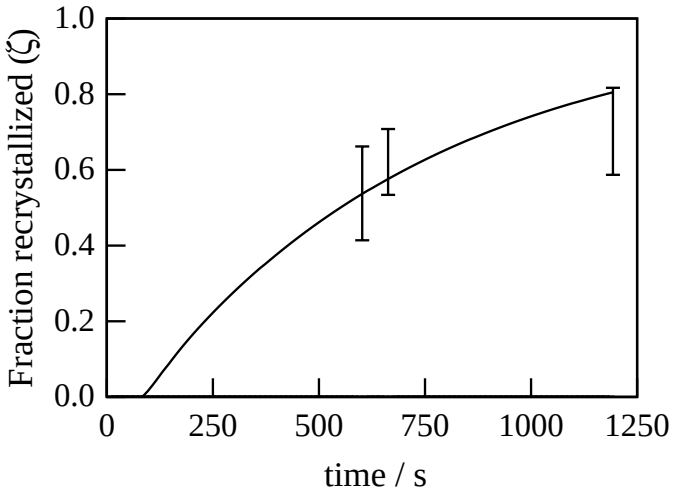

Fig. 6.10 b) Chart showing the variation of fraction recrystallized (ζ) with time for a set furnace temperature $T_f = 709$ °C and a heating regime illustrated in Fig. 6.10 a). The solid line represents the predicted variation of ζ with time, the error bars represent experimental data.

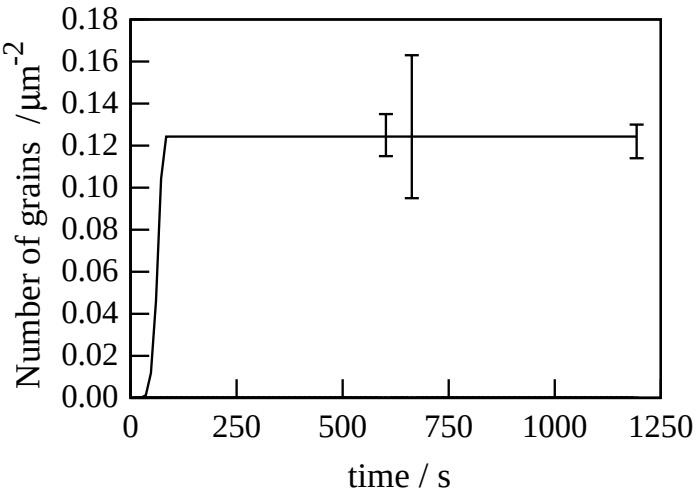

Fig. 6.10 c) Chart showing the variation of the number of recrystallization nuclei per μm^2 of observed surface for a sample anisothermally annealed at 709 °C undergoing a heating regime illustrated in Fig. 6.10 a). The solid line represents the predicted variation with time, the error bars represent experimental data. It should be noted that number of nuclei per μm^2 levels off early in the annealing process. This illustrates that site saturation is occurring.

by examining a sample annealed at 728 °C and comparing experiment to prediction. After calibration it was found that predicted and experimental fraction recrystallized showed poor fit (Fig. 6.11)

For samples annealed at higher temperatures than that at which the model was originally

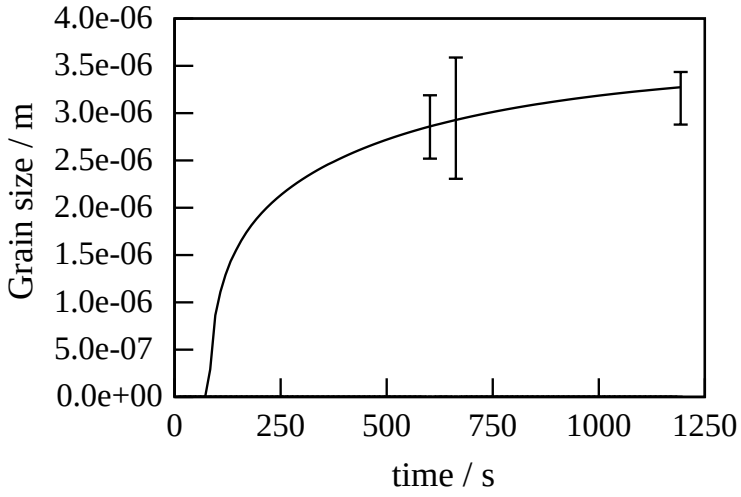

Fig. 6.10 d) Chart showing the variation of the number of recrystallized grain diameter for a sample anisothermally annealed at 709 °C undergoing a heating regime illustrated in Fig. 6.10 a).

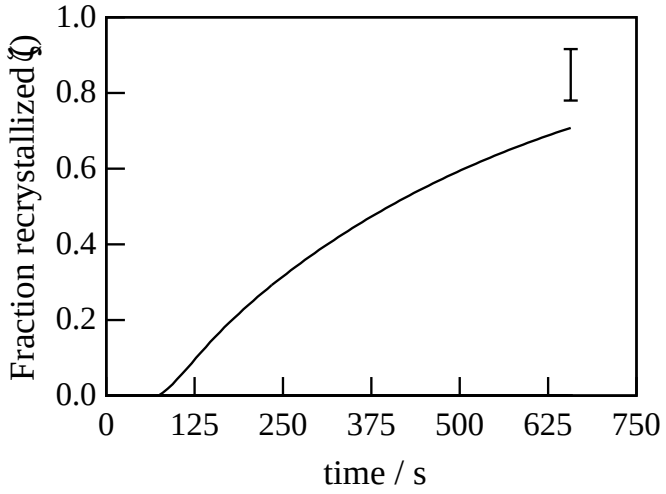

Fig. 6.11 Chart showing the variation of fraction recrystallized (ζ) with time for a set furnace temperature $T_f = 728$ °C and a Newtonian type heating regime of the form $t = t_f - \left(T_f - T_R\right) exp(-at)$. The solid line represents the predicted variation of ζ with time, the point with error bars represent experimental data.

calibrated, the prediction was always lower than the experimental value, similarly for a temperature lower than that of the calibration temperature, the predicted values were consistently higher than those observed.

In all the above cases and as shown by Figure 6.8 c) site saturation occurs rapidly and recrystallization then becomes a function of growth rate alone. The equation used in the

calculation of growth rate was:

$$\Upsilon = \delta_\varsigma \nu \exp\left(-\frac{Q}{RT}\right)\left[1 - \exp\left(-\frac{\Delta G}{RT}\right)\right] \tag{2.15}$$

It is clear therefore that if site saturation occurs before the temperature stabilised, the grain boundary velocity Υ must be made more temperature sensitive The value of ΔG may, reasonably, been taken to be constant, dependent on only initial microstructure and chemical composition. Therefore, it is probable that a better fit with respects to temperature dependence can be obtained by adjusting the activation energy Q for the transfer of atoms across the boundary during growth.

6.6.1 The physical meaning of Q

As stated above Q is the activation energy needed for an atom to jump across a grain boundary. Generally, this is taken to be independent of temperature but, as with all free energies it can never be truly temperature independent. Defining the free energy Q in the standard way we see that:

$$Q = \Delta H_{act} - T\Delta S_{act} \tag{6.20}$$

wherein ΔH_{act} is the difference in enthalpy between activated and stable states and ΔS_{act} is the difference in entropy between activated and stable states. Equation (2.15) may be expanded thus:

$$\Upsilon = \delta_\varsigma \nu \exp\left(-\frac{(\Delta H_{act} - T\Delta S_{act})}{RT}\right)\left[1 - \exp\left(-\frac{\Delta G}{RT}\right)\right] \tag{6.21}$$

$$\Upsilon = \delta_\varsigma \nu \exp\left(\frac{\Delta S_{act}}{R}\right)\exp\left(-\frac{\Delta H_{act}}{RT}\right)\left[1 - \exp\left(-\frac{\Delta G}{RT}\right)\right] \tag{6.22}$$

If both ΔH_{act} and ΔS_{act} are taken to be temperature independent, then the model may be retrained using these new parameters a fitting constants. ΔH_{act} was restricted to be positive and of the order of the activation energy of self diffusion in pure iron (austenitic polymorph) (286 kJ mol^{-1}). ΔS_{act} was taken to be positive because the boundary layer may safely be assumed to be more disordered than the bulk of the crystal.

In the light of this alteration, the model for nucleation was also inspected. Nucleation had previously been modelled using equation 6.18 which is of the form of a standard Arrhenius equation in which the pre-exponential factor ν_N was assumed to be temperature independent. ν_N physically represents the attempt frequency for nucleation. In fact any vibration must be thermally activated and therefore cannot be temperature independent‡. Although many authors take ν_N to be temperature independent (*e.g.* Sha and Bhadeshia, 1997) and have

‡ This statement is only strictly true for classical and not quantum particles and objects.

achieved an acceptable fit to experimental data, others have taken ν_N to be directly proportional to T (*e.g.* Parker 1997, Cahn 1956) and have also obtained a good fit. Cahn (1956) has derived an expression to describe the variation of ν_N and hence the nucleation rate with temperature such that:

$$\dot{N} = \frac{kT}{h}\frac{K_1^j}{\delta^2}\exp\left\{-\frac{\left(K_2^j G_{Ca} + Q_C\right)}{kT}\right\} \tag{6.23}$$

wherein δ is the grain boundary thickness, K_1^j and K_2^j are factors which depend on the geometry of nucleation and the term $\left(K_2^j G_{Ca} + Q_C\right)$ is equivalent to G^* in equation 6.18. For the purposes of simplifying the modelling procedure this process equation (6.23) was reduced to:

$$\dot{N} = \nu_T T \exp\left(-\frac{G^*}{kT}\right) \tag{6.24}$$

This approach equates $\left(K_2^j G_{Ca} + Q_C\right)$ to G^* and $kK_1^j/h\delta^2$ to ν_T.

Classically, G^* is the activation energy for nucleation, *i.e.* the difference in energy between the activated and stable states. Simple derivations of the activation energy for the formation of a spherical nucleus (*e.g.* Reed-Hill and Abbaschian 1994) show that:

$$G^*_{Class} = \frac{16}{3}\frac{\pi\gamma^3}{\Delta G} \tag{6.25}$$

where G^*_{Class} is the activation energy for classical homogeneous nucleation, γ is the surface energy and ΔG is the driving force for recrystallization (*i.e.* the difference in energy per unit volume between the recrystallized and unrecrystallized states). However, because classical nucleation is generally considered to be inviable in the case of recrystallization (*c.f.* §2.4), many authors (*e.g.* Sha and Bhadeshia, 1997) choose to treat G^* as a fixed material constant. Whilst this approach can produce good fit in the case of a single steel, its applicability has never been tested across a wide range of steels. Furthermore, the process of nucleation involves the discontinuous growth of a small volume of relatively strain free material into the deformed matrix. It is therefore quite unphysical to assume that the difference in stored energy between the deformed and undeformed will not effect the nucleation rate. Because neither of these approaches gave a satisfactory and physically sound result, it was decided to treat G^* as an empirically derived function of ΔG such that:

$$G^* = G_C \Delta G^{-n_G} \tag{6.26}$$

where G_C and n_G are empirically derived fitting constants. The value of n_G was, however, constrained to lie between the expected classical value of 2 and 0 which is commonly assumed in the literature.

6.7 Second Anisothermal Cahn kinetics model - type 302 stainless steel

6.7.1 Data used for training model

The applicability of this revised Cahn model was tested initially on a type 302 stainless steel supplied as-rolled sheet by Avesta Sheffield Ltd. Samples were prepared and tested using the methodology outlined in Chapter 4.

The chemical composition of this steel as measured by the producers is given in Table 6.2.

Element	C	Si	Mn	P	S	Cr	Mo	Ni	Al	Cu	Sn	Nb
Weight %	0.045	0.38	1.39	0.028	0.007	18.21	0.28	8.61	0.007	0.26	0.012	0.01

Element	W	V	Co	Ti	As	B	Zr	Pb	N	H	Fe
Weight %	0.06	0.05	0.15	0.010	0.01	0.0033	0.00	0.0000	0.049	0.0000	Balance

Table 6.2: Composition of type 302 stainless steel used in this study

All samples were identical squares of 1 cm $\times$ 1 cm $\times$ 0.08 cm cut from the same sheet of material. The initial Vickers hardness of 465 HV $\pm$ 15 (measured with a load of 5 kg). The temperature of each samples was monitored continuously and these data fitted to a Newtonian heating curve (equation 5.7). A model based on Cahn kinetics was coded using FORTRAN77 programming language and is given in full in Appendix 1. The model was fitted to the experimental data; no distinct values of G_C and n_G could be calculated because only a single rolling reduction (and hence stored energy) was used and therefore the effects of different driving forces for recrystallization could not be assessed.

Output from the model is given in Table 6.3 and figures 6.13 to 6.17.

Generally, the annealing cycle was sufficiently long to ensure that the final temperature of the strip T was stable and hence was approximately equal to the true furnace temperature (T_f). However in the case of short annealing cycles the sample did not reach thermal equilibrium, so that the true furnace temperature (which is a required input for the computer program) was not directly measurable. In such cases the measured time (t) against stock temperature (T) were compared with a standard Newtonian heating curve of the form $T = T_f - ((T_f - T_R)\exp(-at))$ allowing the true furnace temperature (T_f) to be calculated. Calculated values of T_f are indicated in Table 6.3 by the symbol ‡.

a)

Predicted ζ	Measured ζ	a	T_f / °C	time / s
0.80	0.70 ± 0.12	0.035	709	1200
0.52	0.54 ± 0.13	0.035	709	600
0.57	0.62 ± 0.09	0.035	707	660
0.82	0.85 ± 0.07	0.035	723	615
0.91	0.85 ± 0.07	0.035	728	660
0.14	0.12 ± 0.06	0.070	880‡	30
0.87	0.84 ± 0.07	0.070	830‡	45

b)

Predicted Grain size / μm	Measured Grain size / μm	a	T_f / °C	time / s
3.23	3.16 ± 0.28	0.035	709	1200
2.80	2.85 ± 0.34	0.035	709	600
2.87	2.95 ± 0.64	0.035	707	660
2.90	2.94 ± 0.22	0.035	723	615
2.91	2.82 ± 0.16	0.035	728	660
0.78	2.13 ± 0.67	0.070	880‡	30
1.59	3.12 ± 0.24	0.070	830‡	45

c)

Predicted G_a / μm^{-2}	Measured G_a / μm^{-2}	a	T_f / °C	time / s
0.13	0.12 ± 0.01	0.035	709	1200
0.13	0.13 ± 0.01	0.035	709	600
0.13	0.13 ± 0.04	0.035	707	660
0.16	0.16 ± 0.02	0.035	723	615
0.17	0.17 ± 0.01	0.035	728	660
0.68	0.08 ± 0.03	0.070	880‡	30
0.56	0.14 ± 0.02	0.070	830‡	45

Table 6.3: Tables 6.3 **a) b)** and **c)** are a comparison of model results with experimental results on a grade 302 stainless steel. All samples underwent a Newtonian heating regime fully described by the given parameters a and T_f. *(The symbol ‡ next to a value of T_f denotes that this is a calculated value. In these cases a measured value was not available because the short annealing times used meant the temperature of the sample did not equilibrate)*

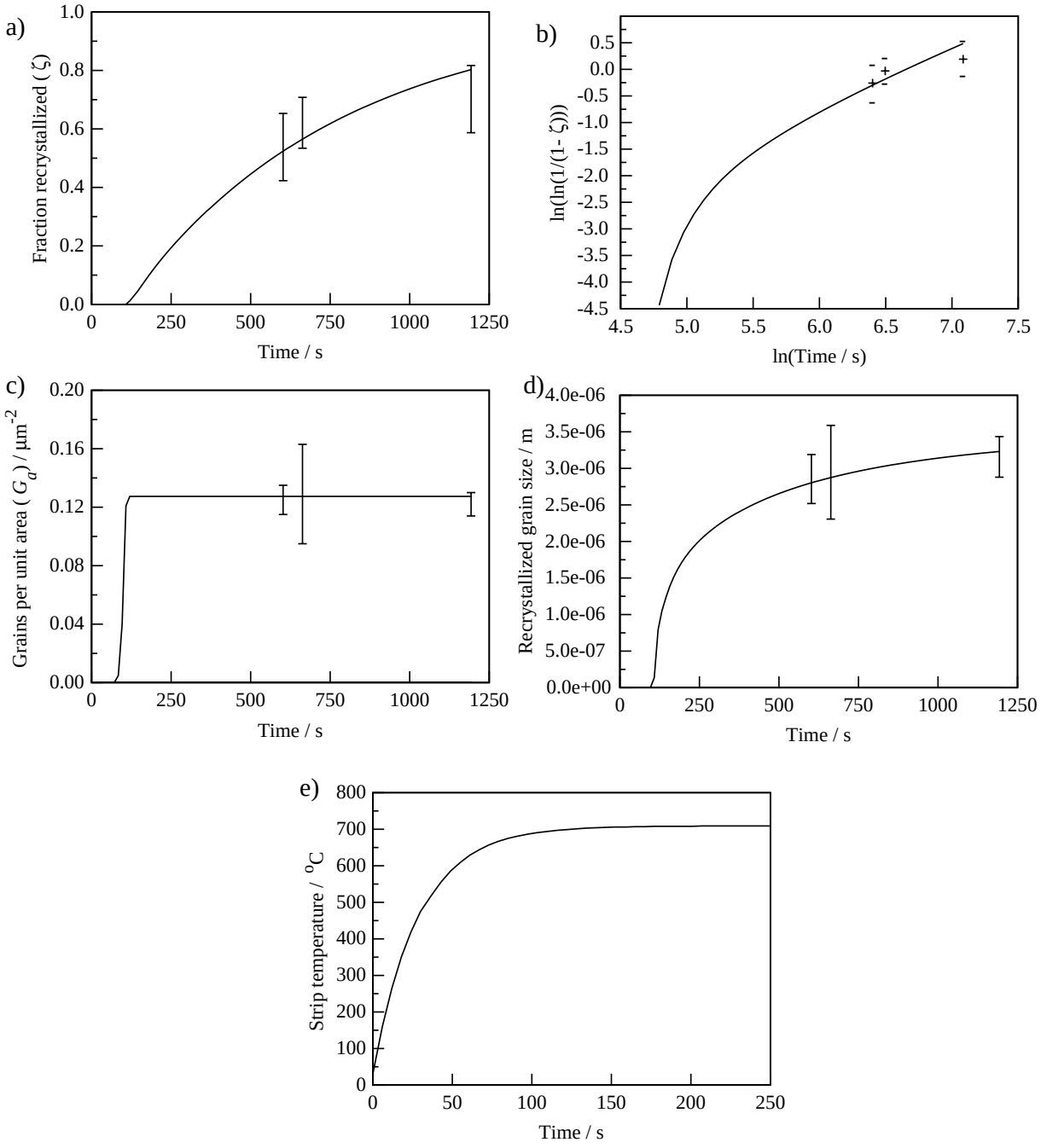

Fig. 6.12 Graphical representation of output from anisothermal recrystallization model trained on a type 302 stainless steel. Samples were annealed at a furnace temperature of 709 °C with $a = 0.035$ for times illustrated. In all charts the solid line indicates the model's prediction and the error bars an experimental datapoint. **a)** Plot of ζ against time, showing modified sigmoidal curve characteristic of Cahn kinetics. **b)** Standard "Avrami" plot of $\ln(\ln(1/1\text{-}\zeta)))$ against $\ln(t)$ showing a slope of 4 on the right-hand side of the graph. This indicates that site saturation has occurred. **c)** Chart showing the variation of number of grains per unit area G_a with time. Since G_a does not vary with time or fraction recrystallized, this would concur with the prediction from chart b) that site saturation has occurred. **d)** Chart showing the variation of grain size with time. **e)** The variation of strip temperature with annealing time (predicted).

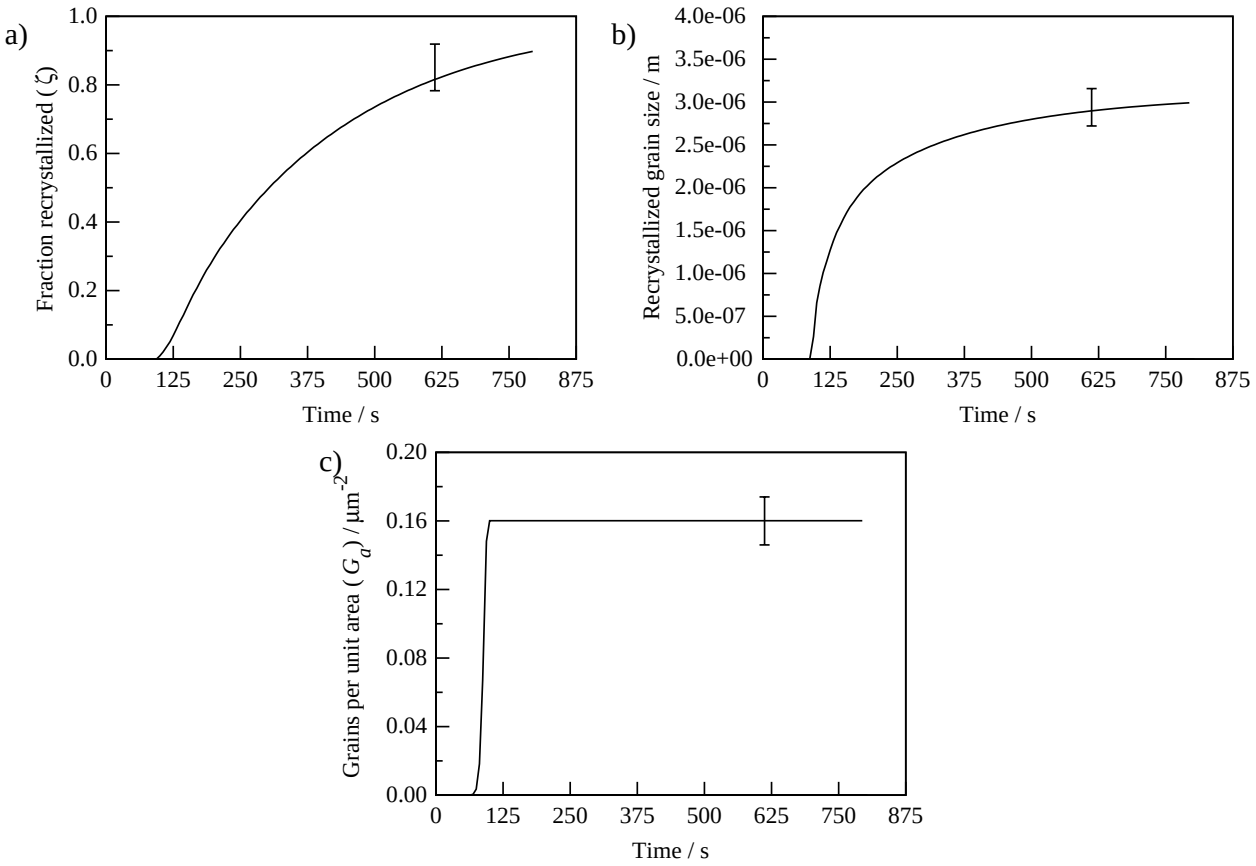

Fig. 6.13 Output from anisothermal recrystallization model trained on a type 302 stainless steel. Samples were annealed at a furnace temperature of 723 °C with $a = 0.035\,\mathrm{s}^{-1}$ for times illustrated. In all charts the solid line indicates the model's prediction and the error bars an experimental datapoint. **a)** Plot of ζ against time, showing modified sigmoidal curve characteristic of Cahn kinetics. **b)** Chart showing the variation of number of grains per unit area G_a with time. Since G_a does not vary with time or fraction recrystallized, this would indicate that site saturation has occurred. **c)** Chart showing the variation of grain size with time.

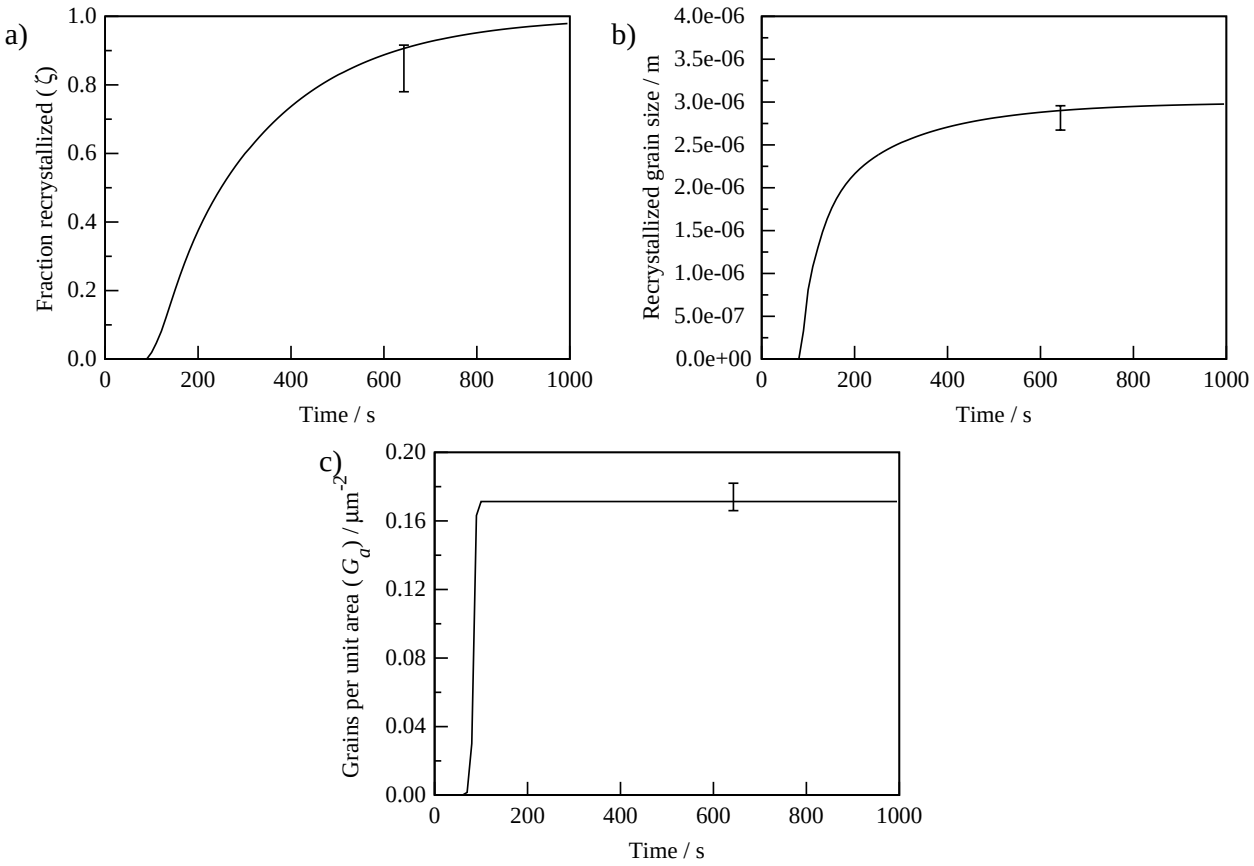

Fig. 6.14 Graphical representation of output from anisothermal recrystallization model trained on a type 302 stainless steel. Samples were annealed at a furnace temperature of 728 °C with $a = 0.035$ for times illustrated. In all charts the solid line indicates the model's prediction and the error bars an experimental datapoint. **a)** Plot of ζ against time, showing modified sigmoidal curve characteristic of Cahn kinetics. **b)** Chart showing the variation of number of grains per unit area G_a with time. Since G_a does not vary with time or fraction recrystallized, this would indicate that site saturation has occurred. **c)** Chart showing the variation of grain size with time.

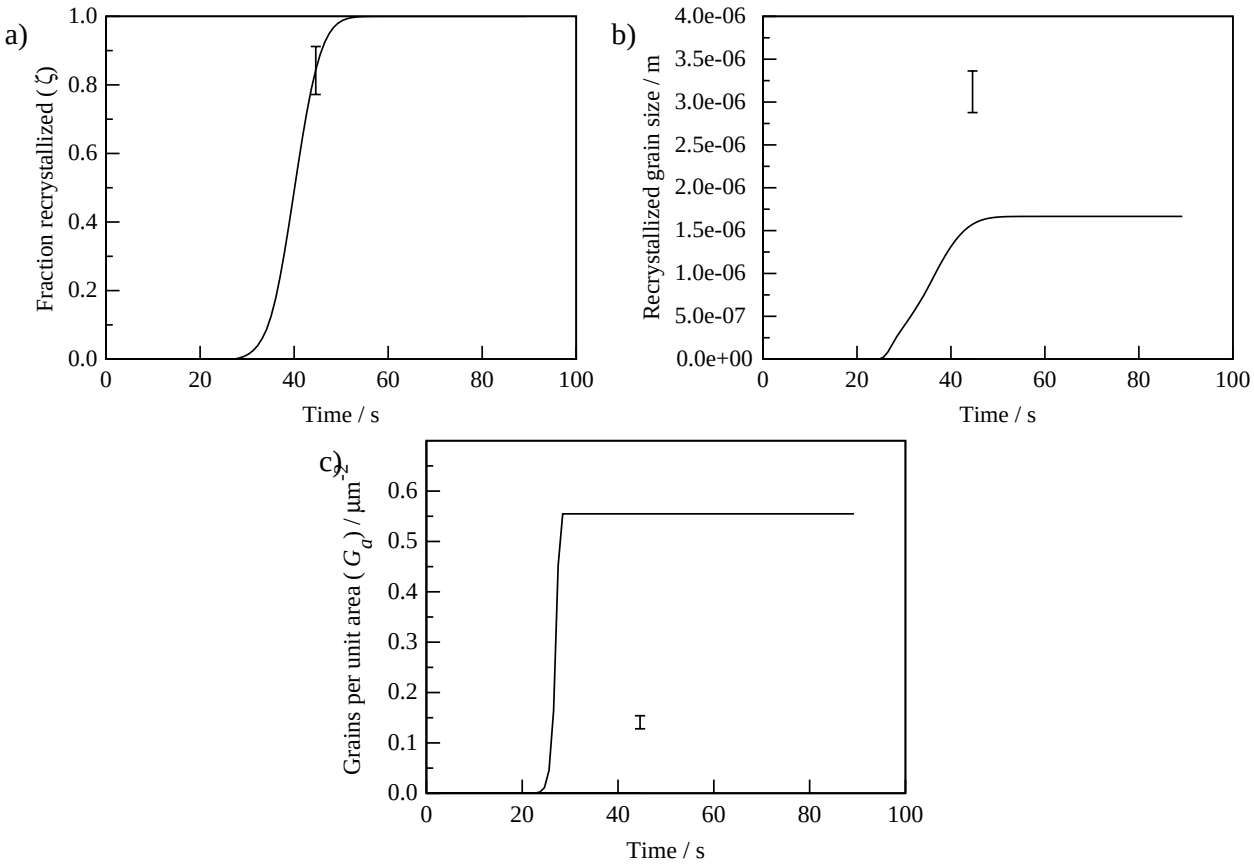

Fig. 6.15 Graphical representation of output from anisothermal recrystallization model trained on a type 302 stainless steel. Samples were annealed at a furnace temperature of 830 °C with $a = 0.07$ for times illustrated. In all charts the solid line indicates the model's prediction and the error bars an experimental datapoint. **a)** Plot of ζ against time, showing modified sigmoidal curve characteristic of Cahn kinetics. **b)** Chart showing the variation of number of grains per unit area G_a with time. Since G_a does not vary with time or fraction recrystallized, this would indicate that site saturation has occurred. **c)** Chart showing the variation of grain size with time.

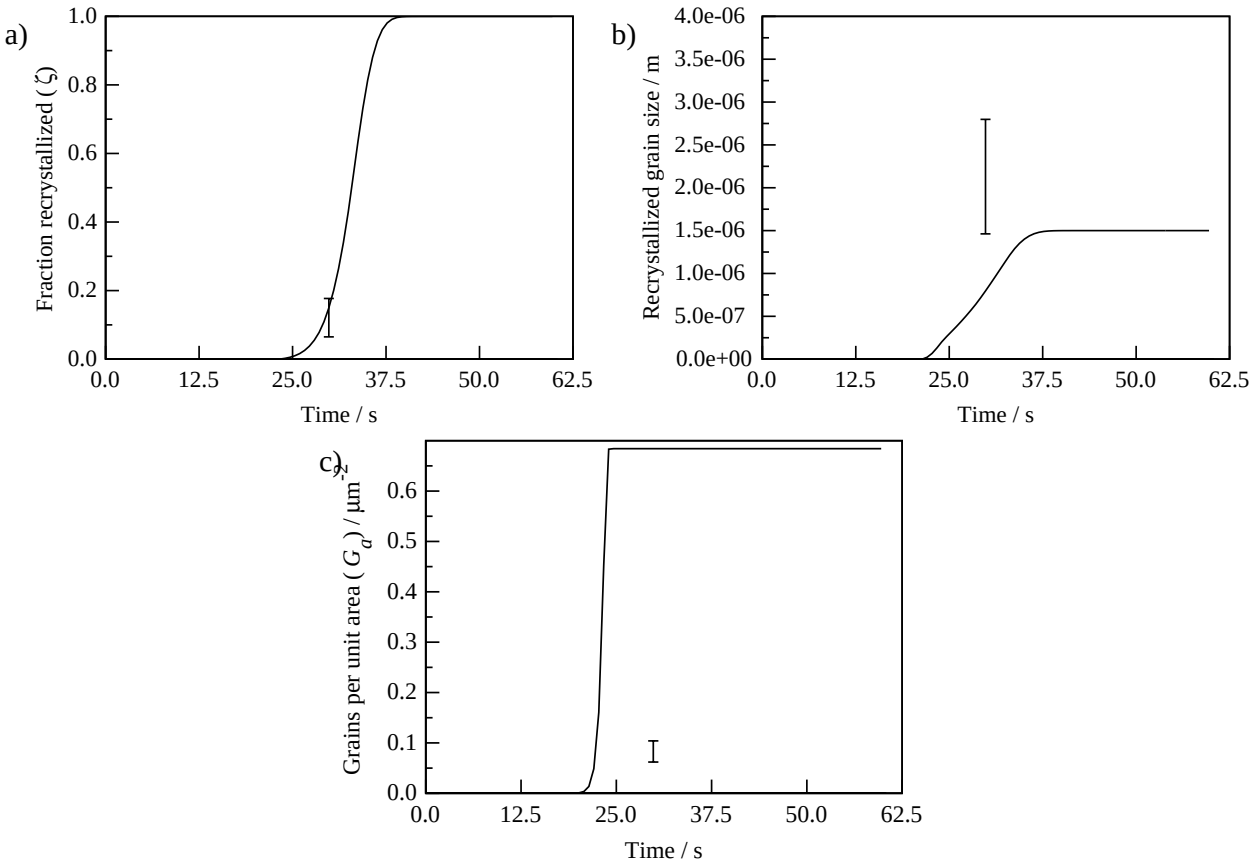

Fig. 6.16 Graphical representation of output from anisothermal recrystallization model trained on a type 302 stainless steel. Samples were annealed at a furnace temperature of 880 °C with $a = 0.07$ for times illustrated. In all charts the solid line indicates the model's prediction and the error bars an experimental datapoint. **a)** Plot of ζ against time, showing modified sigmoidal curve characteristic of Cahn kinetics. **b)** Chart showing the variation of number of grains per unit area G_a with time. Since G_a does not vary with time or fraction recrystallized, this would indicate that site saturation has occurred. **c)** Chart showing the variation of grain size with time.

6.7.2 Discussion of results from type 302 stainless steel

Figures 6.13 to 6.15 illustrate the good agreement of predictions with experimental data for fraction recrystallized, number of grains per unit area and grain size, all well within the limits of experimental error. This indicates that the Cahn approach to site saturation is useful in the modelling of recrystallization. An important achievement is the ability to explain the frequently observed value of unity for the Avrami exponent.

However, the agreement is less satisfactory for samples annealed at temperatures above 800 °C; although there is good fit for fraction recrystallized, the agreement is weak for number of grains per unit area and grain size.

The likely explanation for this anomaly is that heating rates for the two high temperature samples were greater than those for the lower temperature samples ($a = 0.070$ s^{-1} in this case as compared to $a = 0.035$ s^{-1} for the lower temperature samples). Type 302 stainless steel has a relatively low nickel content, therefore heavy rolling deformation causes this steel to experience a degree of strain induced martensitic transformation. This is experimentally verifiable because the martensitic α' is magnetic and prior to annealing, the steel is magnetic. This martensite will revert back to austenite on heating, this is observed experimentally by the fact that after annealing is non-magnetic. The reversion of martensite to austenite has been known to stimulate the nucleation of recrystallization (Humphreys and Hatherly, 1996). The morphology of the observed zones of nucleation consists of planar bands of nuclei (see Fig. 6.17). This morphology is consistent with '*grain boundary*' nucleated Cahn kinetics, the only difference being the planes involved in nucleation are transition zones or other high strain, martensite inducing planar features and not grain boundaries.

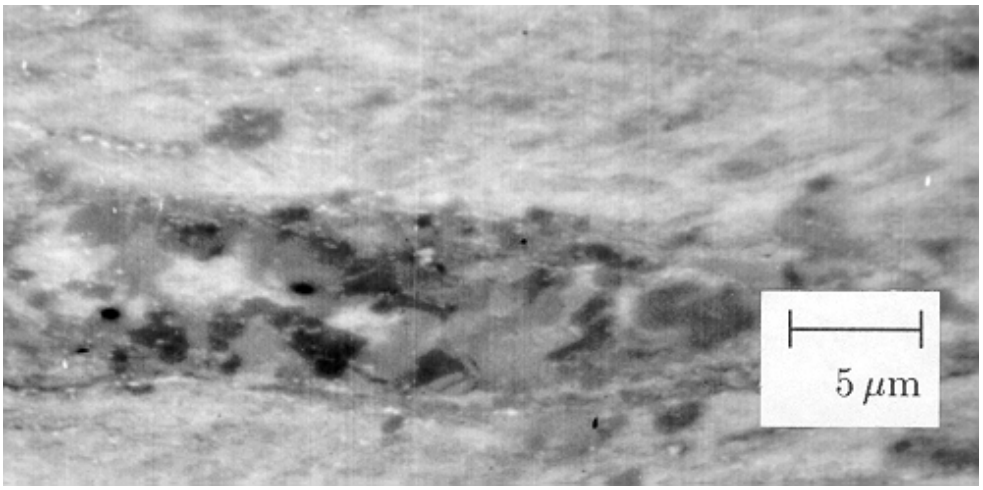

Fig. 6.17 "Plane" of recrystallization nuclei in a type 302 stainless steel annealed for 600 s at a nominal furnace temperature of 700 °C

After reversion, there may be an incubation period†, as discussed in §2.4.3. This delay in nucleus formation would mean that nucleation was occurring at a higher temperature because of the higher heating rates. Growth at the higher temperature would be faster and therefore recrystallization planes would be completely consumed before the expected number of nuclei passed their incubation period. At present an incubation period is absent from the model.

6.8 Second Anisothermal Cahn kinetics model - Stainless steel types 304L, 254SMO, 904L

6.8.1 Data used for training models

After the validity of the Cahn theory model was confirmed using type 302 stainless steel, it was extended to a number of different stainless steels: 304L, 254SMO and 904L. Samples were provided by either the Shepcote lane works of Avesta Polarit Ltd, or the Stocksbridge works of Avesta Polarit and were subsequently prepared and tested using the methodology outlined in Chapter 4. The measured chemical compositions for these steels are given in Table 6.4a), b), and c).

Stainless steel grade	C	Si	Mn	P	S	Cr	Mo	Ni
254SMO	0.023	0.47	0.54	0.022	0.001	20.07	6.03	17.96
304L	0.016	0.46	1.39	0.023	0.001	18.31	0.31	10.12
904L	0.011	0.26	1.51	0.022	0.001	19.72	4.28	24.25

Stainless steel grade	Ti	Nb	Co	N	Cu	Sn	Al	V
254SMO	0.00	0.01	0.19	0.204	0.67	0.005	0.011	0.05
304L	0.01	0.01	0.00	0.039	0.47	0.015	0.006	0.07
904L	0.00	0.00	0.22	0.066	1.41	0.000	0.000	0.00

Table 6.4: Chemical composition of each steel studied.

Samples of each steel were supplied as rolled sheet of different rolling reduction. Each sheet was taken from the same cast of steel and hence can be assumed to be chemically identical. The different thicknesses of sheet available for each steel are given in Table 6.5.

Each sample was cut into 1 × 1 cm squares, after which samples of the same composition were resistance welded together at several points to ensure good thermal contact and then a

† The incubation period is a period of time at the start of the recrystallization process before which no nucleation is observed

Stainless steel grade	Gauges available / mm
254SMO	0.1 0.125 0.15 0.21 0.28
304L	0.19 0.26 0.42 0.49 0.55 0.8 1.4 1.8 3.0
904L	0.8 0.95 1.1 1.8 2.3 3.0

Table 6.5: Variation in gauge for each steel studied.

thermocouple was welded onto the composite sample which was then annealed as described in Chapter 4. In this way several samples of different gauges but similar chemistry underwent exactly the same thermal treatment, this allowed direct comparison of the effect of rolling reduction on the recrystallization behaviour.

A separate model was trained for each grade of steel using exactly the same structure of model as described in the previous section (§6.7), utilising the same source code as detailed for type 302 stainless steel in Appendix 1. Each model differed only in the values of thermodynamic fitting factors used.

6.8.2 Modelling results - type 904L stainless steel

These are presented in Table 6.6 and in Figures 6.19 to 6.21:

T_f / °C	t / s	Final strip T / °C	Gauge / mm	Predicted G_a / μm^{-2}	Measured G_a / μm^{-2}	a	Flow stress / MPa
855‡	240	846	0.80	0.087	0.083 ± 0.004	0.0190	125.4 ± 3.6
855‡	240	846	0.95	0.054	0.060 ± 0.007	0.0190	121.5 ± 4.1
855‡	240	846	1.10	0.030	0.033 ± 0.008	0.0190	116.6 ± 5.0
970‡	180	887	0.80	0.137	0.131 ± 0.008	0.0135	125.4 ± 3.6
970‡	180	887	0.95	0.092	0.086 ± 0.003	0.0135	121.5 ± 4.1
970‡	180	887	1.10	0.059	0.063 ± 0.007	0.0135	116.6 ± 5.0

T_f / °C	t / s	Final strip T / °C	Gauge / mm	Predicted ζ	Measured ζ	a	Flow stress / MPa
855‡	240	846	0.80	0.832	0.83 ± 0.06	0.0190	125.4 ± 3.6
855‡	240	846	0.95	0.633	0.63 ± 0.11	0.0190	121.5 ± 4.1
855‡	240	846	1.10	0.391	0.44 ± 0.12	0.0190	116.6 ± 5.0
970‡	180	887	0.80	0.969	0.95 ± 0.03	0.0135	125.4 ± 3.6
970‡	180	887	0.95	0.855	0.87 ± 0.05	0.0135	121.5 ± 4.1
970‡	180	887	1.10	0.616	0.73 ± 0.12	0.0135	116.6 ± 5.0

Table 6.6: Comparison of model results with experimental results on a grade 904L stainless steel. All samples underwent a Newtonian heating regime ($T = T_f - ((T_f - T_R)\exp(-at))$) fully described by the given parameters a and T_f. *(The symbol ‡ next to a values of T_f denotes that this is a calculated value. In these cases a measured value was not available because the short annealing times used meant the temperature of the sample did not equilibrate)*

6.8.2.1 Discussion of model for 904L stainless steel

The model shows excellent fit over the whole range of heating rates, stored energies and rolling reductions studied. It gives meaningful values of ζ and G_a and in terms of the data studied it fully reflects the complexity of the system.

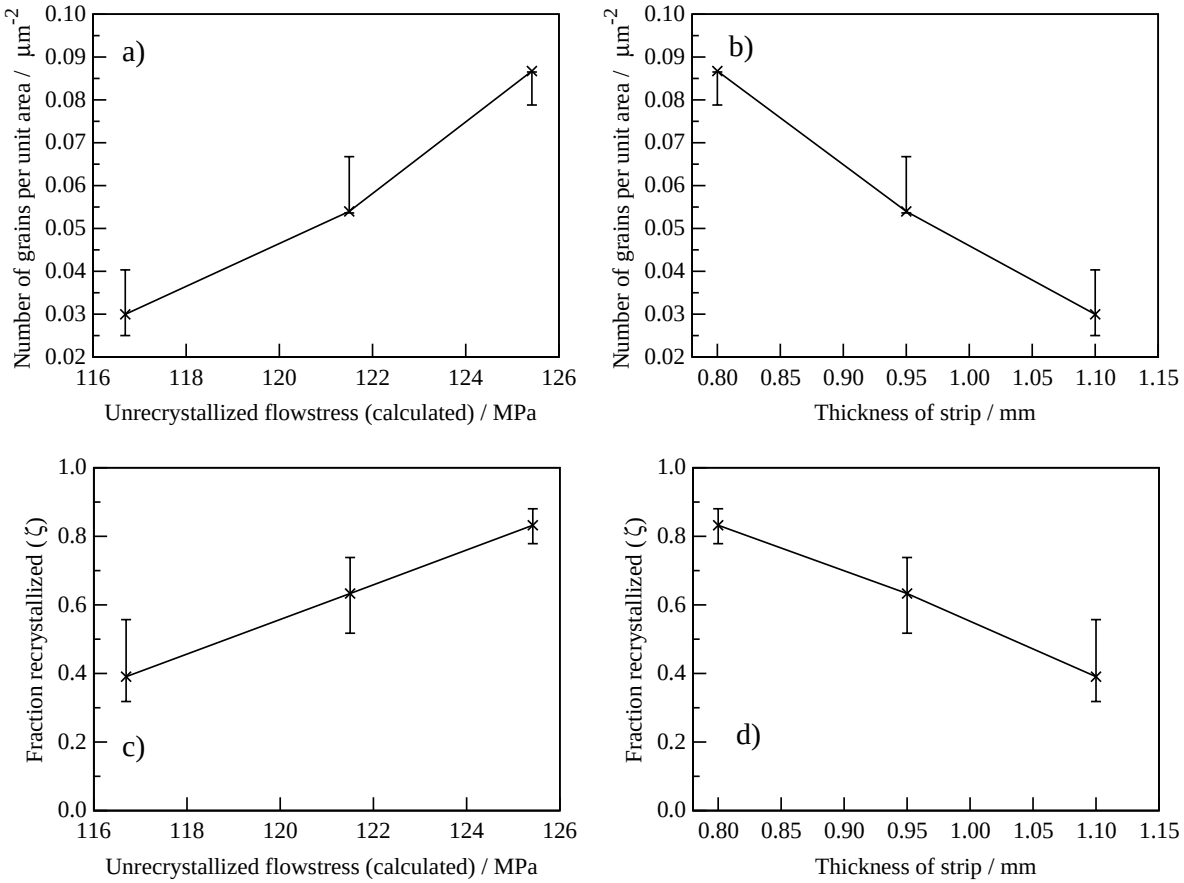

Fig. 6.18 Graphical representation of output from anisothermal recrystallization model trained on a type 904L stainless steel. Samples were annealed at a furnace temperature of 855 °C with $a = 0.019$ for initial strip conditions illustrated. In all charts the solid line indicates the model's prediction and the error bars an experimental datapoint. **a)** Plot of Number of grains per unit area G_a against calculated flow stress σ_f in the unrecrystallized material. **b)** Plot of Number of grains per unit area G_a against gauge of material. **c)** Plot of fraction recrystallized (ζ) against calculated flow stress (σ_f) in the unrecrystallized material. **d)** Plot of fraction recrystallized (ζ) against gauge of material

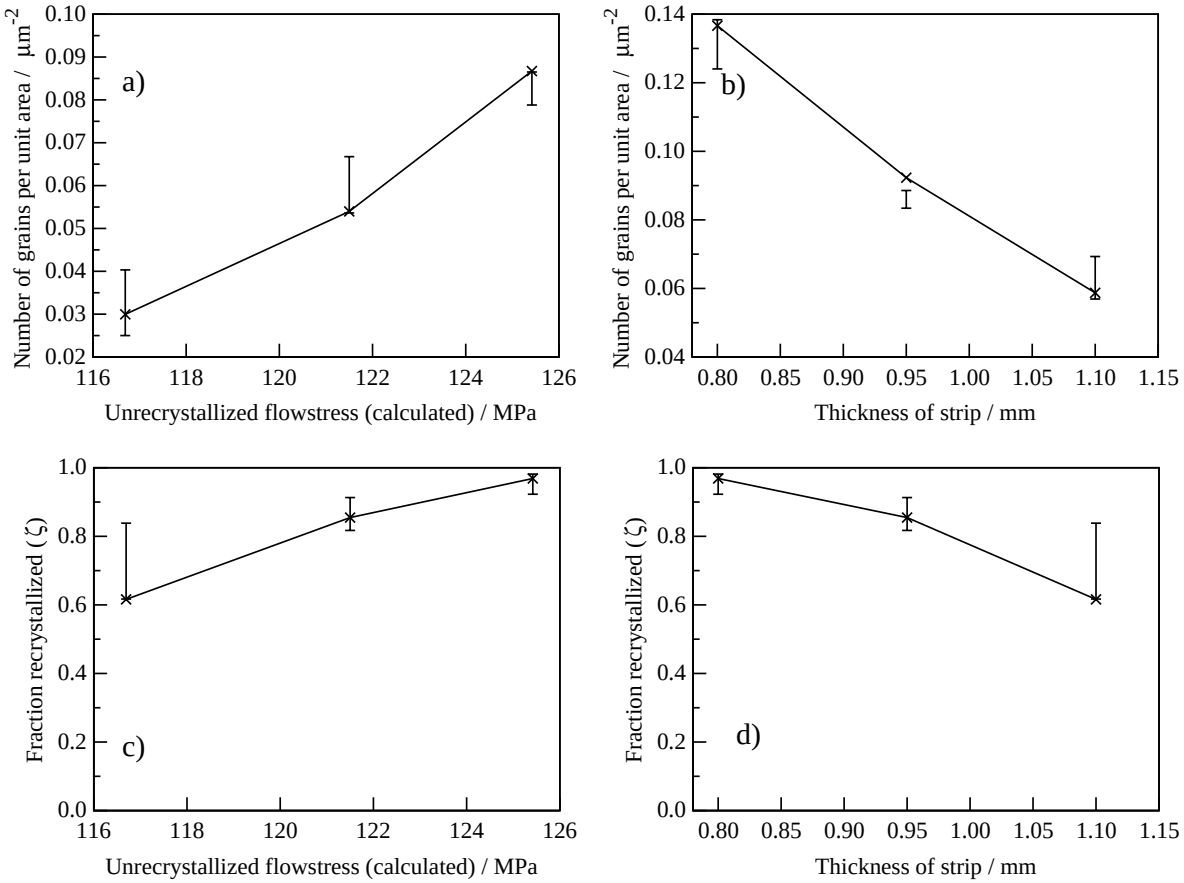

Fig. 6.19 Graphical representation of output from anisothermal recrystallization model trained on a type 904L stainless steel. Samples were annealed at a furnace temperature of 970 °C with $a = 0.0135$ for initial strip conditions illustrated. In all charts the solid line indicates the model's prediction and the error bars an experimental datapoint. **a)** Plot of Number of grains per unit area G_a against calculated flow stress (σ_f) in the unrecrystallized material. **b)** Plot of Number of grains per unit area G_a against gauge of material. **c)** Plot of fraction recrystallized (ζ) against calculated flow stress σ_f in the unrecrystallized material. **d)** Plot of fraction recrystallized (ζ) against gauge of material

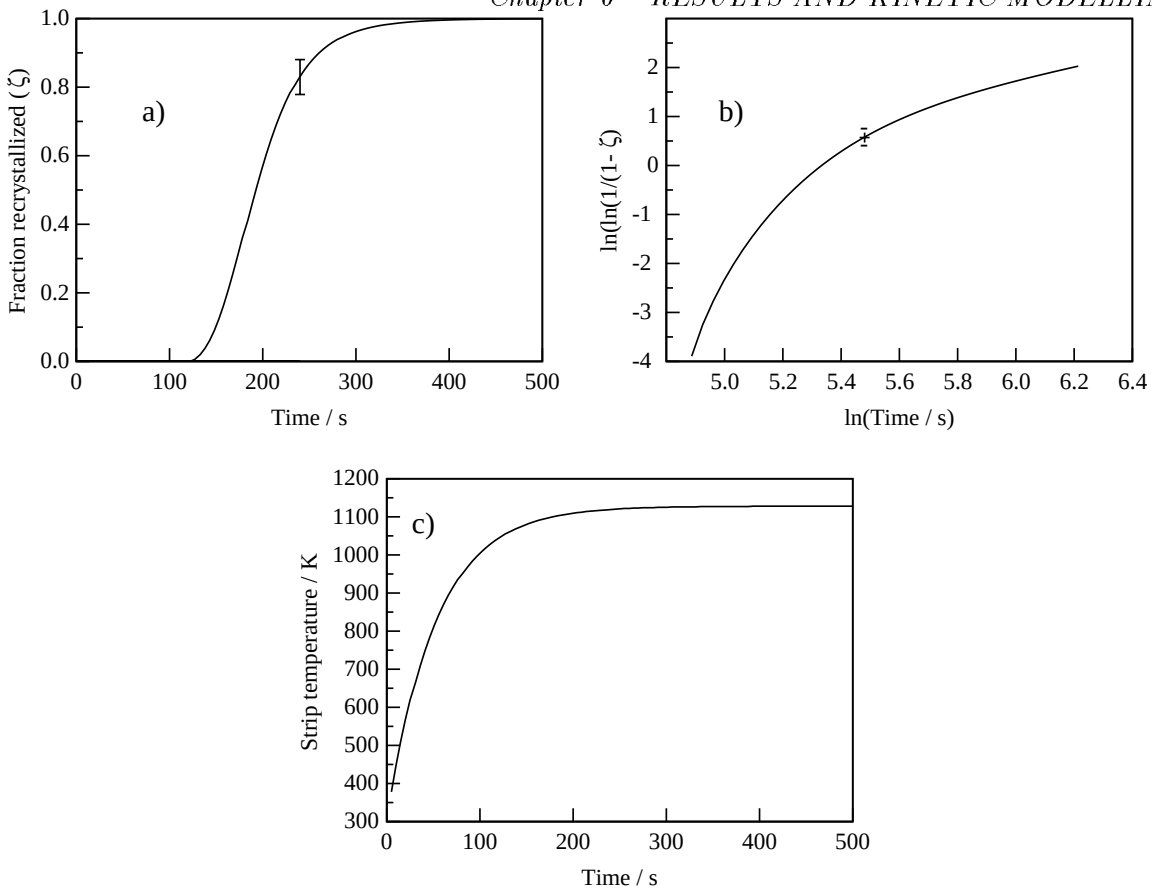

Fig. 6.20 Graphical representation of output from anisothermal recrystallization model trained on a type 904L stainless steel. Samples were annealed at a furnace temperature of 855 °C with $a = 0.0135$ for a 0.8 mm gauge strip of initial hardness 125.42 ± 3.6 HV (measured with a load of 5 kg). In all charts the solid line indicates the model's prediction and the error bars an experimental datapoint. **a)** Plot of ζ vs time showing classical sigmoidal shape. **b)** "Avrami plot" of $\ln(\ln(1/1\text{-}\zeta)))$ against $\ln(t)$. This plot does not show a distinct transition from $n = 4$ to $n = 1$ because the temperature of the strip is a function of annealing time, this further time factor blurs observation of the changeover from pseudo-random nucleation to site saturation. **c)** The variation of strip temperature with time (predicted).

6.8.3 Modelling results - type 254SMO stainless steel

Output from the model is given tabularly in Table 6.7 and graphically in figures 6.22 and 6.23.

6.8.3.2 Discussion of model for 254SMO stainless steel

The fit of the model is generally good across all rolling reductions and initial flow stresses with good transferability between different temperatures and heating rates. There are a few points which lie off the predicted curve. Notably, predictions for the sample annealed at 975 °C

T_f / °C	t / s	Final strip T / °C	Gauge / mm	Predicted G_a / μm^{-2}	Measured G_a / μm^{-2}	a	Flow stress / MPa
950‡	60	943	0.100	0.0944	0.095 ± 0.009	0.085	151.5 ± 6.0
950‡	60	943	0.125	0.0750	0.086 ± 0.005	0.085	149.9 ± 7.0
950‡	60	943	0.150	0.0413	0.043 ± 0.009	0.085	142.8 ± 5.6
950‡	60	943	0.210	0.0220	0.020 ± 0.006	0.085	136.1 ± 4.7
975‡	35	950	0.100	0.1071	0.103 ± 0.006	0.120	151.5 ± 6.0
975‡	35	950	0.125	0.0848	0.086 ± 0.009	0.120	149.9 ± 7.0
975‡	35	950	0.150	0.0475	0.051 ± 0.014	0.120	142.8 ± 5.6
975‡	35	950	0.210	0.0259	0.005 ± 0.002	0.120	136.1 ± 4.7

T_f / °C	t / s	Final strip T / °C	Gauge / mm	Predicted ζ	Measured ζ	a	Flow stress / MPa
950‡	60	943	0.100	0.952	0.96 ± 0.02	0.085	151.5 ± 6.0
950‡	60	943	0.125	0.874	0.92 ± 0.06	0.085	149.9 ± 7.0
950‡	60	943	0.150	0.507	0.75 ± 0.19	0.085	142.8 ± 5.6
950‡	60	943	0.210	0.200	0.24 ± 0.22	0.085	136.1 ± 4.7
975‡	35	950	0.100	0.931	0.95 ± 0.02	0.120	151.5 ± 6.0
975‡	35	950	0.125	0.838	0.78 ± 0.06	0.120	149.9 ± 7.0
975‡	35	950	0.150	0.476	0.54 ± 0.21	0.120	142.8 ± 5.6
975‡	35	950	0.210	0.188	0.06 ± 0.03	0.120	136.1 ± 4.7

Table 6.7: Comparison of model results with experimental results on a grade 254SMO stainless steel. All samples underwent a Newtonian heating regime ($T = T_f - ((T_f - T_R)\exp(-at))$) fully described by the given parameters a and T_f. *(The symbol ‡ next to a values of T_f denotes that this is a calculated value. In these cases a measured value was not available because the short annealing times used meant the temperature of the sample did not equilibrate)*

having a gauge of 0.21 mm lie off the measured values in all cases. The possible explanations for this are as follows; It may be that the model does not reflect the metallurgy of the sample (*e.g.* the nucleation rate calculation is not representative of the true mode of nucleation *etc.*). This is possible, however, in the absence of other plausible methods of nucleation and growth, it is not likely because the model is behaving well for the sample of gauge 0.21 mm annealed

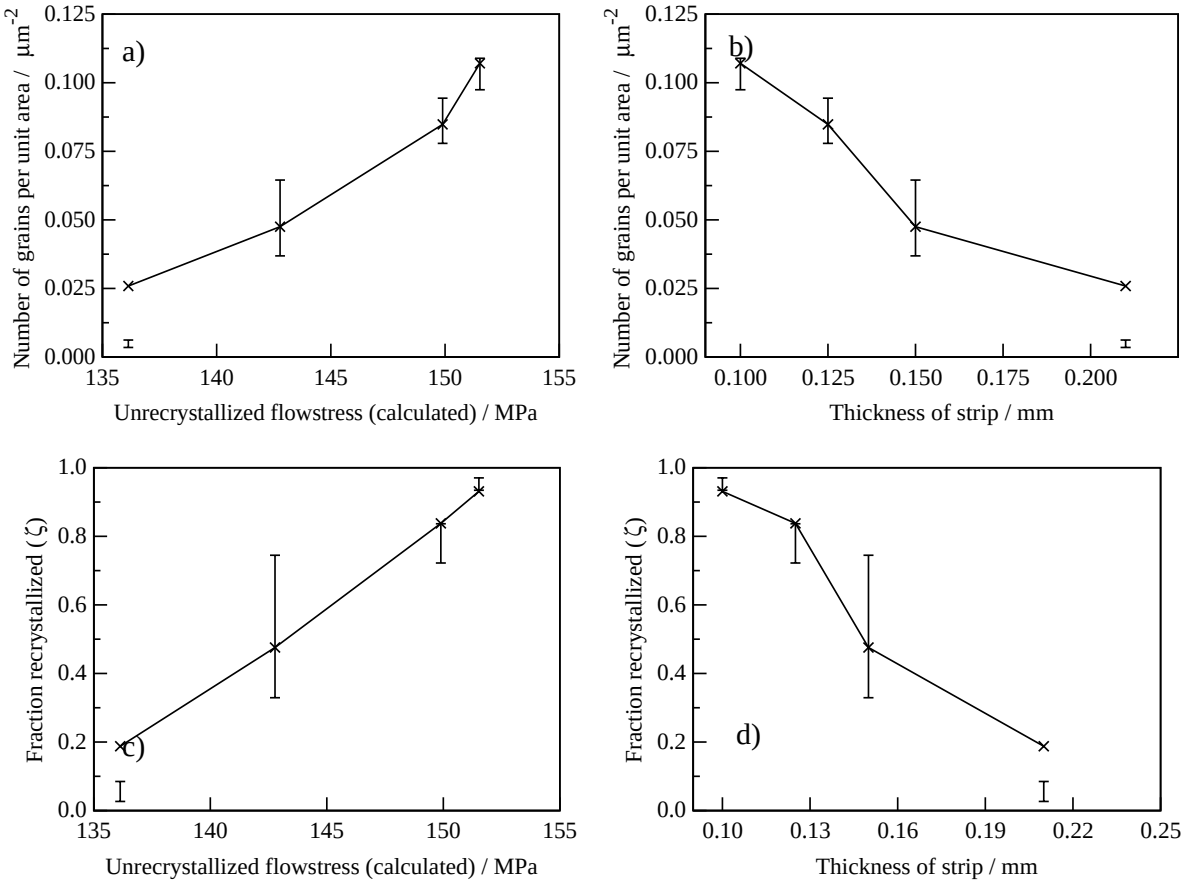

Fig. 6.21 Graphical representation of output from anisothermal recrystallization model trained on a type 254SMO stainless steel. Samples were annealed at a furnace temperature of 975 °C with $a = 0.120$ for initial strip conditions illustrated. In all charts the solid line indicates the model's prediction and the error bars an experimental datapoint. **a)** Plot of Number of grains per unit area G_a against calculated flow stress σ_f in the unrecrystallized material. **b)** Plot of Number of grains per unit area G_a against gauge of material. **c)** Plot of fraction recrystallized (ζ) against calculated flow stress σ_f in the unrecrystallized material. **d)** Plot of fraction recrystallized (ζ) against gauge of material

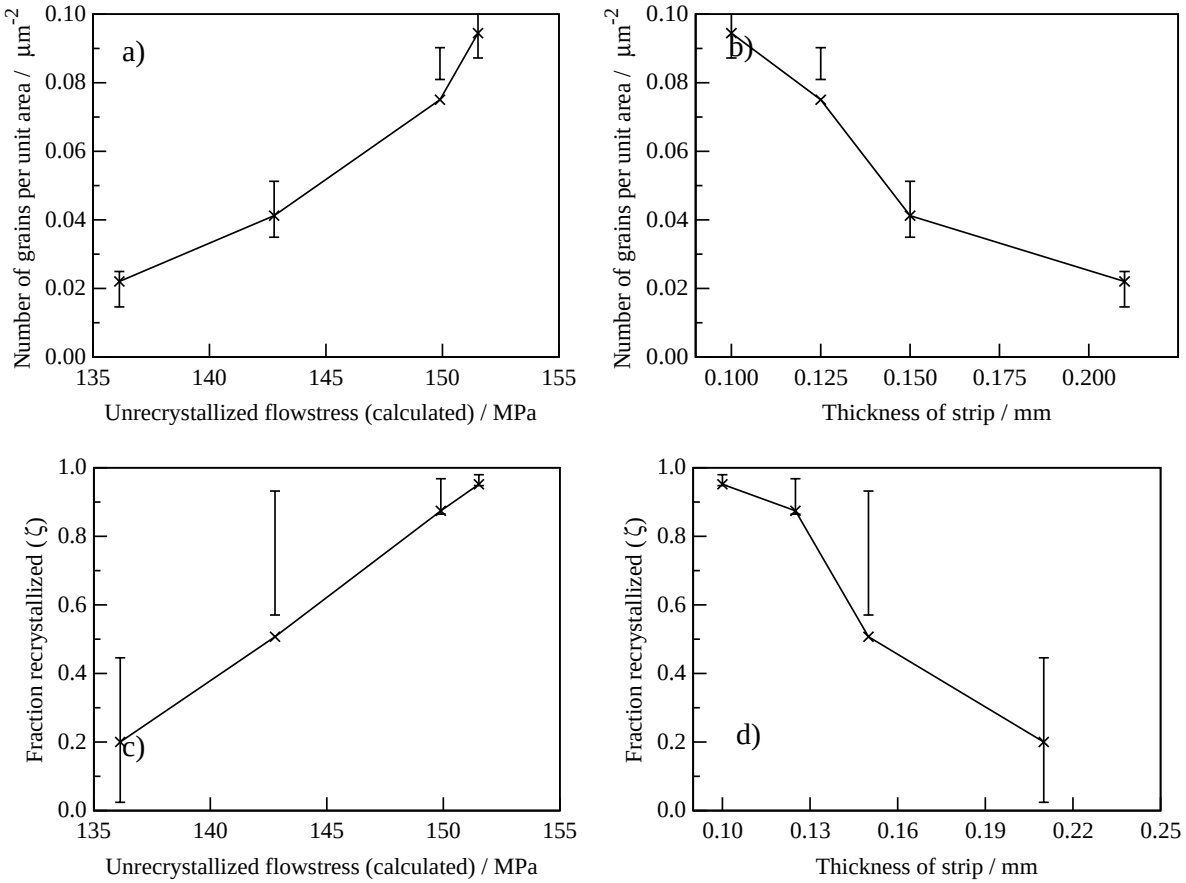

Fig. 6.22 Graphical representation of output from anisothermal recrystallization model trained on a type 254SMO stainless steel. Samples were annealed at a furnace temperature of 950 °C with $a = 0.085$ for initial strip conditions illustrated. In all charts the solid line indicates the model's prediction and the error bars an experimental datapoint. **a)** Plot of Number of grains per unit area G_a against calculated flow stress σ_f in the unrecrystallized material. **b)** Plot of Number of grains per unit area G_a against gauge of material. **c)** Plot of fraction recrystallized (ζ) against calculated flow stress σ_f in the unrecrystallized material. **d)** Plot of fraction recrystallized (ζ) against gauge of material

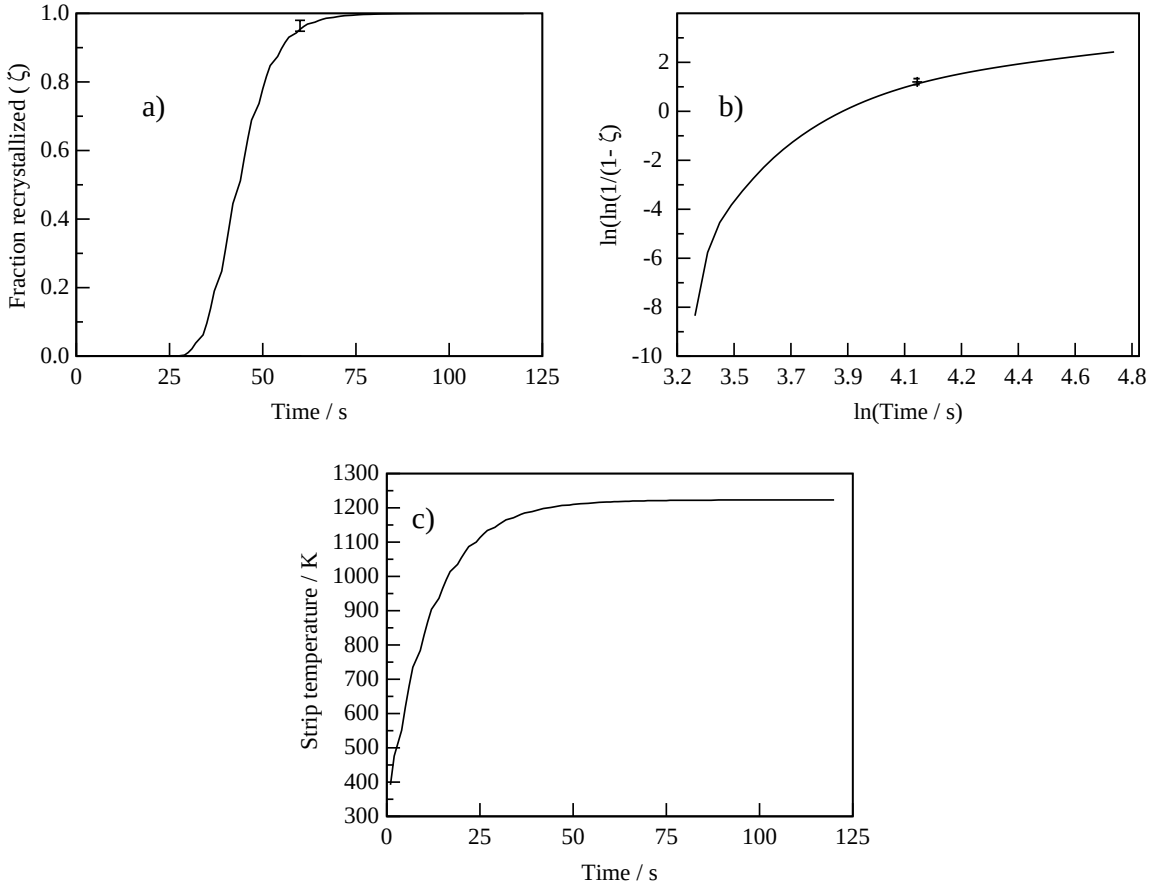

Fig. 6.23 Graphical representation of output from anisothermal recrystallization model trained on a type 254SMO stainless steel. Samples were annealed at a furnace temperature of 950 °C with $a = 0.085$. In all charts the solid line indicates the model's prediction and the error bars an experimental datapoint. **a)** Plot of ζ vs time showing classical sigmoidal shape. **b)** "Avrami plot" of $\ln(\ln(1/1\text{-}\zeta)))$ against $\ln(t)$. This plot does not show a distinct transition from $n = 4$ to $n = 1$ because the temperature of the strip is a function of annealing time, this further time factor blurs observation of the changeover from pseudo-random nucleation to site saturation. **c)** The variation of strip temperature with time (predicted).

at 950 °C . The second possible reason is that 0.21 mm material in the composite sample had poor thermal contact with the rest of the sample, hence it many have experienced a lower temperature due to a slower heating rate. This would explain the anomalously low values of G_a and ζ.

The second point which does not match predicted values is from the sample annealed at 950 °C of gauge 0.125 mm for G_a and gauge 0.15 mm for ζ. Since the material was so thin, it was very difficult to obtain an accurate value of flow stress, as illustrated in Fig. 6.24.

There is a good deal of overlap between expected hardnesses of each gauge, and within

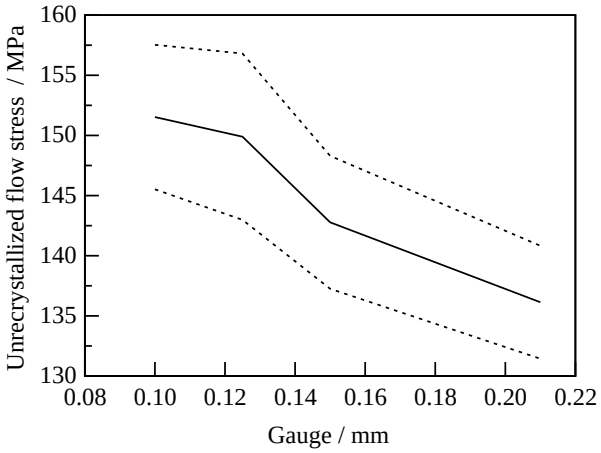

Fig. 6.24 Variation of unrecrystallized flow stress with gauge of material. Measured as an average of 12 micro-hardness indents at a load of 200g traversing the width of the sample

each gauge there was a lot of variation in the measurement.

Moreover the samples were hard to electropolish because of the tendency to dissolve more at the edges of the sample (Fig. 6.25), making edge observations very difficult. This effect will be most accentuated for thin gauge samples such as 254SMO.

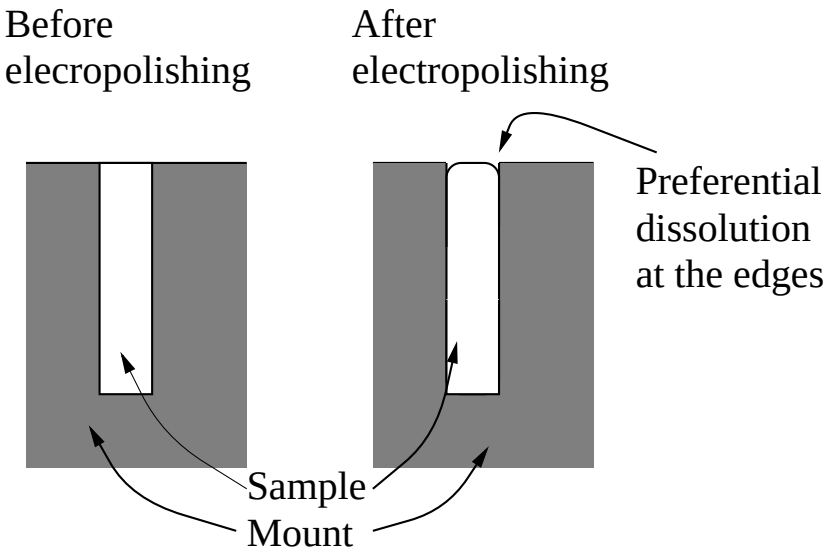

Fig. 6.25 Illustration of the tendency of the process of electropolishing to give preferential dissolution of the sample at the edges.

These experimental difficulties will partially explain any deviation from theory. However, despite this, the trends in the data are reflected well in the model. Moreover as illustrated in figure 6.26, the model is giving meaningful trends of fraction recrystallized against time and G_a against time.

This model and Cahn type kinetics in general provide an accurate indication of trends in the data. They not only provide a good qualitative grasp on the problem, but moreover provide accurate and meaningful quantitative output and as such, should be of use to the metallurgist.

6.8.4 Modelling results - type 304L stainless steel

Output from the model is given tabularly in Table 6.8 and graphically in Figures 6.26 to 6.28.

6.8.4.1 Discussion of model for 304L stainless steel

The fit of the model is acceptable (although not as good as either 904L or 254SMO) across most rolling reductions and initial flow stresses and shows good transferability between different temperatures and heating rates.

However, the fit in this case is not as good as for 254SMO or 904L, and in fact in a few cases (notably for the sample annealed at 960 °C of thickness 0.26 mm) the model is predicting incorrectly by a factor of up to three!

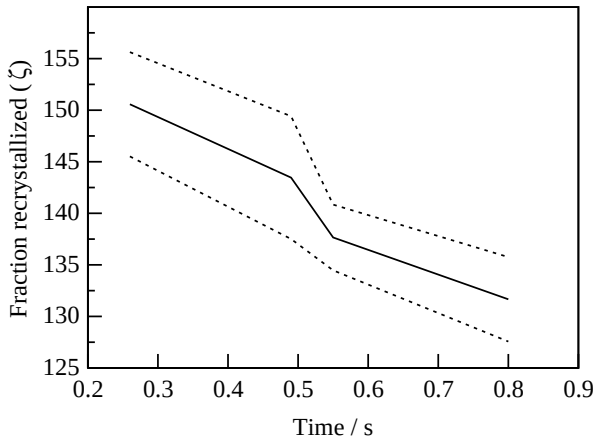

Fig. 6.28 Variation of unrecrystallized flow stress with gauge of material. Measured as an average of 12 micro-hardness indents at a load of 200g traversing the width of the sample

As with grade 254SMO, there is a good deal of overlap between hardnesses values for each gauge because within each gauge there was a lot of variation in the measurement.

Furthermore the problem of preferential dissolution at the edges was also present in 304L (see figure 6.28), however this was not as pronounced as in 254SMO because the samples of 304L were, in general, of a thicker gauge than 254SMO.

T_f / °C	t / s	Final strip T / °C	Gauge / mm	Predicted G_a / μm^{-2}	Measured G_a / μm^{-2}	a	Flow stress / MPa
822‡	120	795	0.42	0.166	0.18 ± 0.04	0.015	148.0 ± 3.5
822‡	120	795	0.49	0.091	0.07 ± 0.01	0.015	143.5 ± 6.0
822‡	120	795	0.55	0.040	0.04 ± 0.01	0.015	137.7 ± 3.2
822‡	120	795	0.80	0.014	0.01 ± 0.01	0.015	131.7 ± 4.1
960‡	80	822	0.26	0.711	0.35 ± 0.04	0.027	150.6 ± 5.1
960‡	80	822	0.49	0.336	0.28 ± 0.03	0.027	143.5 ± 6.0
960‡	80	822	0.55	0.233	0.25 ± 0.02	0.027	137.7 ± 3.2
960‡	80	822	0.80	0.135	0.14 ± 0.03	0.027	131.7 ± 4.1

T_f / °C	t / s	Final strip T / °C	Gauge / mm	Predicted ζ	Measured ζ	a	Flow stress / MPa
822‡	120	795	0.100	0.95	0.97 ± 0.02	0.015	148.0 ± 3.5
822‡	120	795	0.125	0.87	0.92 ± 0.06	0.015	143.5 ± 6.0
822‡	120	795	0.150	0.51	0.75 ± 0.19	0.015	137.7 ± 3.2
822‡	120	795	0.210	0.20	0.28 ± 0.22	0.015	131.7 ± 4.1
960‡	80	822	0.100	0.93	0.95 ± 0.02	0.027	150.6 ± 5.1
960‡	80	822	0.125	0.84	0.78 ± 0.06	0.027	143.5 ± 6.0
960‡	80	822	0.150	0.48	0.54 ± 0.21	0.027	137.7 ± 3.2
960‡	80	822	0.210	0.19	0.06 ± 0.03	0.027	131.7 ± 4.1

Table 6.8: Comparison of model results with experimental results on a grade 304L stainless steel. All samples underwent a Newtonian heating regime ($T = T_f - ((T_f - T_R)\exp(-at))$) fully described by the given parameters a and T_f. *(The symbol ‡ next to a values of T_f denotes that this is a calculated value. In these cases a measured value was not available because the short annealing times used meant the temperature of the sample did not equilibrate)*

The main reason for the comparatively poor performance of this model was the interrelationship between fraction recrystallized and nucleation rate. As can be seen in figure 6.28 b), there is a clear transition from $n = 1$ to $n = 4$. Of critical importance is the fact that *this transition occurs approximately half way through the recrystallization process.* This will have a profound effect on the applicability of the Scheil approximation which must be addressed;

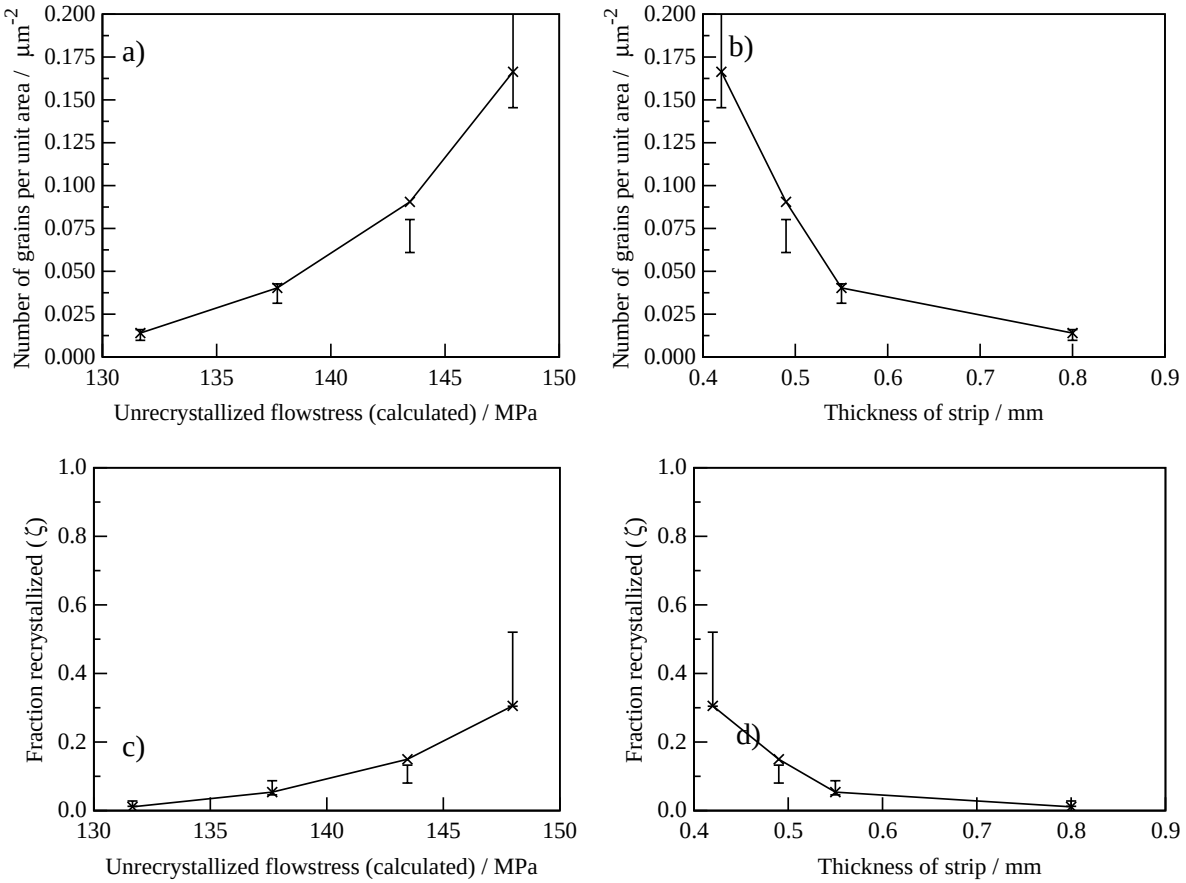

Fig. 6.26 Graphical representation of output from anisothermal recrystallization model trained on a type 304L stainless steel. Samples were annealed at a furnace temperature of 910 °C with $a = 0.015$ for initial strip conditions illustrated. In all charts the solid line indicates the model's prediction and the error bars an experimental datapoint. **a)** Plot of Number of grains per unit area G_a against calculated flow stress σ_f in the unrecrystallized material. **b)** Plot of Number of grains per unit area G_a against gauge of material. **c)** Plot of fraction recrystallized (ζ) against calculated flow stress σ_f in the unrecrystallized material. **d)** Plot of fraction recrystallized (ζ) against gauge of material

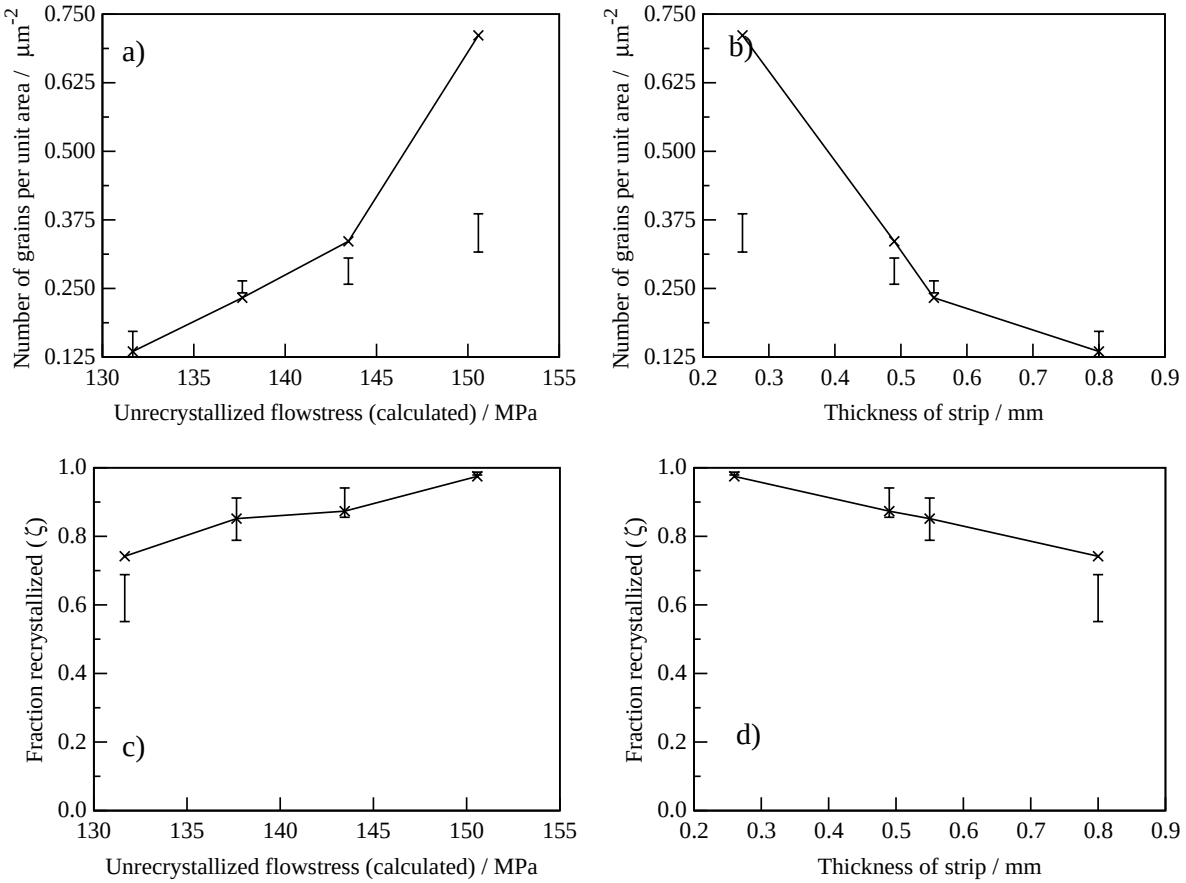

Fig. 6.27 Graphical representation of output from anisothermal recrystallization model trained on a type 304L stainless steel. Samples were annealed at a furnace temperature of 960 °C with $a = 0.027$ for initial strip conditions illustrated. In all charts the solid line indicates the model's prediction and the error bars an experimental datapoint. **a)** Plot of Number of grains per unit area G_a against calculated flow stress σ_f in the unrecrystallized material. **b)** Plot of Number of grains per unit area G_a against gauge of material. **c)** Plot of fraction recrystallized (ζ) against calculated flow stress σ_f in the unrecrystallized material. **d)** Plot of fraction recrystallized (ζ) against gauge of material

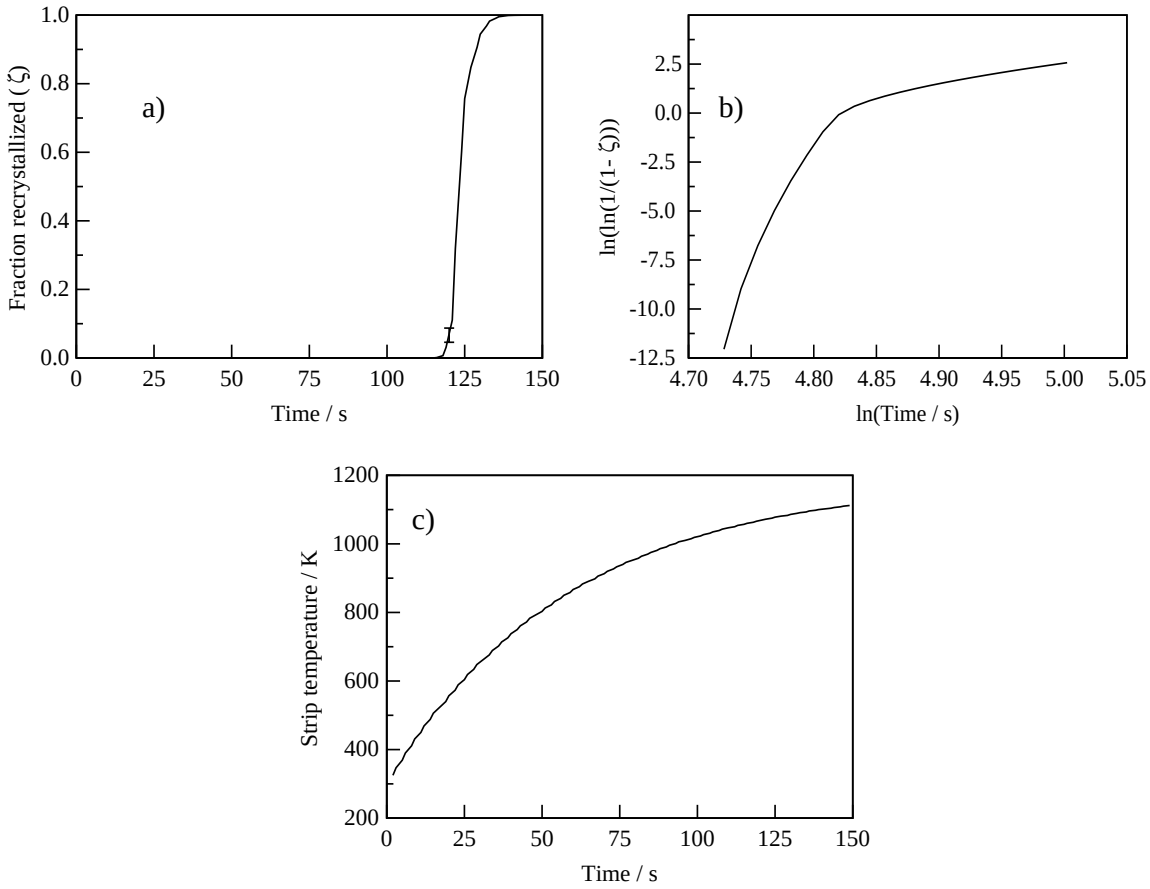

Fig. 6.28 Graphical representation of output from anisothermal recrystallization model trained on a type 304L stainless steel. Samples were annealed at a furnace temperature of 910 °C with $a = 0.015$. In all charts the solid line indicates the model's prediction and the error bars an experimental datapoint. **a)** Plot of ζ vs time showing classical sigmoidal shape. **b)** "Avrami plot" of $\ln(\ln(1/1\text{-}\zeta)))$ against $\ln(t)$. This plot does not show a distinct transition from $n = 4$ to $n = 1$ because the temperature of the strip is a function of annealing time, this further time factor blurs observation of the changeover from pseudo-random nucleation to site saturation. **c)** The variation of strip temperature with time (predicted).

however, firstly experimental evidence that site saturation is not occurring must be gathered.

Evidence for the lack of site saturation in all the samples of 304L stainless steel is available by inspection of the micrographs shown in Fig. 6.29.

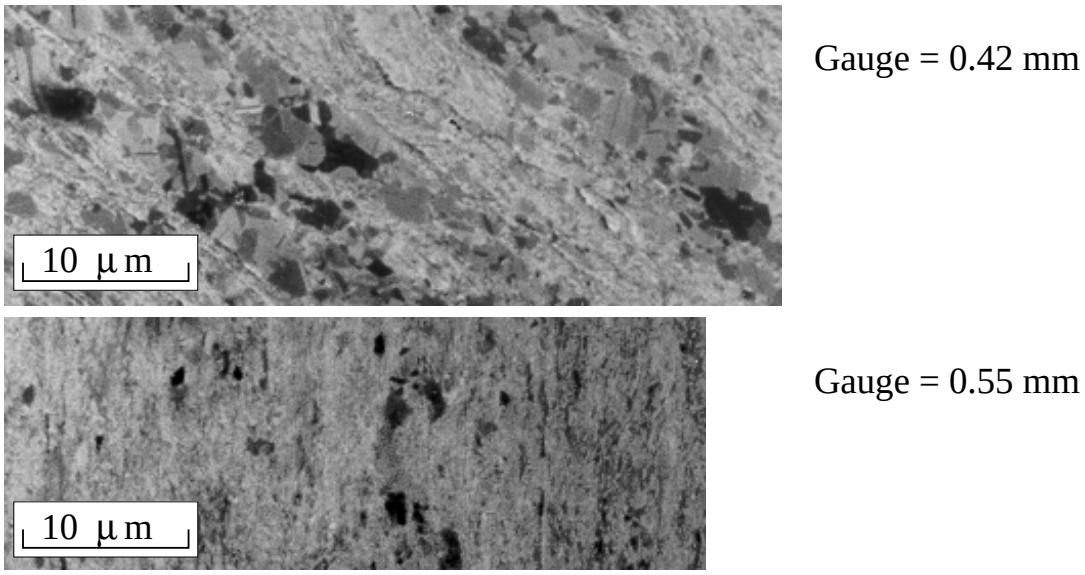

Fig. 6.29 Samples of 304L stainless steel annealed for 120 s at a furnace temperature (T_f) of 910 °C . The sample of gauge 0.42 mm shows clear bands of recrystallized material, however, these bands are not completely filled with recrystallized grains, therefore it is unlikely that site saturation has occurred, consequently the Scheil approximation may be invalid. The sample of gauge 0.55 mm shows only a few isolated grains; site saturation has not occurred and therefore the Scheil approximation will not apply.

The trends in ζ in the experimental data are reflected in the model, but G_a proved to be impossible to estimate, because the isokinetic assumption is not valid in this case. There is currently no mathematical modelling technique available to cope with this problem. For this grade of steel, therefore it would be advisable not to pay credence to calculated values of G_a although there is some success in predicting the value of ζ. The model does however warn the observer that G_a calculations will be unreliable. By observing plots of $\ln(\ln(1/(1\text{-}\zeta)))$ against $\ln(t)$ we see that the value of n changes during the observable progress of the recrystallization procedure. This means that site saturation is also occurring during the observable progress of the recrystallization. This observation of the model's progress implies that the calculated values of G_a are unreliable without comparison with experimental observation.

6.9 Transferability and comparison of models

From §6.7 and §6.8, it is clear that the Cahn approach to transformation kinetics is appli-

cable not only over a range of temperatures, heating rates and initial microstructures within one grade of steel, it is also applicable across a range of different stainless steels compositions. Because the chemistry of the steels is known, it may eventually be possible to link the kinetic theory present in the model to the chemistry of the steels, thereby going some way to produce a model of recrystallization which is truly transferable across all grades of stainless steels.

To perform this comparison, the thermodynamic fitting factor used to train the model must be compared. As described in §6.6.1, these fitting factors were:

ΔS_{act} - The difference in entropy between the activated and unrecrystallized states.

ΔH_{act} - The difference in enthalpy between the activated and unrecrystallized states.

G_C - The driving force independent activation energy of nucleation.

n_G - The exponent of dependence between ΔG and activation energy of nucleation.

ν_T - The temperature independent attempt frequency of nucleation.

As described by the equations:

$$\Upsilon = \delta_\varsigma \nu \exp\left(\frac{\Delta S_{act}}{R}\right) \exp\left(-\frac{\Delta H_{act}}{RT}\right)\left[1 - \exp\left(-\frac{\Delta G}{RT}\right)\right] \tag{6.22}$$

$$G^* = G_C \Delta G^{-n_G} \tag{6.27}$$

$$\dot{N} = \nu_T T \exp\left(-\frac{G^*}{RT}\right) \tag{6.24}$$

The values of the above thermodynamic fitting factors are given in Table 6.9 below.

	302	254SMO	904L	304L
ν_T / $s^{-1}K^{-1}$	1.7×10^{102}	8.0×10^{50}	1.3×10^{152}	8.0×10^{120}
G_C / J mol^{-1}	206000†	1320000	3540000	2450000
n_G	0.2†	0.3	0.22	0.055
ΔH_{act} / kJ mol^{-1}	450	530	350	250
ΔS_{act} / kJ mol^{-1} K^{-1}	6.8×10^{15}	2.6×10^{16}	1.8×10^{9}	7.0×10^{4}

Table 6.9: Values of thermodynamic fitting factors used in the training of the model for each steel. † *For the 302 stainless steel, data were only obtainable for on set of initial conditions i.e. a gauge of 0.8mm and initial hardness of 464.5 HV. This meant that a true value of* n_G *cannot be obtained,* $n_G = 0.2$ *is an estimate and thereby* $G_C = 2060000\ J\ mol^{-1}$ *will only be correct if the estimated value of* n_G *is accurate*

6.9.1 Discussion of thermodynamic fitting factors

Since thermodynamic fitting factors such as ΔH_{act} have physical meaning, this provides a method of comparison across each of the models produced. For instance ΔH_{act} is the difference in enthalpy (heat energy) between the recrystallized and activated states (Schematically illustrated as Q in figure 2.3). This process is similar the process of self diffusion (*c.f.* §6.1), wherein an atom hops from a lattice point into an activated position between lattice points and subsequently into an adjacent vacant lattice point. It is therefore intuitively obvious that the value of ΔH_{act} will be of the order of Q.

The activation energy for self diffusion in pure α iron (Kaye and Layby 1986) is quoted as 286 kJ mol^{-1} and in pure γ iron as 291.3 ± 4.5 (Oikawa 1982). In the above study only 304L stainless steel has a value of ΔH_{act} below this at 250 kJ mol^{-1}. Although for stainless steels and other high alloy metals the energy of self diffusion will be higher that that of pure iron because of precipitates and solute atom pinning and other interactions between the alloying elements and the grain boundaries, this cannot, however, account for energies as high as 450 kJ mol^{-1} as observed in the case of the 302 steel.

The values for G_C and n_G are of the order of magnitude expected, however it is not possible to make any direct comparison because of the different behaviours present in each steel (*i.e.* martensitic recession in the case of 302 and lack of site saturation in the case of 304L). In the case of n_G the expected value lying between 0 and 2 was observed in all cases.

6.10 Summary of kinetics model and thermodynamic factors

The Cahn kinetics model has proven to predict accurate annealing curves for fraction recrystallized (ζ), number of grains per unit area (G_a) and grain size over a range of different rolling reductions, stored energies furnace temperatures and heating rates. The model is based physically meaningful theories which are mathematically sound. As such this theory has been proven to be a good starting point towards the ultimate goal of a physical model which, through metallurgical understanding, is truly transferable across different grades of steel.

It is likely, however that the figures for the thermodynamic fitting factors do not reflect accurately enough the complex interrelationships between nucleation and growth. Problems such as different modes of nucleation must be addressed before the transferability of the model can be guaranteed.

This said, the model as it stands represents a significant advance towards providing a physical thermodynamic description of the process of recrystallization.

CHAPTER 7

ASSESSMENT OF INDUSTRIAL DATA

7.1 Applicability of neural network approach.

There are a number of studies in the literature involving the modelling of annealing and heat treatment processes using neural network approaches (*e.g.* Kusiak and Wajda 1999). However, most of these have dealt with purely research tasks, for example, prediction of the time taken to achieve 50% recrystallization. The work presented in chapter five indicates that, given a set of input variables which completely describe the system, neural networks can model highly complicated phenomena such as anisothermal annealing.

However, the model described in chapter five is specific to data from controlled laboratory experiments. The neural network used (MacKay 1992) has been designed to cope with interpolation of noisy data, as would be produced during the industrial process of annealing.

In industrial practice thermocouples are embedded in the walls of the furnace to monitor the temperature. This indicated temperature is almost certain to differ from the true temperature profile of the furnace, but using this reading, knowing the gauge of the strip and comparing these with metallurgical knowledge and past experience, the speed at which the strip should pass through the furnace may be estimated.

This situation is an ideal candidate for neural network modelling. A number of sets of data from an industrial furnace were therefore analysed using neural network techniques.

7.2 Initial model

Data were supplied from an annealing furnace at Avesta Polarit Ltd., Sheffield, U.K. These data consisted of a coil composition code, strip gauge† and width, hot-band gauge‡, grade of steel, time of processing, position on the strip at which the sample was taken (*i.e.* head, middle or tail) and an output. In this instance there were two different outputs monitored:

i) Final hardness of the strip.

ii) Final grain size of the finished strip.

The hardness was expressed as a Vickers hardness value derived from measurements of Rockwell hardness and the grain size was expressed as a mean linear intercept determined

† *Gauge*, in this instance is the thickness of the strip.

‡ *Hot-band gauge* is the gauge of material after the hot rolling process but before cold rolling.

using an ultra-sonic technique. All measurements were made on site at the Avesta Polarit laboratories.

7.2.1 Problems with dataset

The ultrasonic measuring device works by monitoring the frequencies of ultrasound vibrations which are reflected from within the sample. The instrument was accurate to within approximately 1 ASTM number. There were also problems with ascertaining the exact speed of the strip and temperature at which the different zones of furnace were set; the nominal temperature settings are indicated in Table 7.1 and the strip speed is given in Fig. 7.1, both as a function of strip gauge.

Gauge / mm	Temperature / °C								
	Zone 1	Zone 2	Zone 3	Zone 4	Zone 5	Zone 6	Zone 7	Zone 8	Zone 9
0.75 – 4.10	1100	1120	1100	1180	1200	1180	1170	1190	1170
0.64 – 0.74	1100	1120	1100	1160	1180	1160	1150	1170	1150
0.38 – 0.64	800	800	800	1160	1180	1160	1150	1170	1150

Table 7.1: The variation of furnace temperature setting with gauge for the annealing furnace.

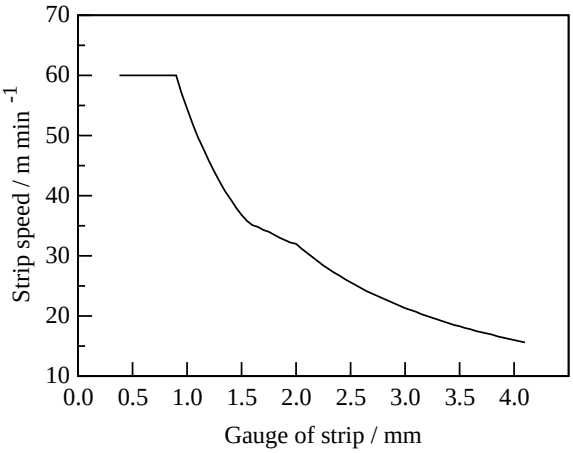

Fig. 7.1) The schematic variation of strip speed with gauge for furnace at Avesta Polarit Ltd.

Modern commercial furnaces are designed to operate continuously, *i.e.* the end of one strip is welded to the beginning of the next. This enables the continuous running of the furnace with a zero stop time for rethreading between coils, thus maximising productivity. However, this frequently means that two strips of different width and gauge will be welded together to pass through the furnace. Different strip geometries may then be in the furnace at the same time. To cope with this, the furnace is run at the settings corresponding to the hotter and slower specifications. This is to ensure complete recrystallization. These non-ideal

situations constitute a large proportion of the experimental data available since most samples were acquired at strip ends. The relative difference between the hot-band gauge and strip gauge on annealing is an indication of cold rolling reduction and hence, indirectly, stored energy. The input dataset used in this analysis therefore consisted of:

i) A set of nominal furnace temperatures.

ii) A line speed chosen to allow for any possible variations in gauge.

iii) Strip gauge

iv) Strip width

v) Hot-band gauge

7.2.2 Results from initial model

The results given in this section are for a neural network trained across all different grades irrespective of their chemistry. The neural network used was the "Bigback5" neural network developed by MacKay (1992), as outlined in chapter 3 and illustrated in chapter 5. The dataset used has 524 rows of data each consisting of the following information:

Column 1 - Width of strip in mm

Column 2 - Hot-band gauge in mm

Column 3 - Line gauge in mm (the expected gauge of the material)

Column 4 - Test gauge in mm (the gauge of the material measured after annealing)

Column 5 - Strip speed in m min^{-1}

Columns 6–14 - Indicated temperature of furnace zones 1–9 (Fig. 1.8) in °C

Columns 15–26 - Indicators of stainless steel grade

Column 27 - Output (*i.e.* hardness in HV or grain size in μm)

Columns 15 to 26 effectively define the composition of the stainless steel, using a single 1 and eleven zeros to make a unique identification. The grades investigated and their corresponding column numbers are given in Table 7.2.

A model was first trained to predict recrystallized hardness from the input data described herewith. The minimum, maximum and standard deviation for each variable are given in Table 7.3.

The optimum committee consisted of two neural networks of two and three hidden units, example outputs are given in Fig. 7.2.

It can be seen from Fig. 7.2a), that the fit of the committee model to the experimental data is moderately good. However there are a few points of concern. Firstly the models chosen

Column number	15	16	17	18	19	20
Grade of steel	301AJ	302AS	302XD	304AB	304LP	304LT

Column number	21	22	23	24	25	26
Grade of steel	316VO	316XF	316ZA	320XB	321AA	316VO

Table 7.2: Different grades of stainless steel studied as part of the first neural network model.

are both relatively simple (two and three hidden units) because the test error and log predictive error were a minimum at an unusually low number of hidden units (*c.f.* Lalam (2000), Cole (2000)). However, the plot of the perceived noise in the output (σ_ν) against number of hidden units follows the expected trend.

To better understand the trends observed in these graphs, values of partial correlation co-efficients (σ_w) were compared. The results are given in Fig. 7.3

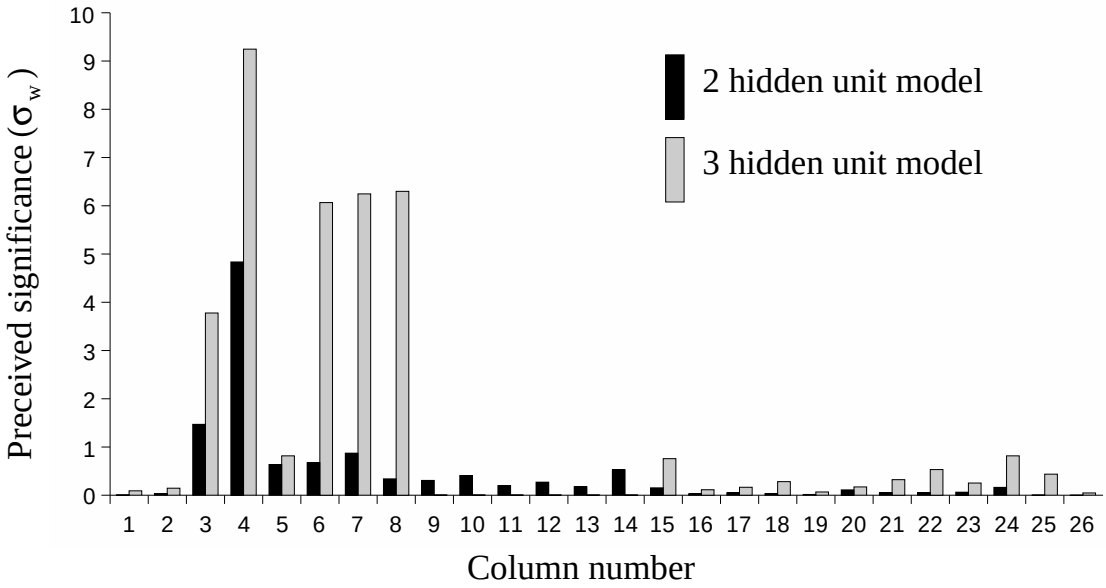

Fig. 7.3 The perceived significance (σ_w) for each input in the first industrial neural network model trained to predict hardness. The subject of each column is given in Table 7.3.

It should be noted that for both models, strip width and hot-band gauge have a low significance. The process of recrystallization occurs because the cold rolling process introduces defects into the crystal, these defects provide the driving force for recrystallization (*c.f.* §1.4). In general, the more deformation has been applied to the steel, the greater this driving force will be. The rolling reduction (and hence the amount of deformation) is a function of gauge and

Column	Minimum	Maximum	Mean	Standard Deviation
1	1019.00	1561.00	1246.91	195.72
2	2.52	6.14	4.38	1.08
3	0.46	4.04	1.67	0.81
4	0.48	4.12	1.67	0.82
5	16.00	60.00	38.62	13.29
6	800.00	1100.00	1095.42	36.82
7	800.00	1120.00	1115.11	39.27
8	800.00	1100.00	1095.42	36.82
9	1160.00	1180.00	1178.70	4.93
10	1180.00	1200.00	1198.70	4.93
11	1160.00	1180.00	1178.70	4.93
12	1150.00	1170.00	1168.70	4.93
13	1170.00	1190.00	1188.70	4.93
14	1150.00	1170.00	1168.70	4.93
15	0.0000	1.0000	0.0153	0.1227
16	0.0000	1.0000	0.0210	0.1435
17	0.0000	1.0000	0.4427	0.4972
18	0.0000	1.0000	0.0782	0.2688
19	0.0000	1.0000	0.0038	0.0617
20	0.0000	1.0000	0.2099	0.4076
21	0.0000	1.0000	0.0038	0.0617
22	0.0000	1.0000	0.0496	0.2174
23	0.0000	1.0000	0.1088	0.3117
24	0.0000	1.0000	0.0382	0.1918
25	0.0000	1.0000	0.0248	0.1557
26	0.0000	1.0000	0.0038	0.0617
27	132.00	187.00	158.42	7.15

Table 7.3: Table showing minimum, maximum, mean and standard deviation of for each variable, column 27 representing Vickers hardness.

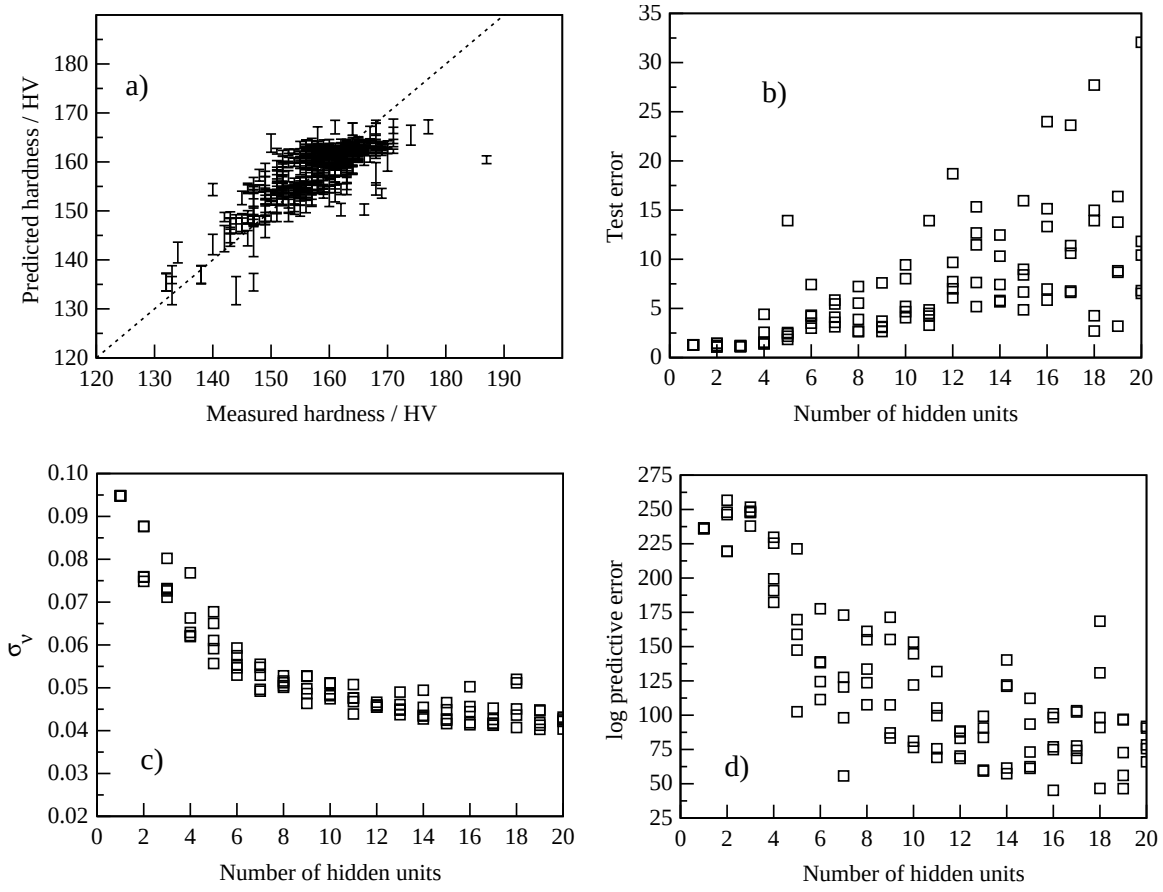

Fig. 7.2 Output from first neural network predicting hardness. **a)** Comparison of predicted hardness with measured hardness across the whole data-set (error bars include perceived noise in the data and fitting error). **b)** Shows the variation of test error with number of hidden units. **c)** Shows the variation of the perceived noise in the normalised hardness (σ_ν) as a function of number of hidden units. **d)** Shows the variation of the log predictive error with number of hidden units

hot-band gauge, therefore any model which deems the effect of these factors to be negligible does not reflecting the physical metallurgy of the problem.

Moreover, the significance of the temperatures in zones four to nine (Columns 9 to 14) were negligible according to the 3 hidden unit model. This model assigned a large significance to the temperature of the first three zones of the furnace (Columns 6 to 9), however it is obvious to the trained metallurgist that hardness cannot be completely insensitive to variations in furnace temperature.

Another important feature common to both models was that each column representing the grade of steel had a relatively low significance. This indicates that the steel grade is not being used to explain variations in hardness. Since grade of steel is known to have a significant

effect on annealing properties, it was decided to assess each grade of steel separately to see if this improves the analysis.

7.2.3 Analysis of individual grades

Considerable data were available for grades 302XD and 304LT. Separate neural networks were therefore trained for each grade; one to estimate hardness and the other to estimate grain size.

Since the alloy composition no longer featured as a variable the number of columns of input data was dramatically reduced. To further reduce this number, it was decided to remove data from the model pertaining to the furnace temperature in zones 3, 6 and 9. This was possible because temperatures in these zones were equal to those in zones 1, 4 and 7 respectively.

This produces a different set of input variables:

Columns 1–5 as before

Column 6 - The indicated temperature of furnace zone 1 (figure 1.8) in °C

Column 7 - The indicated temperature of furnace zone 2 (figure 1.8) in °C

Column 8 - The indicated temperature of furnace zone 4 (figure 1.8) in °C

Column 9 - The indicated temperature of furnace zone 5 (figure 1.8) in °C

Column 10 - The indicated temperature of furnace zone 7 (figure 1.8) in °C

Column 11 - The indicated temperature of furnace zone 8 (figure 1.8) in °C

Column 12 - Output data (either hardness in HV or grain size in μm)

Details of all the datasets used in this analysis are given in Table 7.4 a–d.

Typical compositions of a type 302 and 304L stainless steels are given in Table 7.5.

Grade	Maximum C	Maximum Mn	Maximum Si	Maximum P	Cr	Ni
302	0.15	2.00	1.00	0.045	18.00	9.00
304L	0.03	2.00	1.00	0.045	19.00	10.00

Table 7.5: Typical chemical compositions in wt.%

Training of the neural networks was carried out as described in chapter 5, in each case the optimum number of models in the committee was one, details of these models is given in Table 7.6. Output from each model is included in figures 7.4 to 7.7. In all the graphs described in this chapter, the error bars shown include both the fitting error and the perceived noise in the data.

Column	Minimum	Maximum	Mean	Std. Dev.
1	1019.00	1540.00	1230.44	191.50
2	2.52	6.14	4.20	1.09
3	0.46	4.04	1.51	0.83
4	0.48	4.12	1.51	0.83
5	16.00	60.00	41.79	14.39
6	800.00	1100.00	1093.10	45.09
7	800.00	1120.00	1112.64	48.10
8	1160.00	1180.00	1177.13	7.04
9	1180.00	1200.00	1197.13	7.04
10	1150.00	1170.00	1167.13	7.04
11	1170.00	1190.00	1187.13	7.04
12	5.90	9.70	8.1615	0.64

Table 7.4: a) Data used to characterise the grain-size model in type 302XD stainless steel

7.2.4 Discussion

Although the general trends in the data are well observed, there remain a large number of outliers. Furthermore the error bars on predicted data are very large, notably in the case of the hardness prediction for grade 304LT. The fact that the best committee in each case consisted of a single model is unusual. It was decided that these models provide an insufficient description of the recrystallization process and must be improved.

As was discussed in chapter 5, the major limiting factors on the ability of a neural network to predict systematic behaviour in a given system is insufficient information on the trends therein. Although the current neural network is able to detect noise in the data and train to ignore it, if noise is detected, this will lead to a very large error bar (as seen in figure 5.1). In a noisy system such as the industrial data presently being studied, often a large number of data must be gathered before the noise and trends may be identified by the model. It is possible that the datasets used in this analysis may be insufficient to do this.

There is also a possible source of error in the indicated value of temperature. Care was taken to ensure that when two strips were passing through the furnace attached to one another, the values of temperature and strip speed given to the neural network model was the hotter and

Column	Minimum	Maximum	Mean	Std. Dev.
1	1019.00	1540.00	1223.79	182.05
2	2.52	6.14	4.19	1.08
3	0.46	4.04	1.48	0.81
4	0.48	4.12	1.48	0.81
5	16.00	60.00	42.47	13.82
6	800.00	1100.00	1091.82	48.97
7	800.00	1120.00	1111.28	52.24
8	1160.00	1180.00	1177.64	6.47
9	1180.00	1200.00	1197.64	6.47
10	1150.00	1170.00	1167.64	6.47
11	1170.00	1190.00	1187.64	6.47
12	132.00	177.00	158.86	7.75

Table 7.4: b) Data used to characterise the hardness model in type 302XD stainless steel

Column	Minimum	Maximum	Mean	Std. Dev.
1	1025.00	1558.00	1265.59	233.02
2	2.62	6.14	4.61	1.05
3	0.76	3.97	1.94	0.77
4	0.77	4.07	1.94	0.79
5	16.20	57.00	33.26	10.33
6	1160.00	1180.00	1178.00	7.04
7	1180.00	1200.00	1198.00	7.04
8	1160.00	1180.00	1178.00	7.04
9	1150.00	1170.00	1168.00	7.04
10	1170.00	1190.00	1188.00	7.04
11	1150.00	1170.00	1168.00	7.04
12	151.00	170.00	161.4018	4.4891

Table 7.4: c) Data used to characterise the grain-size model in type 304LT stainless steel

Column	Minimum	Maximum	Mean	Std. Dev.
1	1025.00	1558.00	1288.00	217.58
2	2.6200	6.1400	4.3193	1.06
3	0.6700	3.9700	1.6996	0.78
4	0.7000	4.0500	1.6890	0.78
5	16.2000	60.00	37.7370	12.25
6	1160.00	1180.00	1178.00	6.03
7	1180.00	1200.00	1198.00	6.03
8	1160.00	1180.00	1178.00	6.03
9	1150.00	1170.00	1168.00	6.03
10	1170.00	1190.00	1188.00	6.03
11	1150.00	1170.00	1168.00	6.03
12	6.30	9.70	8.52	0.67

Table 7.4: d) Data used to characterise the hardness model in type 304LT stainless steel

Steel	302XD		304LT	
Output	Hardness	Grainsize	Hardness	Grainsize
Number of data	174	220	100	112
Number of hidden units	2	2	12	3

Table 7.6: Number of data and number of hidden units in final neural network model for each steel and target variable

slower values respectively. However, whilst this represents the indicated settings on the furnace, it does not represent the entire complexity of the system. If we consider two strips, strip S_1 having a gauge 0.65 mm and strip S_2 having a gauge of 0.60 mm. Under ideal conditions both of these strips will pass through the furnace at a speed of 60 m min^{-1}, however, strip S_1 will require a higher furnace temperature than strip S_2. If the two strips were passing through furnace simultaneously (*i.e.* they were welded together) then the temperature experienced would be the hotter of the two temperatures, *i.e.* the ideal temperature for strip S_1. If S_1 enters the furnace before S_2 then the furnace will already be at the correct temperature, the controls will not be altered as the head end of S_2 enters and the furnace. This means that S_2 will undergo the ideal furnace conditions for S_2. However if S_2 enters the furnace first, then initially the set furnace conditions will be the ideal conditions for S_2. When S_1 enters the furnace, the controls will be set to the hotter temperature required for S_2, however, the furnace cannot heat up instantly! Therefore the head end of strip S_1 will experience a gradient of temperatures spanning the ideal temperatures for either strip.

Because most of the data available was taken at either the head or the tail of the strip, simply using the indicated furnace temperatures into the neural network is likely to be insufficient to represent the systematic variation in temperature of the furnace.

A complete revision of the neural network input data was therefore undertaken.

7.3 Second industrial neural network model

To alleviate the problems described in §7.2.4 involving temperature variations, instead of giving the model direct information about the furnace temperatures, the model was given information about the gauge of the strip, the gauge of the adjacent strips and the position at which the measurement was taken. These data contain all the relevant information about how the furnace temperature controls were manipulated (table 7.1 and figure 7.1).

Again it was decided to train the models using data from only one grade of stainless steel at a time. The two grades chosen were 302XD and 304LT because, again, these two grades were the most populous in the dataset. To alleviate the possible problem of telling trends in the dataset from experimental noise, the number of rows in each dataset was increased by a

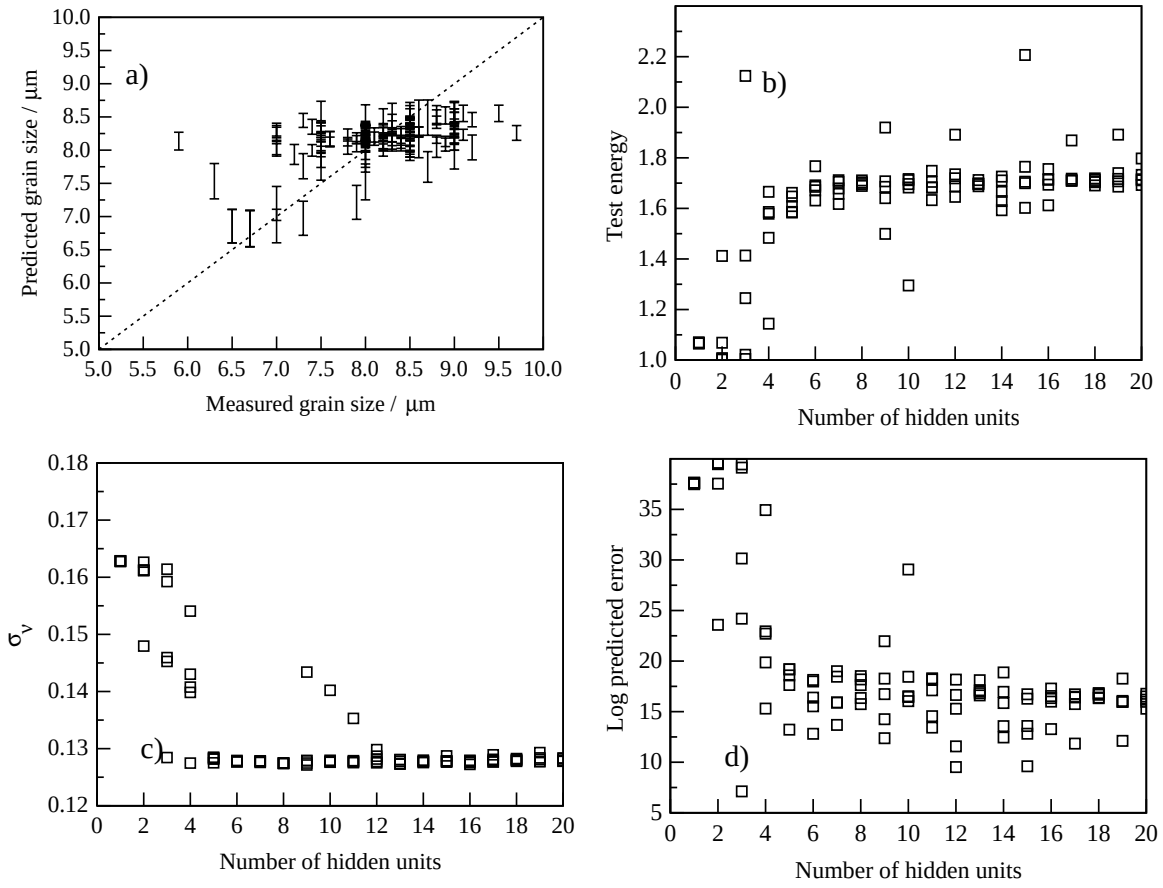

Fig. 7.4 Grain size model for type 302XD stainless steel. **a)** Predicted grain size against experimental grain size. **b)** Variation of test error as a function of number of hidden units. **c)** Perceived noise in the data (σ_ν) as a function of number of hidden units. **a)** The log predictive error as a function of number of hidden units

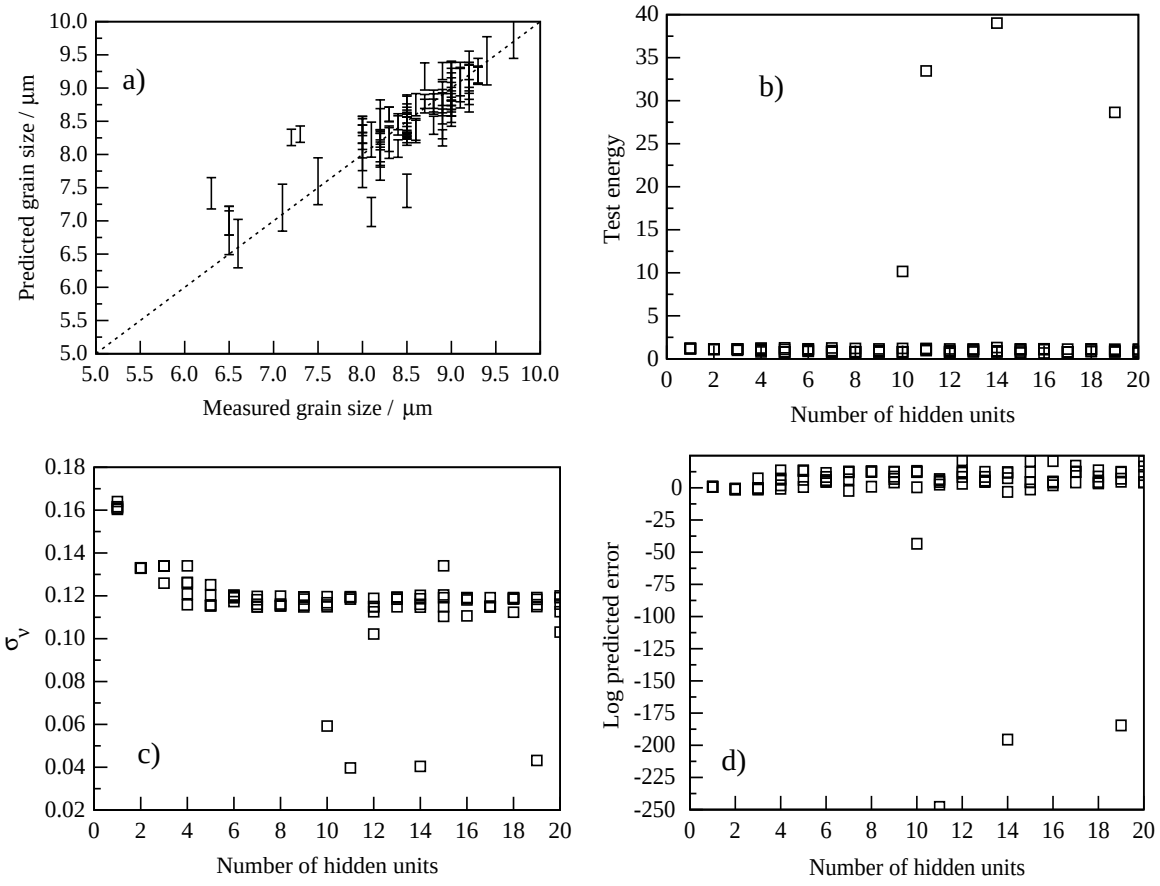

Fig. 7.5 Grain size model for type 304LT stainless steel. **a)** Predicted grain size against experimental grain size. **b)** Variation of test error as a function of number of hidden units. **c)** Perceived noise in the data (σ_ν) as a function of number of hidden units. **a)** The log predictive error as a function of number of hidden units

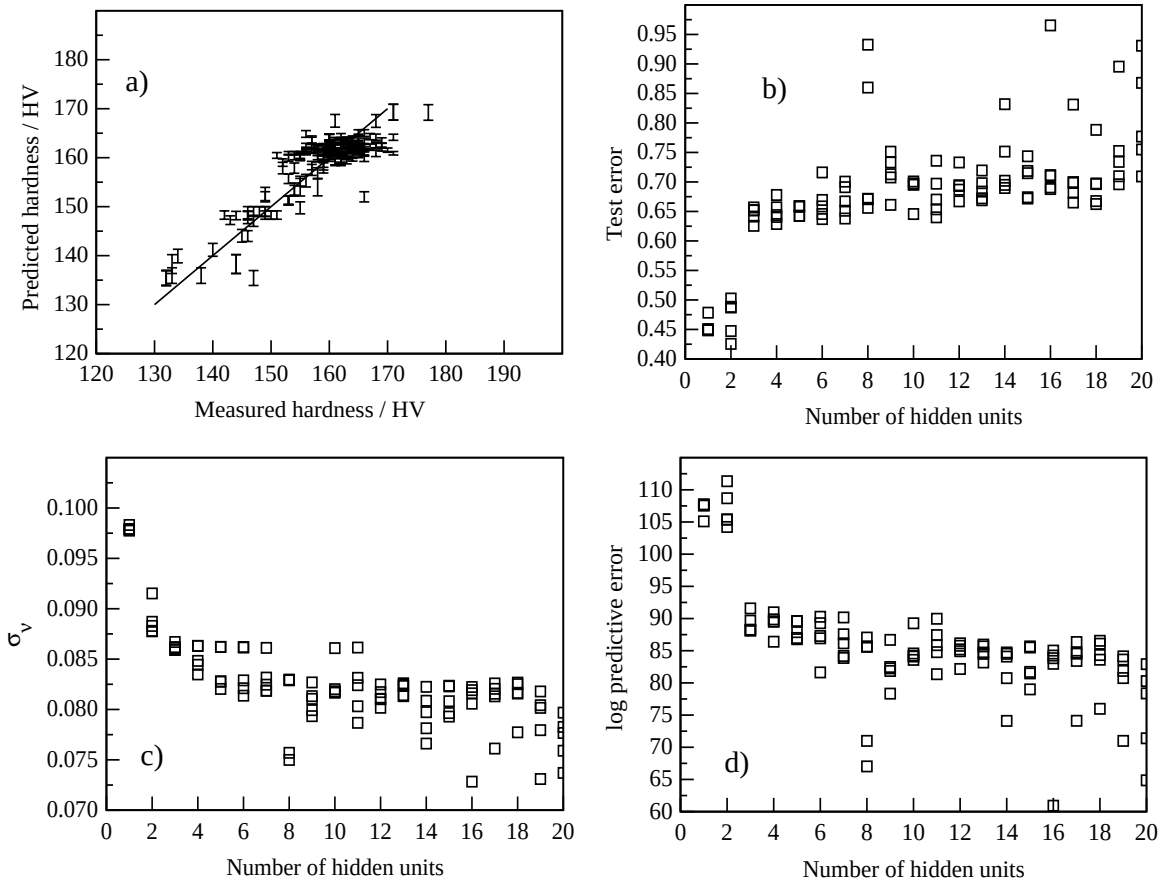

Fig. 7.6 Hardness model for type 302XD stainless steel. **a)** Predicted grain size against experimental grain size. **b)** Variation of test error as a function of number of hidden units. **c)** Perceived noise in the data (σ_ν) as a function of number of hidden units. **a)** The log predictive error as a function of number of hidden units

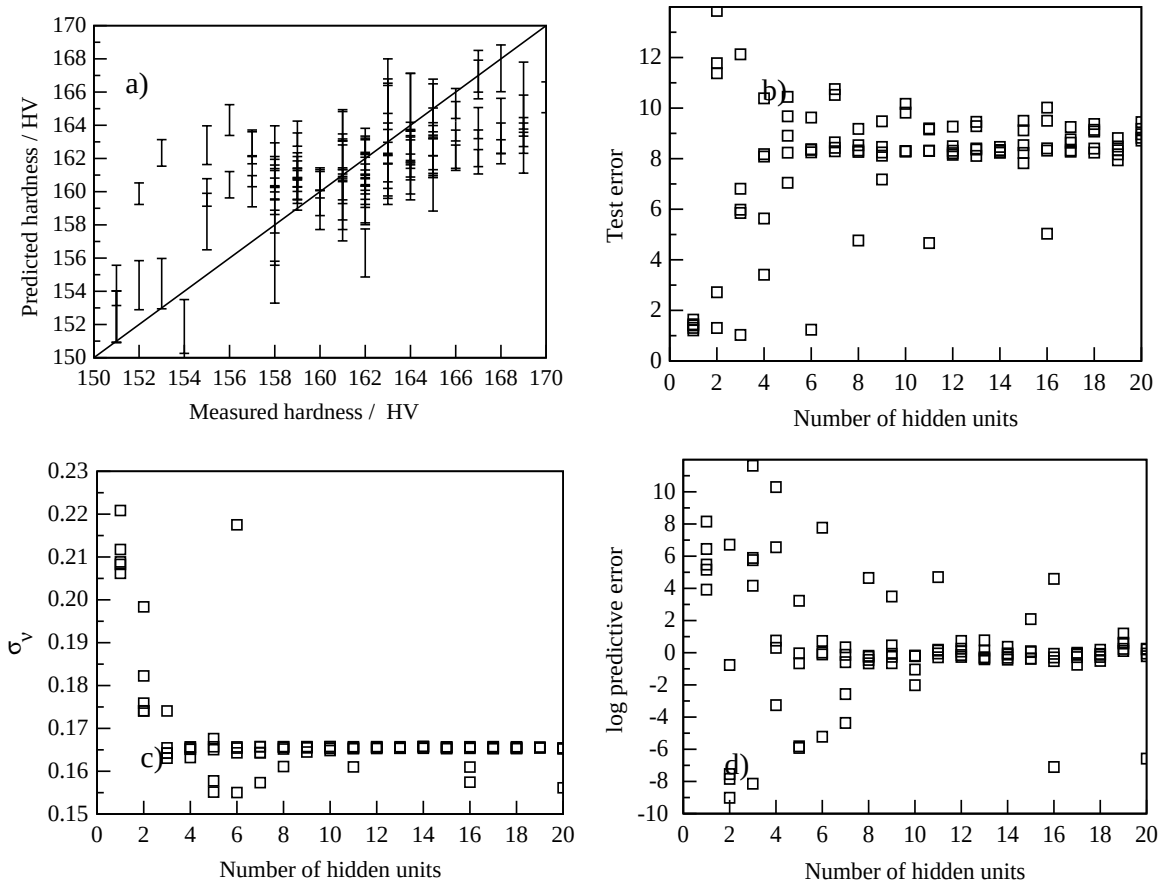

Fig. 7.7 Hardness model for type 302XD stainless steel. **a)** Predicted grain size against experimental grain size. **b)** Variation of test error as a function of number of hidden units. **c)** Perceived noise in the data (σ_ν) as a function of number of hidden units. **a)** The log predictive error as a function of number of hidden units

Steel	302XD			304LT		
Output	Hardness	Grain size	UTS	Hardness	Grain size	UTS
Number of data	2004	1944	2004	1044	1014	1044

Table 7.7: Table showing number of rows of data in each dataset.

factor of approximately 10, the actual sizes of the datasets used are give in Table 7.7: The columns included in the dataset were as follows as follows:

Column 1 - The final gauge in mm

Column 2 - The width in mm

Column 3 - The hot-band gauge in mm

Column 4 - The gauge of strip immediately preceding the current strip in mm

Column 5 - The gauge of strip immediately after current strip in mm

Column 6 - The position of the measurement on the strip (1 for head or 0 for tail)

Column 7 - Output variable (*i.e.* hardness in HV, grain size in μm or UTS in MPa)

The data for each of each model are summarised in Table 7.8a–f.

Neural network models were trained for each of these datasets in the same manner as in chapter5, in each case a committee of models was then formed. The number of neural networks in the optimum committee and the number of hidden units in these are given in Table 7.9:

Steel	302XD			304LT		
Output	Hardness	Grain size	UTS	Hardness	Grain size	UTS
Number of models	6	5	3	4	13	16
Number of hidden units	4 to 20	8 to 20	5 to 18	5 to 19	2 to 6	6 to 20
Max σ_ν	0.079	0.124	0.113	0.086	0.131	0.115

Fig. 7.7 Table showing number of models in committees from second neural network analysis, the spread of hidden units in these models and the maximum value of perceived noise in the output (σ_ν) in the committee.

Example output from these committees are included in Fig. 7.8.

7.3.1 Discussion

Inspection of graphs Fig. 7.8a–f shows that the fit of the model to the experimental data is, in general, very poor.

Out of the three outputs modelled (*i.e.* hardness, grain size and UTS), the best fit, both visually and in terms of σ_ν, was achieved in the hardness model. The comparatively lower value of σ_ν in this case means that the model is detecting less noise in the data *i.e.* the output variable shows a lower level of random fluctuation. However this value of σ_ν is still

Column	Minimum	Maximum	Mean	Std. dev.
1	0.46	4.02	1.50	0.66
2	1019	1546	1257	191
3	2.90	6.13	4.12	0.99
4	0.46	4.03	1.61	0.69
5	0.46	3.33	1.44	0.61
6	0.00	1.00	0.50	0.50
7	5.40	10.30	8.28	0.68

Table 7.8: a) Table showing minimum, maximum and standard deviation in all columns for neural network predicting grainsize of 302XD stainless steel

Column	Minimum	Maximum	Mean	Std. dev.
1	0.46	4.03	1.51	0.66
2	1019	1546	1255	191
3	2.90	6.30	4.13	0.99
4	0.46	4.04	1.63	0.71
5	0.46	4.04	1.44	0.63
6	0.00	1.00	0.50	0.50
7	135.0	190.0	162.2	6.3

Table 7.8: b) Table showing minimum, maximum and standard deviation in all columns for neural network predicting hardness of 302XD stainless steel

Column	Minimum	Maximum	Mean	Std. dev.
1	0.46	4.03	1.51	0.66
2	1019	1546	1255	191
3	2.90	6.30	4.12	0.99
4	0.46	4.04	1.63	0.71
5	0.46	4.04	1.44	0.63
6	0.00	1.00	0.50	0.50
7	596	684	635	11

Table 7.8: c) Table showing minimum, maximum and standard deviation in all columns for neural network predicting ultimate tensile strength (UTS) of 302XD stainless steel

Column	Minimum	Maximum	Mean	Std. dev.
1	0.47	4.10	1.75	0.70
2	1018	1543	1285	211
3	2.95	6.15	4.43	1.02
4	0.47	4.10	1.55	0.65
5	0.49	4.10	1.90	0.74
6	0.00	1.00	0.50	0.50
7	6.10	10.30	8.71	0.60

Table 7.8: d) Table showing minimum, maximum and standard deviation in all columns for neural network predicting grainsize of 304LT stainless steel

Column	Minimum	Maximum	Mean	Std. dev.
1	0.47	4.10	1.75	0.70
2	1018	1543	1289	213
3	2.95	6.15	4.44	1.02
4	0.46	4.10	1.61	0.65
5	0.44	4.10	1.87	0.73
6	0.00	1.00	0.50	0.50
7	136.0	185.0	164.0	5.3

Table 7.8: e) Table showing minimum, maximum and standard deviation in all columns for neural network predicting hardness of 304LT stainless steel

Column	Minimum	Maximum	Mean	Std. dev.
1	0.47	4.10	1.75	0.70
2	1018	1543	1289	212
3	2.95	6.15	4.44	1.02
4	0.46	4.10	1.61	0.65
5	0.44	4.10	1.87	0.73
6	0.00	1.00	0.50	0.50
7	583	670	616	29

Table 7.8: f) Table showing minimum, maximum and standard deviation in all columns for neural network predicting ultimate tensile strength (UTS) of 304LT stainless steel

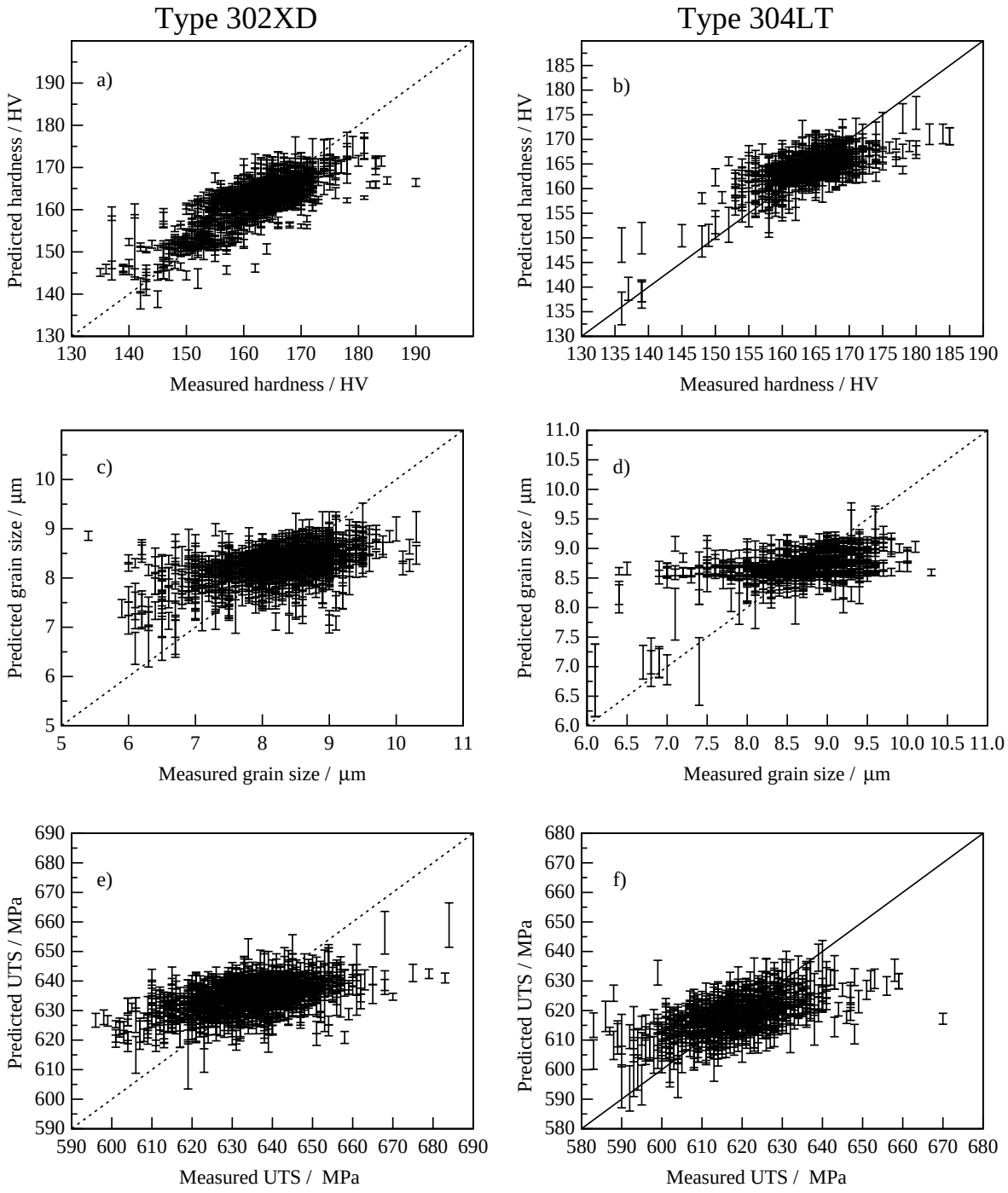

Fig. 7.8 Predicted output against measured output after retraining over the whole dataset. Error bars are a combination of fitting error and the perceived noise in the data. **a**) Hardness committee model for 302XD stainless steel. **b**) Hardness committee model for 304LT stainless steel. **c**) Grain size committee model for 302XD stainless steel. **d**) Grain size committee model for 304LT stainless steel. **e**) UTS committee model for 302XD stainless steel. **f**) UTS committee model for 304LT stainless steel.

several times greater than the majority of examples from the literature (*e.g.* Cole *et al.* 2000). This indicates that there is a large amount of experimental scatter in the case of the hardness measurements and a very large experimental scatter in the case of the grain size and UTS measurements.

7.3.1.1 Comparison of first and second models

Comparing the results of the second neural network (Fig. 7.8) with those from the first (Fig. 7.4–7.7), by visual inspection it might be concluded that the fit of the second model is poorer than the first. However this is not necessarily the case. Because of the much greater number of data in the second model, all the points appear as a mass obscuring the true trends in the data. By selecting 200 points on the graph at random this problem may be alleviated. To illustrate this, 200 randomly selected points from hardness model for type 302XD stainless steel have been plotted on Fig. 7.9.

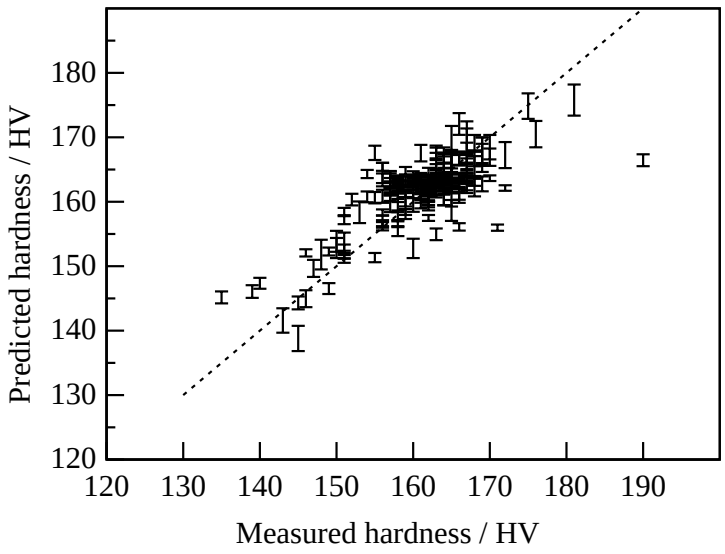

Fig. 7.9 Predicted hardness against measured hardness for a type 302XD stainless steel using only 200 randomly selected points from the dataset of 2004 originally used to retrain the model

Visually there is very little difference between Fig. 7.9 and Fig. 7.6a. However, due to the different input variables, the second model will have a different structure and hence differences in the significance of each input (σ_w). The relative significances of each variable for each model in the hardness committee is given in Fig. 7.10.

From Fig. 7.10 it can be seen that each model very little emphasis is put on the position on the strip at which the reading was taken (Column 6). Also, in contrast to the initial model

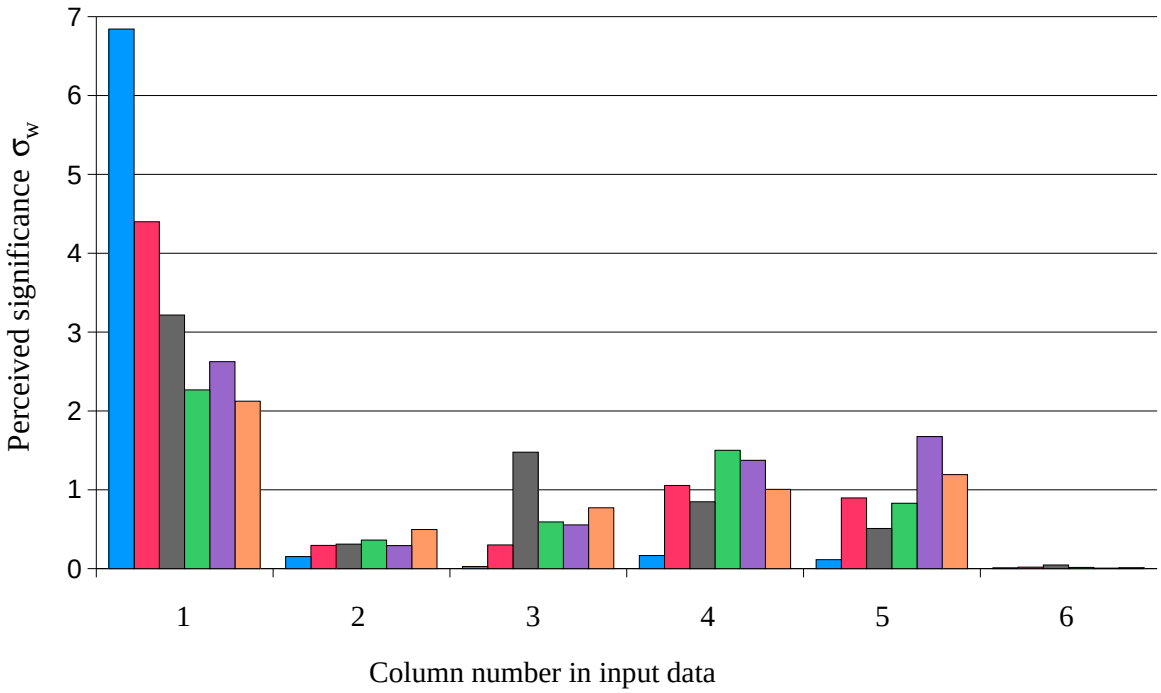

Fig. 7.10 Chart showing values of σ_w from all models in the final committee, modelling hardness in type 302XD stainless steel. Each bar represents the value of σ_w from a single model for a single input input variable. There were 6 models in the committee, bars of the same colour represent values of σ_w from a single model.

(Fig. 7.3) the hot-band gauge has a non-negligible effect on the final hardness. The hot-band gauge, together with the final gauge define the rolling reduction and hence the stored energy. A model which gives the hot-band gauge a negligible significance (as was observed in the initial model) cannot deal with variations in stored energy and therefore will be of limited use.

For each separate neural network model we see that the most significant column of input data is for strip gauge (Column 1). This is a metallurgically sound observation. The extent of recrystallization and recrystallized grain size is expected to be two of the most important factors controlling hardness. These factors are both strongly influenced by annealing temperature and time, which, in the industrial process, are both a function of strip gauge.

Therefore in conclusion, although there is little visible difference between the first and second neural network analyses, the values of σ_w derived from these models show more emphasis is put on known metallurgically important phenomena in the second analysis. This indicates that the second model is more likely to be able to predict well over a wider range of these metallurgically important variables.

7.3.1.2 Reason for poor fit

Although there is some degree of fit for the model predicting hardness, the models predicting grain size and UTS are both very poor.

As was demonstrated in chapter 5, if the output varies systematically with the input data and that the input data is a complete and comprehensive description of system, the process of recrystallization may be modelled using neural networks. Therefore the most likely reason why the model is failing to predict the observed variations in UTS and grain size is that there is insufficient or random information in the input variables, leading to random fluctuations of the output variable. By inspection of how each input variable varies with each output variable, it may be possible to see if input and output show any correlation (method after Lalam, 2000). This is illustrated in Fig. 7.11–7.16.

By inspection of the charts relating input variables to hardness (Fig. 7.9 and 7.10), it may be seen that although there is a large spread of possible hardnesses for each value of each input variable, there is some correlation between input and output variables (*e.g.* hardness increases as hot-band gauge increases). However on inspection of the charts relating the input variables to grain size and UTS, no such correlation is observed for any input or output. This implies that variation of any such input has a negligible effect on the output variable. This would explain the poor fit for grain size and UTS as compared with the better fit seen for hardness.

It has been seen that, although there is a correlation between the hardness and the input variables, however, there is no such correlation visible for UTS. This goes against the conventional metallurgical thinking that there is a strong correlation between hardness and UTS (*e.g.* Boyer and Gall, 1984‡) and therefore any observable trends in hardness should be mirrored by trends in UTS. There are two possible reasons why this relationship has not been observed:

- There is poor control on the measurement of hardness or UTS.
- The relationship is not valid for these materials.

As was previously stated, the hardness of the material is measured as a Rockwell hardness where a conical indenter in lowered onto the sample and indent size measured. This was then converted to a Vickers hardness by the use of look-up tables. Since there was an observed correlation between hardness and each input variable it can be assumed that there is adequate

‡ In the referenced work, conversions are claimed to be accurate for "*...Carbon and alloy steels in annealed, normalised and quenched-and-tempered conditions. Less accurate for cold worked condition and austenitic steels...*"

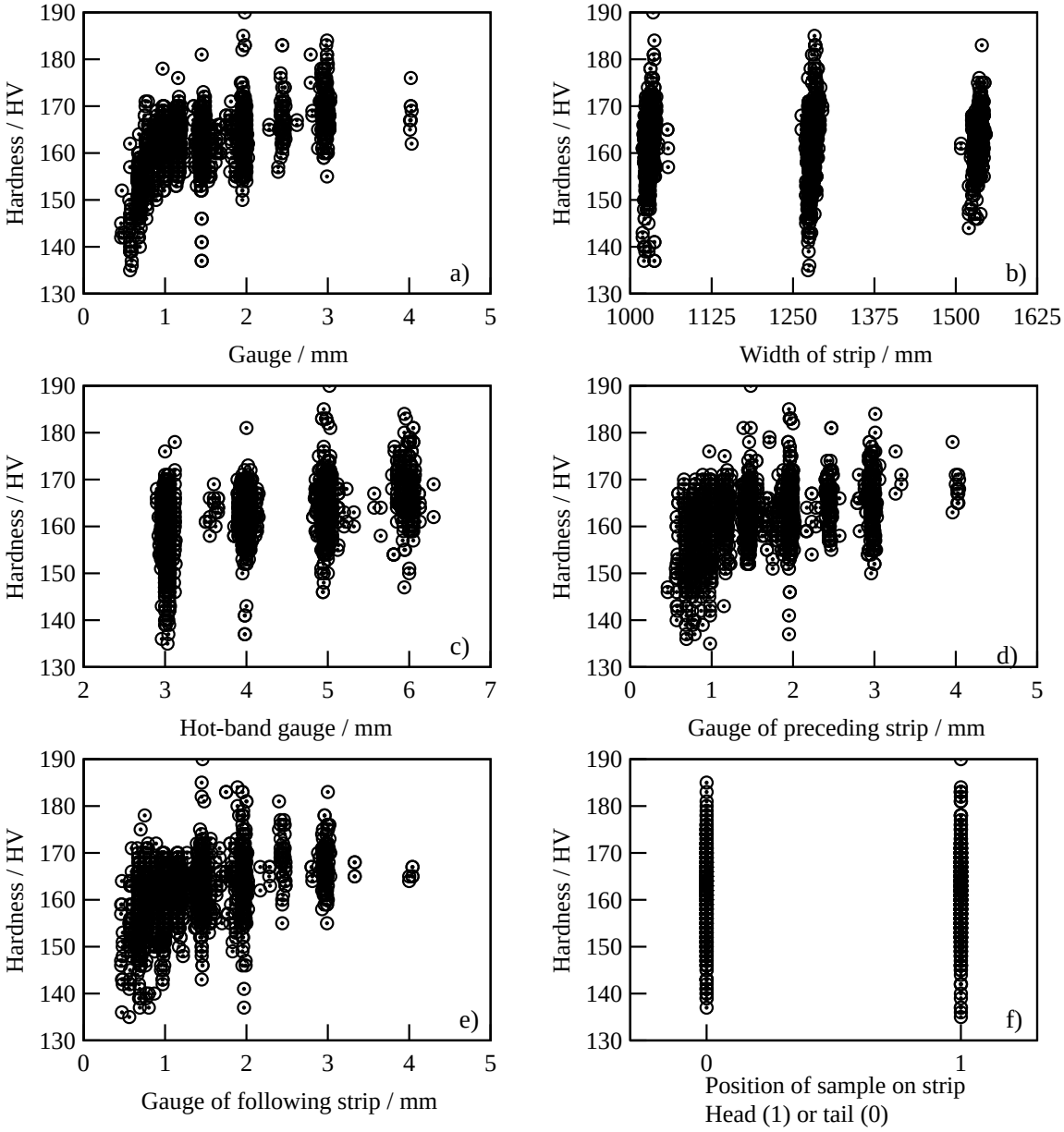

Fig. 7.11 Variation of hardness with different input variable in type 302XD stainless steel; **a**) Gauge, **b**) Strip width, **c**) Hot-band gauge, **d**) Gauge of preceding strip, **e**) Gauge of following strip, **f**) Position of measurement on strip.

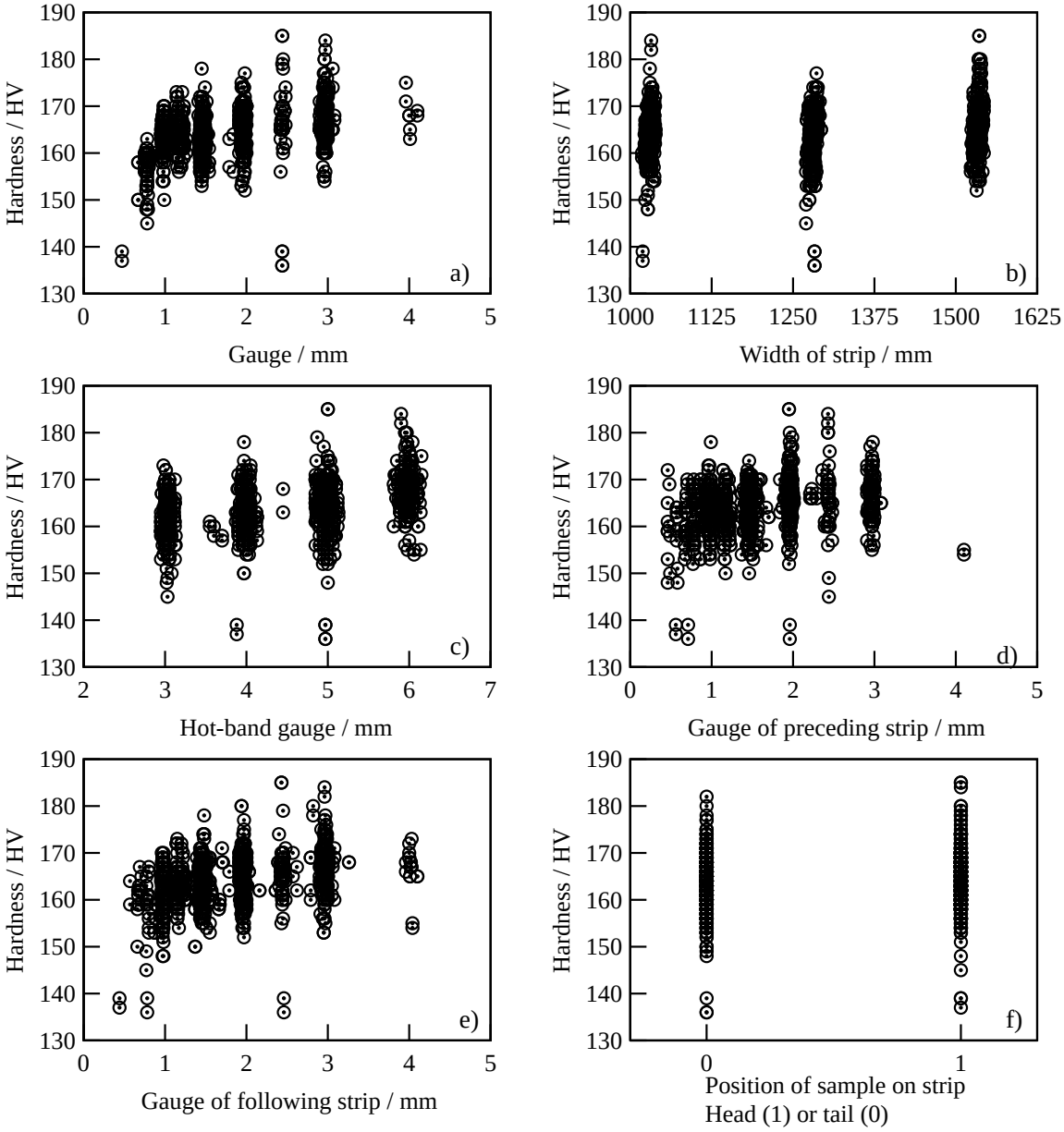

Fig. 7.12 Variation of hardness with different input variable in type 304LT stainless steel; **a**) Gauge, **b**) Strip width, **c**) Hot-band gauge, **d**) Gauge of preceding strip, **e**) Gauge of following strip, **f**) Position of measurement on strip.

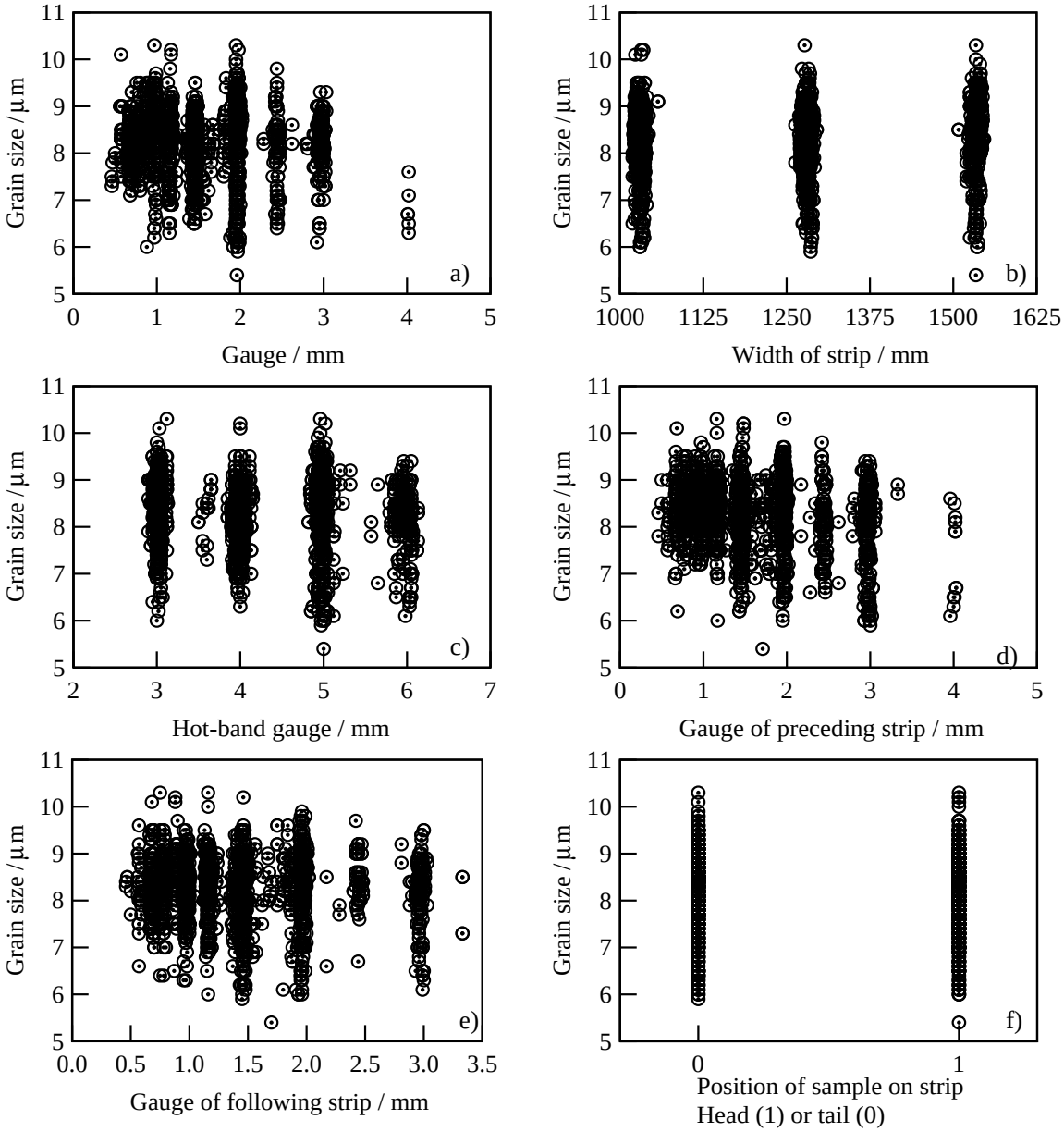

Fig. 7.13 Variation of grain size with different input variable in type 302XD stainless steel; **a**) Gauge, **b**) Strip width, **c**) Hot-band gauge, **d**) Gauge of preceding strip, **e**) Gauge of following strip, **f**) Position of measurement on strip.

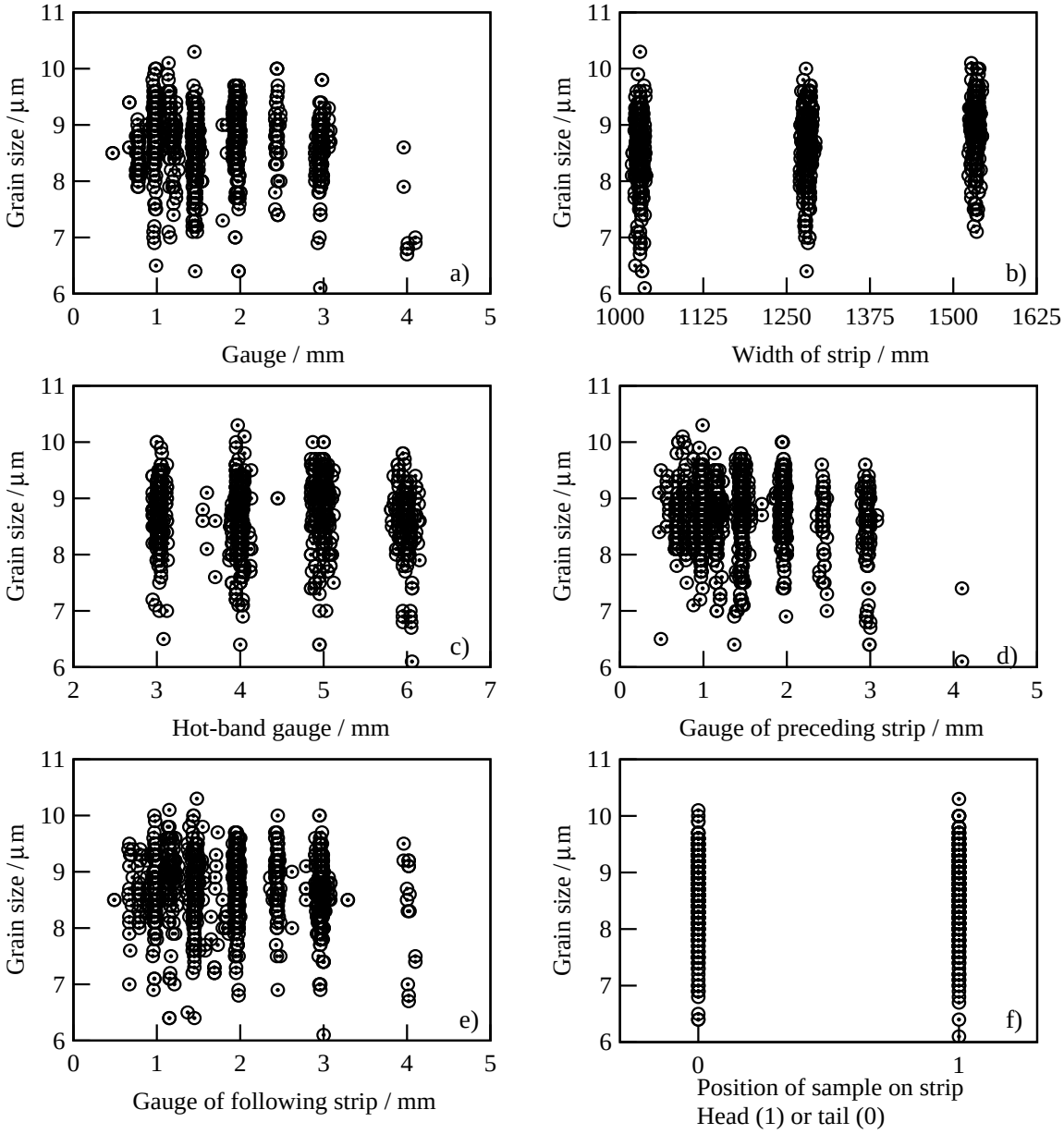

Fig. 7.14 Variation of grain size with different input variable in type 304LT stainless steel; **a**) Gauge, **b**) Strip width, **c**) Hot-band gauge, **d**) Gauge of preceding strip, **e**) Gauge of following strip, **f**) Position of measurement on strip.

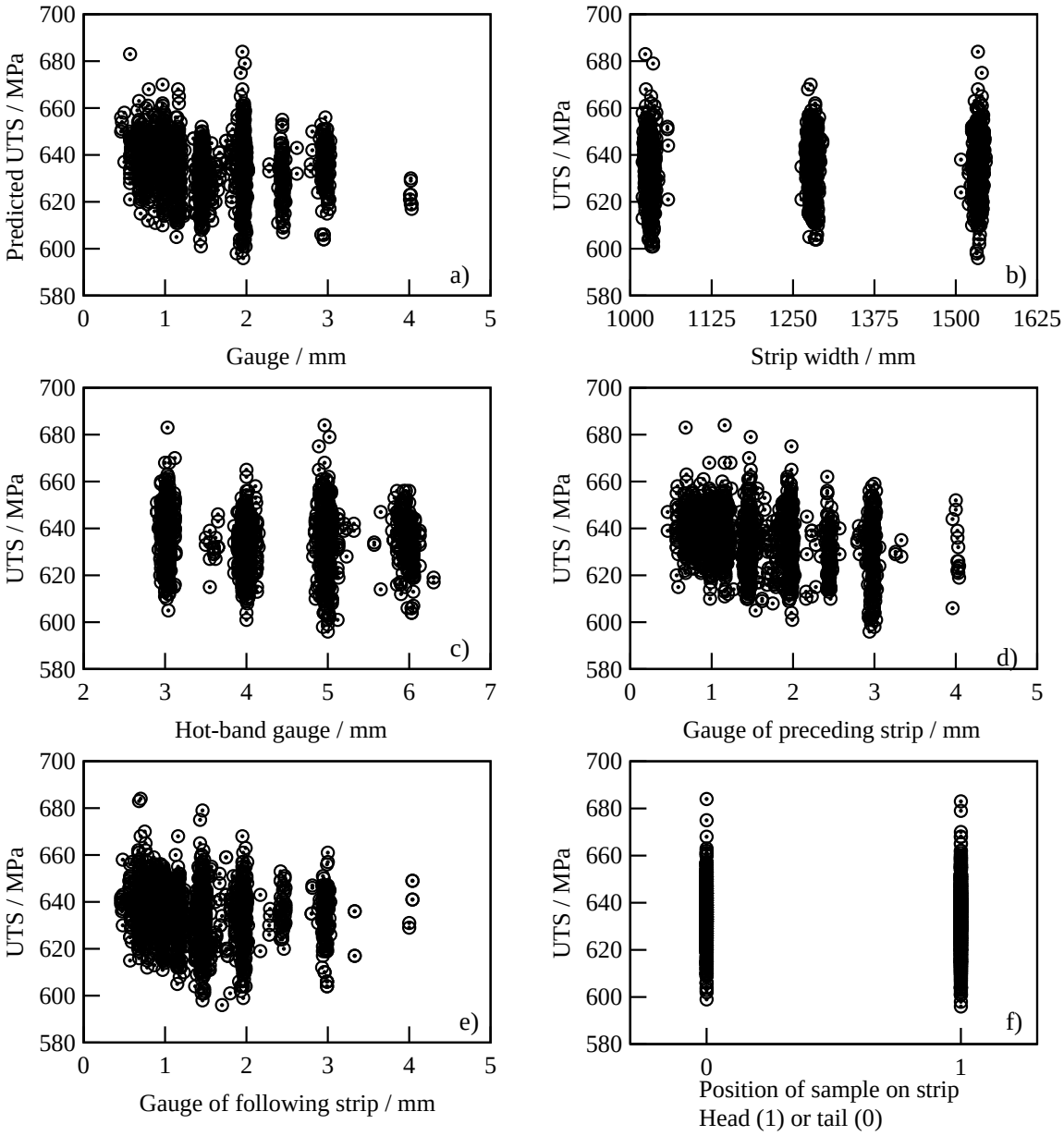

Fig. 7.15 Variation of UTS with different input variable in type 302XD stainless steel; **a**) Gauge, **b**) Strip width, **c**) Hot-band gauge, **d**) Gauge of preceding strip, **e**) Gauge of following strip, **f**) Position of measurement on strip.

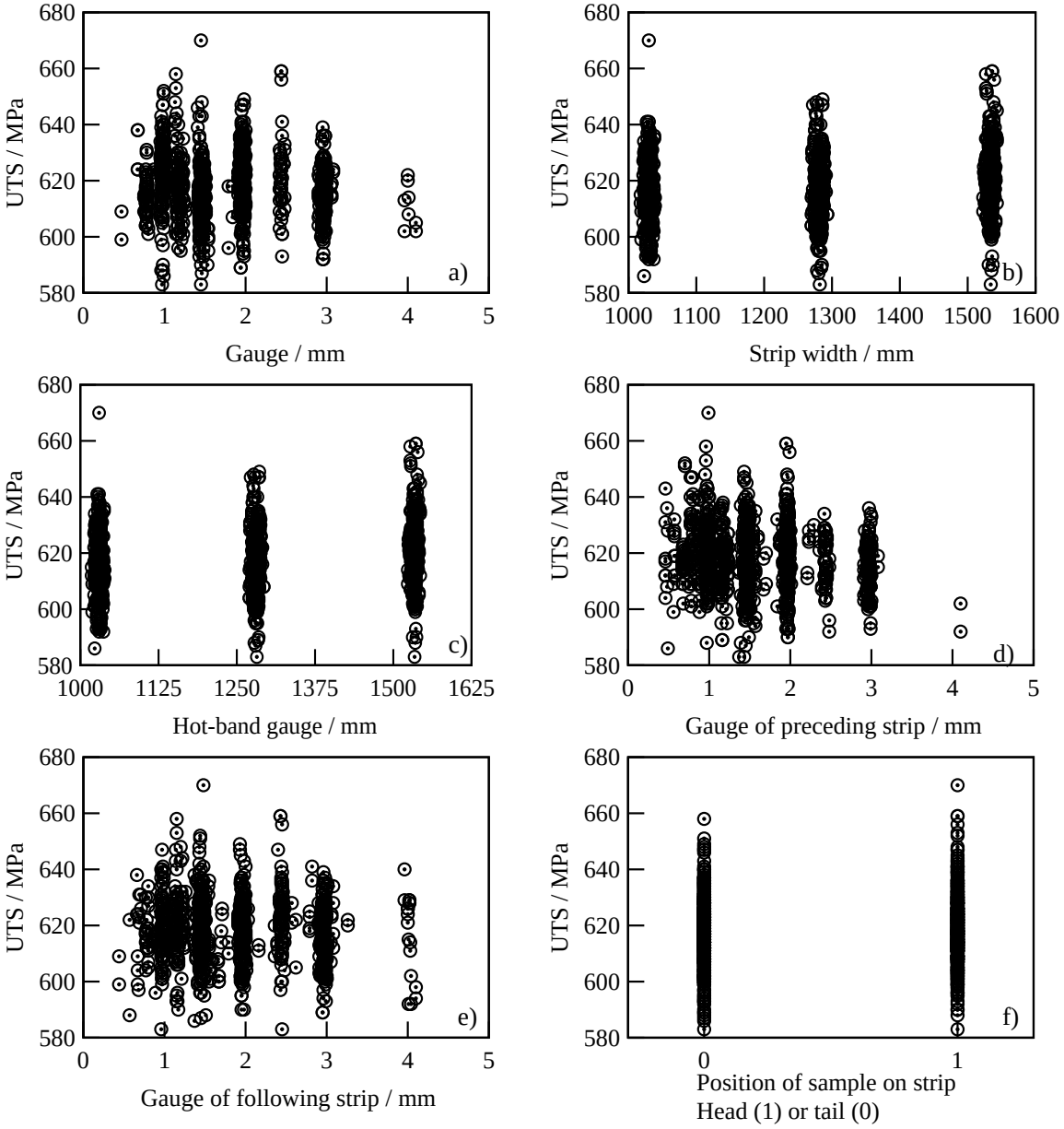

Fig. 7.16 Variation of UTS with different input variable in type 304LT stainless steel; **a**) Gauge, **b**) Strip width, **c**) Hot-band gauge, **d**) Gauge of preceding strip, **e**) Gauge of following strip, **f**) Position of measurement on strip.

control over the measurement of hardness. Flow-stress is measured by performing a simple tensile test using apparatus illustrated in Fig. 7.17.

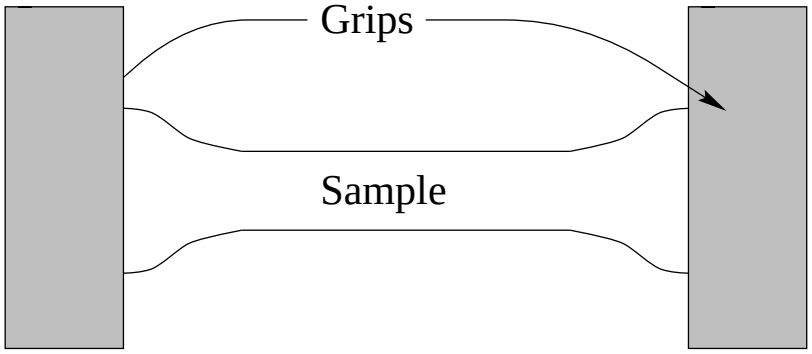

Fig. 7.17 Apparatus used for tensile testing.

The sample consists of a strip of material usually cut from either the head or the tail of the coil which is then mounted on grips and deformed in tension until failure occurs. There are a number of possible ways in which error may be introduced into this test, including jagged edges on the sample, poor contact between sample and grip and poor sample mounting. However, the measurement of UTS is considered to be very reproducible with only a few percent variation upon repeating tests (Backhouse, private communication). Hence, it is likely that the UTS results are reliable and therefore the UTS and hardness are varying independently.

7.3.2 Predictions

The criteria set out in §3.1 indicate that a good model must be able to make predictions which can be verified. Therefore, using the models derived in §7.3, predictions of how each of the three outputs varied as a function of gauge, strip width and hot-band gauge were made. The predictions for hardness, grain size and hot-band gauge variations are included in figures 7.16, 7.17 and 7.18 respectively.

As one input variable was changed, the other variables were kept at a constant value. These values was taken to be the average of that particular input variable over the whole dataset. These values are given in Table 7.10:

Input Variable	Gauge	Strip width	Hot-band gauge	Gauge of preceding strip	Gauge of following strip
Value	1.51	1255	4.13	1.63	1.44

Table 7.10: Fixed values of input variables used in predictions.

All measurements were assumed to be taken on samples from the head of the strip *i.e.* the input value in column 6 was 1.

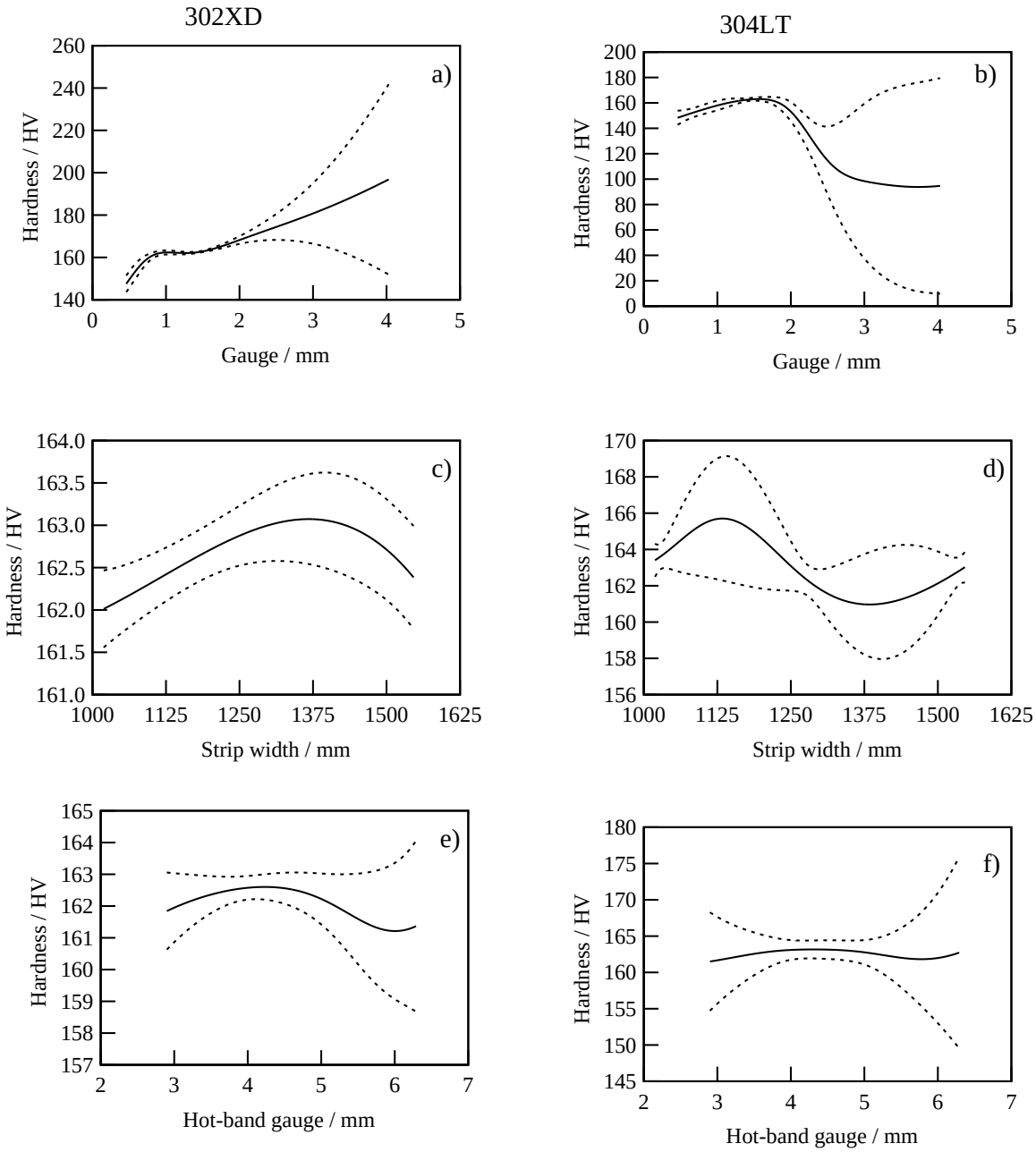

Fig. 7.18 Predictions of hardness as a function steel grade and certain input variables: **a**) Type 302XD and gauge. **a**) Type 304LT and gauge. **a**) Type 302XD and strip width. **a**) Type 304LT and strip width. **a**) Type 302XD and hot-band gauge. **a**) Type 304LT and hot-band gauge.

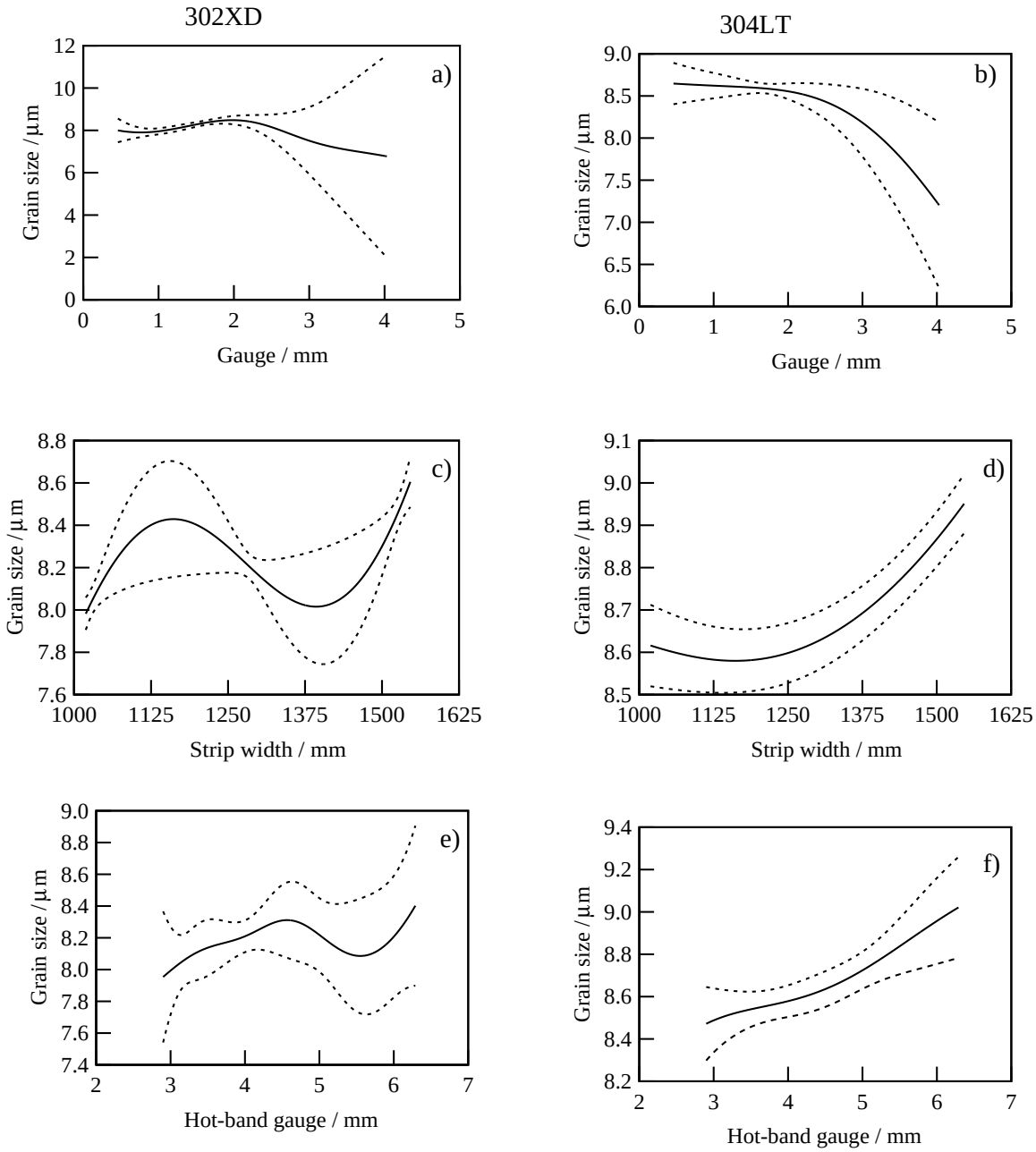

Fig. 7.19 Predictions of grain size as a function steel grade and certain input variables: **a**) Type 302XD and gauge. **a**) Type 304LT and gauge. **a**) Type 302XD and strip width. **a**) Type 304LT and strip width. **a**) Type 302XD and hot-band gauge. **a**) Type 304LT and hot-band gauge.

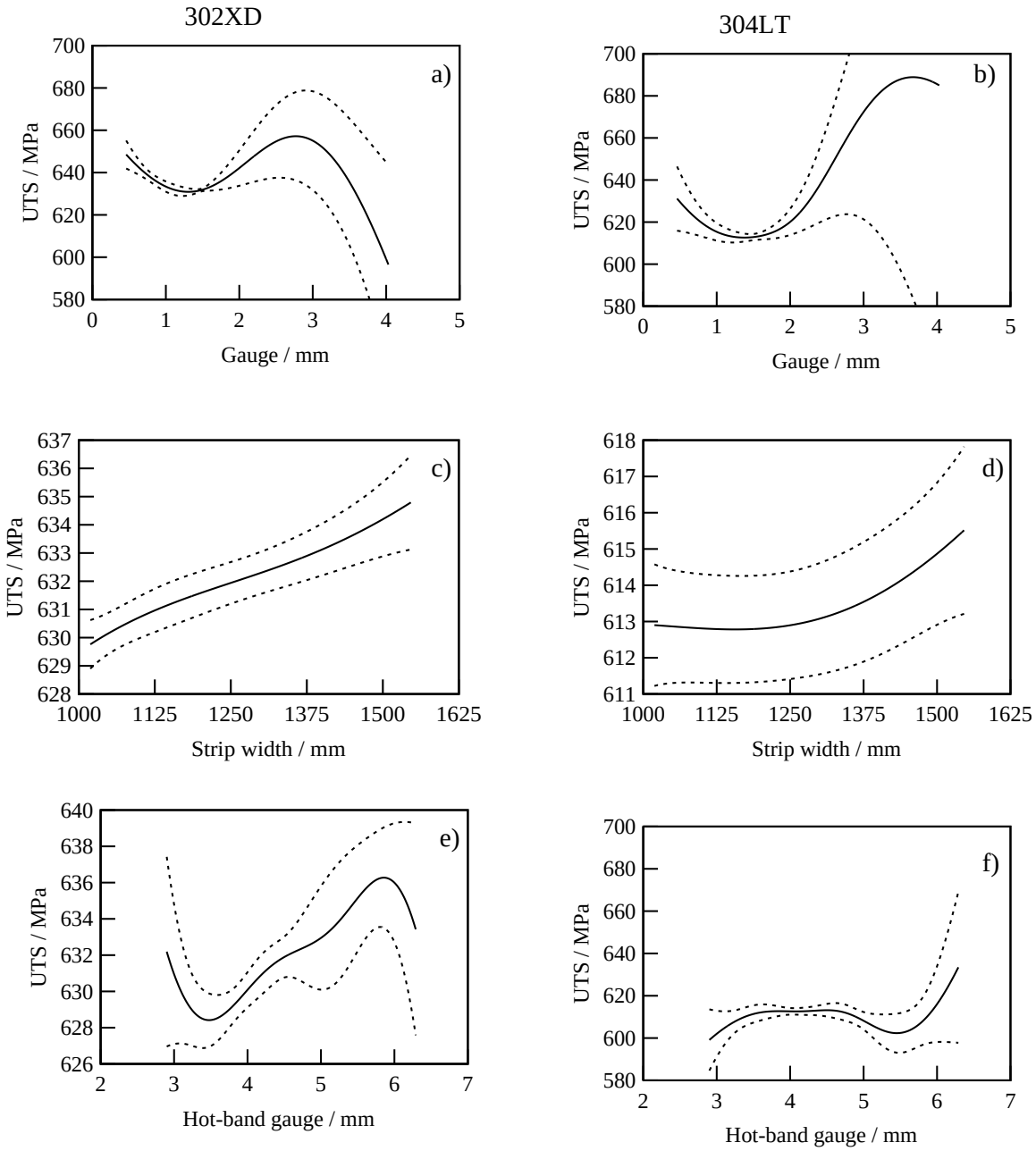

Fig. 7.20 Predictions of UTS as a function steel grade and certain input variables: **a**) Type 302XD and gauge. **a**) Type 304LT and gauge. **a**) Type 302XD and strip width. **a**) Type 304LT and strip width. **a**) Type 302XD and hot-band gauge. **a**) Type 304LT and hot-band gauge.

The furnace is generally set to produce as constant a value of each output as possible. This is to provide as reliable a product as possible for the customer. Therefore, it is expected that the value of each output will vary little with varying gauge. For all three outputs only a small amount of variation is observed as a function of gauge for gauges less than approximately 2 mm. Above this value all inputs tend to fluctuate erratically with large error bars, this behaviour indicates that there is insufficient data in this area to make accurate predictions.

Generally, the furnace temperature and line speed are set as a function of gauge only, *i.e.* they are independent of strip width. However, the wider the strip, the higher the thermal mass it has, although any increase in strip width will have a corresponding increase in surface area through which heat may be absorbed. Therefore, when a wide strip enters the furnace after a narrow strip it will cause an increase in heat flux from the furnace. Initially this will be provided by absorbing heat from the body of the furnace thus cooling it down. Once the thermocouples embedded in the furnace walls detect this cooling, the heat flux into the furnace will be increased to compensate. However, this means that the head of a wide sample will not heat to as high a temperature as the head of narrow sample. Therefore as strip width increases, the hardness and UTS should both increase at the head of the strip with increasing width, however grain size should decrease at the head of the strip with increasing width. The expected trends are only observed in the UTS models and the hardness model for 302XD stainless steel.

Finally, varying the hot-band gauge at constant final gauge is equivalent to varying the rolling reduction, and hence the stored energy. As stored energy increases, nucleation becomes easier and hence the grain size (and thereby hardness and UTS) of the resultant steel is expected to reduce. However, the grain size predicated increases as hot-band gauge increases, this is evidence of a poor fitting model. Similar behaviour is observed in the prediction of UTS, however, as the hot-band gauge increases very little variation is observed in the prediction of hardness.

Overall the predictions for hardness, grain size and UTS do not consistently follow expected trends in metallurgical behaviour. This behaviour is indicative of a poor fitting model.

7.3.3 Comparison with conventional regression

Conventionally regression techniques focussed on methods such as linear regression, wherein a dataset, such as is described in §7.3, is best fitted to a linear function. This process is described in §3.2. For completeness, the dataset from the best fitting model in the second neural network analysis, (hardness predictions in 302XD stainless steel), was compared with linear regression. Fitting of this model was done using a least squares technique.

Using the same dataset as for the neural network, the following equation was derived:

$$\text{Hardness (HV)} = 8.35C_1 - 0.00152C_2 - 0.916C_3 - 1.57C_4 - 0.632C_5 - 0.369C_6 + 158.94 \quad (7.1)$$

wherein C_n is the value in the dataset from the n^{th} column (as stated at the beginning of §7.3).

Unlike in the neural network techniques, the weights on each variable in the linear regression technique are not directly comparable. This is because values of the input variables were not normalised prior to the analysis.

The conventional graph of measured against predicted values is given in Fig. 7.21.

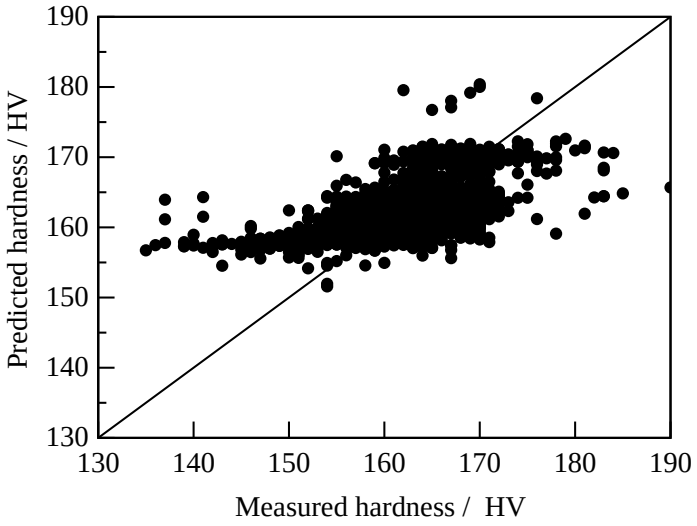

Fig. 7.21 Linear regression analysis using dataset from second neural network analysis for hardness in type 302XD stainless steel

By comparing Fig. 7.21 with the neural network prediction of the same dataset (see figure 7.8a)), we see that the fit from conventional regression is extremely poor. Conclusive proof, if it were needed, that neural networks represent a significant improvement in regression analysis.

7.4 Summary of neural network modelling.

As was demonstrated in chapter 5, given a complete and comprehensive description of the system of study, non-linear regression techniques, such as neural networks can accurately predict annealing behaviour.

In this chapter, the neural network modelling technique has been expanded to the modelling of industrial data. Although the first set of models seemed to produce a fairly accurate description of the experimental dataset, doubts were cast over whether or not they were actually capturing the trends in the data as they directly related to physical metallurgy of the

situation. Moreover, if these models are to be applied they must be trained directly from industrial data. The production of a dataset giving actual set line speed and actual indicated furnace temperature from a list of grades, gauges and a running schedule is non-trivial. Production of the datasets used in this analysis took upwards of 1 week to prepare, this is unacceptable in an industrial situation.

The second neural network analysis therefore used a greatly simplified dataset which was adapted directly from the data available to the operator of the furnace and by which the nominal furnace conditions are set. Despite this simplification, this second dataset contained all the information included in the first. The revised neural network, having a greatly reduced number of columns of input data represents a significant reduction in training time.

By inspection of values of σ_w derived from the second neural network analysis we see that the model deemed known metallurgically important factors, such as rolling reduction, to be significant. This would suggest that the model is capturing trends in the data as they relate to the physical metallurgy of the situation.

However, not all models showed an acceptable degree of fit. The fit of the models illustrated in figures 7.8e and 7.8f, showing the predictions for UTS behaviour, are very poor. The most probable reason for this was that the input dataset did not have sufficient information to fully describe the development of the UTS. As was described in §7.3.1.2 factors such as test conditions also may have an effect on the final value of UTS. Other possible inputs such as the chemical analysis of each coil of stainless steel is routinely measured. However, in this study it was not possible to correlate data from the furnaces with their respective chemical compositions.

Predictions from the current models were produced and compared with the trends expected. These trends were not generally observed. This is further evidence that the input dataset was insufficient to fully train a regression model.

Further work on in this area should employ a greatly expanded dataset including not only what is available to the operator of the machine but also all other available data. This would clarify what advantage would be gained by increasing the complexity of control during the annealing cycle. A more complete dataset would include such factors as; Chemical composition which, although it varies very little within one grade of steel, this small variation may have a significant effect on the final mechanical properties, *e.g.* the chemistry of a strip is a critical factor determining how much strain induced martensite is produced, hence affecting the hardness and UTS. The presence (or absence) and rolling reduction of a "pinch pass" during which the steel is given a small rolling reduction after the final anneal to improve surface finish

and strip flatness. This information was not readily available for inclusion into the dataset. UTS and other measurements are taken after this operation. Since this happens *downstream* from the annealing process the furnace operator cannot know if it is to occur, therefore it can play no part in a furnace control model. However, it may prove to be a significant source of variation in the final measured UTS and therefore could be included in a model to predict UTS after the completion of the production cycle. Also such factors as rolling history and number of passes used prior to annealing, emissivity and surface finish of the steel and, if such things could be properly quantified initial microstructure and furnace atmosphere should be included in the input dataset.

Finally, and for completeness, a linear regression model was produced describing the hardness variation of type 302XD stainless steel. Linear regression was shown to be vastly inferior to neural network regression.

CHAPTER 8

SUMMARY AND SUGGESTIONS FOR FUTURE WORK

8.1 Summary of kinetic modelling

The research presented in this thesis was undertaken with the aim of creating a model for the recrystallization of deformed austenitic stainless steel during a continuous annealing cycle.

A survey of the literature indicated that there has been a great deal of work published on the analysis of isothermal recrystallization using what is commonly known as "Avrami theory". The theory incorporates nucleation growth and hard impingement effects. It is suited particularly to recrystallization where the parent and product phases have the same chemical composition such that soft impingement effects may be completely neglected. Growth involves the uncoordinated transfer of atoms across the phase interface under the action of a driving force which is provided by the elimination of defects created during deformation. It is found that a representative way of expressing this driving force is through the experimentally measured flow stress of austenitic stainless steels as a function of the extent of rolling deformation and chemical composition.

There are a number of models describing the nucleation of recrystallization. Owing to the observed absence of dislocation cell structures in the austenitic stainless steels studied, the strain induced grain boundary migration (SIGBM) model was selected as the most useful in the present context. Experimental observations indicated that nucleation tended to occur most frequently at the grain boundaries of the original undeformed microstructure. Owing to this observation and the fact that the Avrami exponent n has frequently been found to have a value of unity, it was decided to account for this nucleation site preference in the Avrami theory for the anisothermal recrystallization problem.

Such a theory was published by Cahn in 1956 but has only rarely been applied to the recrystalliztion problem. The theory essentially applies the extended space concept twice first to cope with particles forming as a grain boundary plane and hence eliminating that boundary from further participation of that boundary in the recrystallization process. Secondly, allowing for impingement between particles which have originated from different grain boundaries.

One consequence is that the Avrami exponent can change towards unity during the course of the reaction. When grain boundaries are decorated completely with recrystallized material, nucleation ceases and growth essentially becomes one dimensional. This 'site saturation' also permits the rigourous application of the Schiel rule in adapting the overall transformation

kinetics theory to anisothermal heat treatments.

Once the heating section of the thermal cycle was included in the model (using Newtonian heating), it was possible to accurately account for and model the observed evolutions of number of grains per unit area and fraction recrystallized. This was modelling technique was extended over four different types of steel.

There was a good deal of success in the modelling of the chosen parameters, however there were some shortcomings in the model. Firstly, the present work does not take into account the possibility of recovery effects which may be significant at sufficiently low heating rates. The influence of such effects could be investigated in the future by annealing samples at low temperatures to induce recovery without recrystallization. Secondly there was a failure to predict the number of grains per unit area in the case of the type 316 stainless steel. This was traced down to the inability of the Schiel rule to cope with conditions that are not isokinetic. The model must be used with extreme caution in these circumstances, although it does give an indication that the isokinetic condition is not met. Thirdly, the function used for nucleation (SIGBM) does not appear to be applicable to all of the steels studied, particularly those which form a strain induced martensite phase. Nucleation is, and for the foreseeable future will remain, the most difficult and controversial subject in the kinetic modelling of stainless steels. The different models discussed in chapter 2 go some way towards the provision of a universal model, however this goal has not yet been reached. Finally, the thermodynamic fitting factors obtained for each model vary greatly. The most likely explanation for this is that the dataset used in the training of the models was not sufficiently accurate and diverse. For the model to be of academic and commercial use, these data must be refined so that the calculated thermodynamic factors obtain more rational values. Only then can the further progression towards making the model truly transferrable across steels of different chemical composition be made.

Despite these difficulties, it has been proven that this approach provides a significant step forward in the modelling of recrystallization.

8.2 Summary of empirical modelling

Empirical modelling involves the fitting of data from prior experience to form a model which, although not based on physical metallurgy, may predict the behaviour of the system studied. There are a number of different data fitting techniques available, however it was demonstrated in chapter 5 that neural networks, when correctly applied, are an adequate description of the recrystallization process.

Chapter 5 dealt entirely with the application of neural networks to well controlled laboratory data, this not only validated the approach but also highlighted certain potential pitfalls and secondary information which can be gathered. It was seen that without the inclusion of the heating rate in the analysis, the model fitted poorly. This highlights that it is essential not only to have accurate data, but that the dataset must be a comprehensive description of the problem at hand.

The production of stainless steel strip involves the passage of cold deformed material through a series of furnaces. The desired properties are achieved by setting a number of control parameters. Assuming that it is these parameters which determine the final properties of the steel studied, it should be possible to produce an empirical model which expresses the influence of the parameters on a quantitative basis, useful in industrial practice.

Neural network models to describe the grain size, hardness and UTS of industrially manufactured stainless steel according to the control parameters used during their production were produced. The primary observation was that with such a complex problem and noisy dataset, a large number of data are required to produce an accurate model.

Particular success was achieved in the modelling of hardness, however the models for grain size and UTS were less successful. This is a cause for concern because, conventionally, hardness and UTS have been considered to vary proportionally to each other.

8.3 Future work for kinetic theory model

The kinetic theory model has been demonstrated to be applicable to the problem of recrystallization. However there remain a number of problems with the method yet to be solved. These were outlined in §8.1.

The model would benefit from more work into the effect of recovery on the driving force for recrystallization. The heating stage of the annealing process may well be causing annihilation and a degree of polygonisation in the material before it recrystallizes. The rate of recovery and the relative temperatures at which recrystallization and recovery start will almost certainly vary with chemical composition. It will be important to not only calculate the relative start temperatures of recovery and recrystallization for each steel, but also how these temperatures vary with chemical composition so that the recovery may be truly integrated into a transferable model.

When the isokinetic approximation is contravened, the Schiel rule will fail to give meaningful answers. There is currently no mathematical framework available to cope with this problem. It would be useful to incorporate a number of warning flags so that software opera-

tors can see that the model is giving misleading answers. These warnings would be flagged up if nucleation and significant quantities of growth were observed simultaneously, *i.e.* ζ would be significantly above zero whilst n still had a value of 4.

Nucleation remains a difficult problem. Possibly the most pressing problem for this study is the question of the reversion of martensite contributing to the nucleation of recrystallization. This will also have an influence on the hardness and hence on the calculated stored energy, this may lead to a profound change in the calculated values of the thermodynamic fitting factors. Also in these instances the SIGBM model may not be valid. Nucleation remains the most contentious and difficult to quantify parameter in any model of recrystallization.

The disparate values of the thermodynamic fitting factors remains a worrying problem. This can best be addresses by more work into expanding the size of the dataset and resolving the issue of exactly what mechanism for nucleation is predominating in each steel. It may also be worth separating out steels which form strain induced martensite from those that do not and considering them separately with a separate model for nucleation for each each with its own values of thermodynamic fitting factors tailored to suit the applicable nucleation mechanism.

8.4 Future work for neural network model

It is clear from the models of UTS that there is some distance to go before this model is well controlled enough to be applied to a production situation. It is doubtful that simply increasing the number of data in the dataset will improve this, it is more likely that there are other factors which control the UTS that are not included in the input data.

Future studies must therefore increase the breadth of the input dataset. This should include factors such as the deformation history of the sample, the initial grain size before rolling, a more accurate description of the chemical composition and possibly other factors such as which shift were on duty when the readings were taken (*i.e.* the possible variations due to human involvement during measuring input and target data).

Currently chemical data and deformation history are not routinely fed into the input parameters for furnace control, however, the facilities to do so exist. The first step in the future development of the neural network model should therefore be their inclusion in the dataset. Should these be insufficient to correct the poor fit of the UTS model, then grain size of the metal prior to rolling would also be a useful input and the installation of apparatus to measure it should be considered.

APPENDIX 1

FORTRAN77 CODE FOR KINETIC MODEL

The kinetic models based on overall transformation kinetics and Cahn modified overall transformation kinetics were all pragrammed using FORTRAN77 programming language. The final version of the most advanced model (anisothermal Cahn modified overall transformation kinetics model, as discribed in §6.5–§6.7. The model described herein has been trained for a type 302AA stainless steel. However, the same code was used when training all the other types of stainless steel .

A1.1 The anisothermal recrystallization model – 302AA.for

```
C
C Anisothermal multifactor recrystallization program
C (C) 1999 G Hopkin & H Bhadeshia
C
C
C
C
C This program assumes spherical grains - i.e. shape factor of 4.188
C
C
      IMPLICIT DOUBLE PRECISION (A-Y)
C      CHARACTER*1 ZED
      OPEN(11,FILE='/users/gareth/recrystmodel/defaults10')
      OPEN(3,FILE='302AA_report')
      OPEN(9,FILE='302AA_CHECKER')
      OPEN(4,FILE='302AA_progress')
      OPEN(2,FILE='302AA_observables')
      WRITE (4,959) "X","TIMRUN","TIMTOT", "TMPRUN" ,"N" ,
     &  "RXDIA", "LN(TIMTOT)", "LN(LN(1/(1-X)))"
      WRITE (2,961) "X", "Strip Temp.", "    RX Grain Diam."
     &,"Time","Grains/Micron^2"
961   FORMAT (A15,A15,A15,A12,A15)
962   FORMAT (F15.10,F15.0,F17.13,X,X,F10.2,X,F15.12)
      WRITE (6,*)
      WRITE (6,*)
      WRITE (6,*) 'RECRYSTALLIZATION PROGRAM - Gareth Hopkin'
      WRITE (6,*)
      WRITE (6,*)
      WRITE (6,*)
      READ (11,*) SIGFLOW
      READ (11,*) G
```

```
      READ (11,*) D
      READ (11,*) GAMMA
      READ (11,*) REDN
      READ (11,*) TWOQ
      READ (11,*) VOLFRAC
      READ (11,*) RADPART
      READ (11,*) EDSORT
100   WRITE (6,*) 'Please input Time into recrystallization'
      CALL REED (TIME)
      WRITE (6,*)
      WRITE (6,*) 'Please input Furnace Temperature'
      CALL REED (T)
      T = T + 273D0
      HEADER = 1.0D0
      WRITE (6,*)
      WRITE (6,*) ' Input gauage of materials in mm'
      CALL REED (GUAGE)
      WRITE (6,*)
      WRITE (6,*) 'Please indicate whether sample touches furnace'
      WRITE (6,*) '1 for YES and 2 for NO'
      CALL REED (ATC)
      IF (ATC .EQ. 1.0d0) THEN
        ATC = (0.07D0/GUAGE)*0.8D0
        WRITE (6,*) 'SAMPLE TOUCHING SELECTED!!!!!'
      ELSE
        ATC = (0.035D0/GUAGE)*0.8D0
        WRITE (6,*) 'Standard sample selected'
      END IF
      WRITE (6,*)
      WRITE (6,*)
C
      XCOLD =1.0D0
      BOTTIM =0.0D0
101   FORMAT (A4,A42,A12)
102   FORMAT (A4,A42,F10.4,A12)
105   WRITE (6,101) 'Ref','Property','Value'
      WRITE (6,*)
      CALL DGCALC (DG,SIGFLOW,G,VOLFRAC,GAMMA,RADPART)
      GSTAR = 25000D0*(5D0**2)/(DG**2D0)
      WRITE (6,102) '1','Flow Stress =',SIGFLOW/1000000D0,'M Pa'
      WRITE (6,102) '2','Shear Modulus =',G/1000000000D0,'G Pa'
      WRITE (6,102) '3','Mean linear intercept before rolling ='
     &  ,D*1000000, 'Microns'
      WRITE (6,102) '4','Incoherent Grain Boundary Energy =',GAMMA
     & ,'J m^-2'
      WRITE (6,102) '5','Activation Energy for self diffusion =',
     & TWOQ/1000D0 , 'kJ mol^-1'
      WRITE (6,102) '6','Volume Fraction of Included Particles =',
     & VOLFRAC
      WRITE (6,102) '7','Mean Radius of Included Particles =',
     & RADPART*1000000D0 , 'Microns'
```

```
      WRITE (6,102) '8','Temperature of Furnace=',T - 273D0,'Centigrade'
      WRITE (6,102) '9','Time of Recrystallization =',TIME,'Seconds'
      WRITE (6,102) '10','Rolling Reduction =',REDN*100D0,'%'
      WRITE (6,102) '11','Gauage (thickness) of material =',GUAGE,'mm'
      WRITE (6,*)
      WRITE (6,102) '11','RESTORE DEFAULT VALUES'
      WRITE (6,102) '999','STOP!'
      WRITE (6,102) '0'  ,'RUN THE PROGRAM!'
      WRITE (6,*)
      WRITE (6,*) C
103   WRITE (6,*) 'PLEASE INPUT ''Ref'' NUMBER TO CHANGE VALUE'
C
      CALL REED (WOT)
      WRITE (6,*)
      WRITE (6,*)
      IF (WOT .EQ. 11) THEN
        WRITE (6,*) 'Please input Gauage (thickness) of material'
        WRITE (6,*)
        CALL REED (GUAGE)
        WRITE (6,*)
        GOTO 105
      ELSE IF (WOT .EQ. 1) THEN
        WRITE (6,*) 'Please input Flow Stress in M pa'
        WRITE (6,*)
        CALL REED (SIGFLOW)
        SIGFLOW = SIGFLOW*1000000D0
        WRITE (6,*)
        GOTO 105
      ELSE IF (WOT .EQ. 2) THEN
        WRITE (6,*) 'Please input Shear Modulus  in G Pa'
        WRITE (6,*)
        CALL REED (G)
        G = G*1000000000D0
        WRITE (6,*)
        GOTO 105
      ELSE IF (WOT .EQ. 3) THEN
        WRITE (6,*) 'Please input Grain size in Microns'
        WRITE (6,*)
        CALL REED (D)
        D = D/1000000D0
        WRITE (6,*)
        GOTO 105
      ELSE IF (WOT .EQ. 4) THEN
        WRITE (6,*) 'Please input Grain Boundary energy in Jm^-2'
        WRITE (6,*)
        CALL REED (GAMMA)
        WRITE (6,*)
        GOTO 105
      ELSE IF (WOT .EQ. 5) THEN
        WRITE (6,*) 'Please input Self Diffusion Activation Energy'
        WRITE (6,*) 'in kJ mol^-1'
```

```
  WRITE (6,*)
  CALL REED (TWOQ)
  TWOQ = TWOQ*1000D0
  WRITE (6,*)
  GOTO 105
ELSE IF (WOT .EQ. 6) THEN
  WRITE (6,*) 'Please input Volume Fraction of Particles'
  WRITE (6,*)
  CALL REED (VOLFRAC)
  WRITE (6,*)
  GOTO 105
ELSE IF (WOT .EQ. 7) THEN
  WRITE (6,*) 'Please input Particle Radius in Microns'
  WRITE (6,*)
  CALL REED (RADPART)
  RADPART = RADPART/1000000D0
  WRITE (6,*)
  GOTO 105
ELSE IF (WOT .EQ. 8) THEN
  WRITE (6,*) 'Please input Furnace Temperature in Centigrade'
  WRITE (6,*)
  CALL REED (T)
  T = T + 273
  WRITE (6,*)
  GOTO 105
ELSE IF (WOT .EQ. 9) THEN
  WRITE (6,*)
  WRITE (6,*) 'Please input Time in Seconds'
  WRITE (6,*)
  CALL REED (TIME)
  WRITE (6,*)
  GOTO 105
ELSE IF (WOT .EQ. 10) THEN
  WRITE (6,*)
  WRITE (6,*) 'Please input rolling reduction in %'
  WRITE (6,*)
  CALL REED (REDN)
  REDN=REDN/100D0
  WRITE (6,*)
  GOTO 105
ELSE IF (WOT .EQ. 11) THEN
  WRITE (6,*) ' Restoring from internal values'
  G = 840000000000D0
  D = 20D0/1000000D0
  GAMMA = 0.5D0
  GSTAR = 50000D0
  REDN =.75D0
  TWOQ = 286000D0
  VOLFRAC = 0.005D0
  RADPART = .1D0/1000000D0
  GOTO 100
```

```
      ELSE IF (WOT .EQ. 999) THEN
        PAUSE
        WRITE (6,*) ' '
        WRITE (6,*)
        GOTO 105
      ELSE IF (WOT .EQ. 0) THEN
        GOTO 104
      ELSE
        WRITE (6,*)
        WRITE (6,*) 'Not Recognised'
        WRITE (6,*)
        GOTO 103
      ENDIF
C
C
104   Q = TWOQ/2D0
C
C
C{}{}{}{}{}{}{}{}{}{}{}{}{}{}{}{}{}{}{}{}{}{}{}{}{}{}{}{}{}{}{}{}{}{}{}{}{}{}{}{}{}{}{}{}{}{}{}{}{}{}{}{}{}{}{}{}{}{}{}{}{}{}{}{}{}{}{}{}{}{}
C
C   NEW ANISOTHERMAL MAIN PROGRAM - 4th VERSION 4/8/99
C
C{}{}{}{}{}{}{}{}{}{}{}{}{}{}{}{}{}{}{}{}{}{}{}{}{}{}{}{}{}{}{}{}{}{}{}{}{}{}{}{}{}{}{}{}{}{}{}{}{}{}{}{}{}{}{}{}{}{}{}{}{}{}{}{}{}{}{}{}{}{}
C
C
      TSTP = 0.05
C
      TJMP = TIME/100D0
      CHOOSE = 1D0
      TIMRUN = 0.0D0
      TOTTIM = 0.0D0
      TMPMIN = 30D0+273D0
      CALL TEMPC (TOTTIM,T,CHOOSE,TMPRUN,TMPMIN,ATC,GUAGE)
C  THIS IS THE AMIBIENT TEMPERATURE OUTSIDE THE FURNACE
C
      CALL GBPUVP (GBPUV,D,REDN)
      CALL DGCALC (DG,SIGFLOW,G,VOLFRAC,GAMMA,RADPART)
      CALL GSTARC (GSTAR,DG,GAMMA)
C
C
953   FORMAT (F8.6,F15.8,F15.8,F15.3,E15.8,F15.12,F15.10,F15.10)
959   FORMAT (A8,A15,A15,A15,A15,A15,A15,A15)
960   CALL VELCALC (VEL,Q,TMPRUN,DG,EDSORT)
      CALL NEUNCALC (NEUN,D,GAMMA,TMPRUN)
      CALL NDOTCALC (NDOT,NEUN,GSTAR,TMPRUN,DG)
      IF (NDOT .EQ. 0.0D0) THEN
        WRITE (6,*) 'NUCLEATION IMPOSSIBLE'
        GOTO 100
      ENDIF
      CALL ABCALC (NDOT,VEL,TIMRUN,AB)
      CALL INTEGRAL (AB,INT)
```

```
      CALL BBP (NDOT,GBPUV,VEL,BB)
C
      CALL XCALC (AB,BB,INT,X)
      CALL NARXDC (TSTP,NDOT,VEL,RXDIA,GBPUV,XRUN,NRUN,X)
C
C
      IF (BOTTIM .GE. TJMP) THEN
      WRITE (4,953) X, TIMRUN,TOTTIM, TMPRUN , NRUN,RXDIA,
     &              DLOG(TOTTIM),DLOG(DLOG(1.0D0/(1.0D0-X)))
      WRITE (2,962) X,TMPRUN,RXDIA,TOTTIM,((NRUN*GBPUV)
     & **(2.0D0/3.0D0))*1.0D-12
        BOTTIM=0.0D0
      ELSE
        BOTTIM=BOTTIM+TSTP
      ENDIF
C
C
      FC=1.0D0
      TIMRUN = TIMRUN + TSTP
      TOTTIM = TOTTIM + TSTP
      IF (TOTTIM .GE. TIME+TSTP)  THEN
        GOTO 952
      ENDIF
      CALL TEMPC (TOTTIM,T,CHOOSE,TMPRUN,TMPMIN,ATC,GUAGE)
C
      IF (X .LT. 1.0D-12) THEN
         TIMRUN = 0.0D0
         GOTO 951
      END IF
      TIMRUN = TIMRUN - TSTP
955   CALL VELCALC (VEL,Q,TMPRUN,DG,EDSORT)
      CALL NDOTCALC (NDOT,NEUN,GSTAR,TMPRUN,DG)
      CALL BBP (NDOT,GBPUV,VEL,BB)
956   CALL ABCALC (NDOT,VEL,TIMRUN,AB)
      CALL INTEGRAL (AB,INT)
      HEELNX=1.0D0
C
C
      CALL XCALC (AB,BB,INT,XCHECK)
C
C
C  This bit sees if Xcheck is within 1% of X and if so accepts the current
C  value of timrun
C
      XCMX = XCHECK-X
      XMXC = X-XCHECK
      IF (XCMX .LT. XMXC) THEN
        XTHING = XMXC
      ELSE
        XTHING = XCMX
      ENDIF
```

```
C
      XTHING = XTHING/X
      IF (XTHING .LT. 0.01D0) THEN
        FC =FC**2.0D0
        GOTO 951
      END IF
C
C
957   FORMAT (F19.15,F19.15,F15.6,F15.0)
C      write (9,957) x,xcheck ,timrun ,fc
      HELEN = X-XCHECK
      AONE= (X-XCHECK)**2.0D0
      ATWO = (XOLD-XCOLD)**2.0D0
      GRUFF= (AONE-ATWO)
      IF (GRUFF .GT. 1D-80) THEN
        FC = FC/50.0D0
        HEELNX=2.0D0
      ENDIF
      IF ((X .LT. 0.000002D0) .AND. (HEELNX .EQ. 1.0D0)) THEN
        HELEN=HELEN*1000D0
      ENDIF
      IF (X .GT. 0.08D0) THEN
        HELEN=HELEN/1000.0D0
      ENDIF
      FACTOR = (1D0 +(HELEN))**FC
      TIMRUN = TIMRUN * FACTOR
      XOLD = X
      FC = FC +1D0
      XCOLD = XCHECK
      GOTO 956
C
C
951   TIMRUN = TIMRUN+TSTP
      GOTO 960
C
C
C
952   WRITE (3,101) 'Ref','Property','Value'
      WRITE (3,*)
      WRITE (3,102) '1','Flow Stress =',SIGFLOW/1000000D0,'M pa'
      WRITE (3,102) '2','Shear Modulus =',G/1000000000D0,'G Pa'
      WRITE (3,102) '3','Grain Size before rolling =' ,D*1000000,
     &  'Microns'
      WRITE (3,102) '4','Incoherent Grain Boundary Energy =',GAMMA
     & ,'J m^-2'
      WRITE (3,102) ' ','Activation Energy for Nucleation =',GSTAR/1000
     & , 'kJ mol^-1'
      WRITE (3,102) '5','Activation Energy for self diffusion =',
     & TWOQ/1000D0 , 'kJ mol^-1'
      WRITE (3,102) '6','Volume Fraction of Included Particles =',
     & VOLFRAC
```

```
      WRITE (3,102) '7','Mean Radius of Included Particles =',
     & RADPART*1000000D0 , 'Microns'
      WRITE (3,102) '8','Temperature =',T-273D0,'Centigrade'
      WRITE (3,102) '9','Time of Recrystallization =',TIME,'Seconds'
      WRITE (3,102) '10','Rolling Reduction =',REDN*100D0,'%'
      WRITE (3,*)
      WRITE (3,*) 'VEL   =',VEL
      WRITE (3,*) 'NDOT  =',NDOT
      WRITE (3,*) 'AB    =',AB
      WRITE (3,*) 'BB    =',BB
      WRITE (3,*) 'INT   =',INT
      WRITE (3,*) 'GBPUV =',GBPUV
      WRITE (3,*) 'DG    =',DG
      END
C
C
C
C~~~~~~~~~~~~~~~~~~~~~~~~~~~~~~~~~~~~~~~~~~~~~~~~~~~~~~~~~~~~~~~~~~~~~~~~~~~~
C~~~~~~~~~~~~~~~~~~~~~~~~~~~~~~~~~~~~~~~~~~~~~~~~~~~~~~~~~~~~~~~~~~~~~~~~~~~~
C~~~~~~~~~~~~~~~~~~~~~~~~~~~~~~~~~~~~~~~~~~~~~~~~~~~~~~~~~~~~~~~~~~~~~~~~~~~~
C~~~~~~~~~~~~~~~~~~~~~~SUBROUTINES START HERE~~~~~~~~~~~~~~~~~~~~~~~~~~~~~~
C~~~~~~~~~~~~~~~~~~~~~~~~~~~~~~~~~~~~~~~~~~~~~~~~~~~~~~~~~~~~~~~~~~~~~~~~~~~~
C~~~~~~~~~~~~~~~~~~~~~~~~~~~~~~~~~~~~~~~~~~~~~~~~~~~~~~~~~~~~~~~~~~~~~~~~~~~~
C~~~~~~~~~~~~~~~~~~~~~~~~~~~~~~~~~~~~~~~~~~~~~~~~~~~~~~~~~~~~~~~~~~~~~~~~~~~~
C  N CALC AND RXDIA CALC
C
C
      SUBROUTINE NARXDC (TIME,NDOT,VEL,RXDIA,GBPUV,XRUN,NRUN,X)
      DOUBLE PRECISION TIME,NDOT,VEL,RXDIA,GBPUV,XRUN,NRUN,X
      DOUBLE PRECISION NRUN,TSTEP,RXVOL,XRUN,TEQUIV
C
C
C TIME is the time into the anneal NOT the total annealing time
      NRUN = NRUN+(NDOT*TSTEP*(1.0D0-XRUN))
      TEQUIV = (3.0d0*(DLOG(1.0D0-XRUN))/(-3.1415926536D0*NDOT*VEL*VEL))
      TEQUIV = TEQUIV**(0.33333333333333333333D0)
      IF ((VEL*NDOT) .EQ. 0.0D0) THEN
        TEQUIV = 0.0D0
      ENDIF
      TSTEP= TIME/100D0
      TRUN =0D0
      DO WHILE (TRUN .LT. TIME)
        TRUN = TRUN +TSTEP
        TEQUIV =  TEQUIV +TSTEP
        XRUN = (1D0- DEXP(-(3.14159D0*NDOT*VEL*VEL*
     &         (TEQUIV**3.0D0))/3.0D0))
C        write (22,*) xrun , trun
      END DO
C
C
      RXVOL = X/(NRUN*GBPUV)
```

```
      RXDIA = 2.0D0*((3.0D0*RXVOL)/(4.0D0*3.14159D0))
     & **(0.33333333333333333D0)
C       write (21,*) tequiv,tstep,testre
C
      RETURN
      END
C
C ~~~~~~~~~~~~~~~~~~~~~~~~~~~~~~~~~~~~~~~~~~~~~~~~~~~~~~~~~~~~~~~~~~~~
C X CALCULATING SUBROUTINE
C
      SUBROUTINE XCALC (AB,BB,INT,X)
      DOUBLE PRECISION AB,BB,INT,X
C  \\\\\\\\\\\\\\\\\\\\\\\\\\\\\\\\\\\\\\\\\\\\\\\\\\\\\\\\\\\\\\\\\\\\\\\\
C
C
C THIS DOES THE CALCULATION OF ZETA (X)
C
C
C
      X = 1 - DEXP(-(BB**(-0.33333333333D0))*AB*INT)
C
C
C\\\\\\\\\\\\\\\\\\\\\\\\\\\\\\\\\\\\\\\\\\\\\\\\\\\\\\\\\\\\\\\\\\\\\\\\
      RETURN
      END
C
C
C-------------------------------------------------------------
C
C
      SUBROUTINE TEMPC (TIME,T,CHOOSE,TMPRUN,TMPMIN,ATC)
      DOUBLE PRECISION TIME,T,CHOOSE,TMPRUN,TMPMIN,ATC
C  This subroutine is currently based on a Newtonian heating regime
C  i.e. interface controlled.  and uses the equation:
C  T = To  - (To - Ts)*exp(-A * time)
C  T is the current temperature (TMPRUN)
C  To is the furnace temperatre (T)
C  Ts is the start temperature  (TMPMIN)
C  A is an experimentally obtained parameter = 0.035 in my studies for
C  Non-contact (industrial heating) however 0.075 for some samples
C
C  Choose is currently unused but is in position should I ever wish
C  to encorporate a choice of heating regimes
      TMPRUN = T - ((T-TMPMIN)*DEXP(-ATC*TIME))
      RETURN
      END
C
C-------------------------------------------------------------
C-------------------------------------------------------------------------
      SUBROUTINE REED (B)
      DOUBLE PRECISION B
```

```
996    READ  (*,*,ERR=999) B
       WRITE (6,*)
       GOTO 998
999    WRITE (*,997)
997    FORMAT (19X,'INCORRECT INPUT TRY AGAIN!'/)
      GOTO 996
998     RETURN
      END
C-----------------------------------------------------------------------
C
C  DRIVING FORCE (DG) CALCULATION SUBROUTINE
C BASED ON PAGE 17 OF H&H
C
      SUBROUTINE DGCALC (DG,SIGFLOW,G,VOLFRAC,GAMMA,RADPART)
      REAL*8 DG,SIGFLOW,G,VOLFRAC,GAMMA,RADPART
      DG = ((2D0*(SIGFLOW**2D0))/G) - ((3D0*VOLFRAC*GAMMA)/
     & (2D0*RADPART))
C CONVERSION BETWEEN J M-3 AND J mol-1
      DG = DG*(7.06D-6)
      RETURN
      END
C-----------------------------------------------------------------------
C
C GROWTH RATE SUBROUTINE
      SUBROUTINE VELCALC (A,B,C,D,E)
C a = vel , b = Q , c = T , d = delta G, e = edsort
      DOUBLE PRECISION A,B,C,D,E
      A = E*3.2D0*2.0837D0*C*(2.718281828D0**(-B/(8.314D0*C)))*
     &(1-(2.718281828D0**(-D/(8.314D0*C))))
C      WRITE (6,*) A,B,C,D
C      WRITE (6,*) 'test'
C ***MOTHBALLED*** 2034 IS A PRODUCT OF DELTA & NEU - SEE BHADESHIA & SHA
C ***FIXED VALUE OF delta.nu NOT PHYSICAL - SEE PAGE 62 OF THESIS***
      RETURN
      END
C-----------------------------------------------------------------------
C
C CALCULATION OF AB AS GIVEN BY CHRISTIAN PAGE 527
C
      SUBROUTINE ABCALC (NDOT,VEL,TIME,AB)
      REAL*8 NDOT,VEL,TIME,AB
      AB = ((NDOT*(VEL**2D0))**0.333333333333333D0)*TIME
      RETURN
      END
C-----------------------------------------------------------------------
C
C  A SUBROUTINE TO EVALUATE THE INTEGRAL ON P. 527 OF CHRISTIAN
C
      SUBROUTINE INTEGRAL (AB,INT)
      REAL*8 AB,XI,INT,RUNTOT
      PI = 3.141592654D0
```

```
      RUNTOT = 0.0D0
      XI = 0.0D0
      DO WHILE (XI .LE. 1.0D0)
         RUNTOT = RUNTOT + 1 - DEXP((-3.141592654D0/3)*(AB**3D0)*
     &             (1 - (3D0*(XI**2D0)) + (2D0*(XI**3D0))))
         XI = XI + 0.01D0
      END DO
      INT = RUNTOT / 100D0
      RETURN
      END
C-----------------------------------------------------------------------
C
C TO CALCULATE THE GRAIN BOUNDARY AREA PER UNIT VOLUME
C BASED ON A TETRAKAIDECAHEDRON
C
C ****************************************
C        REDONE COMPLETELY USING MEAN LINEAR INTERCEPT 19/5/99
C ****************************************
       SUBROUTINE GBPUVP (GBPUV,D,REDN)
       DOUBLE PRECISION GBPUV,D,REDN,B,C
       GBPUV = 2/D
C
C  As stated by Harry - in Lab book 13/5/99
C
       C = (1D0-REDN)
       B = 1D0/C
       GBPUV = GBPUV*(B+(3D0*(B*(DSQRT(1+(2D0*(B**2D0)*(C**4D0))))+
     &  DSQRT((B**2D0)+(2D0*(C**2D0))))) + C*DSQRT(2D0*(1D0+
     &  ((B**4D0)*(C**2D0)))))/(13.392*B*C)
       RETURN
       END
C-----------------------------------------------------------------------
C
C TO CALCULATE BB
C
C
      SUBROUTINE BBP (NDOT,GBPUV,VEL,BB)
      REAL*8 NDOT,GBPUV,VEL,BB
      BB=NDOT/(8.0D0*(GBPUV**3.0D0)*VEL)
      RETURN
      END
C-----------------------------------------------------------------------
C
C ****************************************
C MOTHBALLED 19/5/99 IN FAVOUR OF FIXED VALUE
C ****************************************
C Fixed value is not physical - this is a vibration
C and MUST be T dependent!  Changed as per S.V. Parker
C thesis, Reed & Bhadeshia 1992 and Cahn 1956 20/5/00
C ****************************************
C
```

```
C LATTICE VIBRATION (ATTEMPT FREQUENCY ) SUBROUTINE
      SUBROUTINE NEUNCALC (BNEUN,BD,BGAMMA,BT)
      DOUBLE PRECISION BNEUN,BD,BGAMMA,BT
C
C ****************************************
C
C      BNEUN = (0.764D0/(1.58*BD/2.9))*620.412D0*(BGAMMA**0.5D0)
C 620.412  = 1 OVER SQRT OF EFFECTIVE MASS PER AREA OF MONOLAYER OF
C OCTAHEDRAL Fe. (THIS IS A MAX FIGURE) HENCE 500 TAKEN
C
C ****************************************
C
      BNEUN = 1.7D102*BT
      END
C-----------------------------------------------------------------------
C NUCLEATION FREQUENCY SUBROUTINE
      SUBROUTINE NDOTCALC (ANDOT,ANEUN,AGSTAR,AT,ADG)
      DOUBLE PRECISION ANDOT,ANEUN,AGSTAR,AT,ADG
      DOUBLE PRECISION LOPPY
C      READ (*,*) LOPPY
      LOPPY = 0
C loppy is the standard addition to the nucleation
C      WRITE (6,*) ANDOT,ANEUN,AVOL,AGSTAR,AT
       ANDOT=ANEUN*(2.718281828D0**
     &  (-(AGSTAR+(1000D0*LOPPY))/(8.314D0*AT)))
C                    WRITE (6,*) 'ANDOT' ,ANDOT
      RETURN
      END
C-----------------------------------------------------------------------
C  NEW SUBROUTINE GSTAR CALCULATOR 29/7/99 - Altered 17/7/00
C       SUBROUTINE GSTARC (GSTAR,DG,GAMMA)
      DOUBLE PRECISION GSTAR,DG,GAMMA
C      GSTAR = 3.14159265359D0*(((1D0/2D0)*(GAMMA**3D0)*(DG**-2D0)))
C CONVERTION FROM J m-6 mol2 to J mol-1
C      GSTAR = (GSTAR * 6.02214D23 * 7.06D-6 * 7.06D-6)
C
C CLASSICAL NUCLEATION NOT APPLICABLE FOR RECRYSTALLIZATION  -  H&H 1996
C Modified to reflect Delta G dependence 29/8/00
C MOTHBALLED IN FAVOUR OF FIXED VALUE.
C
      GSTAR = 1700000
      END
C
C-----------------------------------------------------------------------
C~~~~~~~~~~~~~~~~~~~~~~~~~~~~~~~~~~~~~~~~~~~~~~~~~~~~~~~~~~~~~~~~~~~~~~~
C~~~~~~~~~~~~~~~~~~~~~~~~~~~~~~~~~~~~~~~~~~~~~~~~~~~~~~~~~~~~~~~~~~~~~~~
C~~~~~~~~~~~~~~~~~~~~~~~~~~~~~~~~~~~~~~~~~~~~~~~~~~~~~~~~~~~~~~~~~~~~~~~
C~~~~~~~~~~~~~~~~~~~~~~~SUBROUTINES  END  HERE~~~~~~~~~~~~~~~~~~~~~~~~~
C~~~~~~~~~~~~~~~~~~~~~~~~~~~~~~~~~~~~~~~~~~~~~~~~~~~~~~~~~~~~~~~~~~~~~~~
C~~~~~~~~~~~~~~~~~~~~~~~~~~~~~~~~~~~~~~~~~~~~~~~~~~~~~~~~~~~~~~~~~~~~~~~
C~~~~~~~~~~~~~~~~~~~~~~~~~~~~~~~~~~~~~~~~~~~~~~~~~~~~~~~~~~~~~~~~~~~~~~~
```

APPENDIX 2

MAP DOCUMENTATION

The FORTRAN77 code given in the previous appendix is documented so as to be consistent with the Materials Algorithms Project (MAP), which is a perpetual source code library of complete programs and simple subroutines and functions which are of relevent to the materials sceintist. The sole perpose of the library is to freely distribute programs and their contained theories to the scientific community. The MAP library is available over the internet at the following URL:

http://www.msm.cam.ac.uk/map/mapmain.html

A2.1 Provenance of code

G.J. Hopkin and H.K.D.H Bhadeshia, Phase Transformations and Complex Properties Group, Department of Materials Science and Metallurgy, University of Cambridge, Cambridge, England. Near Wales.

A2.2 Purpose of code

This code is for modelling the fraction recrystallized, grain size and number of grains per unit area observed. It is based on Cahn modified overall transformation kinetics as detailed in the PhD thesis "*Modelling anisothermal recrystallization in austenitic stainless steels*" G.J. Hopkin, University of Cambridge (2001).

For a given set of input parameters as described in the following sections, it predicts fraction recrystallized, grain size and number of grains per unit area observed and their development as a function of time.

A2.3 References

CAHN, J.W. (1956), *Acta Metallurgica*, **4**, 449

CHRISTIAN, J.W. (1975), *The Theory of Transformations in Metals and Alloys: Equilibrium and General Kinetic Theory*, p.15–20, p.525–531, Pergamon Press, Oxford

SHA, W. & BHADESHIA H.K.D.H. (1997), *Mat. Sci & Eng.*, **A223**, 91

HOPKIN G.J. (2001), *PhD thesis, University of Cambridge, UK*, Chapters 2 and 6

A2.4 Program arguments

A2.4.1 Input parameters

SIGFLOW - Double precision

The flow stress of the material (Pa)

G - Double precision
The shear modulus of the material (Pa)

D - Double precision
Undeformed grain diameter (m)

GAMMA - Double precision
The grain boundary energy (Jm^{-2})

REDN - Double precision
The rolling reduction

TWOQ - Double precision
Twice the activation energy for grain boundary motion ($Jmol^{-1}$)

VOLFRAC - Double precision
Volume fraction of included particles (redundant variable set to 0.0)

RADPART - Double precision
Radius of above particles (redundant variable set to 1.0)

EDSORT - Double precision
The naperian exponential of the activation entropy for grain boundary motion divided by the ideal gas constant.

TIME - Double precision
The total annealing time (s)

T - Double precision
The furname temperature (°C)

GUAGE - Double precision

The gauge of the material (mm)

ATC - Double precision

Indicate whether the sample toughes the furnace or not

A2.4.2 Output parameters

X - Double precision

The fraction recrystallized

TIMRUN - Double precision

Equivelent time in Scheil calculation

TOTTIM - Double precision

The actual time through the annealing process

TMPRUN - Double precision

The temperature at time given by TOTTIM

NRUN - Double precision

The number of grains per unit area (m^{-2})

RXDIA - Double precision

The recrystallized grain size (m)

VEL - Double precision

The final value of grain boundary velocity (ms^{-1})

NDOT - Double precision

The nucleation rate per unit area ($m^{-2}s-1$)

AB - Double precision

The final value of the function a^B

BB - Double precision

The final value of the function b^B

INT - Double precision

The final value of the integral $\int_0^1 \left[1 - \exp\left\{\left(-\frac{\pi}{3}\right)\left(a^B\right)^3\left(1 - 3\Xi^2 + 2\Xi^3\right)\right\}\right] .\mathrm{d}\Xi$

GBPUV - Double precision

Grain boundary per unit volume after rolling

DG - Double precision

ΔG the driving force for recrystallization

A2.5 Error indicators

None

A2.6 Further comments

None

A2.7 Example

A2.7.1 Input text

```
Please input Time into recrystallization in s
1200

Please input Furnace Temperature in degrees centigrade
709

Input gauage of materials in mm
0.8

Please indicate whether sample touches furnace
1 for YES and 2 for NO

2
```

A2.7.2 Input file

```
124900000D0     SIGFLOW
84000000000D0   G
0.0001D0        D
0.3D0           GAMMA
0.75D0          REDN
900000D0        TWOQ
0.000D0         VOLFRAC
0.0000001D0     RADPART
6.8D15          EDSORT
```

A2.7.3 Program results

2.7.3.1 Output file 302AA_report

Ref	Property	Value	
1	Flow Stress =	124.9000	M pa
2	Shear Modulus =	84.0000	G Pa
3	Grain Size before rolling =	100.0000	Microns
4	Incoherent Grain Boundary Energy =	0.3000	J m^-2
5	Activation Energy for self diffusion =	900.0000	kJ mol^-1
6	Volume Fraction of Included Particles =	0.0000	
7	Mean Radius of Included Particles =	0.1000	Microns
8	Temperature =	709.0000	Centigrade
9	Time of Recrystallization =	1200.0000	Seconds
10	Rolling Reduction =	75.0000	%

```
VEL   =    1.6519089307945D-08
NDOT  =    6.2048069910058D+14
AB    =    605.89852299693
BB    =    51012752.712435
INT   =    1.0000000000000
GBPUV =    45150.005732118
DG    =    2.6222873952381
```

2.7.3.2 Output file 302AA_observables

X	Strip Temp	RX Grain Di	Time	Grains/Micron^2
0.0000000000	536	0.0000000000000	12.00	0.000000000000
0.0000000000	689	0.0000000000000	24.05	0.000000000000
0.0000000000	790	0.0000000000000	36.10	0.000000000000
0.0000000000	856	0.0000000000000	48.15	0.000000000463
0.0000000000	899	0.0000000000000	60.20	0.000001418594
0.0000000000	928	0.0000000000000	72.25	0.000202827555
0.0000000000	946	0.0000000001546	84.30	0.004911940863
0.0000000000	959	0.0000000002808	96.35	0.040063703171
0.0000570035	967	0.0000001373107	108.40	0.120928008145
0.0117741157	972	0.0000007908323	120.45	0.127384871335
0.0275153490	975	0.0000010494619	132.50	0.127384871335
0.0451804333	978	0.0000012381078	144.55	0.127384871335
0.0636985324	979	0.0000013883047	156.60	0.127384871335
0.0821878422	980	0.0000015113934	168.65	0.127384871335
0.1002947162	981	0.0000016151059	180.70	0.127384871335
0.1178497567	981	0.0000017043203	192.75	0.127384871335
0.1348022306	981	0.0000017824089	204.80	0.127384871335
0.1511741014	982	0.0000018518286	216.85	0.127384871335
0.1670161774	982	0.0000019143786	228.90	0.127384871335
0.1823853078	982	0.0000019713857	240.95	0.127384871335
0.1973340366	982	0.0000020238376	253.00	0.127384871335
0.2119068875	982	0.0000020724784	265.05	0.127384871335
0.2261398833	982	0.0000021178769	277.10	0.127384871335
0.2400614506	982	0.0000021604744	289.15	0.127384871335
0.2536937692	982	0.0000022006193	301.20	0.127384871335

0.2670541256	982	0.0000022385910	313.25	0.127384871335
0.2801560900	982	0.0000022746173	325.30	0.127384871335
0.2930104696	982	0.0000023088871	337.35	0.127384871335
0.3056260464	982	0.0000023415590	349.40	0.127384871335
0.3180101312	982	0.0000023727682	361.45	0.127384871335
0.3301689720	982	0.0000024026310	373.50	0.127384871335
0.3421080494	982	0.0000024312489	385.55	0.127384871335
0.3538322882	982	0.0000024587110	397.60	0.127384871335
0.3653462074	982	0.0000024850961	409.65	0.127384871335
0.3766540261	982	0.0000025104748	421.70	0.127384871335
0.3877597370	982	0.0000025349101	433.75	0.127384871335
0.3986671588	982	0.0000025584591	445.80	0.127384871335
0.4093799713	982	0.0000025811734	457.85	0.127384871335
0.4199017410	982	0.0000026031002	469.90	0.127384871335
0.4302359383	982	0.0000026242823	481.95	0.127384871335
0.4403859498	982	0.0000026447592	494.00	0.127384871335
0.4503550870	982	0.0000026645672	506.05	0.127384871335
0.4601465923	982	0.0000026837397	518.10	0.127384871335
0.4697636436	982	0.0000027023076	530.15	0.127384871335
0.4792093578	982	0.0000027202997	542.20	0.127384871335
0.4884867931	982	0.0000027377425	554.25	0.127384871335
0.4975989513	982	0.0000027546609	566.30	0.127384871335
0.5065487794	982	0.0000027710780	578.35	0.127384871335
0.5153391709	982	0.0000027870154	590.40	0.127384871335
0.5239729673	982	0.0000028024935	602.45	0.127384871335
0.5324529589	982	0.0000028175312	614.50	0.127384871335
0.5407818861	982	0.0000028321464	626.55	0.127384871335
0.5489624404	982	0.0000028463559	638.60	0.127384871335
0.5569972650	982	0.0000028601755	650.65	0.127384871335
0.5648889564	982	0.0000028736201	662.70	0.127384871335
0.5726400642	982	0.0000028867039	674.75	0.127384871335
0.5802530929	982	0.0000028994401	686.80	0.127384871335
0.5877305024	982	0.0000029118415	698.85	0.127384871335
0.5950747085	982	0.0000029239200	710.90	0.127384871335
0.6022880843	982	0.0000029356870	722.95	0.127384871335
0.6093729604	982	0.0000029471532	735.00	0.127384871335
0.6163316258	982	0.0000029583290	747.05	0.127384871335
0.6231663288	982	0.0000029692241	759.10	0.127384871335
0.6298792779	982	0.0000029798479	771.15	0.127384871335
0.6364726419	982	0.0000029902092	783.20	0.127384871335
0.6429485511	982	0.0000030003164	795.25	0.127384871335
0.6493090978	982	0.0000030101778	807.30	0.127384871335
0.6555563372	982	0.0000030198010	819.35	0.127384871335
0.6616922878	982	0.0000030291935	831.40	0.127384871335
0.6677189319	982	0.0000030383623	843.45	0.127384871335
0.6736382169	982	0.0000030473141	855.50	0.127384871335
0.6794520551	982	0.0000030560557	867.55	0.127384871335
0.6851623252	982	0.0000030645931	879.60	0.127384871335
0.6907708720	982	0.0000030729323	891.65	0.127384871335
0.6962795076	982	0.0000030810792	903.70	0.127384871335
0.7016900118	982	0.0000030890392	915.75	0.127384871335

0.7070041329	982	0.0000030968177	927.80	0.127384871335
0.7122235878	982	0.0000031044198	939.85	0.127384871335
0.7173500628	982	0.0000031118503	951.90	0.127384871335
0.7223852143	982	0.0000031191142	963.95	0.127384871335
0.7273306691	982	0.0000031262158	976.00	0.127384871335
0.7321880252	982	0.0000031331597	988.05	0.127384871335
0.7369588519	982	0.0000031399500	1000.10	0.127384871335
0.7416446907	982	0.0000031465909	1012.15	0.127384871335
0.7462470555	982	0.0000031530864	1024.20	0.127384871335
0.7507674334	982	0.0000031594401	1036.25	0.127384871335
0.7552072848	982	0.0000031656559	1048.30	0.127384871335
0.7595680444	982	0.0000031717374	1060.35	0.127384871335
0.7638511209	982	0.0000031776878	1072.40	0.127384871335
0.7680578984	982	0.0000031835107	1084.45	0.127384871335
0.7721897359	982	0.0000031892091	1096.50	0.127384871335
0.7762479686	982	0.0000031947863	1108.55	0.127384871335
0.7802339074	982	0.0000032002453	1120.60	0.127384871335
0.7841488405	982	0.0000032055889	1132.65	0.127384871335
0.7879940325	982	0.0000032108200	1144.70	0.127384871335
0.7917707260	982	0.0000032159415	1156.75	0.127384871335
0.7954801411	982	0.0000032209558	1168.80	0.127384871335
0.7991234763	982	0.0000032258657	1180.85	0.127384871335
0.8027019088	982	0.0000032306736	1192.90	0.127384871335

A2.8 Auxiliary routines

None

A2.9 Keywords

Stainless steel , overall transformation kinetics , anisothermal, recrystallization

REFERENCES

ANDERSON, W. A. and MEHL, R. F. (1945). *Transactions of the Metallurgical Society of the AIME*, **161**, 140–

ATKINS, P. W. (1994). *"Physical chemistry."* Fifth edition, published by Oxford University Press.

AVRAMI, M. (1939) *Journal of Chemical Physics*, **7**, 1103–1112

BAILEY, J. E. and HIRSCH, P. B. (1960). *Philosophical Magazine*, **5**, 485–497

BARRACLOUGH, D. R. and SELLARS, C. M., (1979). *Metal Science*, 257–267.

BATE, P. and HUTCHINSON, B., (1997). *Scripta Materialia*, **36**(2), 195–198

BAUER, C. L. (1974). *Canadian Metallurgical Quarterly,* **13**, 303–

BAYES, T. (1763). *Philosophical Transactions of the Royal Society of London,* **53**, 370-418. Reprinted in *Biometrika* (1958), **45**, 293–315.

BELLIER, S. P. and DOHERTY, R. D. (1977). *Acta Metallurgica*, **25**, 521–

BHADESHIA, H. K. D. H. (1999a). *ISIJ International*, **39**, 966–979

BHADESHIA, H. K. D. H. (1999b). *"Trends in Welding Research"*, ASM International Symposium, Ohio. 795–804

BHADESHIA, H. K. D. H., MACKAY, D. J. C. and SVENSSON L.-E., (1995). *Materials Science and Technology*, **11**, 1046–1051.

BHATIA, M. L., (1997). *Progress in Materials Science*, **42**, 59–77.

BOYER, H. E. and GALL, T. L. (eds.) (1984). *"Metals handbook — Desk edition."* First edition, published by the ASM, Ohio.

BRUN, F., YOSHIDA, T., ROBSON, J. D., NARAYAN, V., BHADESHIA, H. K. D. H., and MACKAY, D. J. C. (1999). *Materials Science and Technology*, **15**, 547–554

BUNN, A. M., EVANS P. V., BRISTOW, D. J. and GREER, A. L. (1997).

BYRNE J. G., (1965), *"Recovery, recrystallization and grain growth."* First Edition, published by MacMillan.

CAHN, J. W., (1956). *Acta Metallurgica*, **4**, 449–459

CAHN, J. W., (1962). *Acta Metallurgica*, **10**, 789–

CAHN, J. W., (1967) *Transactions of the metallurgical society of the AIME,* **239**, 610–

CAHN, R. W., (1945). *Journal of the Institute of Metals*, **76**,121–

CARR, C., (1997). *"Recrystallization behaviour of cold worked austenitic stainless steels."* Master of research dissertation, Sheffield Hallum University.

CHEN, H. and DHAR, V. (1991). *Information Processing and Management,* **25**(5), 405–432.

CHRISTIAN, J. W., (1975). *"Theory of transformations in metals and alloys, part 1."* Second edition, published by Pergamon press.

COLE, D. G. (2000). *"Design of heat-resistant steels for small power plant."* PhD thesis, University of Cambridge.

COLE, D., MARTIN-MORAN C., SHEARD, A. G., BHADESHIA, H. K. D. H., and MACKAY, D. J. C., (2000). *Science and Technology of Welding and Joining*, **5**(2), 81–89.

COTTRELL A., (1995) *"An introduction to metallurgy."* Second Edition, published by the Institute of Matherials

DILLAMORE, I. L., MORRIS, P. L., SMITH, C. J. E., and HUTCHINSON, W. B. (1972). *Proceedings of the Royal Society of London A.* **329**, 405–420

DINGLEY, D. J., and MCLEAN, D., (1967). *Acta Metallurgica*, **15**, 885–901.

DOHERTY, R. D., (1974). *Metal Science Journal*, **8**, 132–142

DOHERTY, R. D., HUGHES, D. A., HUMPHREYS, F. J., JONAS, J. J., JUUL JENSEN, D., KASSNER, M. E., KING W. E., MCNELLY, T. R., MCQUEEN, H. J. and ROLLETT A. D. (1997). *Materials Science and Engineering*, **A238**, 219–274.

GALE W. K. V., (1969) *"Iron and steel."* First Edition, published by Longmans

GARVARD, L., BHADESHIA, H. K. D. H., MACKAY, D. J. C. and SUZUKI, S. (1996). *Materials Science and Technology*, **12**, 453–463

GIBBS, M. (1997). *"Bayesian gaussian processes for regression and classification."* PhD thesis, University of Cambridge.

GLOVER, G and SELLARS, C. M. (1972), *Metallurgical Transactions of the AIME*, **3**, 2271–2280

HAESSNER, F. (1990). in *Recrystallization 90*, TMS, Warrendale, USA. 511–

HAYAKAWA, Y. and SZPUNAR, P. A., (1997). *Acta Materialia*, **45**(9), 3721–3730.

HERMANN, H., (1998). *Europhysics Letters*, **41**(3), 245-250

HILLERT, M. (1976). *Metal Science*, **13**, 118–

HILLERT, M. and SUNDMAN, B. (1976). *Acta Metallurgica*, **24**, 731–

HONEYCOMBE, R. W. K. and BHADESHIA, H. K. D. H., (1995). *"Steels, microstructure and properties."* Second Edition, published by Edward Arnold.

HOPKIN, G. J. and BHADESHIA, H. K. D. H. (2000), in *"Recrystallization — Fundamental aspects and relations to deformed microstructure."* Risø national laboratory, Denmark. 353–358.

HUMPHREYS, F. J. (1997). *Acta Materialia*, **45**(10), 4231–4240.

HUMPHREYS F. J. and HATHERLY M., (1996). *"Recrystallization and other annealing phenomena."* Corrected First Edition, published by Elsevier Science Ltd.

HUTCHINSON, B., (1992) *Scripta Metallurgica et Materialia*, **27**, 1471–1475.

HUTCHINSON, B., JONSSON, S. and RYDE L., (1989). *Scripta Metallurgica*, **23**, 671–676.

HUTCHINSON, B. (1998). *Philosophical Transactions of the Royal Society of London A.* **357**(1756), 1471–1485

HUTCHINSON, W. B., BESAG, F. M. C. and HONESS C. V. (1973). *Acta Metallurgica*, **21**, 1685–1691

JEFFREYS, H. (1939). *"Theory of probability."* First edition, Published by Oford University press.

JEFFERY J. W., (1971) *"Methods in X-ray crystallography."* First Edition, published by Academic Press

JOHNSON, W. A., and MEHL, R. F., (1939). *Transactions of the Metallallurgical Society of the AIME* **135**, 416–458

JONES, S. J. and BHADESHIA, H. K. D. H. (1997). *Acta Materialia*, **45**, 739–748

KOLMOGOROV A. N. (1937). *Izv. Akad. Nauk. USSR-Ser-Matemat.* **1**(3), 335-359.

KRUPP, F. A. (1912), Patent with imperial patent office, Berlin, Germany.

KUSIAK, J. and WAJDA, W. (1999). *Metallurgy Foundry Engineering,* **25**, 207–218

LALAM, S. H. (2000). *"Modelling of mechanical properties of ferritic steel weld metals."* PhD thesis, University of Cambridge.

LALAM, S. H., BHADESHIA, H. K. D. H. and MACKAY, D. J. C. (2000). *Australian Welding Journal*, **45** 33–37

LI, J. C. M., (1962). *Journal of Applied Physics*, **33**(10), 2958–2965

LÜCKE, K. and DETERT K. (1957). *Acta Metallurgica*, **5**, 628–

LÜCKE K. and STÜWE, H. P. (1963), in *"Recovery and recrystallization in metals."* Published by Interscience publications

MACKAY, D. J. (1992). *"Bayesian methods for Adaptive Models."* PhD thesis, Califionia Institute of Technology, Pasadena, USA.

MCELROY, R. J. and SZKOPIAK, Z. C. (1972). *International Metallurgical Reviews*, **17**, 175–202

NARAYAN, V., ABAD, R., LOPEZ, B., BHADESHIA, H. K. D. H. and MACKAY, D. J. C. (1999). *ISIJ International*, **39**(10), 999-1005.

NES, E., RYUM, N, and HUNDERI, O. (1985). *Acta Metallurgica*, **33**, 11–

NES, E., VATNE, H. E., PETTERSON, T., FURU, T. and MARTGINSEN, K. (2000), in *"Recrystallization — Fundamental aspects and relations to deformed microstructure."* Risø national laboratory, Denmark. 139–155

OATLEY, C. W. (1972). *"The scanning electron microscope, part 1, the instrument."* First edition, published by Cambridge University Press.

PARKER, S. V. (1997). *"Modelling of phase transformations in hot-rolled steels."* PhD thesis, University of Cambridge.

PUTNIS, A. (1992). *"Introduction to mineral sciences."* First edition, published by Cambridge University press.

READ, W. T. and SHOCKLEY, W. (1950). *Physics Reviews*, **78**, 275–

REED-HILL, R. E. and ABBASCHIAN R. (1994). *"Physical metallurgy principles."* Third Edition, published by PWS Press.

ROLLETT, A. D., (1997). *Progress in Materials Science*, **42**, 79-99

ROLLETT, A. D., SROLOVITZ, D. J., ANDERSON, M. P. and DOHERTY, R. D. (1992). *Acta Metallurgica et Materialia*, **40**(12), 3475–3495.

RYDE, L., HUTCHINSON, W. B., and JONSSON, S. (1990). in *Recrystallization 90*, TMS, Warrendale, USA. 313–

SANDBERG, A. and SANDSTRÖM, R., (1986a). *Materials Science and Technology*, **2**, 917–925.

SANDBERG, A. and SANDSTRÖM, R., (1986b). *Materials Science and Technology*, **2**, 926–937.

SCHEIDER and CLIMAX MOLYBDENUM COMPANY, (1960). *Foundry Trade Journal*, **108**, 562–

SCHMIDT, J. (1989). *Thermochim Acta*, **81**, 251–

SEIGEL, B. M., (1964) *"Modern developments in electron microscopy."* First Edition, published by Academic Press.

SHA, W. A., and BHADESHIA, H. K. D. H., (1997). *Materials Science and Engineering*, **A223**, 91–98.

SINGH, S. B. and BHADESHIA H. K. D. H., (1988). *Materials Science and Technology*, **14**, 832–834

SMITH, C. S. (1948). *Transactions of the Metallurgical Society of the AIME*, **127**, 15

SPEICH, G. R. and FISHER, R. M. (1966) in *Recrystallization, Grain Growth and Textures*, ASM, Ohio. 563–

SROLOVITZ, D. J., GREST, G. S. and ANDERSON, M. P., (1986) *Acta Metallurgica*, **34**(9), 1833-1845.

SROLOVITZ, D. J., GREST, G. S., ANDERSON, M. P. and ROLLETT, A. D. (1988). *Acta Metallurgica*, **36**(8), 2115–2128.

STEVEN, W. and HAYES, A. J. (1956). *Journal of the Iron and Steel Institute*, **183**, 349–359

STIGLER, S. M. (1986). *Statistical Science*, **1**(3), 359–378

SVENSSON, L.-E., and BHADESHIA, H. K. D. H. (1998). *Svetsaren*, **53**, 22–25.

TANCRET, F., BHADESHIA, H. K. D. H. and MACKAY, D. J. (1997). *ISIJ International*, **39**, 1020–1026.

TATEM, A. J., LEWIS, H. G., ATKINSON, P. and NIXON, M. S. (2000). *Proceedings of the 28^{th} Symposium on the Remote Sensing of the Environment*, **10**, 47–51.

TSUJI, N., TSUZAKI, K. and MAKI, T., (1994). *ISIJ International*, **34**(12), 1008–1017.

VANDER VOORT, G. F. (1984). *"Metallography, Principals and practice."* Second edition, published by McGraw-Hill.

VANDERMEER, R. A. (2000), in *"Recrystallization — Fundamental aspects and relations to deformed microstructure."* Risø national laboratory, Denmark. 179–200.

VANDERMEER, R. A. and JUUL JENSEN, D. (1995). *Metallurgical and Materials Transactions A*, **26A**, 2227-2234

VANDERMEER, R. A., MASUMARA, R. A. and RATH, B. B. (1991). *Acta Metallurgica et Materialia*, **39**(3), 383–389

VANDERMEER, R. A. and RATH, B. B. (2000), in *"Recrystallization — Fundamental aspects and relations to deformed microstructure."* Risø national laboratory, Denmark. 617–630.